

**FRACTURE REACTIVATION AND GOLD  
MINERALIZATION IN THE  
EPITHERMAL ENVIRONMENT: STRUCTURAL  
EVOLUTION OF THE ENDEAVOUR 42 GOLD DEPOSIT,  
NEW SOUTH WALES, AUSTRALIA**

by

**AMBER DAWN HENRY**

BSc (Honours in Geology), University of Alberta, 2002

A THESIS SUBMITTED IN PARTIAL FULFILMENT OF  
THE REQUIREMENTS FOR THE DEGREE OF

MASTER OF SCIENCE

in

THE FACULTY OF GRADUATE STUDIES  
(Geological Sciences)

THE UNIVERSITY OF BRITISH COLUMBIA  
(Vancouver)

July 2008

© Amber Dawn Henry, 2008

## ABSTRACT

The development of an open pit mine at the Endeavour 42 (E42) epithermal gold deposit, situated in the Junee-Narromine Volcanic Belt of the Ordovician Macquarie Arc, central New South Wales, has provided a 3D view of the structurally controlled deposit which was hitherto not available due to the paucity of outcrop in the region. Outcropping geological relationships present a complicated history of overprinting structural deformation and vein events, including the spatial characterization of the gold-mineralizing system. Host rocks consisting of interbedded sedimentary and resedimented volcanoclastic facies, trachyandesite and porphyritic andesite lavas and intrusions (coherent and autoclastic facies), intruded by a large diorite sill, were initially tilted and faulted, followed by the emplacement of multiple dyke phases along faults. Economic gold mineralization at E42 is restricted to faults, fault-hosted breccias, and veins, and was deposited over a period spanning two distinct structural regimes. Early gold-bearing veins are steeply dipping and interpreted as forming coevally along two sets of faults and dykes within a tensional stress regime. High grade fault-hosted, hydrothermally cemented breccia intervals are included temporally with early gold-bearing veins based on comparable mineralogy and steep, fault parallel orientations. Crosscutting the early steep gold-bearing vein sets are two populations of coeval inclined gold-bearing veins, dipping moderately to the southwest and northwest, respectively, which formed in a compressional stress regime with tension directed subvertically. The E42 epithermal deposit likely developed in the period of overall crustal extension, ca. 443-433 Ma, following Phase 1 of the Late Ordovician – Early Silurian Benambran Orogeny.

The generation of permeability, styles of fracture propagation, and the reactivation of pre-existing planes of weakness in the rock package are key factors in the development and current geometry of the E42 gold deposit. High grade veins and faults are commonly flanked by sericite-quartz  $\pm$  carbonate alteration haloes, which exhibit consistent geochemical patterns for metals and pathfinder elements, both laterally away from structures, and vertically within the deposit. Au, Ag, As, Hg, Sb, Tl, Cu, Pb, and Zn, all display increasing concentrations towards high-grade structures, as well as higher up in the epithermal system, with varying dispersion haloes.

# TABLE OF CONTENTS

<b>ABSTRACT .....</b>	<b>ii</b>
<b>TABLE OF CONTENTS .....</b>	<b>iii</b>
<b>LIST OF TABLES.....</b>	<b>vii</b>
<b>LIST OF FIGURES.....</b>	<b>viii</b>
<b>ACKNOWLEDGEMENTS.....</b>	<b>xi</b>
<b>DEDICATION .....</b>	<b>xii</b>
<b>CHAPTER 1: INTRODUCTION .....</b>	<b>1</b>
<b>1.1 Aims of Study.....</b>	<b>1</b>
<b>1.2 Location.....</b>	<b>2</b>
<b>1.3 Exploration History.....</b>	<b>2</b>
<b>CHAPTER 2: REGIONAL GEOLOGY .....</b>	<b>5</b>
<b>2.1 Introduction .....</b>	<b>5</b>
<b>2.2 Lachlan Orogen .....</b>	<b>5</b>
2.2.1 Multiple Subduction Zone Scenario.....	6
2.2.2 Strike-Slip Subduction Zone Scenario .....	8
Delamerian Cycle.....	8
Lachlan Supercycle.....	8
Benambran Cycle.....	8
Tabberabberan Cycle .....	10
Kanimblan Cycle .....	10
2.2.3 Scenario Used in This Study .....	11
<b>2.3 Macquarie Arc.....</b>	<b>12</b>
2.3.1 Nature and Distribution of Ordovician Volcanic Rocks .....	12
The Junee-Narromine Volcanic Belt.....	12
The Molong and Rockley-Gulgong Volcanic Belts.....	13
2.3.2 Tectonic Evolution of the Macquarie Arc.....	13
Benambran Cycle.....	14
Tabberabberan Cycle .....	15
Kanimblan Cycle .....	16
<b>2.4 Lachlan Orogen-scale Structures.....</b>	<b>16</b>
2.4.1 Gilmore and Tullamore Trends.....	16
2.4.2 Lachlan Transverse Zone .....	17
Rock Chemistry in the Lachlan Transverse Zone.....	18
Mineralization and Structure in the Lachlan Transverse Zone .....	18
<b>2.5 Cowal Igneous Complex .....</b>	<b>19</b>
2.5.1 Cowal Igneous Complex Lithology .....	19
2.5.2 Overlying Silurian-Devonian Stratigraphy .....	20

2.5.3 Tectonic Setting of the Cowal Igneous Complex .....	21
Booberoi and Marsden Faults .....	21
Imbricate Zone .....	22
Fault Blocks within the Cowal Igneous Complex .....	22
<b>2.6 Ordovician Mineralization .....</b>	<b>23</b>
2.6.1 Metallogeny of the Macquarie Arc .....	23
2.6.2 Mineralization of the Cowal Igneous Complex .....	23
<b>CHAPTER 3: ENDEAVOUR 42 GEOLOGY .....</b>	<b>37</b>
<b>3.1 Introduction .....</b>	<b>37</b>
<b>3.2 Stratigraphic Overview.....</b>	<b>37</b>
3.2.1 Upper and Lower Volcaniclastic Sequences .....	37
Description .....	37
Lower Volcaniclastic Sequence .....	37
Upper Volcaniclastic Sequence .....	38
Interpretation .....	39
3.2.2 Eastern Volcaniclastic Sequence .....	40
Description .....	40
Interpretation .....	40
3.2.3 Trachyandesite Lava .....	40
Description .....	40
Interpretation .....	41
3.2.4 Porphyritic Andesite .....	41
Description .....	41
Coherent Andesite .....	42
Monomictic Andesite Breccia .....	42
Interpretation .....	42
<b>3.3 Intrusive Units .....</b>	<b>43</b>
3.3.1 Diorite Sill Complex .....	43
Description .....	43
Interpretation .....	44
3.3.2 Pre-gold Dykes .....	44
Description .....	44
Interpretation .....	45
3.3.3 Post-gold Dykes .....	45
Description .....	45
Interpretation .....	46
<b>3.4 Breccia Facies .....</b>	<b>47</b>
3.4.1 E42 Breccia Complex .....	47
Description .....	47
Interpretation .....	48

<b>CHAPTER 4: STRUCTURAL HISTORY OF THE E42 DEPOSIT .....</b>	<b>52</b>
<b>4.1 Introduction .....</b>	<b>52</b>
<b>4.2 Field Methods and Data Presentation .....</b>	<b>52</b>
<b>4.3 Review of Mineralizing Fluid Characteristics .....</b>	<b>53</b>
<b>4.4 Radiometric Dating at E42 and Timing of Gold Mineralization .....</b>	<b>54</b>
4.4.1 Sericite Alteration Haloes .....	54
4.4.2 Adularia in Gold-bearing Veins .....	55
<b>4.5 Structure Fabrics.....</b>	<b>56</b>
4.5.1 Bedding .....	56
4.5.2 Faults .....	56
4.5.3 Dykes .....	57
<b>4.6 Vein Paragenesis.....</b>	<b>58</b>
4.6.1 Previous Work.....	58
4.6.2 Variations in Vein Composition along Length .....	58
4.6.3 Pre-gold Veins.....	59
4.6.4 Syn-gold Veins.....	60
Steep Gold-bearing Carbonate-Base Metal Veins .....	60
Steep Fault-hosted Breccias .....	61
Stage 1: Gold-bearing Breccias .....	62
Stage 2: Ankerite-Pyrite-Sphalerite Breccias .....	62
Stage 3: Barren Ankerite Breccias.....	63
Inclined Gold-bearing Carbonate-Base Metal Veins .....	63
Quartz-Pyrite ± Calcite Veins .....	64
4.6.5 Post-gold Veins .....	64
Carbonate Reactivation of Gold-bearing Structures .....	64
Steep North-striking Carbonate Event .....	65
Youngest Carbonate-Chlorite-Hematite Veins and Faults.....	65
<b>4.7 Geometry of Veins and Structures at E42.....</b>	<b>66</b>
4.7.1 Fault and Dyke Development.....	66
4.7.2 Pre-gold Veins.....	67
4.7.3 Syn-gold Veins.....	67
Steep Gold-bearing Carbonate-Base Metal Veins .....	67
Steep Fault-hosted Breccias .....	69
Quartz-Sulfide Breccia Formation – Scenario One .....	69
Quartz-Sulfide Breccia Formation – Scenario Two.....	70
Quartz-Sulfide Breccia Predictability .....	71
Late Inclined Gold-bearing Veins .....	72
4.7.4 Post-gold Veins .....	73
Carbonate Reactivation of Gold-bearing Structures .....	73
Steep North-trending Carbonate Event .....	73
Late Carbonate Event, Carbonate-Chlorite-Hematite Veins and Faults .....	74
<b>4.8 Discussion .....</b>	<b>75</b>
4.8.1 Deposit-scale Structural Interpretations .....	75

Local Pre-gold Deformation .....	75
Formation of Gold-bearing Vein System at E42 .....	75
Steep Gold-bearing Vein Formation .....	75
Inclined Gold-bearing Vein Formation.....	76
4.8.2 Cowal Igneous Complex-scale Structural Interpretations.....	78
Bounding Faults to the Cowal Igneous Complex .....	78
Fault Blocks within the Cowal Igneous Complex .....	78
4.8.3 Macquarie Arc-scale Structural Interpretations .....	79
Timing of Deformation .....	80
Benambran Cycle.....	80
Benambran Orogeny Phase 1 ca. 443 Ma.....	81
Extension after Phase 1 Deformation ca. 443-433 Ma .....	81
Benambran Orogeny Phase 2 ca. 433-430 Ma .....	82
Tabberabberan Cycle .....	82
Tabberabberan Orogeny ca. 411 Ma.....	82
Kanimblan Cycle .....	83
Kanimblan Orogeny ca. 340 Ma.....	83
<b>CHAPTER 5: GEOCHEMICAL ZONATION AT E42.....</b>	<b>122</b>
<b>5.1 Introduction .....</b>	<b>122</b>
<b>5.2 E42 Deposit-scale Alteration .....</b>	<b>122</b>
5.2.1 Chlorite-Carbonate-Hematite ± Epidote .....	122
5.2.2 Chlorite-Carbonate-Pyrite .....	123
5.2.3 K-feldspar-Quartz .....	123
5.2.4 Sericite-Quartz ± Carbonate.....	124
<b>5.3 Geochemical Zonation of Sericite Alteration Haloes .....</b>	<b>125</b>
5.3.1 Sampling and Analytical Methods.....	125
5.3.2 Compositional Variations.....	126
5.3.3 Alteration Indices .....	126
5.3.4 Horizontal Zonation .....	128
5.3.5 Vertical Zonation .....	131
5.3.6 Interpretation.....	132
<b>CHAPTER 6: SUMMARY.....</b>	<b>144</b>
<b>6.1 Conclusions .....</b>	<b>144</b>
<b>6.2 Exploration Implications .....</b>	<b>146</b>
<b>6.3 Future Work .....</b>	<b>147</b>
<b>REFERENCES .....</b>	<b>148</b>
<b>APPENDIX A: Vein Adularia <sup>40</sup>Ar-<sup>39</sup>Ar: Detailed Dating Methodology, Data Tables, and Summary Plots.....</b>	<b>159</b>
<b>APPENDIX B: 48 Multielement + Hg + Au Geochemistry Data Tables.....</b>	<b>170</b>

## LIST OF TABLES

<b>TABLE 2.1</b> SCHEMATIC TIME-SPACE PLOT OF DEFORMATIONAL EVENTS IN THE MACQUARIE ARC .....	26
<b>TABLE 4.1</b> SUMMARY OF DRILLCORE MEASUREMENTS WITHIN EACH DEPOSIT-SCALE FAULT BLOCK .....	85
<b>TABLE 4.2</b> SUMMARY OF AVERAGE STRUCTURES AND VEIN ORIENTATIONS AND COMPOSITIONS FOR E42 .....	86
<b>TABLE 4.3</b> SUMMARY OF FAULT-HOSTED BRECCIA STAGES: RELATIVE TIMING, MINERALOGY, AND AVERAGE ORIENTATIONS .....	87
<b>TABLE 4.4</b> SCHEMATIC TIME-SPACE PLOT OF DEFORMATIONAL EVENTS IN THE MACQUARIE ARC .....	88
<b>TABLE 5.1</b> SUMMARY OF ALTERATION ASSEMBLAGES, THEIR PREDOMINANT ROCK TYPES, AND DISTINGUISHING CHARACTERISTICS.....	134
<b>TABLE 5.2</b> DETECTION LIMITS FOR MULTIELEMENT GEOCHEMICAL DATA, FROM ALS CHEMEX.....	135

## LIST OF FIGURES

<b>FIGURE 1.1</b> MAP OF WEST WYALONG AND SURROUNDING AREA .....	4
<b>FIGURE 2.1</b> EXTENTS OF THE LACHLAN OROGEN IN THE TASMANIDES .....	27
<b>FIGURE 2.2</b> MULTIPLE SUBDUCTION ZONE MODEL FOR THE TECTONIC EVOLUTION OF THE LACHLAN OROGEN .....	28
<b>FIGURE 2.3</b> EXTENTS OF MACQUARIE ARC AND DEPOSITIONAL BASINS, THE LOCATION OF PRINCIPAL ORE DEPOSITS AND OROGEN-SCALE TRANSVERSE ZONES .....	29
<b>FIGURE 2.4</b> STRIKE-SLIP MODEL FOR THE TECTONIC EVOLUTION OF THE LACHLAN OROGEN	30
<b>FIGURE 2.5</b> EXTENTS OF JUNEE-NARROMINE VOLCANIC BELT .....	31
<b>FIGURE 2.6</b> INTERPRETED SEISMIC PROFILES ACROSS THE JUNEE-NARROMINE BELT .....	32
<b>FIGURE 2.7</b> AEROMAGNETIC SURVEY OVER THE COWAL IGNEOUS COMPLEX .....	33
<b>FIGURE 2.8</b> INTERPRETED GEOLOGY OF THE COWAL IGNEOUS COMPLEX .....	34
<b>FIGURE 2.9</b> EXAMPLES OF THE MANNA CONGLOMERATE IN THE BOOBEROI FAULT .....	36
<b>FIGURE 3.1</b> SCHEMATIC EAST-WEST CROSS SECTION THROUGH E42 ALONG 7800N .....	50
<b>FIGURE 3.2</b> SCHEMATIC PLAN VIEW OF E42 AT 150M BELOW SURFACE .....	51
<b>FIGURE 4.1</b> SCHEMATIC EAST-WEST CROSS SECTION THROUGH E42 ALONG 7800N .....	89
<b>FIGURE 4.2</b> ENDEAVOUR 42 OPEN PIT PLAN AS OF MAY 2007 .....	90
<b>FIGURE 4.3</b> STERONETS DISPLAYING BEDDING AND FAULTS .....	91
<b>FIGURE 4.4</b> EXAMPLES OF FAULTS IN THE OPEN PIT .....	92
<b>FIGURE 4.5</b> STERONETS DISPLAYING FAULTS, DYKES, AND EARLY CARBONATE VEINS .....	93
<b>FIGURE 4.6</b> PANORAMIC PHOTO OF THE WESTERN PIT WALL ALONG 1155RL .....	94
<b>FIGURE 4.7</b> EXAMPLES OF VARIATION IN MINERALOGY ALONG VEIN LENGTH .....	95
<b>FIGURE 4.8</b> PHOTOMICROGRAPHS OF EARLY CARBONATE VEINS AND GOLD-BEARING VEINS	96
<b>FIGURE 4.9</b> STERONETS DISPLAYING STEEP AND INCLINED GOLD-BEARING VEINS .....	97
<b>FIGURE 4.10</b> PHOTOMICROGRAPHS OF GOLD-BEARING VEINS .....	98
<b>FIGURE 4.11</b> EXAMPLES OF GOLD-BEARING AND BARREN FAULT-HOSTED BRECCIAS .....	99
<b>FIGURE 4.12</b> FAULT-HOSTED BRECCIA ALONG THE WESTERN PIT WALL .....	100
<b>FIGURE 4.13</b> STERONETS OF FAULT-HOSTED BRECCIAS, CROSSCUTTING GOLD-BEARING VEIN PAIRS, AND QUARTZ-PYRITE VEINS .....	101
<b>FIGURE 4.14</b> EXAMPLES OF GOLD-BEARING VEINS .....	102

<b>FIGURE 4.15</b> STEREAONETS OF POST-GOLD CARBONATE DOMINATED VEIN POPULATIONS AND SLICKENFIBRES .....	103
<b>FIGURE 4.16</b> EXAMPLES OF CARBONATE REACTIVATION OF GOLD-BEARING VEINS.....	104
<b>FIGURE 4.17</b> EXAMPLES OF POST-GOLD CARBONATE DOMINATED VEINS .....	105
<b>FIGURE 4.18</b> BEDDING PARALLEL VEINS, SLICKENFIBRES, AND STEPPED VEIN GEOMETRY ..	106
<b>FIGURE 4.19</b> STEREAONETS DISPLAYING ROTATION OF BEDDING, FAULTS, AND DYKES .....	107
<b>FIGURE 4.20</b> MAP OF WEST WYALONG AND SURROUNDING AREA .....	108
<b>FIGURE 4.21</b> STRUCTURAL PERMEABILITY IN A TRIAXIAL STRESS REGIME.....	109
<b>FIGURE 4.22</b> COMPOSITE FAILURE ENVELOPE AND THE RESHEAR CONDITIONS FOR A COHENSIONLESS FAULT, AND EXPECTED ORIENTATIONS OF SHEAR, EXTENSIONAL SHEAR, AND EXTENSIONAL FRACTURES RELATIVE TO PRINCIPAL STRESS AXES.....	110
<b>FIGURE 4.23</b> CONDITIONS FOR RESHEAR ALONG A COHENSIONLESS FAULT, AND THE ORIENTATION OF PRINCIPAL COMPRESSIVE STRESS FOR THE COEVAL TENSIONAL OPENING OF BOTH STEEP GOLD-BEARING VEIN POPULATIONS .....	111
<b>FIGURE 4.24</b> SCHEMATIC FAULT TRACE DIAGRAMS .....	112
<b>FIGURE 4.25</b> TWO SCENARIOS FOR QUARTZ-SULFIDE BRECCIA FORMATION.....	113
<b>FIGURE 4.26</b> BRITTLE FAILURE MODES FOR EXTENSIONAL AND COMPRESSIONAL REGIMES	114
<b>FIGURE 4.27</b> EXAMPLES OF STEPPED GEOMETRY IN INCLINED GOLD-BEARING VEINS, AND GROWTH FIBRES ALONG A REACTIVATED VEIN.....	115
<b>FIGURE 4.28</b> STEREAONETS OF PRINCIPAL COMPRESSIVE STRESS FOR CARBONATE REACTIVATION OF GOLD-BEARING STRUCTURES, AND POLES TO BEDDING AND MAIN GOLD-BEARING VEIN SETS AT E41 AND E42 .....	116
<b>FIGURE 4.29</b> SCHEMATIC BLOCK DIAGRAMS AND STEREAONET FOR LATE SLICKENFIBRE FORMATION.....	117
<b>FIGURE 4.30</b> SCHEMATIC BLOCK DIAGRAMS FOR THE DISTRIBUTION OF GOLD-BEARING VEINS AT E42 .....	118
<b>FIGURE 4.31</b> MOHR DIAGRAMS FOR THE EXTENSIONAL REFRACTURE OF STEEP FAULTS AND DYKES .....	119
<b>FIGURE 4.32</b> INTERPRETED SEISMIC PROFILES ACROSS THE JUNEE-NARROMINE BELT .....	120
<b>FIGURE 4.33</b> AEROMAGNETIC SURVEY OVER THE COWAL IGNEOUS COMPLEX.....	121
<b>FIGURE 5.1</b> PHOTOS OF FAULT AND VEIN DISPLAYING SERICITIZED ALTERATION HALOES ..	136
<b>FIGURE 5.2</b> MODIFIED $Zr/TiO_2$ VERSUS $Nb/Y$ DIAGRAM FOR THE TRACHYANDESITE LAVA AND THE UPPER AND LOWER VOLCANICLASTIC ROCKS AT E42 .....	137
<b>FIGURE 5.3</b> ALTERATION BOX PLOT (CCPI VS. AI).....	138
<b>FIGURE 5.4</b> MOLAR ELEMENT RATIO PLOT OF $K/Al$ VERSUS $(2Ca+Na+K)/Al$ .....	139

**FIGURE 5.5** MOLAR  $K/(2Ca+Na+K)$  VALUES VERSUS DISTANCE FROM GOLD-BEARING VEINS AND DEPTH .....140

**FIGURE 5.6** CONCENTRATIONS OF METALS AND POTENTIAL PATHFINDER ELEMENTS VERSUS MOLAR  $K/(2Ca+Na+K)$  VALUES FOR SAMPLES SURROUNDING GOLD-BEARING VEINS .....141

**FIGURE 5.7** CONCENTRATIONS OF METALS AND POTENTIAL PATHFINDER ELEMENTS VERSUS DISTANCE FROM GOLD-BEARING VEINS .....142

**FIGURE 5.8** CONCENTRATIONS OF METALS AND POTENTIAL PATHFINDER ELEMENTS VERSUS DEPTH.....143

## ACKNOWLEDGEMENTS

This thesis was completed as part of an MDRU-CODES research project investigating shallow and deep-level alkalic mineral deposits. Full sponsorship for the project was provided by Barrick Gold Corp., Newmont Mining, TeckCominco, and AngloGold Ashanti, with logistical and field support provided by Barrick Gold of Australia Ltd. Additional funding for the E42 project was provided by a personal NSERC postgraduate scholarship and SEG student research grant.

Big thanks to my supervisor, Dick Tosdal, for good ideas, calming advice, and being patient while forcing me to learn to drive a manual ute on the opposite side of the road, and my co-supervisor, Ken Hickey, for mind-bending conceptual structure conversations and the Pie Club. Claire Chamberlain, Kirstie Simpson, and Thomas Bissig were all invaluable sources of great ideas, discussions, and edits, for which I am exceedingly grateful. Thanks to Tom Ullrich (PCIGR) for dating my adularia, and to Arne Toma who was always around to fix whatever I had done wrong with my computer.

To all the guys and girls at the mine: so many people to thank, but especially Paul McInnes and Andrew Bywater for all their time and assistance, T.J. Strickland for many good times driving to and from the pit, and all the galahs up at Exploration (yes, Casey, you're one of them).

Wojtek, for your laugh and wonderful smile and enthusiasm - you kept me laughing even with all the głupie ćmy i przetpotopowy skały. For Moorilla wine, Clifton Beach surfing, and hot rum and stuffed llamas in Tarma: serdecznie ci dziękuję!

Thanks to Jack&Dianne and Schneer for all the Salads and Science (and mindless chatter) enjoyed in 059; Luke for the train mishaps and the Gypsy Bar; Vic for being a shoulder, sounding board, and all around amazing friend; and Stefan for providing Swiss chocolate in my (multiple) times of direst need. My fellow grad students and co-sufferers, too many to list here, but you've all provided refreshing insights, much needed coffee breaks, and countless laughs – big hugs to all. To Rae, LEG, and Stephannie: what would I do without you guys?

And finally, a mis papás: no te puedo decir cuanto tu amor y tus oraciones me han bendecido. Te quiero más cada día que pasa, y estoy tan orgullosa de ustedes y como viven con integridad. Es algo a que aspiro, y soy tan agradecida por tu ejemplo – besotes!

## **DEDICATION**

This work is dedicated to Papa, for loving this Martha immeasurably  
more than she could ask or imagine!

# CHAPTER 1: INTRODUCTION

## 1.1 Aims of Study

The Endeavour 42 (E42) open pit mine, currently owned and operated by Barrick Gold of Australia Ltd., has been in production since June 2006. Located in the Junee-Narromine Volcanic Belt of the Ordovician Macquarie Arc, central New South Wales (Figure 1.1), it is a low grade gold deposit with total estimated gold reserves of 82.8 Mt at 0.99 g/t (2.88 M oz; Barrick Year End Report, 2007). Due to the lack of significant surface outcrop in the region, the E42 open pit provides the first opportunity to view the local geology in three dimensions. In this study, bench mapping of unweathered rock in the E42 open pit as well as the examination of selected drillcore has been used to improve the understanding of the deposit by:

- defining the structural architecture
- distinguishing between multiple vein generations, their structural controls, and relative timing
- determining how gold-bearing veins fit into the regional structural history
- ascertaining if sericite-dominated alteration haloes commonly found surrounding high fluid flow zones, and specifically around gold-bearing veins, exhibit geochemical zoning that may provide a vector towards ore

In examining the evolution of the E42 deposit, this study also aims to:

- determine how permeability is created in a rock package, and how it affects fluid flow in hydrothermal systems and the development of epithermal ore deposits
- examine the style and geometry of fracture/fault propagation
- define the effects of pre-existing heterogeneities in a rock package on the structural history
- place the evolution of the E42 deposit in the regional tectonic framework
- investigate the economic exploration implications for the area surrounding E42

## **1.2 Location**

The E42 mine is situated on the western shore of Lake Cowal, a shallow ephemeral lake located approximately 40km north-northeast of the town of West Wyalong, within the Bland Shire council in central New South Wales (Figure 1.1). The mine is accessed by a series of paved and unpaved secondary Shire roads and local farm station roads. Land surrounding the mine is cultivated for cereal crops, including the lake bed when it is dry, or used for sheep and cattle grazing. Historically, Lake Cowal has been dry for periods of up to 20 years and last contained water in December 2001 (Ingpen, 1995; Strickland, 2005). Much of the natural vegetation in the area has been cleared for farming and grazing purposes, but there are scattered trees and bushes, predominantly eucalyptus trees and lignum bushes (Ingpen, 1995), that remain in many of the paddocks and in a few isolated large stands of natural forest.

## **1.3 Exploration History**

The Lake Cowal area is almost entirely covered by lacustrine deposits, therefore limited exploration had been undertaken prior to 1980 when Geopeko Ltd., the exploration arm of Peko Wallsend Ltd., targeted the area for a porphyry copper-gold exploration program. This exploration program was based on the similarity of aeromagnetic signatures at Lake Cowal to the Goonumbla porphyry deposits located further north in the Junee-Narromine Volcanic Belt (Figure 2.3) (McInnes et al., 1998). E42, among other prospects, was discovered using a combination of aeromagnetic and gravity geophysical surveys, and reconnaissance drilling. Exploration by Geopeko Ltd. in the area was intermittent over the following eight years, interrupted and postponed multiple times by the seasonal flooding of Lake Cowal (McInnes et al., 1998). In 1988, North Ltd. was created as a merger between Geopeko Ltd. and North Broken Hill Ltd., and from 1993 to 1995 completed a preliminary feasibility study, a resource delineation drilling program, and finally a detailed feasibility study on the E42 deposit (McInnes pers. comm., 2008; Strickland, 2005). North Ltd.'s development proposition for E42 was not approved until 1999, by which time the company had been taken over by Rio Tinto. The Lake Cowal property was sold to Homestake Mining in 2001 and as part of its merger with Homestake Mining that year, Barrick Gold of Australia Ltd. acquired the Cowal Gold Project (McInnes pers. comm., 2008). An intensive resource

drilling program and feasibility study on E42 was undertaken by Barrick Gold of Australia Ltd. from 2001 to 2005, and mine production began in June 2006.

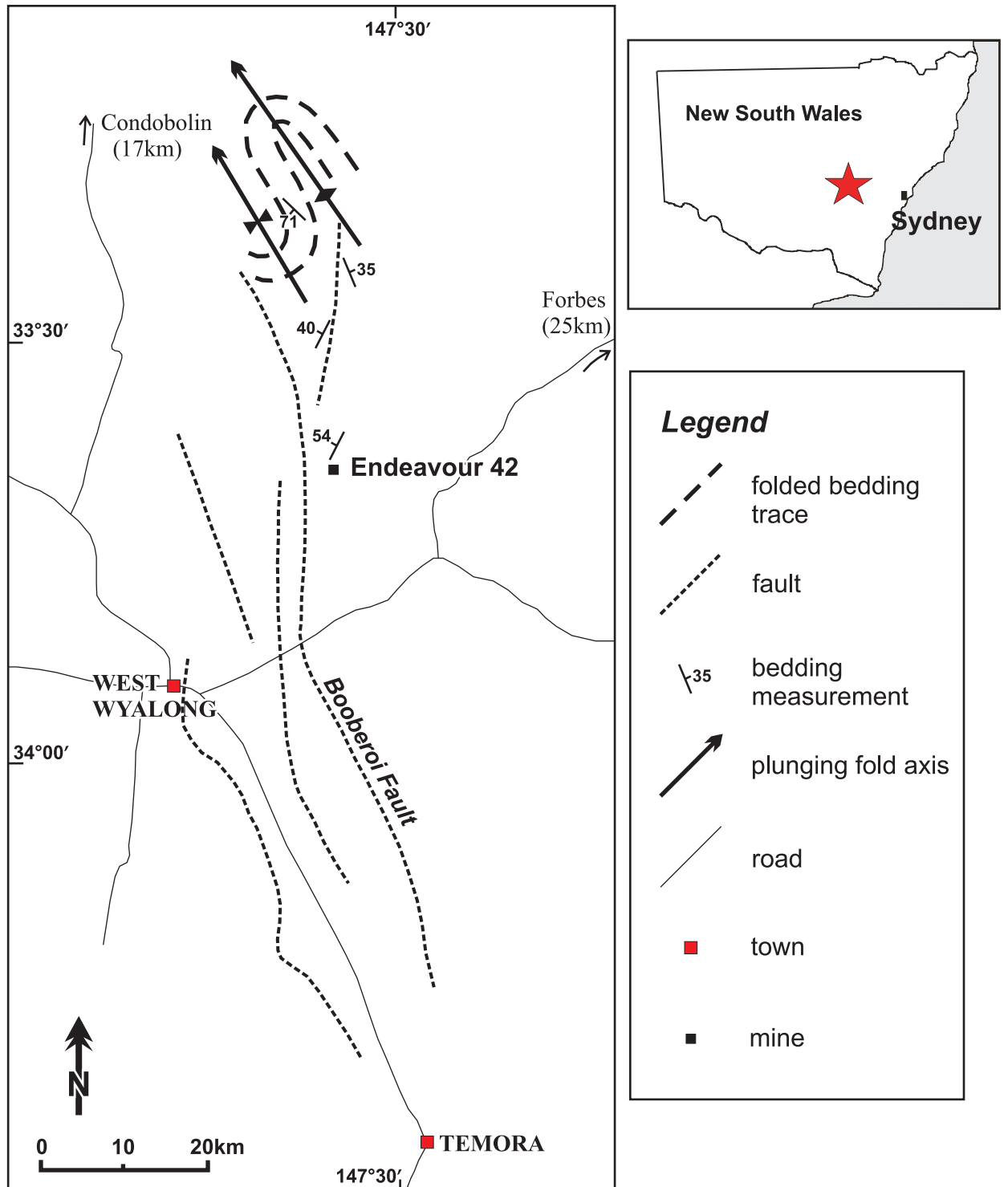


**Figure 1.1** Map of West Wyalong and surrounding area with selected structural interpretations and measurements taken from Ingpen (1995).

## **CHAPTER 2: REGIONAL GEOLOGY**

### **2.1 Introduction**

The Lachlan Orogen is one of several orogenic belts that constitute the Tasmanides of eastern Australia (Figure 2.1). Combined, these orogenic belts record the break-up of a Mesoproterozoic supercontinent, the formation of a Late Neoproterozoic passive margin, and the founding of a series of convergent margin orogenic belts along one sector of the Pacific margin of Gondwana starting in the Middle Cambrian (Glen, 2005). Deformation recorded in these belts spans from the Middle Cambrian up until the Triassic (ca. 227 Ma), with the onset of the Gondwana-Pangaea supercontinental break-up. It is generally agreed that the Australian craton was part of the Rodinia supercontinent and that rifting marked the opening of the proto-Pacific Ocean and separation of Laurentia from Gondwana. Each of the orogenic belts of the Tasmanides has been divided into several Subprovinces (Figure 2.1) which have been further subdivided into structural zones and blocks. The current study focuses on a portion of the Lachlan Orogen's Eastern Subprovince.

This chapter includes an overview of the tectonic history of the Lachlan Orogen and specifically of the Macquarie Arc, major structural features influencing the Eastern Subprovince of the orogen, rocks of the Cowal Igneous Complex and adjacent regions, and the metallogeny and distribution of mineralization of the Macquarie Arc and the Cowal Igneous Complex.

### **2.2 Lachlan Orogen**

The Lachlan Orogen extends approximately 1000km by 700km (Fergusson and Coney, 1992) and contains a diverse array of base and precious metal deposits, including abundant copper and gold. The orogen is divided into four structurally distinct Subprovinces, each separated by major faults and sutures (Figure 2.1). Historically, the subdivision of the Tasmanides was based predominantly on the age distributions of rock units within each of the Subprovinces, with a generalized eastward-younging of ages within each belt. However, subsequent work has demonstrated the presence of older rocks in the so-called younger provinces, indicating that the development of the Tasmanides was not so simple (Glen, 2005). The Western, Southwestern, and Central Subprovinces are dominated by turbidite

successions consisting of quartz-rich sandstones and black shales. The Eastern Subprovince consists of mafic volcanic, volcanoclastic, and carbonate rocks, as well as quartz-rich turbidites and extensive black shales in the easternmost region (VandenBerg and Stewart, 1992; Gray et al., 2002). The substrate of the Lachlan Orogen is no older than Early Ordovician, and is mafic and igneous in character (Williams and Chappell, 1998; Keay et al., 1997; Collins, 1998). These observations, which preclude a continental substrate, are consistent with high positive  $\epsilon_{Nd}$  data (Glen et al., 1998; Crawford et al., 2007a), as well as primitive Pb isotopic ratios (Carr et al., 1995) from the Ordovician Macquarie Arc. The formation of the Lachlan Orogen is a topic of much debate and controversy, and though multiple different scenarios are suggested, there is no full consensus on the tectonic setting. There are, however, two more widely accepted models.

### **2.2.1 Multiple Subduction Zone Scenario**

According to Gray et al. (2002), deformation in the Lachlan Orogen commenced between ca. 460 and 430 Ma. Although there is little consensus on the tectonic evolution of eastern Australia, it is generally accepted that there was a long-lived, craton-directed subduction zone off Gondwana during the Palaeozoic. Two west-dipping subduction zones along the eastern margin of Gondwana are suggested by Gray et al. (2002) to explain the presence of two zones of eastward migrating deformation and granitic plutonism preserved in the Lachlan Orogen. The granites in question young to the east, as does the east-vergent deformation; two lines of evidence which support slab rollback associated with west-dipping subduction. An alternative explanation for these two eastward-migrating belts requires strike-slip duplication within the orogen (see following section), but Gray and Foster (1998) argue there is no preserved structural evidence of large displacement strike-slip translation.

Gray et al. (2002) suggest that three Silurian subduction zones in a relatively complex oceanic setting are responsible for the complexity of deformation patterns in the Lachlan Orogen (Figure 2.2). The proposed differences in the tectonic positions of the Western, Central, and Eastern Subprovinces are reflected by the differences in the deformational, metamorphic, and magmatic characters of each. Subduction zone 1 in the west (Figure 2.2) (Gray and Foster, 1997; Gray et al., 2002) was west-dipping and present from 460-420 Ma (Foster et al., 1999). Since the subducting slab was probably no more than ca. 50 million years old, the oceanic crust would be buoyant, resulting in a shallowly dipping subduction

zone. Melting would not occur due to the shallow subduction angle, accounting for the lack of volcanic arc associated with subduction zone 1 (Gray et al., 2002). Subduction zone 2 was east-dipping (Figure 2.2), short-lived from ca. 440 to 420 Ma (Foster et al., 1999), and lay at the boundary between the Central and Western Subprovinces (Gray et al., 2002); a boundary interpreted as the margin between the Central and Southwestern Subprovinces of the Lachlan Orogen by Glen (2005). The third subduction zone interpreted by Gray et al. (2002) is at the Gondwana-Proto-Pacific plate boundary (Figure 2.2), the associated arc of which is the Macquarie Arc (e.g. Glen, 2005).

During the Late Ordovician-Silurian, deformation of the Cambrian to Middle Ordovician marginal basin (Figure 2.2) was controlled by subduction occurring in both the Western and Central-Eastern Lachlan Orogen. This phase in the tectonic evolution of the orogen was terminated by the closure of the backarc basin in the Western Subprovince by the docking of an island arc/forearc system, which is the present day Central and Eastern Subprovinces. Deformation caused by this proposed collision preceded the development of the major regional, fold-belt-wide angular conformity separating the Western and Central Subprovinces (Gray et al., 2002). The Lachlan Orogen also experienced several periods of extension throughout the Paleozoic which were characterized by the development of localized rift basins and half-grabens. Ages of volcanic and sedimentary rocks within the rifts provide an approximate extensional timing of Early to Late Silurian, and Late Silurian to Early Devonian (Gray et al., 2002).

In summary, Gray et al. (2002) propose a complex, multiple subduction zone scenario in order to accommodate the patterns of deformation, metamorphism, and magmatism observed in the Lachlan Orogen. The doubly subducting nature of the oceanic basement of a marginal basin in the Middle Devonian (400-380 Ma) (Figure 2.2, numbers 1 and 2) resulted in the closure of this basin and the amalgamation of the Central and Eastern Subprovinces with the Western Subprovince. This marked the termination of the Lachlan Orogeny as defined by Gray et al. (2002). From ca. 400-360 Ma, slab rollback and the oceanward migration of the long-lived outboard subduction zone (Figure 2.2, number 3) resulted in extension, voluminous magmatism, and a high geothermal gradient in the Eastern Subprovince (Gray et al., 2002).

## **2.2.2 Strike-Slip Subduction Zone Scenario**

Glen (2005) proposes an alternative evolutionary history of the Australian sector of Gondwana in terms of tectonic cycles, encompassing both the depositional and magmatic events and the contractional deformational history of rock packages developed along plate margins. The events directly affecting the Lachlan Orogen of the Tasmanides are summarized here.

### **Delamerian Cycle**

The Delamerian Cycle is the oldest orogenic cycle developed in the Tasmanides. It is best evidenced in the mainland Delamerian Orogen and in western Tasmania (Figure 2.1), but this cycle is also represented in the early history of several other orogenic belts. On mainland Australia, this cycle lasted ca. 350 million years, from 830 Ma to 480 Ma (Glen, 2005). Within the Lachlan Orogen, Delamerian convergence is represented solely in the Southwestern Subprovince by thin regions of Cambrian mafic and ultramafic units. The development of mafic-ultramafic complexes across the Tasmanides reflects convergence, dated between 520-510 Ma, between the extended west Tasmania craton and the proto-Pacific plate (Glen, 2005).

### **Lachlan Supercycle**

The Lachlan Supercycle includes three orogenic cycles which affected the Tasmanides after the Delamerian Cycle (Glen, 2005). This Supercycle spans ca. 170 million years, from 490 Ma to 320 Ma, and encompasses the Ordovician to Carboniferous deformational history of the Lachlan Orogen. Three cycles, the Benambran, the Tabberabberan, and the Kanimblan, are defined by major contractional episodes that appear to be orogen-wide in space and time, although they naturally vary in intensity, and may be multiphase and diachronous in character.

#### Benambran Cycle

The first cycle is the Benambran, which spans ca. 50 million years from 490 to 440 Ma. The intra-oceanic Macquarie Arc developed during this cycle (Figure 2.3) between the earliest Ordovician to the Llandovery (494-438 Ma). Following the cratonic accretion of Cambrian forearc crust in the Delamerian Cycle, the Australian proto-Pacific plate boundary

experienced a rollback of approximately 1000km, reflected in part by the development of a wide back-arc basin, the Wagga Basin, across the Western and Central Subprovinces. The Wagga Basin, infilled by Early to Middle Ordovician turbidites and floored by Cambrian igneous crust, is linked to the Macquarie Arc by the presence of Ordovician back-arc basin basalts (Glen, 2005).

The Benambran Cycle in the Lachlan Orogen was terminated by the Benambran Orogeny, which is divided into two distinct phases in the Central and Eastern Subprovinces (Glen, 2005). Phase 1, initiated ca. 443 Ma at the end of the Ordovician, was caused by the northwards movement and collision of the Bega terrane into the northern part of the Gondwana-proto-Pacific plate boundary (Figure 2.4a and b), with oblique compression causing both east-west and north-south shortening. The Bega Terrane was translated along a largely transform boundary between east Gondwana and the proto-Pacific plate (Glen and Percival, 2003; Glen, 2004; Glen et al., 2004). Most of the rocks of the Bega terrane are composed of Early to Middle Ordovician craton-derived quartz-rich turbidites which are in fault contact with the eastern extent of the Macquarie Arc (Glen et al., 1998; Meffre et al., 2007). The Macquarie Arc was driven into the back-arc basin of the Girilambone-Wagga terrane by the translated Bega terrane (Figure 2.4b), and the turbiditic Wagga Basin fill took up most of this deformation, in the form of multiple cleavages, folds, and oblique thrusts (Glen, 2005).

After Phase 1 convergence, there was a period of extension resulting from rollback of the proto-Pacific plate outboard of the docked Bega terrane (Glen et al., 2007c). Phase 2 of the Benambran Orogeny followed this period of crustal relaxation and is predominantly defined by the oblique thrusting of Ordovician turbidites from the Central Subprovince over the Macquarie Arc, which was itself being translated to the southwest (Glen, 2005). This second collisional phase renewed deformation of the turbidites, and resulted in the syn-deformational emplacement of granites (Glen et al., 2007b). Phase 2 shortening was accommodated by the development of folds, thrusts, major strike-slip faults, and multiple cleavages in the Ordovician turbidites and overlying black shales of the Central and Eastern Subprovinces (Glen, 2005).

### Tabberabberan Cycle

The Tabberabberan Cycle, the second division of the Lachlan Supercycle, spans ca. 50 million years, from 430-380 Ma. Within the Lachlan Orogen, this cycle is characterized by widespread rifting, major basin formation and the emplacement of granitoids (Glen, 2005). Rifting and transtension was caused by the rollback of the proto-Pacific plate, a result of the northward migration of the Bega terrane and the subsequent jamming of the subduction zone in the Late Ordovician (Figure 2.4b). Extension was terminated by the late Early-mid Devonian Tabberabberan Orogeny.

The early collisional stage of the Tabberabberan Orogeny was due to south-southeast translation of the Central Subprovince which concentrated deformation along a linked system of faults: the Tullamore Fault zone, the Gilmore Fault zone, and the Indi-Long Plain Fault zone, all of which define the boundary between the Central and Eastern Subprovinces (Figure 2.1) (Glen, 1991; Morand and Gray, 1991). The main stage of the Tabberabberan Orogeny is characterized by Middle Devonian major basin inversion coupled with localized reverse/oblique reactivation of early Devonian faults (Glen, 1995). The last stage of the Tabberabberan Orogeny is represented by conjugate sets of brittle northeast and northwest-trending faults which experienced east-west shortening and offset major plutons in the Eastern Subprovince (Glen, 1992). The Tabberabberan Orogeny was caused by the accretion of the Bendigo terrane to Gondwana (Figure 2.4c). This terrane, structurally represented by the Southwestern Subprovince, moved northwards and was inserted between the Delamerian Orogeny in the west and the Eastern and Central Subprovinces of the Lachlan Orogen in the east. This was accomplished by a combination of mild north-south shortening, strike-slip deformation and strong east-west shortening (Glen et al., 1992; Miller et al., 2001) which occurred during the Late Silurian-Middle Devonian.

### Kanimblan Cycle

The onset of the Kanimblan Cycle, which lasted ca. 60 million years, from 380-320 Ma, is marked in the Eastern Subprovince of the Lachlan Orogen by a brief late Early-Middle Devonian episode of rifting (Glen, 2005). The main deformational phase of this cycle, the Kanimblan Orogeny, is dated at ca. 340 Ma, and is the last regional deformation to affect the

Lachlan Orogen. Glen (2005) attributes most deformation in the Eastern Subprovince to east-west Carboniferous shortening, with lesser strike-slip movement, which led to out-of-sequence thrusting. Depositional basins exhibit north-trending folds, faults, and cleavages that are also Carboniferous in age, and reflect a second phase of basin inversion by thick-skinned reverse faults (Vassallo et al., 2003). In the Eastern Subprovince, Carboniferous strain decreases to the south and to the west, where broad north to northwest-trending synclinoria and anticlinoria may also show evidence of north-south shortening (Glen, 1992; Glen et al., 1996). The final stage of the Kanimblan Cycle is marked by the intrusion of high-level I-type granitoids in the Eastern Subprovince, which were generated by the melting of underlying Ordovician volcanic rocks (Glen, 2005).

### **2.2.3 Scenario Used in This Study**

There are various other models in the literature to explain the tectonic evolution of the Tasmanides of Eastern Australia. Other theories include a strike-slip model employed by VandenBerg et al. (2000) and Willman et al. (2002) which is similar to Glen (2005), but utilizes the opposite sense of terrane movement for the presence of two volcanic arcs in the Lachlan Orogen, with the Eastern and Central Subprovinces moving dextrally to the south-southeast, rather than the Bendigo terrane moving to the north. The multiple subduction zone model has been expanded in many different directions, of which Collins and Vernon (1992), Soesoo et al. (1997), Collins and Hobbs (2001), and Fergusson (2003) represent a few examples.

Glen (2005) argues against a multiple subduction zone scenario by submitting that subduction zones do not turn on and off easily; they require special conditions to form. The proposed strike-slip transpressional tectonic model, combined with models in which the subduction signatures of Silurian-Early Devonian granites are inherited from Ordovician subduction, are alternatives to this dilemma. Due to the lack of kinematic evidence for hundreds of kilometers of strike-slip movement, the strike-slip model is based primarily on palaeogeographical reconstructions, which is a problem with this model. Except in rare cases where convergence is exactly perpendicular to a perfectly planar plate boundary, and where most of the displacement can be derived from small movements (tens of kilometers) along small faults, the chances of strike-slip deformation being a significant component of the deformational history is quite large (e.g. Teyssier and Tikoff, 1995). Therefore, explaining

two subparallel volcanic arcs by means of a strike-slip model in the Eastern Lachlan Orogen may be more feasible than invoking the development of multiple subduction zones.

Tectonic cycles as defined by Glen (2005) are used in this study to explain the evolution of the Endeavour 42 deposit and post-gold deformation experienced by the Cowal Igneous Complex within the Macquarie Arc.

## **2.3 Macquarie Arc**

### **2.3.1 Nature and Distribution of Ordovician Volcanic Rocks**

The Macquarie Arc consists of several separate igneous complexes which were deformed during accretion to the Gondwana margin and strongly influenced in geometry by the interplay of two major fault systems: the Tullamore and Gilmore Fault Zones (Glen, 2005). Ordovician volcanic and related volcanoclastic rocks, displaying low metamorphic grades of prehnite-pumpellyite facies throughout (Barron, 1999), occur in four elongate belts in the eastern part of the Lachlan Orogen. The three northern belts are the Junee-Narromine, the Molong and the Rockley-Gulgong Volcanic Belts. The Kiandra Volcanic Belt is the fourth, which is a much smaller belt found in the southern extents of the Lachlan Orogen (Figure 2.1). Cross sections and interpretations across the volcanic belts are variable, due to an absence of data on the geometry and kinematics of faults, as well as lack of surficial outcrop. Using geochemical data, Crawford et al. (2007b) suggest that each of the volcanic belts belong to a single arc which rifted apart, resulting in the current spatial distribution. Only the western and central belts, the Junee-Narromine and Molong, are host to significant ore deposits (Figure 2.3).

#### **The Junee-Narromine Volcanic Belt**

The Junee-Narromine Volcanic Belt is the most westerly, the most poorly exposed, and the longest of the volcanic belts that compose the Macquarie Arc (Figure 2.3). The southern portion of this belt trends generally north-northwest and lies to the east of the Gilmore Fault Zone (Figure 2.5). The central portion of the belt lies to the east of the Tullamore Fault, and is predominantly north-trending (Figure 2.5). Volcanoclastic units in this belt range in age from Early Ordovician to Early Silurian, with a major hiatus in volcanism from the Middle to Late Ordovician (Glen et al., 1998). Despite the lack of

outcrop along this belt, drillhole, seismic, and aeromagnetic and gravity data have been combined to interpret at least 16 different igneous complexes composed of variable mixtures of volcanoclastic, coherent extrusive, and intrusive units (Glen et al., 2002). The variations in geochemical affinity, ages, and intrusive history across these igneous complexes suggest that each represents a separate igneous centre within the Junee-Narromine Volcanic Belt. This belt is interpreted as most closely resembling the magmatic core of the Macquarie Arc (Glen et al., 2007a).

### **The Molong and Rockley-Gulgong Volcanic Belts**

The Molong Volcanic Belt is the best studied region of the Macquarie Arc and is well exposed, except in the northernmost parts (Figure 2.3). Both the Molong and Rockley-Gulgong Volcanic Belts are dominated by basal Ordovician to Lower Silurian submarine deep-water volcanoclastic rocks; the most common compositions being andesitic basalt and latite (Glen et al., 2002). Although most igneous rocks are mafic, rare quartz-bearing phases are present with dacite, quartz diorite, rhyolite, and quartz-bearing monzonite (Gray and Foster, 2004). Both of these belts display thin-skinned deformation (Raymond et al., 1998) and lower gravity and magnetic signatures than the Junee-Narromine belt (Spencer, 2004). A volcanic hiatus evident in the Junee-Narromine belt from Middle to Late Ordovician is also present in these belts (Glen et al., 1998). In both belts the major Late Ordovician volcanic centres are located north of and along the Lachlan Transverse Zone, a significant cross arc structure (Figure 2.3) (Glen et al., 2007c).

### **2.3.2 Tectonic Evolution of the Macquarie Arc**

Seismic cross sections through the Junee-Narromine and Molong Volcanic Belts display significant differences in crustal architecture (Glen et al., 2002). Whereas both belts have contractional and extensional features, the Junee-Narromine belt is dominated by major crustal contraction whereas extensional structures predominate in the Molong belt (Glen et al., 2002). Contractional features in both belts have been broadly correlated temporally as reverse-sense reactivation of extensional faults in the late Early and Middle Devonian, and in the Carboniferous.

The Junee-Narromine Volcanic Belt is interpreted as the main volcanic arc, with the Molong and Rockley-Gulgong belts existing as lesser volcanic centres within a larger

volcaniclastic apron (Glen et al., 1998). Extension in the middle Paleozoic (Middle Silurian to Middle Devonian) split the two latter belts from the main arc, the Molong belt rifting from the Junee-Narromine belt to the east and southeast, and the Rockley-Gulgong belt rifting from the Molong belt to the northeast (Glen et al., 2007c). Significant strike-slip faulting is interpreted along the southern extents of the Junee-Narromine Volcanic Belt, off of which the southernmost Kiandra Volcanic Belt was potentially separated by approximately 50km of sinistral displacement (Glen et al., 2007c). Thus, the Macquarie Arc was dismembered following accretion onto the Gondwana Plate by predominantly east-west extension accompanied by arc-parallel left-lateral strike-slip displacement along the southern portion of the Junee-Narromine Volcanic Belt (Glen et al., 2007c). The convergence of the Molong and Rockley-Gulgong belts at the northern end of the Hill End Trough (Figure 2.3), as well as the geochemical, geophysical, and structural evidence that Ordovician volcanic rocks underlie the Cowra and Hill End Troughs (Glen et al., 2002), lend strong support to the theory of arc rifting in the region.

### **Benambran Cycle**

The Macquarie Arc grew during the Benambran Cycle in three pulses (Glen et al., 2003). Evidence for the first pulse (Pulse 1 of Glen et al., 2005) is best preserved in the Junee-Narromine and Molong Volcanic Belts from 490-475 Ma, where the volcanic arc formed on a rifted fragment of Cambrian forearc crust (Crawford et al., 2007a). Pulse 1 consists of volcanic and volcanoclastic rocks, which grade upward into siltstone. The second pulse of arc growth initiated approximately 11 Ma after the first, from 466-455 Ma. The hiatus between pulses possibly reflects a period of back-arc spreading in the region (Glen, 2005). Pulse 2 is represented in the Junee-Narromine and Molong belts by volcanic and volcanoclastic units which grade into thinly-bedded turbidites to the east. Following a third hiatus of volcanism in the Macquarie Arc, Pulse 3 occurred after approximately 4 Ma as a coherent volcanic sequence in the Junee-Narromine and southernmost Molong belts from 452-438 Ma (Glen, 2005). The third pulse of volcanism was shoshonitic in composition, as opposed to the predominantly calc-alkaline chemistry of Pulses 1 and 2 (Glen et al., 2003; Crawford et al., 2007b).

During the first collisional phase of the Benambran Orogeny (Phase 1, Table 2.1), the Molong Volcanic Belt was uplifted as the arc accreted into back-arc basin turbidites. The

Kiandra belt experienced some Phase 1 uplift as well, but the Junee-Narromine and the Rockley-Gulgong belts did not experience any major uplift during this phase (Glen et al., 2007c). Phase 1 uplift has been constrained to the early Llandovery (443-439 Ma) by several regions in the Molong, Kiandra, and possibly the Junee-Narromine belts (Table 2.1) (Glen et al., 2007c). This uplift was followed by Phase 1 relaxation or crustal extension across the Macquarie Arc, resulting in shallow-water basin formation in the Molong and Kiandra belts, and the deposition of deep-water sediments over the Junee-Narromine and Rockley-Gulgong belts. It was during this crustal relaxation that the Llandovery porphyries, several of which are well-mineralized, were emplaced in the Macquarie Arc, and which represent the final stages of igneous activity in the arc (Glen et al., 2007b).

Phase 2 deformation, ca. 433-430 Ma (Table 2.1), which affected all parts of the Macquarie Arc, is characterized by the oblique thrusting of the Ordovician turbidite sequence within the Central Subprovince over the arc, which was itself being translated to the southwest (Glen, 2005). Though being overthrust by turbiditic sequences, the rocks of the Macquarie Arc underwent only low-grade metamorphism and low strain; a type of “soft collision” which is commonly attributed to oblique accretion or collision with a large amount of strike-slip displacement (Glen et al., 2007c). The development of an angular unconformity below late Llandovery-early Wenlock strata across the Macquarie Arc represents renewed arc uplift along sections of the arc during Phase 2 Benambran deformation (Glen et al., 2007c).

### **Tabberabberan Cycle**

The Tabberabberan Cycle is best represented in the arc by extensive rifting and/or transtension along extensional/oblique faults that occurred from the Middle Silurian to the Middle Devonian (Table 2.1), during which the major back-arc basins in the area were created and infilled (e.g. Hill End, Cowra, and Jemalong Troughs, Figure 2.3) (Glen et al., 2002; Vassallo et al., 2003). Seismic reflection profiles suggest that these extensional faults are largely planar (Glen et al., 2002). It was during this cycle that the Macquarie Arc split into four separate belts. A collisional phase during the late Early-Middle Devonian resulted in major basin inversion across the Lachlan Orogen with deformation largely restricted to the sedimentary infill of these basins (Glen, 2005).

## **Kanimblan Cycle**

The Kanimblan Cycle in the Macquarie Arc, and throughout the Eastern Subprovince, is marked by east-west shortening with a strike-slip component in the Carboniferous. This shortening also led to out-of-sequence thrusting attributed to the Kanimblan Orogeny, and is dated at approximately 340 Ma (Table 2.1) (Glen, 2005). Sinistral transpression is documented in the mid Devonian and/or mid Carboniferous by renewed southeast directed thrusting of the Wagga Zone (Stuart-Smith, 1991). In Upper Devonian sedimentary units of the Junee-Narromine Volcanic Belt, Carboniferous thrusting and folding is evident, with some strike-slip faulting in accommodation zones in the Marsden Fault (Figure 2.5) (Glen et al., 2002).

## **2.4 Lachlan Orogen-scale Structures**

### **2.4.1 Gilmore and Tullamore Trends**

The Junee-Narromine Volcanic Belt has been structurally shaped by two major ductile-brittle fault systems which were generated during deformation in the Early Silurian, Early Devonian, and Carboniferous (Glen et al., 2007a). These are the north-northwest trending Gilmore Fault Zone and the north-NNE-trending Tullamore Fault Trend. The Tullamore Trend is subparallel to the Junee-Narromine Volcanic Belt strike, and is reflected most clearly in the central part of the belt. This trend is made up of the Booberoi, Marsden, Springdale, Tullamore, and Parkes Faults (Figure 2.5). The Tullamore Fault marks the western boundary of the Junee-Narromine belt against Ordovician turbidites of the Girilambone Group, but is an inferred fault as it does not outcrop. There is evidence for Carboniferous movement along the Tullamore Fault (Glen et al., 2007a), indicating that these major belt-wide structures underwent several stages of reactivation during the tectonic evolution of the Junee-Narromine Volcanic Belt. Evidence of steep south-striking foliation pervasively developed in rocks on either side of the Booberoi Fault, within Ordovician volcanic units and Siluro-Devonian Derriwong Group (Ingpen, 1995), reflects the pervasive deformation associated with the Tullamore Trend.

The Gilmore Fault Zone forms a portion of the boundary between the Central and Eastern Subprovinces of the Lachlan Orogen (Figure 2.1) and can be traced to depth in seismic profiling (Figure 2.6) (Glen et al., 2002). Structures paralleling the Gilmore Trend

are most abundant in the southern and northern parts of the Junee-Narromine belt, and terminate the belt on both ends (Figure 2.5). In the north, the Gilmore Trend is characterized by the Canonbar Structure, which is recognized as a strong gravity linear (David et al., 2004). In the south, the trend is characterized by the Gilmore Fault Zone, interpreted linked splays, and associated faults subparallel to the northern margins of the Cowal Igneous Complex (Figure 2.5) (Glen et al., 2007a). The Gilmore Fault Zone terminates the southern extent of the Junee-Narromine belt against Ordovician turbidites of the Wagga Group. There was Early Silurian movement along the Gilmore Fault in the south dominated by dextral strike-slip displacement along small-scale steeply easterly dipping faults and shear bands, followed by reactivation in the Early to mid-Devonian as dextral transpression and subsequent east-west compression which reactivated the Booberoi Fault (Ingpen, 1995, Glen et al., 2007a). No clear evidence is known of the Carboniferous movement evident in the Tullamore trend (Glen et al., 2007a).

#### **2.4.2 Lachlan Transverse Zone**

A major basement structure, called the Lachlan Transverse Zone (LTZ), cuts the Macquarie Arc obliquely and had significant influence on magmatism, the distribution of mineral provinces, and the development of several depositional basins in the area (Figure 2.3) (Glen et al., 1998; Glen and Walshe, 1999). In the Eastern Subprovince of the Lachlan Orogen, the LTZ is represented by a corridor of west-northwest or east-west faults and folds. To the west, the LTZ is both broader and less well-defined (Glen and Walshe, 1999). Though the Lachlan Transverse Zone was initially inferred from surficial features, there are two lines of evidence from seismic interpretations which suggest a presence in the subsurface (Glen et al., 2002). These include mid-crustal reflectors which correlate with east-west to west-northwest-trending faults, folds, and elongate intrusions inferred from within the LTZ (Glen and Walshe, 1999), as well as indications from refraction data which suggest significant changes in crustal velocities under the proposed location of the zone (Finlayson et al., 2002). Other cross-structures found within the Australian craton also trend approximately west-northwest, and are attributed to controlling the distribution of mineral provinces within the Tasmanides (Walshe et al., 1995). Included are the combined Nyngan Transverse Zone (NTZ) and Hunter River Transverse Zone (HRTZ) found to the north of the LTZ (Figure 2.3).

## **Rock Chemistry in the Lachlan Transverse Zone**

Within the Macquarie Arc, the majority of rocks exhibit low to medium-K calc-alkalic chemistry, indicative of normal subduction-related melts from the mantle wedge. Local shoshonitic compositions, attributed to intraoceanic volcanic settings and derivation of magma from sources enriched in light rare earth elements (Stern et al., 1988; Wyborn, 1992), are found along the intersections of the volcanic belts with the interpreted LTZ and subparallel transverse zones. Potential sources include fragments of a subducted alkalic seamount, and/or deep mantle which rose through tears in the old subducting slab or during incipient slab rifting (Glen et al., 1998).

The LTZ has been interpreted as a conduit which tapped high-K and shoshonitic melts from a deep, enriched mantle source that had negligible input from continental sources, and which potentially experienced right-lateral movement during magmatism reflected by the emplacement of igneous complexes into dilational sites along the length of the feature (Glen et al., 1998). The oldest identifiable event linked to the Lachlan Transverse Zone, the emplacement of mantle-derived high-K and shoshonitic volcanic rocks, intrusions, and mantle-derived ultramafic magmas, implies that it acted as a major crustal tear oblique to the convergent margin between the proto-Pacific and Australian plates (Glen et al., 1998; Glen and Walshe, 1999). Based on restoration models created for the unrifted Macquarie Arc, this zone possibly developed from a Late Ordovician transform boundary along the southern margin of the eastern Macquarie Arc (Glen et al., 2007b). In addition to already existing as a major structure in the Ordovician, the LTZ was also fundamental in controlling the sources and shapes of Upper Silurian to Lower Devonian granitoids, as well as Carboniferous and Miocene intrusions (Glen and Walshe, 1999).

## **Mineralization and Structure in the Lachlan Transverse Zone**

Porphyry deposits in the Junee-Narromine, Molong, and Rockley-Gulgong Volcanic Belts tend to cluster within the LTZ, although there is some spread along the length of the Junee-Narromine belt (Figure 2.3) (Glen et al., 2007b). In the Cadia district of the Molong belt, dykes, faults, and sheeted veins are subparallel to the west-northwest trend of the LTZ, and Holliday et al. (2002) and Wilson et al. (2003) have suggested that at the time of mineralization  $\sigma_1$  was oriented west-northwest along the zone and  $\sigma_3$  was oriented north-

northeast across the zone during the Late Ordovician. Northwest-trending lineaments interpreted from aeromagnetic data are spatially associated with the porphyry deposits at Northparkes (Heithersay et al., 1990; Hooper et al., 1996) and are included within the Lachlan Transverse Zone (Glen et al., 1998).

## **2.5 Cowal Igneous Complex**

### **2.5.1 Cowal Igneous Complex Lithology**

The Cowal Igneous Complex (CIC) is an Ordovician igneous sequence over 40km long by 15km wide, located within the Junee-Narromine Volcanic Belt (Figure 2.5, 2.7, and 2.8) (Miles and Brooker, 1998). Aeromagnetics, gravity surveys, and reconnaissance drilling were fundamental to the discovery and definition of the CIC and associated ore deposits, as the entire district is completely covered by a poorly consolidated Tertiary to Quaternary lacustrine sequence ranging from less than a metre to over 100 metres thick (McInnes et al., 1998; Miles and Brooker, 1998). Lying directly under this transported sequence is an incomplete Tertiary laterite profile whose thickness also varies from 2 to approximately 100 metres (Miles and Brooker, 1998).

The CIC is characterized by a sequence of interbedded volcanoclastic facies, trachyandesite lava (coherent and associated hyaloclastite facies), and porphyritic andesite (coherent and autoclastic facies). These rocks have been intruded by multiple sills and dykes, including dioritic, gabbroic, and syenitic bodies (McInnes et al., 1998). The volcanoclastic facies include mudstone, sandstone, and polymictic volcanoclastic breccia/sandstone. The environment of deposition is interpreted as a basin or depocentre medial to distal from a volcanic centre (Simpson and Cooke, 2006). The oldest and volumetrically most significant coherent intrusive unit is a heterogeneous, holocrystalline to porphyritic diorite complex called the Muddy Lake Diorite, whose composition ranges from granodiorite to tonalite (McInnes et al., 1998). Smolonogov (2003) indicates the presence of both K-rich and shoshonitic high level intrusive complexes within the volcanic package. For more detailed description of lithology within the CIC, refer to Chapter 3.

## 2.5.2 Overlying Silurian-Devonian Stratigraphy

Outcrops of the overlying Siluro-Devonian Ootha and Derriwong Groups are located in a series of hills, including the Booberoi Hills, and the Wamboyne and Manna Mountains, to the north, south, and west of E42 (McInnes et al., 1998; Raymond et al., 2000b). The Groups consist of marine sedimentary and volcanic rocks, characterized by a laterally equivalent basal conglomerate unit: the Manna Conglomerate for the Ootha Group, and the Edols Conglomerate for the Derriwong Group (Miles and Brooker, 1998; Raymond et al., 2000b). Both unconformable and tectonic contacts are present between the CIC and overlying Siluro-Devonian rocks. Directly west of E42 the Manna Conglomerate is inferred to be in fault contact with the CIC (Figure 2.8) (Miles and Brooker, 1998; Raymond et al., 2000b). The conglomerate is a poorly sorted, massive, matrix-supported unit, containing clasts of dominantly quartz and metasedimentary compositions ranging from 0.5mm to over 1m in diameter (Miles and Brooker, 1998). Epidote-altered igneous clasts resembling Ordovician diorite of the CIC are a minor component, suggesting the complex was at least a local source for the basal Manna unit (Miles and Brooker, 1998). The Manna Conglomerate displays a strong subvertical north-south foliation and a well-developed subvertical lineation (Figure 2.9). Outcrop localities of the conglomerate are interpreted as the surface expression of the Booberoi Fault (Ingpen, 1995).

The Jemalong Trough is a poorly exposed, north-trending belt extending from the town of Junee in the south, to east of Nyngan in the north, lying to the east of the CIC (Figure 2.5). It varies from over 400km long by 15-70km wide with gravity data showing the trough as a continuous, narrow low within the much larger gravity high caused by the underlying Junee-Narromine Volcanic Belt (Raymond et al., 2000a). The Gilmore Fault Zone defines the margins of the trough to the south. The trough formed as a shallow marine rift basin during Silurian to Early Devonian extension of the Macquarie Arc (Raymond et al., 2000a). The Jemalong Trough is composed of sedimentary and volcanic rocks of the Derriwong, Ootha, and Trundle Groups, which lie unconformably on the folded quartz-rich turbidites of the Ordovician Girilambone Group and Kirribilli Formation, and the mafic arc volcanic rocks of the Junee-Narromine belt. The Edols and Manna Conglomerates are basal units, and are overlain by fine-grained sandstone, mudstone, and limestone deposited during marine transgression (Raymond et al., 2000a). The Jemalong Trough underwent initial inversion ca.

400 Ma, with further broad, open folding during the early Carboniferous Kanimblan Orogeny forming the Tullamore Syncline along the axis of the trough (Figure 2.8). Some shortening during this orogenic period was also accommodated along the Marsden Fault and probably along the Gilmore Fault Zone (Figure 2.5) (Glen, 2005).

### **2.5.3 Tectonic Setting of the Cowal Igneous Complex**

#### **Booberoi and Marsden Faults**

The Cowal Igneous Complex is bounded to the west by the Booberoi Fault, a major shear zone associated with the basal conglomerate of the Siluro-Devonian Ootha Group, the Manna Conglomerate (Figure 2.8) (Ingpen, 1995). The bulk of the strain along this fault has been absorbed by the matrix component of the conglomerate, evidenced by the development of shear bands and a strong shear zone parallel foliation (Ingpen, 1995). A portion of the strain within the Booberoi Fault is evident from the stretching (flattening and elongation) of the conglomerate clasts (Figure 2.9). Clasts occasionally display wispy quartz fibre growths developed parallel to the long axis of the clast (Ingpen, 1995). The clast long axis represents the elongation direction, which is consistent with shear foliations observed in the matrix of the conglomerate and indicates subvertical dip-slip movement along the fault. Movement along the Booberoi Fault proximal to E42 is reverse-sense along steeply east-dipping fault sections (Ingpen, 1995; current study). The southern extents of the Booberoi Fault show west-block-up, reverse-sense kinematics (Lyons, 2000) and there is some sinistral strike-slip movement recorded on steeply east-dipping shears along the northern extent of the fault (Lyons, 2000). Overall an east-west shortening event is represented, which was manifested by different displacement directions along separate and variably dipping components of the fault (Lyons, 2000). Localized milky quartz veins, oriented predominantly parallel to the major shear bands within the deformed Manna Conglomerate, have been tightly folded, with vertical slickensides developed along exposed vein walls, indicating there was movement along the fault subsequent to the initial stretching of the conglomerate, and therefore recording multiple deformation events along the Booberoi Fault (Ingpen, 1995).  $^{40}\text{Ar}$ - $^{39}\text{Ar}$  ages from fault sericite indicate a minimum age of  $411 \pm 2$  Ma (Foster et al., 1999; Lyons, 2000). This age has been interpreted by Glen et al. (2007a) as the age of deformation along the Booberoi Fault, which is inferred as middle Early Devonian. Where there are no

exposures of the deformed Siluro-Devonian rock types, the trace of the Booberoi Fault is interpreted from regional aeromagnetic images as the westernmost extent of the CIC (Figure 2.7). To the east, the CIC is bounded by a complex section interpreted as a flower structure associated with an accommodation zone developed in a strike-slip section of the Marsden Fault (Figure 2.6) (Glen et al., 2002).

### **Imbricate Zone**

Interpretations of east-west seismic sections through the CIC distinguish the Gilmore and Booberoi Faults as separate structures (Figure 2.6) (Glen et al., 2002). These faults are not interpreted to connect locally, but are rather on opposite sides of an imbricate fault zone, whose internal structure is complicated and permissible of several different interpretations. The imbricate zone consists of interleaved Ordovician quartz-rich turbidites (Girilambone Group) and Siluro-Devonian sedimentary units and has been interpreted as a shallow high-level thrust that has placed Ordovician volcanic rocks westward over the Wagga Group, as well as a thin sliver of Girilambone Group thrust over Silurian-Devonian sedimentary rocks (Glen et al., 2002). The Girilambone Group is subsequently overthrust on its margins by Ordovician volcanic rocks (Figure 2.6).

### **Fault Blocks within the Cowal Igneous Complex**

Aeromagnetic interpretations from Barrick Gold of Australia Ltd. delineate several major features and lineaments in the CIC (Figure 2.7) (Pittard, 2006). Lineaments distinguish potential fault bounded blocks which may have behaved as distinct bodies during deformation and rotated heterogeneously with respect to each other. The CIC is interpreted to be much less deformed than other Ordovician volcanic rocks to the west and south, due to the shape from aeromagnetics (Glen and Fleming, 2000; Glen et al., 2002). A prominent, steeply west-dipping reflector extends several kilometers to depth within the CIC, and has been correlated with an aeromagnetic lineament on surface which separates highly deformed from less-deformed rocks just east of the E42 deposit (Figure 2.7) (Glen et al., 2002).

## **2.6 Ordovician Mineralization**

### **2.6.1 Metallogeny of the Macquarie Arc**

The early Ordovician to early Silurian Macquarie Arc of the Lachlan Orogen is host to a variety of metallogenic deposits, all of which are consistent with Cenozoic island arc subduction-related processes. These include alkalic and calc-alkalic Au-Cu porphyries, skarns, high sulfidation epithermal Au, and carbonate-base metal epithermal (low sulfidation) Au deposits (Figure 2.3). The arc is host to Australia's only economic porphyry Au-Cu province, and of these deposits, the alkalic Au-Cu porphyries are the most significant economically (e.g. Cooke et al., 2006).

### **2.6.2 Mineralization of the Cowal Igneous Complex**

There are several economic prospects within the Cowal Igneous Complex which are found near the eastern margin of the Booberoi Fault (Figure 2.7 and 2.8). Four of these prospects (E40, E41, E42, and E46) define a north-trending 6km long by 2km wide "gold corridor" which potentially continues to the south, incorporating the weak gold and copper systems at Caloola, Phoenix, and Milly Milly (McInnes et al, 1998). The CIC is located in a complex interaction zone between the northwest-trending Gilmore and north-trending Tullamore Trends (Figure 2.5). The main prospects in this area are described below, except E42 which is described in detail in Chapter 4.

E39 is a large, low grade (0.25% Cu) porphyry copper prospect, hosted by granodiorite and spanning an area of 4km by 2km. It is uneconomic and is considered to be earlier than the regional gold mineralization (McInnes pers. comm., 2007). Bastrakov (2000) concludes that E39 and E42 have different sources of ore-bearing fluids based on different carbonate REE signatures.

The E40 prospect is a structurally hosted, uneconomic gold prospect within volcanoclastic mudstones situated just to the south of the E42 mining lease. Barrick Gold of Australia Ltd. began exploration drilling at this prospect in early 2007 (McInnes pers. comm., 2007).

Two pods of economic gold mineralization (East and West pods) constitute the E41 deposit. E41 is currently being studied in detail by Zukowski (e.g. Zukowski et al., 2007). The West Pod is a lode style deposit within monzogranite intruding a diorite/gabbro body.

The lode (up to 30m thick), is roughly north striking and dips approximately 60° to the east. The East Pod contains vein-hosted mineralization (similar in style to E42) occurring primarily within volcanoclastic mudstones above a moderately south dipping diorite contact. Veins dip 30-45° to the south-southeast. Supergene flat lying oxide blankets are associated with East Pod mineralization. High grade structures (dykes and fault-related breccias) occur at depth beneath the East Pod and trend approximately east (McInnes pers. comm., 2007). Work on fluid inclusions suggests that although the E41 and nearby E42 deposits are separated spatially and display different chemical/mineralogical signatures, they potentially come from the same fluid source (Bastrakov, 2000). E41 appears to be a higher temperature system than E42, exhibiting evidence of both porphyry and epithermal-styles of mineralization (Zukowski et al., 2007). Evidence of high temperature porphyry mineralization is apparent in the East Pod, including early magnetite-chalcopyrite-(albite-quartz) veins, pervasive magnetite and actinolite alteration, and garnet veins. Lower temperature epithermal-style mineralization occurs as adularia and prehnite ± epidote in veins, sericite and adularia alteration haloes, and potential bladed vein calcite (Zukowski et al., 2007).

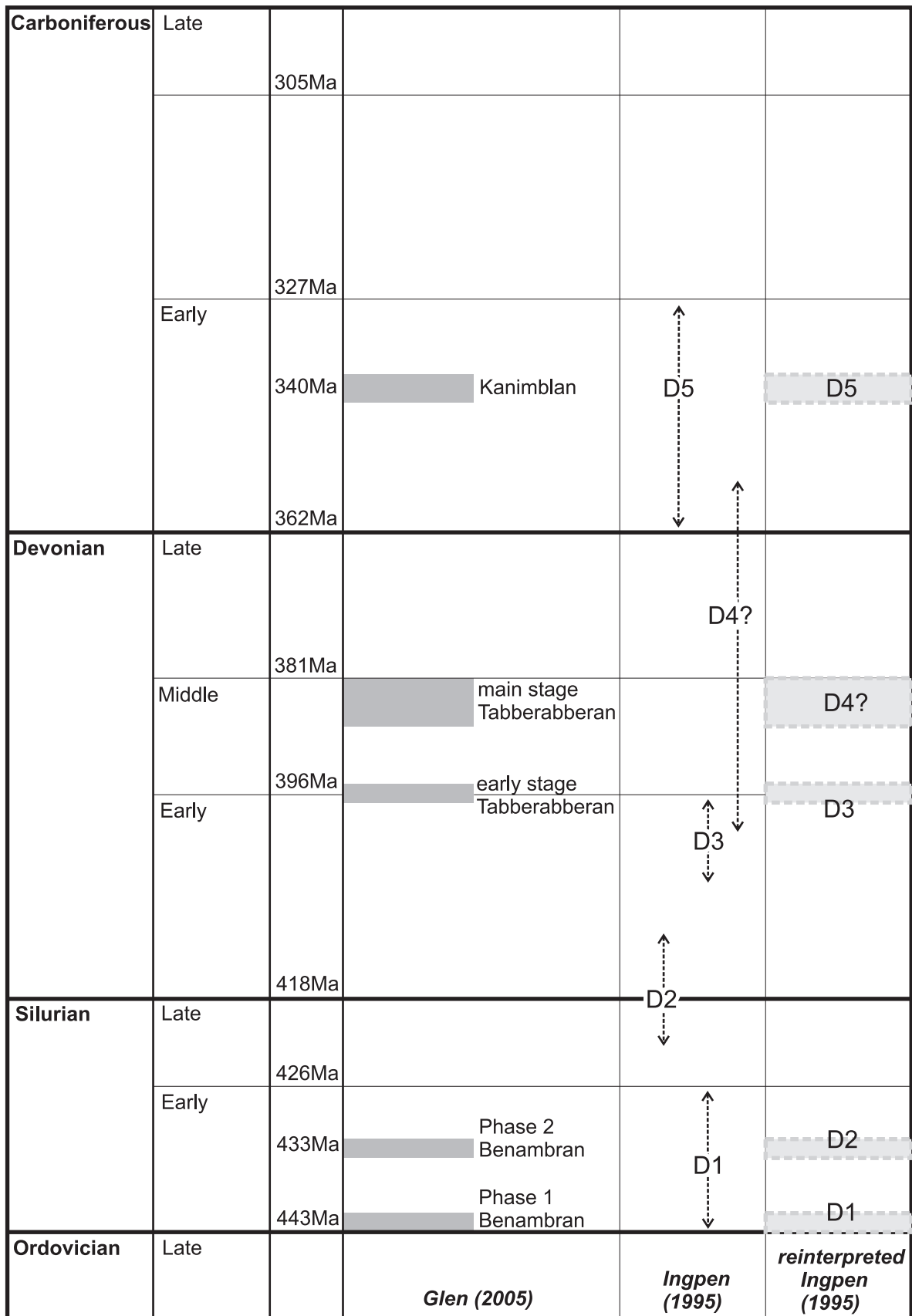
Located approximately 1km north of E42, the E46 prospect has two pods of mineralization aligned roughly north-south. E46 has similar host rocks to E42: a volcanoclastic sequence, lava, and diorite/gabbro sills. Mineralization appears to be related to calcite-quartz-pyrite-sphalerite veins associated with sericite alteration and is found in all three rock types (McInnes pers. comm., 2007).

The E35 prospect was discovered when a large gossanous outcrop was found near an old homestead (McInnes pers. comm., 2007). Exploration drilling by North Ltd. and Geopeko Ltd. returned scattered Au, Cu, Pb, and Zn results without any focus, and no further work has been completed by Barrick Gold of Australia Ltd. The prospect, characterized by kaolinite and possible alunite, is interpreted as a weak, advanced argillic, high sulfidation system (McInnes pers. comm., 2007).

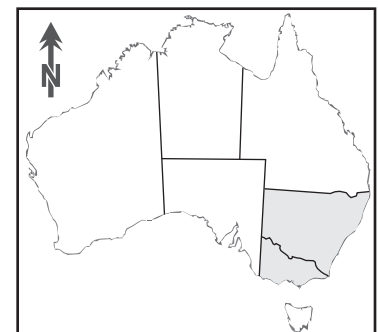
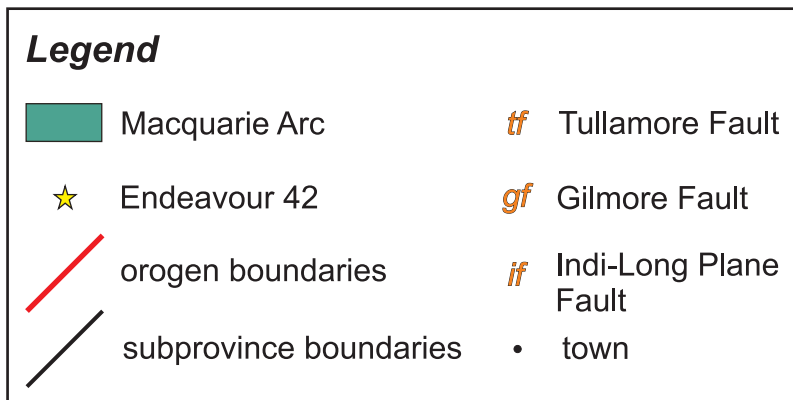
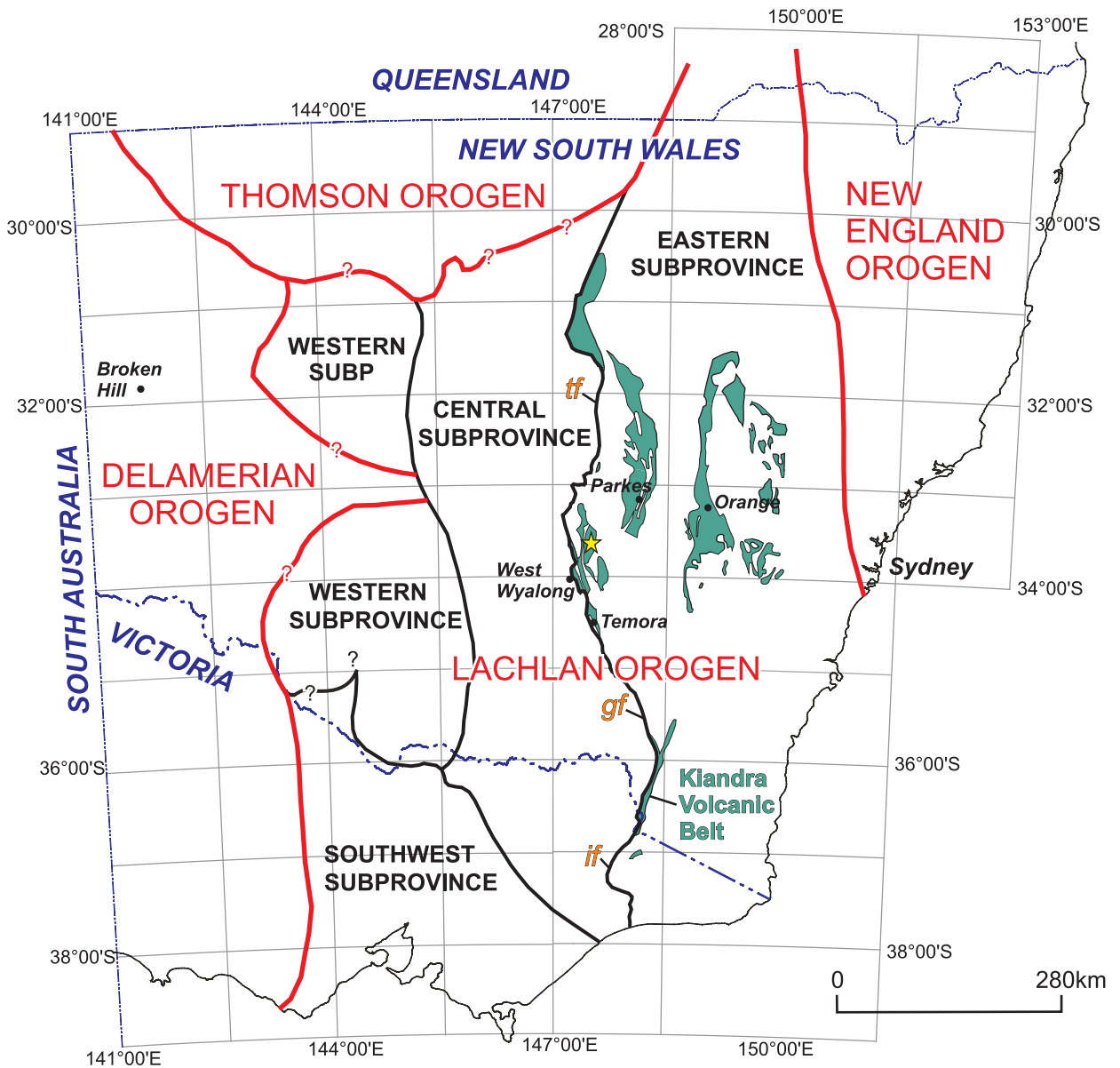
E43 is a subeconomic porphyry copper system with mineralization associated with quartz-chalcopyrite stockwork veins. Host rocks include andesitic lava and volcanoclastic units intruded by fingers of granodiorite and monzodiorite. Similar to E39, this prospect has abundant subeconomic mineralization, with drilling often displaying 150-400m at 0.15-0.2%

Cu (McInnes pers. comm., 2007). Typical “potassic” alteration is present, consisting of pervasive to selective pervasive albite-potassium feldspar-magnetite and biotite.

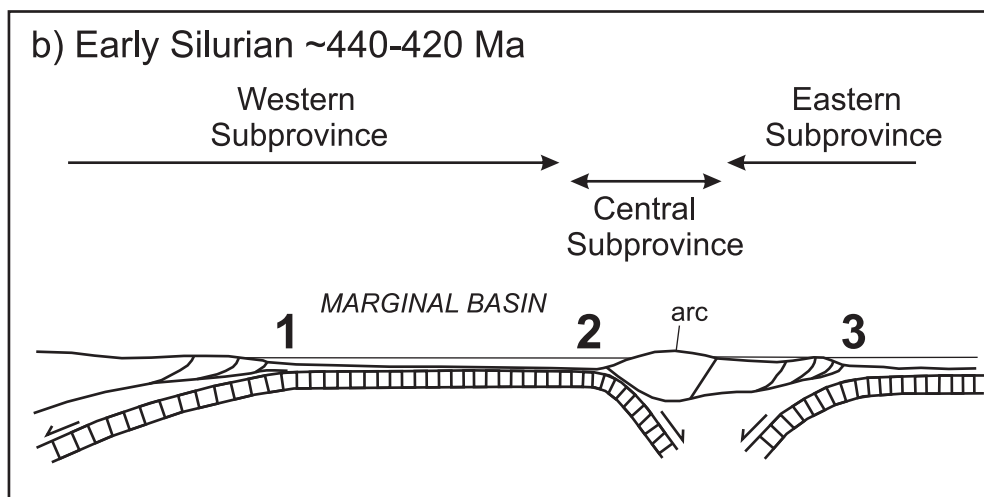
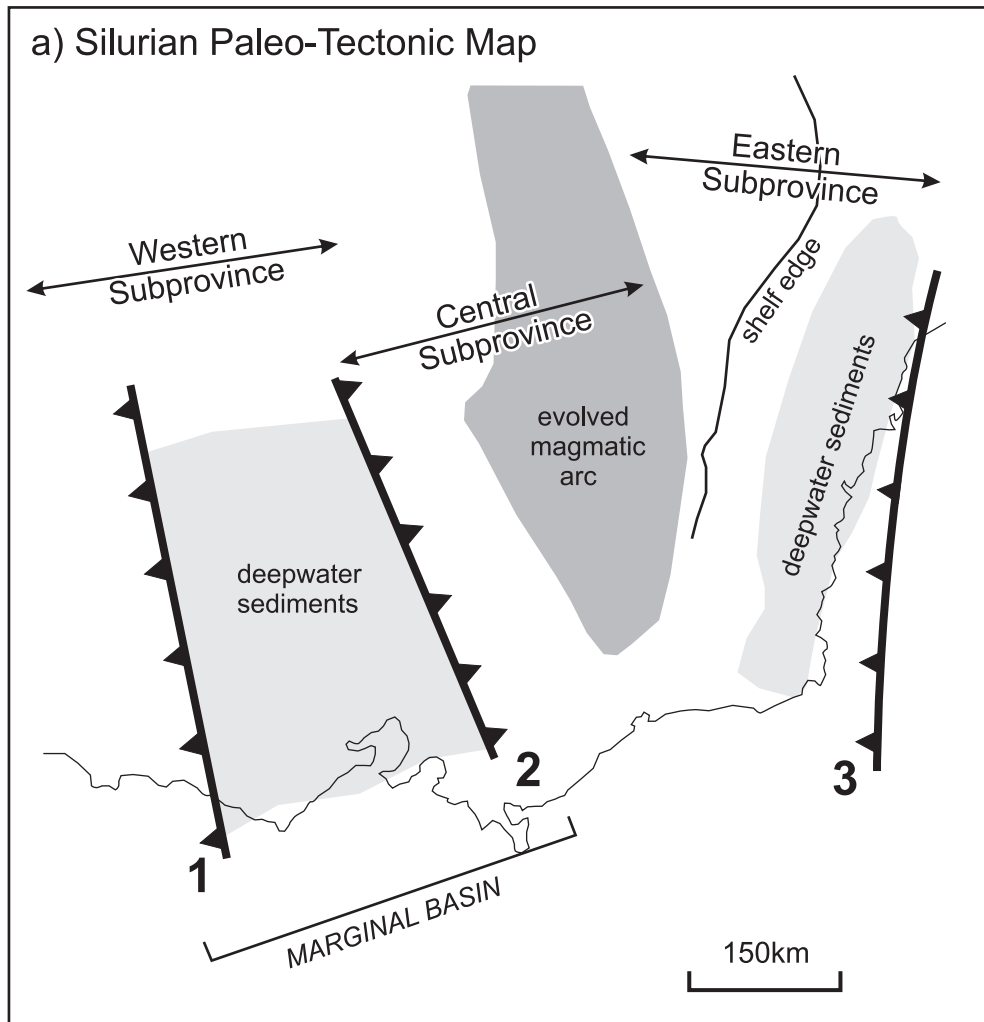
Caloola, Milly Milly, and Phoenix are prospects which occur along the southern extension of the “gold corridor” within EL 1590 (Figure 2.7 and 2.8). Aeromagnetic data suggest Muddy Lake diorite is locally present, being incorporated in a large granodiorite intrusive. These prospects are subeconomic and have an early weak porphyry copper stage overprinted by weak structurally controlled gold mineralization (McInnes pers. comm., 2007). Historical drilling has been primarily by aircore or reverse-circulation methods, so not much detail is known about these prospects. The best Au and Cu results are shallow and possibly due to supergene enrichment; the highest grade hole at Phoenix returned 8m (40-48m) averaging 1.61g/t Au and 0.59% Cu (McInnes pers. comm., 2007).



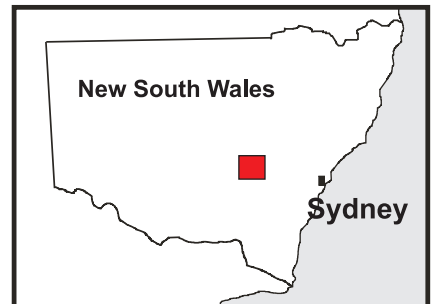
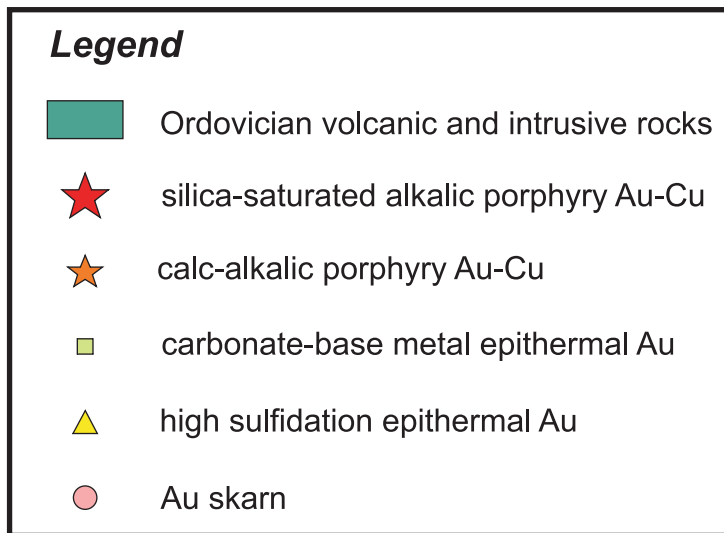
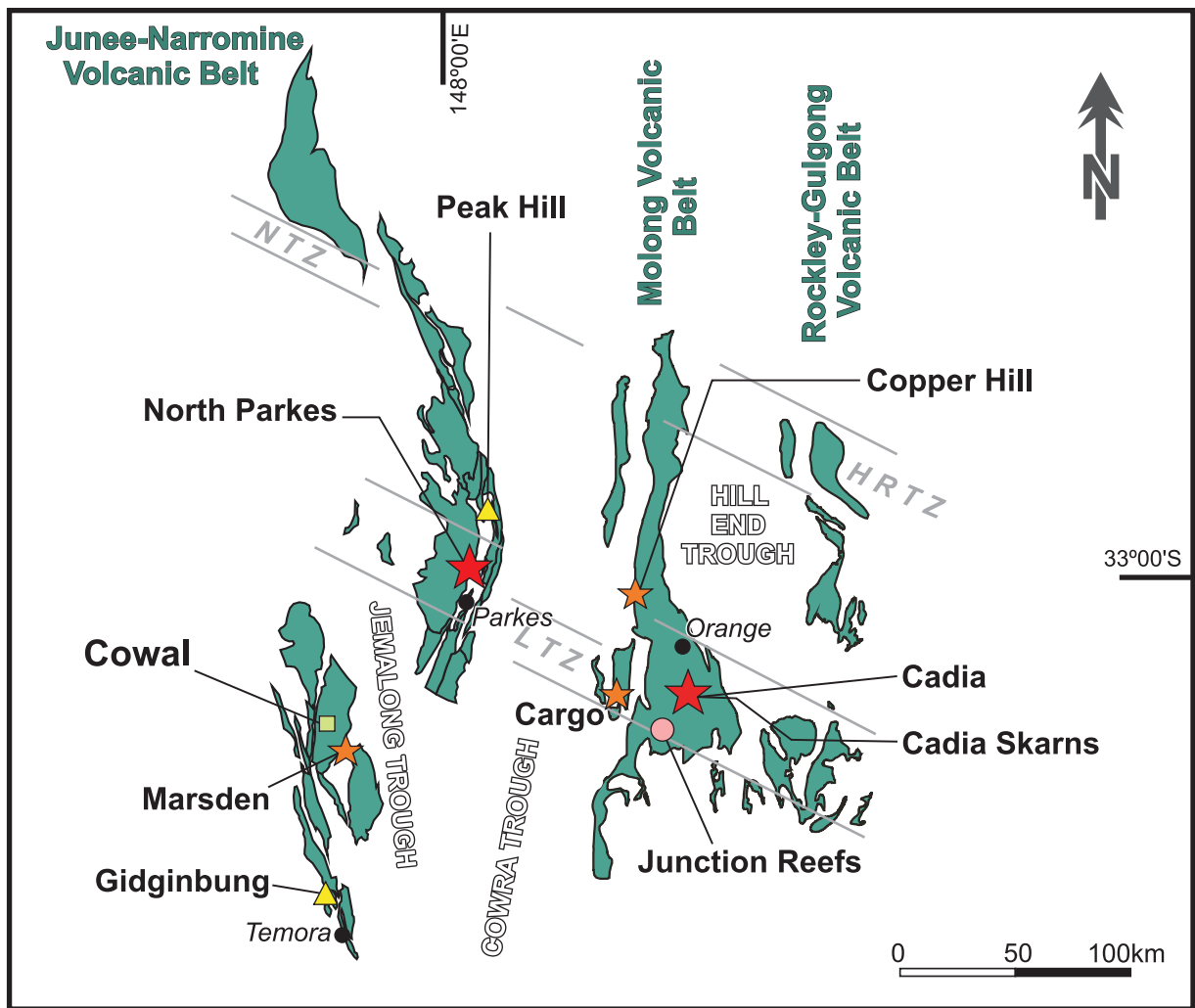
**Table 2.1** Schematic time-space plot of deformational events in the Macquarie Arc.



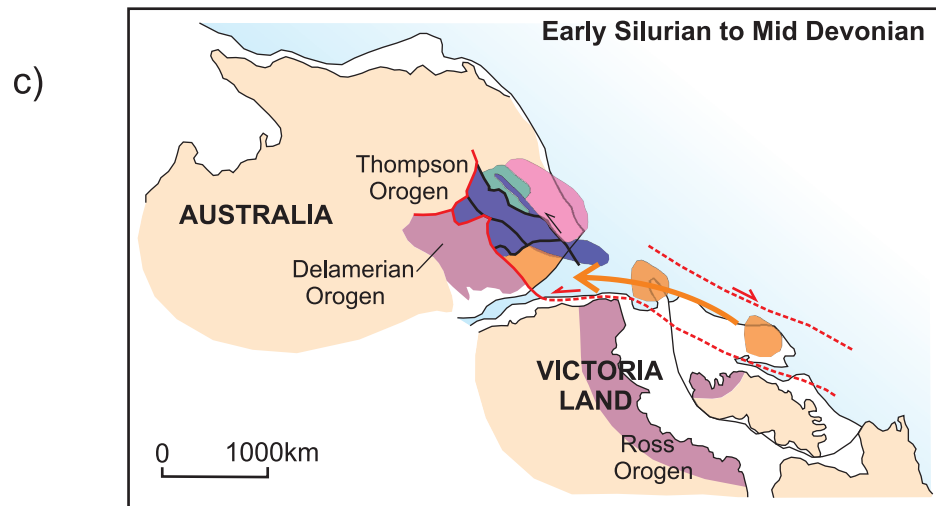
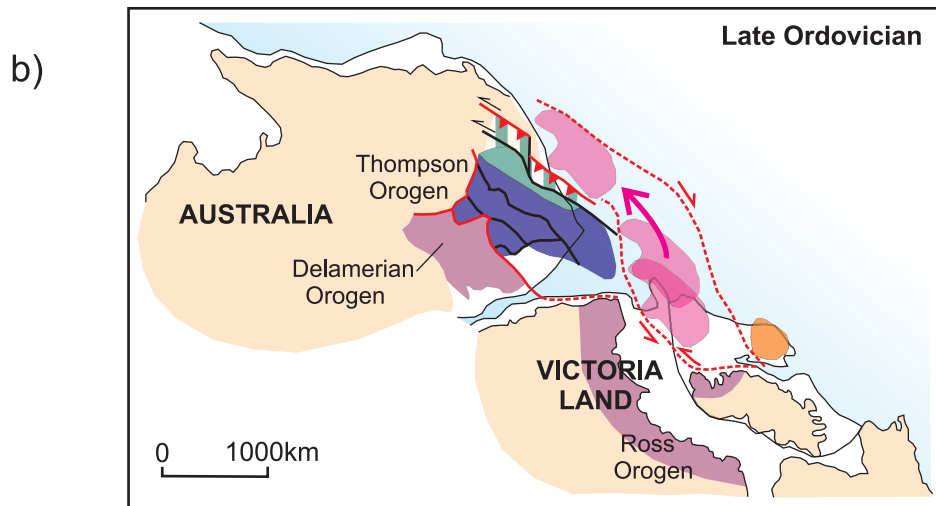
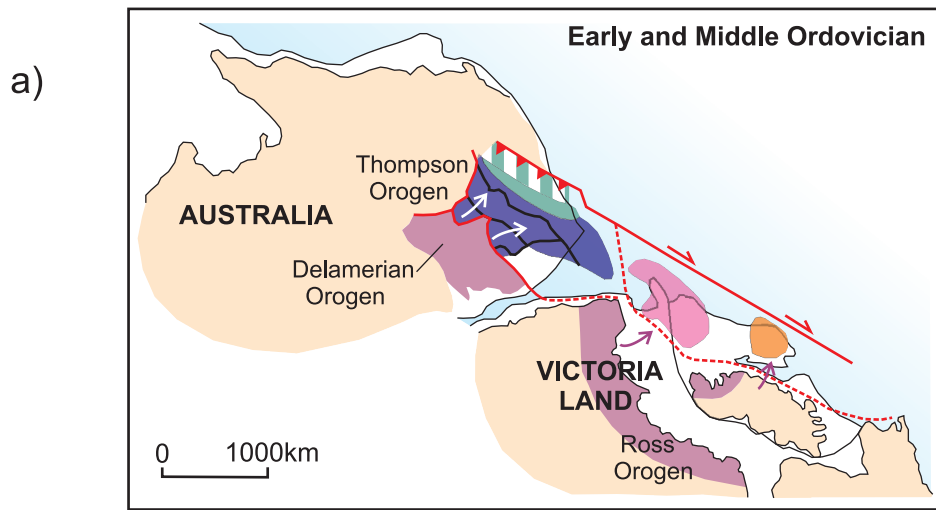
**Figure 2.1** Extents of Lachlan Orogen in the Tasmanides of southeastern Australia, modified from Glen et al. (2006)



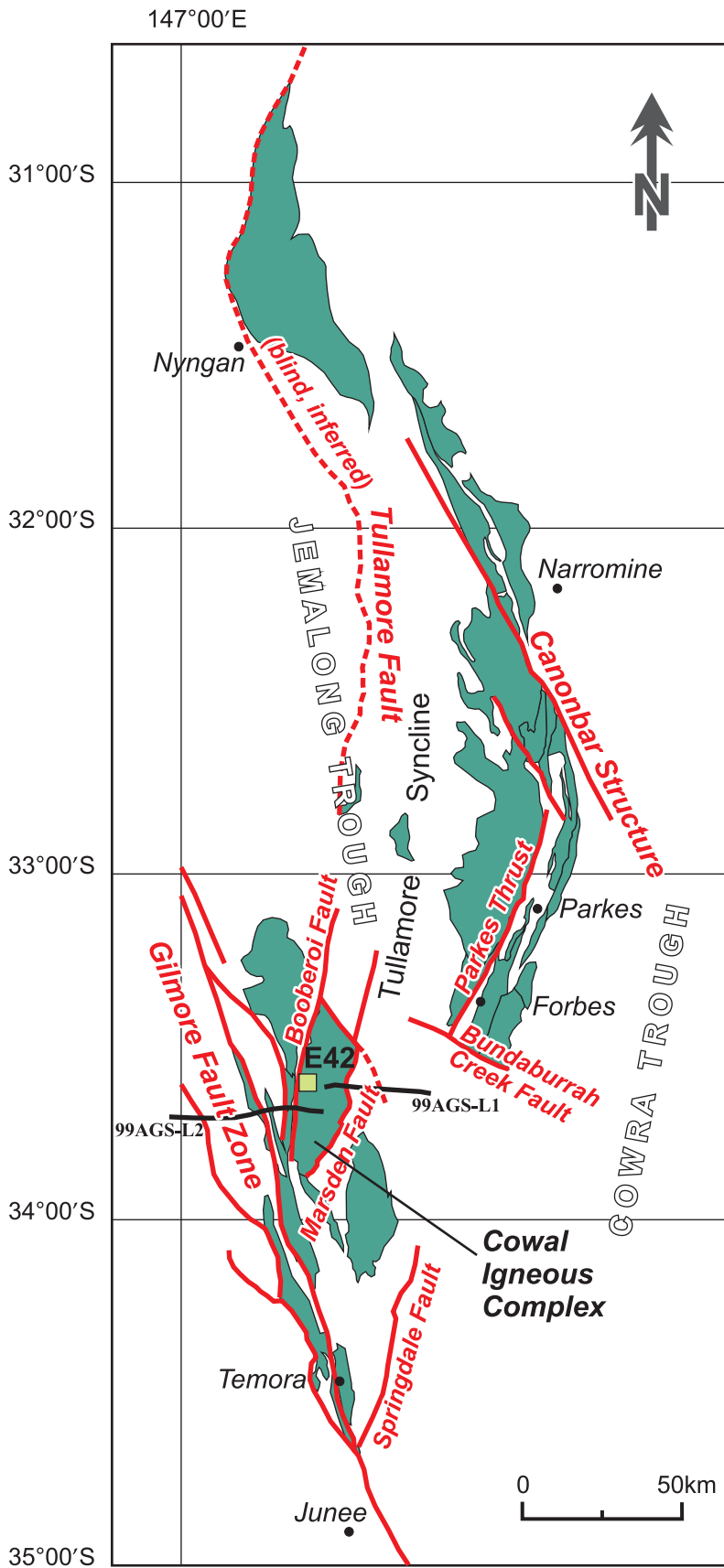
**Figure 2.2** Multiple subduction zone model for the tectonic evolution of the Lachlan Orogen, after Gray et al. (2002). Numbers 1, 2, and 3 represent three subduction zones. **a)** Map view. **b)** Cross-sectional view.



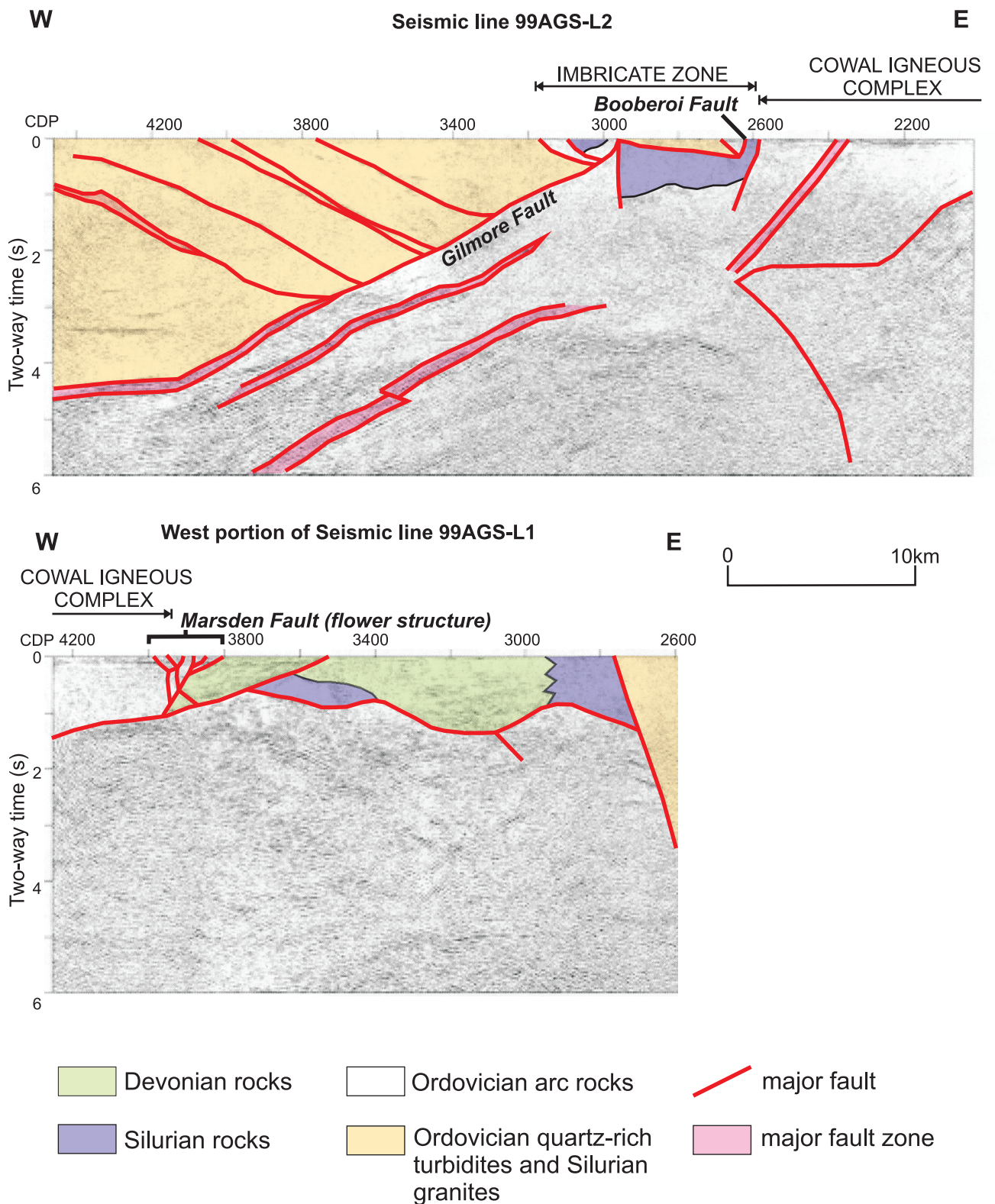
**Figure 2.3** Extents of Macquarie Arc and depositional basins, location of principal gold and copper deposits, and orogen-scale transverse zones, including the Lachlan Transverse Zone (LTZ), Nyngan Transverse Zone (NTZ), and Hunter River Transverse Zone (HRTZ). After Glen et al. (1998), Holliday et al. (2002), and Glen et al. (2007c).



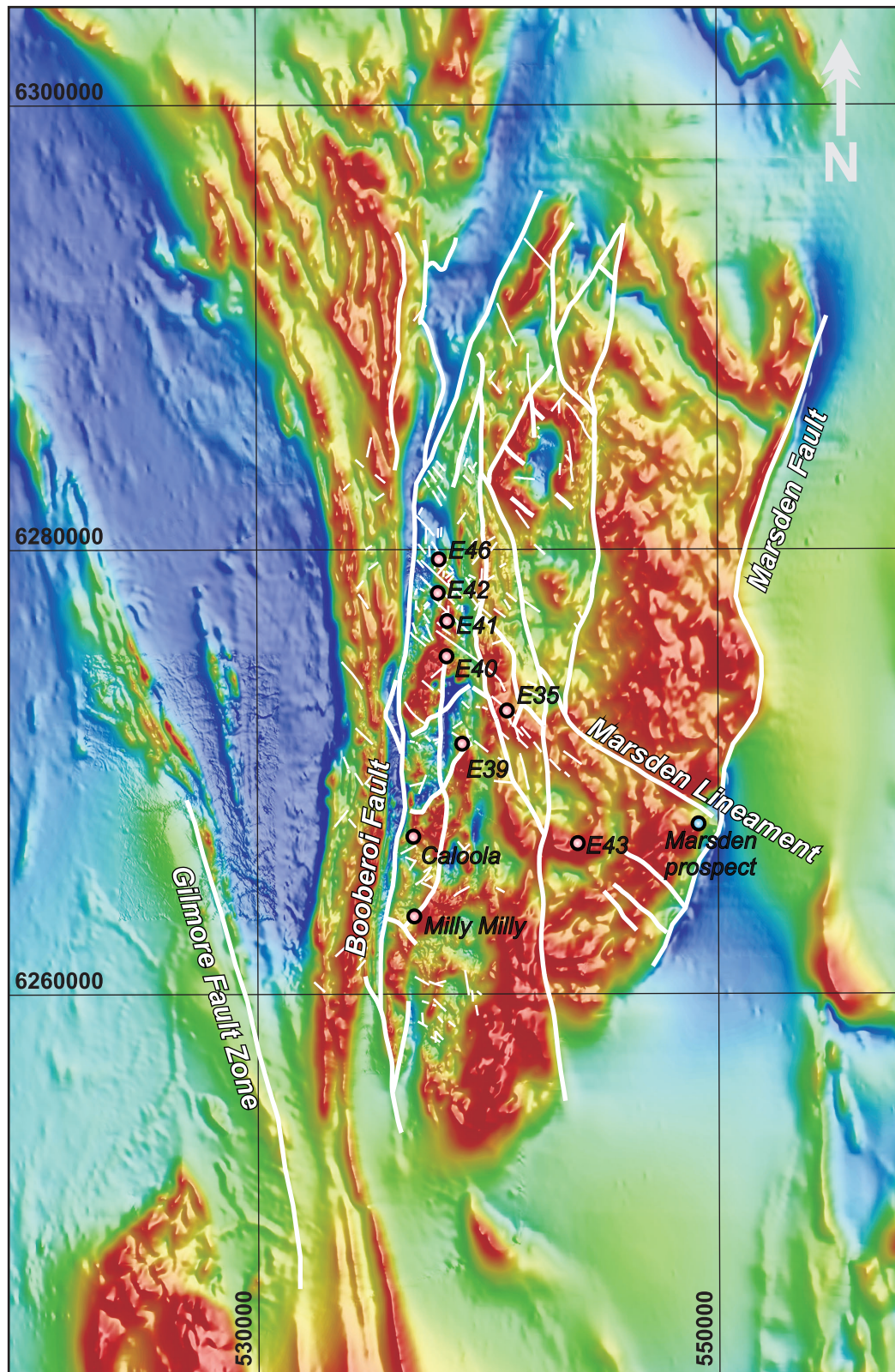
**Figure 2.4** Strike-slip model for the tectonic evolution of the Lachlan Orogen, after Glen (2005).



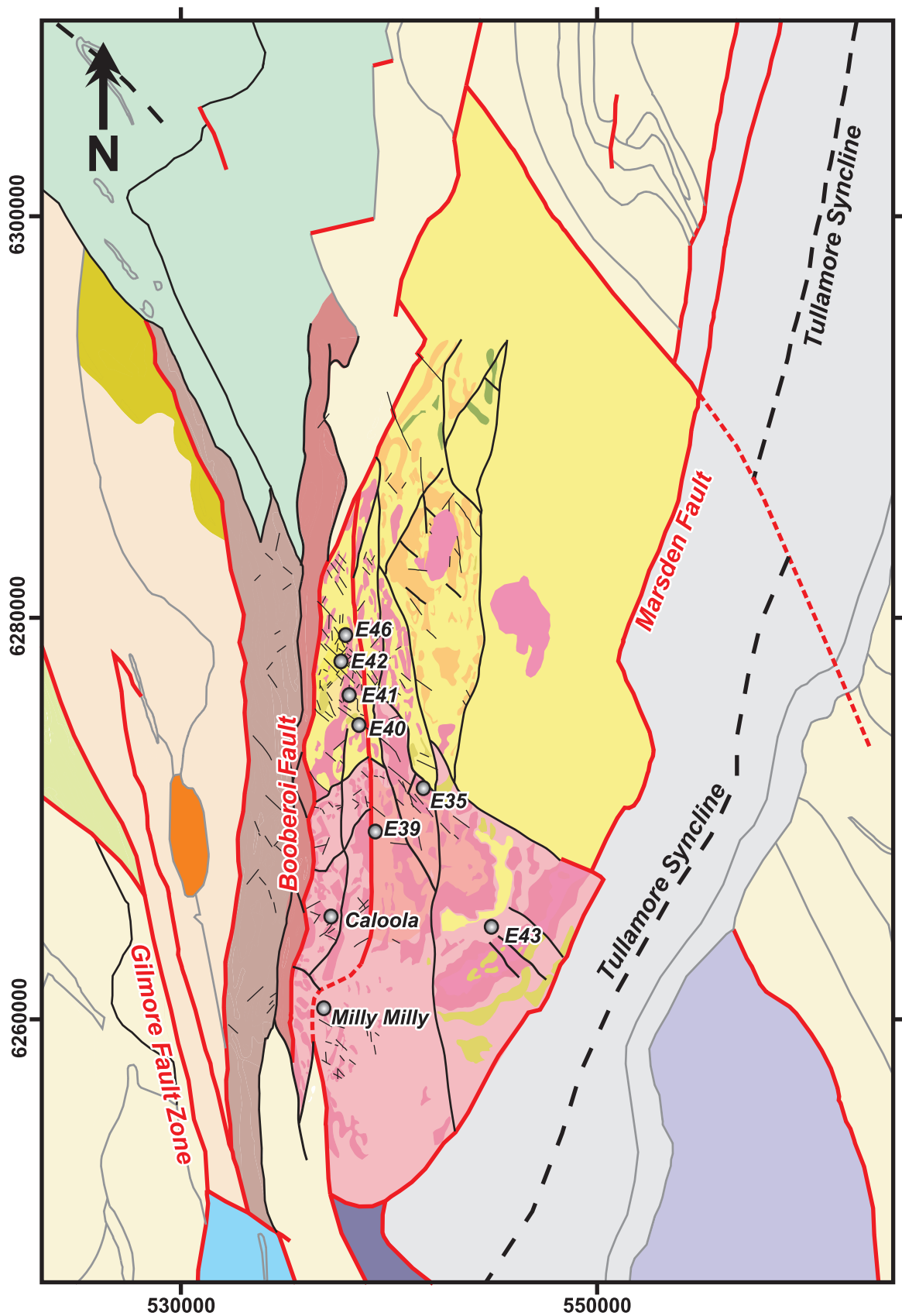
**Figure 2.5** Extents of Junee-Narromine Volcanic Belt, including major faults and basins. After David et al., 2004 and Glen et al., 2007c. Seismic reflection lines 99AGS-L1 and 99AGS-L2 from Figure 2.6 marked by thick black E-W lines.



**Figure 2.6** Interpreted migrated shallow (6s TWT) seismic profiles across the western (99AGS-L2) and eastern (99AGS-L1) parts of the Junee-Narromine Volcanic Belt. Vertical scale equal to horizontal scale, assuming average crustal velocity of 6000 m/s. Simplified from Glen et al., 2002. Location of seismic reflector lines marked in Figure 2.5.

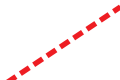


**Figure 2.7** Aeromagnetic survey over the Cowal Igneous Complex. Selected lineaments marked from Pittard (2006): “major” interpreted faults and lineaments marked by thick white lines, “minor” interpreted faults and lineaments marked by thin white lines. Prospects owned by Barrick Gold of Australia Ltd. marked by pink circles, the Marsden prospect (blue circle) owned by Newcrest Mining Ltd. Compare to Cowal Igneous Complex geology map, Figure 2.8. Geophysical image courtesy of Barrick Gold of Australia Ltd.



**Figure 2.8** Interpreted geology of the Cowal Igneous Complex and surrounding rocks. Compiled from Raymond et al. (2000), Smolonogov (2003), Glen et al. (2006), Pittard (2006), and Glen et al. (2007a). See following page for map legend.

## Legend

Devonian		Late Devonian largely fluviatile sedimentary rocks		
Siluro-Devonian		Siluro-Devonian sediments		
		Edol/Manna polymict conglomerate (Derriwong/Ootha Group)		
		Ina Volcanics (ungrouped Silurian unit)		
		Billy's Lookout Granite (ungrouped Silurian intrusion)		
Silurian		Interleaved Ordovician and Siluro-Devonian sediments		
		magnetic unit unspecified		
Ordovician Macquarie Arc		Fairholme Igneous Complex		
			Currumburrama Igneous Complex	
			Belimebung Volcanics	
	Cowal Igneous Complex		Monzonite	
			Diorite	 fault
			Granite	 fault inferred
			Granitoid undifferentiated	 Major lineations (Pittard 2006)
			Andesite	 Minor lineations (Pittard 2006)
			magnetic volcanics	
			Volcanics and volcanics undifferentiated	
			Upper volcanoclastic unit	 prospect
			Trachyandesite	
			Lower volcanoclastic unit	
			Boonabah Volcanics	
		Ordovician		Girilambone Group - phyllite



**Figure 2.9** The Manna stretch pebble Conglomerate outcropping as the surface expression of the Booberoi Fault. **a)** Subvertical north-south foliation with subvertical lineations defined by striations and elongated clasts. Compass for scale. **b)** Subvertical north-south foliation and clasts showing elongation and flattening. Compass for scale.

## **CHAPTER 3: ENDEAVOUR 42 GEOLOGY**

### **3.1 Introduction**

The Endeavour 42 (E42) deposit is hosted by a volcano-sedimentary succession intruded by a diorite sill, an andesite dome, and a breccia body. The deposit scale geology has been well described (McInnes et al., 1998; Miles and Brooker, 1998; Bastrakov, 2000; Cannell, 2003; Smolonogov, 2003; Strickland, 2005) and this chapter presents an overview of past and current observations, including recent work on the volcanic stratigraphy (Simpson and Cooke, 2006).

### **3.2 Stratigraphic Overview**

The Cowal Igneous Complex is dominated by a sequence of interbedded sedimentary and volcanoclastic facies, trachyandesite lava (coherent and associated hyaloclastite facies), and porphyritic andesite (coherent and autoclastic facies) which have been subsequently intruded by multiple sills and dykes (Figure 3.1). The sedimentary and volcanoclastic facies include mudstone, sandstone, and polymictic volcanic breccia and sandstone. Simpson and Cooke (2006), focusing on Endeavour 46 (E46) host rocks, extended broad stratigraphic correlations between units at E46 and E42. The environment of deposition is interpreted as a subaqueous basin or depocentre medial to distal from a volcanic centre (Simpson and Cooke, 2006). Locally, lavas and sub-volcanic intrusions are interbedded with or have intruded the volcano-sedimentary succession.

#### **3.2.1 Upper and Lower Volcanoclastic Sequences**

##### **Description**

##### Lower Volcanoclastic Sequence

The Lower Volcanoclastic Sequence (LVS) is a package of interbedded laminated mudstones, sandstones, and coarse polymictic conglomerates which constitute the basal stratigraphy of E42 (“Cowal Conglomerate” of Miles and Brooker, 1998). The LVS is 25 to 50m thick above the diorite sill, and at least 60m thick below (Cannell, 2003). Volumetrically, the LVS is dominated by sandstones that are massive to graded, moderately

sorted, and polymictic. Three discrete mudstone horizons occur within the LVS, two of which are up to 6m thick, and the third varies in thickness up to 15m (Cannell, 2003).

Polymictic conglomerate units are clast-supported and have weak normal and reverse grading. Clasts are well-rounded to angular, finely to coarsely plagioclase-phyric, with minor felsic to intermediate, equigranular intrusive clasts (Miles and Brooker, 1998; Cannell, 2003). The polymictic conglomerate has a maximum thickness of 15m (Cannell, 2003). The LVS is weak to strongly magnetic due to the presence of mafic volcanic clasts (Purvis, 2002).

### Upper Volcaniclastic Sequence

The Upper Volcaniclastic Sequence (UVS, the “Great Flood Unit” of Miles and Brooker, 1998) has a true thickness of approximately 125m and is separated into several interbedded subunits: pebbly sandstone, laminated mudstone, vitric/lithic-rich tuffaceous sandstone, and polymictic breccia (Strickland, 2005). The UVS is distinguishable from the LVS by the presence of a juvenile pyroclastic component (glass shards and pumice), the predominance of poorly sorted pebbly sandstone, and a lack of magnetism (Cannell, 2003).

The pebbly sandstone horizons constitute the greatest component of the UVS by volume, and are graded to massive, locally bedded and polymictic. Clasts are typically subrounded to subangular, and include porphyritic intermediate volcanic clasts and crystal fragments (feldspars, ferromagnesian minerals, minor FeTi oxides, quartz, and apatite; Ashley, 2003a). Soft sediment deformation structures are commonly observed in these units; flame structures, load clasts, and bioturbation (Miles and Brooker, 1998; current study), as well as slump structures and centimetre-scale faulting indicating syn-depositional deformation (Cannell, 2003; current study).

The vitric/lithic-rich tuffaceous sandstone horizons are massive to weakly graded, medium to coarse-grained, and are variably hydrothermally altered to sericite-quartz-chlorite-carbonate  $\pm$  pyrite-leucoxene-hematite (Ashley, 2003a; Smolonogov, 2003; Strickland, 2005). Clasts include altered microporphyritic to aphanitic, locally pumiceous clasts of intermediate to felsic composition, as well as mudstone fragments and rare accretionary lapilli. Clast sizes range from 2 to 8mm, and matrix is fine-grained and chlorite altered. The aphanitic fragments are pervasively altered to dark green chlorite and display distinctive

cusplate, platy, and curvilinear margins (Cannell, 2003). Rare clasts display relict perlitic textures (Strickland, 2005).

The polymictic breccia of the UVS occurs in two separate horizons, each ranging in thickness from 2 to 25m. The breccia is normally graded from a basal clast-supported cobble breccia, up through pebble breccia, sandstone, to an upper mudstone unit. Clasts are angular to subrounded and consist predominantly of amygdaloidal, feldspar-phyrlic intermediate to mafic clasts (commonly red in color indicating the presence of hematite), with minor volcanic lithic fragments and pyroclasts (Cannell, 2003). This unit is strongly and pervasively altered to an albite-chlorite-carbonate  $\pm$  hematite-sericite-titanite assemblage (Ashley, 2003a). Polymictic breccias display larger clast sizes with increased unit thicknesses, and the breccias pinch out abruptly at the edges (Cannell, 2003).

### **Interpretation**

In the LVS, moderately sorted bedded sandstones are consistent with deposition as mass-flow deposits, or sediment gravity flows. The polymictic cobble conglomerate may represent a high-energy, high-density mass flow or channel deposit (Cannell, 2003). Laminated mudstone units likely represent background sedimentation (suspension settling) in a quiet water environment. The thickness of mudstone beds and the lack of shallow water sedimentary structures, such as cross bedding, in any of the volcanic and sedimentary clastic facies indicates deep water conditions located below-storm-wave-base (Miles and Brooker, 1998).

In the UVS, normal grading and bedding observed in the pebbly sandstones are consistent with mass flow deposits (Miles and Brooker, 1998). The graded polymictic breccia is interpreted as a high-energy subaqueous channel deposit that eroded into underlying unconsolidated sediments (Cannell, 2003). Red hematitic breccia clasts are interpreted to be the result of thermal oxidation which is a common process in subaerial environments (McPhie et al., 1993). Abundant hematite in red mudstone horizons is recorded within a similar volcano-sedimentary package at E46 (1km north of the E42 deposit), and interpreted as background pelagic sedimentation from a subaerial source but deposited in a below-storm-wave-base subaqueous environment (Simpson and Cooke, 2006). Many clast shapes in the polymictic facies appear unmodified (for example, formerly glassy shards still retain cusplate and curvilinear margins) which suggests a syn-eruptive origin (cf.

Simpson and Cooke, 2006). These juvenile clasts were mixed with other volcanic and non-volcanic clasts during transport and deposition (cf. Simpson and Cooke, 2006). The relict perlitic texture in some of the clasts indicates that they were formerly glassy. Abundant glassy clasts with curvilinear clast margins are typical of quench fragmentation in a subaqueous depositional environment (McPhie et al., 1993). In addition, a fossiliferous limestone clast was found within a polymictic lithic breccia at E46, whose stratigraphy is broadly correlatable with E42, supporting a marine environment of deposition (Simpson and Cooke, 2006).

### **3.2.2 Eastern Volcaniclastic Sequence**

#### **Description**

The Eastern Volcaniclastic Sequence (EVS) has historically been included in the LVS but is described most recently as a separate volcaniclastic sequence by Strickland (2005). The EVS is located to the east of the Cowal Fault (Figure 3.1), dips moderately west-northwest, and is at least 200m thick (Cannell, 2003). It is dominated by massive to laminated mudstones, with interbedded clast-rich, pebbly sandstones and polymictic conglomerate, similar compositionally to the LVS. The EVS is variably magnetic and displays strong hematitic alteration. Bedding is variable, suggesting soft sediment deformation during or shortly after deposition (Strickland, 2005).

#### **Interpretation**

The EVS is typically finer grained than the LVS but compositionally similar and may be laterally equivalent strata. Hematite alteration within the EVS is interpreted as secondary, most likely developed during diagenesis (Strickland, 2005).

### **3.2.3 Trachyandesite Lava**

#### **Description**

The trachyandesite unit at E42 consists of both coherent and monomictic volcaniclastic facies, and has a true thickness of 45 to 55m. Multiple coherent plagioclase-phyric trachyandesite lobes are intercalated with a monomictic breccia unit (Miles and Brooker, 1998). The coherent facies is characterized by 10-15% elongate plagioclase

phenocrysts (euhedral to subhedral, 1-6mm in length, commonly glomerocrystic) within a finely crystalline groundmass containing abundant plagioclase microlites (Miles and Brooker, 1998). Plagioclase laths are commonly altered to albite-carbonate-sericite and a secondary alteration assemblage of chlorite-sericite-carbonate-quartz-pyrite has replaced the ferromagnesian minerals as well as the formerly glassy groundmass. Magnetite is present as a minor primary phase and is selectively altered to a leucoxene-chlorite-apatite-pyrite assemblage (Smolonogov, 2003).

Locally, coherent trachyandesite facies have brecciated margins with blocky to globular trachyandesite clasts in a mud-sized sediment matrix (Smolonogov, 2003). Monomictic breccias are commonly observed on both upper and lower margins of the coherent trachyandesite lobes. Clasts range from 1mm to greater than 1m and consist of blocky, angular, curvilinear trachyandesite fragments displaying local in situ jigsaw-fit textures (Miles and Brooker, 1998; Strickland, 2005).

### **Interpretation**

Intervals of globular trachyandesite clasts surrounded by a mud matrix are interpreted as peperite (Cannell, 2003). Peperitic textures are indicative of syn-volcanic interaction of the intruding lava or magma with wet, unconsolidated sediments (McPhie et al., 1993). Blocky, jigsaw-fit breccias at the margins of the coherent lava facies are interpreted as hyaloclastite, and resedimented hyaloclastite (Miles and Brooker, 1998). Hyaloclastite is generated by in situ quench fragmentation of lava as it interacts with water (McPhie et al., 1993). In summary, trachyandesite was extruded as subaqueous lavas, as well as possibly intruded as sills into the surrounding volcano-sedimentary package. The environment of deposition is interpreted as a deep, below-storm-wave-base marine environment.

### **3.2.4 Porphyritic Andesite**

#### **Description**

The porphyritic andesite is subdivided into two distinct units: coherent porphyritic andesite and monomictic andesite breccia. Coherent andesite occurs at the northwestern extent of E42 (Figure 3.2), as an irregularly shaped body in the UVS and occurs along strike of the monomictic andesite breccia (Cannell, 2003).

### Coherent Andesite

The coherent porphyritic andesite unit is fine to medium grained and weakly porphyritic. Up to 15% of the rock is composed of subhedral to anhedral feldspar phenocrysts (maximum 4mm long) and fine, elongated amphibole and hornblende phenocrysts (Cannell, 2003). Wallrock xenoliths are rare and reach diameters of 4cm. Selective epidote alteration of feldspar phenocrysts is a common feature of the coherent andesite (Cannell, 2003). The contact between the andesite and the UVS is sharp with localized weak shearing and an increased abundance of veins and silica-sericite alteration (Cannell, 2003).

### Monomictic Andesite Breccia

Monomictic andesite breccia occurs above the UVS and along strike from the andesite body (Cannell, 2003). The breccia is dark grey, massive, and dominated by angular andesite clasts which are non-vesicular, weakly to moderately porphyritic (5-20%), with fine to medium (1-4mm) feldspar and chloritized mafic phenocrysts (Cannell, 2003). The transition between coherent andesite and monomictic breccia is gradational; from coherent andesite, to jigsaw-fit andesite breccia, to clast-rotated breccia comprised of up to 40% subangular porphyritic andesite clasts in a fine mud-sized matrix. The lateral contact between the monomictic andesite breccia and surrounding volcanoclastic units (UVS) also appears to be gradational (Cannell, 2003).

### **Interpretation**

The porphyritic andesite unit is interpreted as a partially emergent cryptodome. The monomictic breccias are interpreted as peperite, in situ hyaloclastite, and resedimented hyaloclastite (Cannell, 2003). The occurrence of both peperite and in situ hyaloclastite on upper contacts suggest that the andesite was in part intrusive and in part extrusive (McPhie et al., 1993). In addition, the presence of hyaloclastite supports a subaqueous depositional environment. The gradational transition observed laterally from hyaloclastite facies into the adjacent volcano-sedimentary units indicates they were deposited penecontemporaneously.

### **3.3 Intrusive Units**

There are a variety of units which intrude the volcano-sedimentary succession of the Cowal Igneous Complex. These include a volumetrically significant diorite sill complex and multiple stages of dyke emplacement. There are at least six different dyke compositions recorded at E42, distinguished by macroscopic textures and mineralogy, four of which pre-date gold mineralization and two which crosscut mineralization. Pre-gold dykes are the Feldspathic, Megacrystic, Pyroxene-phyric, and Mafic dyke units. Post-gold dykes are the Vesicular and Diorite dyke units. All dyke units, except one of the Diorite dykes, are not wide enough to appear on the scale of the schematic cross sectional and plan views of E42 (Figure 3.1 and 3.2).

#### **3.3.1 Diorite Sill Complex**

##### **Description**

Diorite (“Muddy Lake Diorite” of Miles and Brooker, 1998) is volumetrically the most significant intrusive phase at E42 and occurs at depth throughout the deposit. It was emplaced discordantly into the LVS (Figure 3.1). Locally up to 230m thick, the diorite is characterized by two textural phases: equigranular and porphyritic. The equigranular phase is predominantly fine to medium grained, with euhedral to subhedral phenocrysts ranging from 1-3mm. The porphyritic phase, containing phenocrysts ranging from 5-8mm, is volumetrically less significant than the equigranular phase. The former has been previously called ‘monzodiorite’, due to the larger feldspar phenocryst population (Smolonogov, 2003; Strickland, 2005). Contacts between the two textural phases are irregular, ranging from sharp to gradational (Smolonogov, 2003). Overall, the diorite is composed of approximately 30% subhedral plagioclase phenocrysts (ranging in composition from albite to oligoclase, but originally occurring as andesine), 30% chlorite and calcite (replacing primary biotite, hornblende, and pyroxene), 5-10% interstitial K-feldspar, and 20-30% interstitial hydrothermal quartz (Bastrakov, 2000). Accessory minerals include magnetite (commonly destroyed by hydrothermal alteration), sericite and epidote (both alteration products), and anatase ( $\pm$  rutile). Bastrakov (2000) also records infrequent relict crystals of actinolite-tremolite and clinopyroxene at depth. The diorite has been variably hydrothermally altered and the primary mineralogy is commonly completely obscured. The dominant alteration

assemblage is chlorite-carbonate-epidote, with patches of pervasive chlorite-carbonate-pyrite  $\pm$  hematite (Strickland, 2005). In the latter intervals, cream-coloured leucoxene is commonly found replacing primary magnetite, giving the diorite a distinctive speckled appearance.

### **Interpretation**

A composite series of intrusions have been proposed for the textural variations within the diorite (Miles and Brooker, 1998), as have local differences in fractionation (Strickland, 2005). Bastrakov (2000) dated the main diorite intrusion at  $453 \pm 3.8$  Ma (U-Pb), and Perkins et al. (1995) recorded a hornblende K-Ar date of  $456 \pm 5$  Ma for diorite emplacement.

### **3.3.2 Pre-gold Dykes**

#### **Description**

Feldspathic dykes are the most abundant dyke phase and range from 0.5 to 3m thick (Anderson, 2003). Dykes are porphyritic, containing 7-25% euhedral chlorite-sericite altered plagioclase laths (1-10mm in length) within an aphanitic groundmass (Miles and Brooker, 1998). The groundmass is pervasively altered to chlorite-carbonate  $\pm$  epidote with disseminated pyrite. Primary dyke mineralogy suggests an original composition of andesite or latite (Ashley, 2003b). Plagioclase phenocrysts are commonly flow aligned, and wallrocks are locally sheared parallel to chilled dyke margins. Gold-bearing veins are found along dyke margins, as well as obliquely crosscutting the dykes.

Megacrystic dykes have similar mineralogy to the Feldspathic dykes, and are differentiated from the latter by larger plagioclase phenocrysts. In the Megacrystic dykes, plagioclase phenocrysts are tabular with rounded margins ranging from 10-12 mm in the long dimension. The rounded margins may indicate partial resorption of the phenocrysts during crystallization (Strickland, 2005). The groundmass is finely crystalline to aphanitic and is variably altered to chlorite-carbonate  $\pm$  epidote. Plagioclase phenocrysts are pervasively chlorite-sericite altered. Flow banding is common with phenocrysts aligned parallel to dyke margins.

Pyroxene-phyric dykes comprise a volumetrically small portion of the dykes observed at E42. They range from 0.1 to 2m thick, are weakly to strongly magnetic, and are intermediate to mafic in composition (Smolonogov, 2003). Phenocrysts are characterized by

euohedral sericite altered plagioclase laths (<10 mm in length and comprising up to 40% of the rock) and blocky chloritized clinopyroxene (<4mm and comprising up to 20% of the rock). Groundmass is finely crystalline to aphanitic, and is pervasively replaced by epidote-carbonate ± chlorite-quartz-actinolite-leucoxene (Strickland, 2005). Carbonate-quartz-epidote ± chlorite filled amygdals are common. Patchy pyrite ± chalcopyrite is disseminated throughout, and is thought to be associated with weak gold mineralization (Anderson, 2003).

Mafic dykes at E42 are typically aphanitic, contain abundant fine disseminated pyrite, and are variably amygdaloidal. Less commonly Mafic dykes contain chlorite-carbonate ± pyrite altered mafic phenocrysts (pyroxene or hornblende) up to 2mm in size (Smolonogov, 2003). Ashley (2003b) suggests a primary mafic to intermediate dyke composition, which has been pervasively altered to chlorite-K feldspar-albite-sericite-carbonate ± leucoxene-pyrite. Primary remnant magnetite is patchy and in places has been altered to hematite. Rare amygdals (2-3mm) are filled by quartz and/or carbonate ± epidote-sericite-chlorite (Anderson, 2003).

## **Interpretation**

Gold-bearing veins parallel to dyke margins and crosscutting the dykes, as well as local gold-bearing disseminated sulfides, indicate that these four dyke phases were emplaced prior to the gold mineralization event at E42. A north striking Megacrystic dyke was previously interpreted as post-dating gold mineralization (Anderson, 2003), however the current study shows that all Megacrystic dykes are mineralized, regardless of orientation. Attempts to date the Megacrystic, the Feldspathic, and the Pyroxene-phyric dyke phases all failed to yield suitable zircons (Strickland, 2005; Tosdal pers. comm., 2007).

### **3.3.3 Post-gold Dykes**

#### **Description**

The Vesicular dyke is basaltic andesite in composition (Miles and Brooker, 1998), ranges in thickness from 1 to 3m, and is emplaced along the Central Fault (Figure 3.1). It is composed of 10-15% euohedral chlorite-carbonate altered phenocrysts of amphibole and lesser pyroxene within a finely crystalline trachytic groundmass dominated by plagioclase

microlites (Miles and Brooker, 1998). This dyke is characterized by common (locally up to 10%) carbonate and quartz-filled amygdales, as well as pervasive sericite-silica-hematite alteration of the groundmass. The Vesicular dyke is unmineralized, and crosscuts gold mineralization in the open pit.

Diorite dykes are abundant across the E42 deposit and range from 2 to 30m in thickness. They are porphyritic, composed of up to 60% euhedral and subhedral tabular plagioclase, hornblende, and pyroxene phenocrysts ranging from 2-4mm in long dimension, as well as lesser amounts of Fe-Ti oxides and apatite. The groundmass is finely crystalline, feldspathic, and locally contains minor quartz (Strickland, 2005). The Diorite dykes have been pervasively altered by an albite-chlorite-sericite-carbonate  $\pm$  hematite-quartz-leucoxene assemblage which almost completely replaces the primary igneous mineralogy. Dykes also commonly exhibit a weak red colour due to secondary hematite staining. The Diorite dykes are unmineralized and crosscut gold mineralization in core.

### **Interpretation**

Both the Vesicular and Diorite dykes are unmineralized and crosscut gold mineralization at E42. Ashley (2003b) suggested that the Diorite dykes may have originally been more andesitic or dacitic in composition based on the relict textures and interpreted primary mineralogy of this dyke phase. A U-Pb zircon age of  $447\pm 7$  Ma, with a large associated analytical error, was obtained for the Vesicular dyke by Bastrakov (2000). Strickland (2005) obtained a U-Pb age of  $448\pm 4$  Ma for the Diorite dyke, and a second dating attempt resulted in an age of  $456.3\pm 4.1$  Ma (U-Pb) (Tosdal pers. comm., 2007). These ages overlap within the extreme limits of analytical precision, but accurate dates for these dyke phases may be difficult to obtain due to the complex nature of zoning patterns within the analysed zircons (Tosdal pers. comm., 2007).

## 3.4 Breccia Facies

### 3.4.1 E42 Breccia Complex

#### Description

A breccia body crosscuts the diorite sill and LVS at depth in the northeast corner of the E42 deposit. The breccia has a steep-sided domal shape and is partially fault-bound along both the eastern and western margins by the Cowal and Wamboyne Faults, respectively. Late stage reactivation along the Cowal Fault is evidenced in the breccia by intense shearing along the uppermost eastern margin (Strickland, 2005). The breccia strikes northeast for over 300 metres, has a width of approximately 140 metres at a depth of 350m, and extends up to 200 metres below ground level at its shallowest point (Smolonogov, 2003). The breccia body remains unconstrained to the north and at depth due to limited drilling, but reaches depths of at least 600m. Strickland (2005) defines three different facies within the breccia body based on clast types: a diorite clast dominated rock flour breccia (facies A), a pyroxene-phyric clast dominated rock flour breccia (facies B), and a cemented breccia (facies C, containing >5% hydrothermal cement). Facies A, B, and C have been further separated into eleven subfacies. The following facies descriptions are summarized from Strickland (2005).

Facies A is dominated by porphyritic, chlorite-carbonate altered feldspar-phyric diorite clasts in a rock flour matrix (10-20%) and/or minor hydrothermal cement (carbonate-quartz). Both clasts and matrix have been moderately to strongly hydrothermally altered to carbonate-quartz-chlorite-sericite  $\pm$  hematite-epidote-albite-leucosene.

Facies B is dominated by pyroxene-phyric clasts and is the most volumetrically significant facies present. It occurs within the central part of the breccia body. This facies is subdivided into eight different subfacies, each exhibiting the predominance of moderately to strongly quartz-chlorite-carbonate  $\pm$  hematite altered, porphyritic, pyroxene-phyric basaltic andesite clasts. Clast distribution varies from jigsaw-fit to clast rotated, and there are commonly no distinct textural boundaries within the breccia. Two subfacies are characterized by fluidal pyroxene-phyric clasts as the dominant clast type, which have irregular margins typical of brecciation of non-solidified melt. Other clast compositions include diorite (similar to Facies A) and sedimentary clasts (likely derived from the LVS). B

facies breccias are variably hydrothermally altered to quartz-carbonate-chlorite  $\pm$  sericite-albite-leucoxene-hematite, and display varying amounts of rock flour matrix (anywhere from 5-90% depending on the subfacies) and hydrothermal cement (0-5%).

Facies C is characterized by over 5% hydrothermal cement. It is a volumetrically small unit, found only along 8m of core within one drillhole, near the centre of the breccia body. Clast compositions are similar to clasts found in facies A and B. The cement is characterized by a quartz-carbonate-pyrite-chalcopyrite mineral assemblage.

The breccia complex itself does not host gold but is cut by gold-bearing veins. These veins occur on metre to decimetre-scale spacing, and are themselves cut by a late-stage diorite dyke. The barren diorite dyke exploited a pre-existing weakness defined by ankerite-quartz-pyrite veins in the breccia complex. Pyroxene-phyric and mafic dykes also crosscut the breccia complex (Strickland, 2005) indicating that breccia emplacement occurred prior to the dominant early dyking events of the area. Strickland (2005) documents clasts within the breccia complex that have truncated carbonate veining, and the current study reveals early stage barren carbonate veins crosscutting the breccia complex (refer to Chapter 4), indicating breccia emplacement during an early stage of carbonate veining.

## **Interpretation**

The E42 breccia complex is interpreted to have formed largely due to the release of magmatic-hydrothermal fluids off a crystallizing intrusion at depth (Strickland, 2005). Fluidal and blocky pyroxene-phyric clasts in the breccia are interpreted as the juvenile magmatic component (Strickland, 2005). Additional fragmentation processes that may have been involved in the development of the breccia complex include: subsequent movement along the bounding Cowal and Wamboyne Faults that may have triggered brecciation by rapidly decreasing fluid pressures, continuous degassing of underlying melts, the creation of open space within the breccia complex by spalling and caving of wallrocks, and potential “gas streaming” occurring as a separate phase of the decompression process (Strickland, 2005). The breccia did not breach the paleosurface when it was emplaced, but remained as a subsurface breccia body, based on the lack of a diatreme complex and related features (Sillitoe, 2000). The E42 breccia complex grades from a central chaotic brecciated facies, into polymict and monomict breccia facies, then into fractured diorite with no clast rotation,

and finally into coherent diorite. These vertical and lateral facies associations are typical of blind, subsurface breccia emplacement (Strickland, 2005).

The polymictic facies of the breccia contains both diorite and sedimentary clasts as major components, indicating that brecciation occurred after the emplacement of the diorite sill into the volcano-sedimentary sequence. The breccia is crosscut by early stage carbonate veins as well as several mafic and pyroxene-phyric dykes, constraining a relative age of emplacement. The breccia complex also pre-dates gold mineralization at E42, as evidenced by crosscutting gold-bearing veins. The position and presence of the breccia complex appears to be irrelevant with respect to vein development, as there is no refraction of veins through the breccia complex even though it has a different competency and internal structure than surrounding lithology. This applies to all the veins observed at E42; orientations of vein stages are consistent whether they are measured within the breccia complex or within the surrounding host rocks.

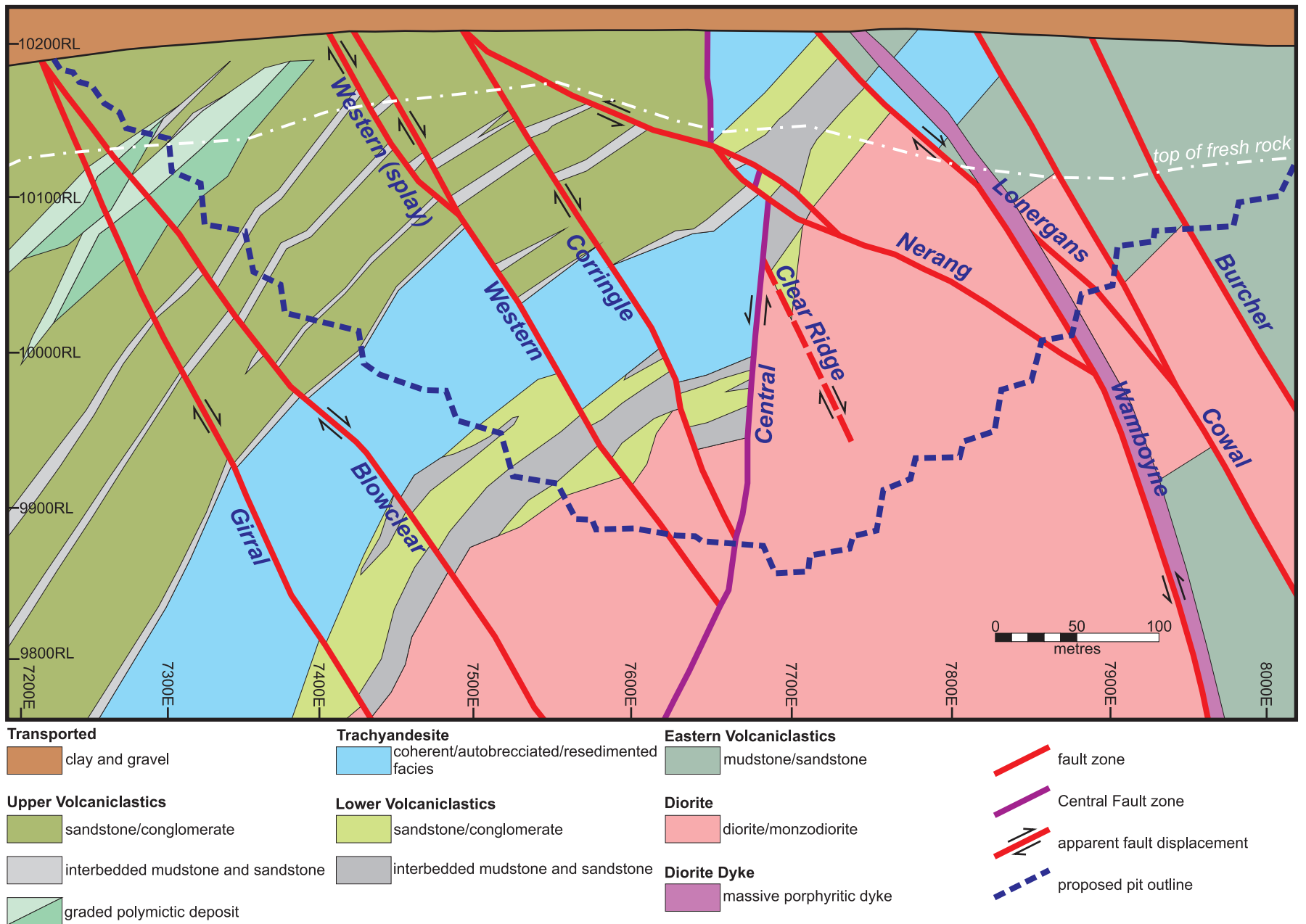


**Figure 3.1** Schematic east-west cross section through E42 along 7800N. Modified from Dijkmans (2003).

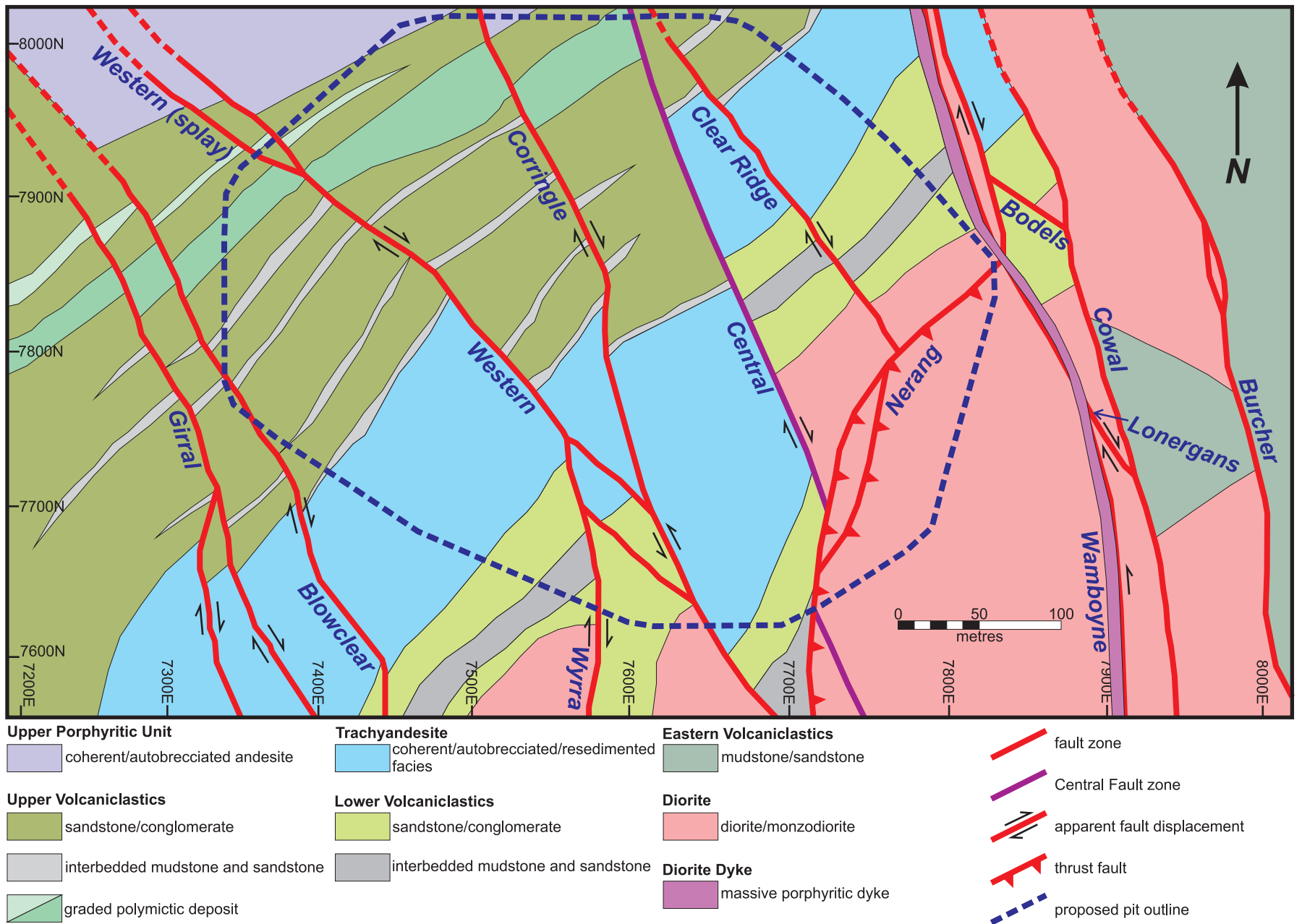


**Figure 3.2** Schematic plan view of E42 at 150m below surface (10050RL). Modified from Dijkmans (2003).

## **CHAPTER 4: STRUCTURAL HISTORY OF THE E42 DEPOSIT**

### **4.1 Introduction**

The E42 deposit is a structurally controlled, vein-hosted gold deposit that has recently begun production as a low-grade open pit mine. Approximately 80% or more of the gold occurs as refractory gold in vein pyrite, and as free particulate gold within veins. The remaining gold occurs as: free particulate gold within fault-hosted quartz-sulfide-cemented breccias; within disseminated sulfides (primarily pyrite, but also sphalerite, galena, and chalcopyrite) found proximal to veins, faults, and fault-hosted breccias; and minor amounts within disseminated sulfides in the E42 Breccia Complex (Smolonogov, 2003). There have been several structural models presented to explain the local geology and vein distribution at E42 including a sinistral Riedel model (Archibald, unpublished data, 1991), local fault geometry and host rock rheology contrasts playing a critical role to vein opening (Miles and Brooker, 1998), and a reverse/sinistral strike-slip model (Munroe et al., 2005).

This chapter explores the structural development of the E42 deposit, including pre-, syn-, and post-gold deformation. Vein paragenesis and crosscutting relationships, together with geometry and relative orientations of brittle structures, are used to create a model of formation for E42. Pre-existing planes of weakness in the rock package play a central role in the structural history of the region as they experienced multiple stages of reactivation under changing stress regimes and evolving fluid compositions.

### **4.2 Field Methods and Data Presentation**

Two sets of data are used for interpreting the structural development of the E42 deposit: data collected from oriented exploration drillcore from previous work by Barrick Gold of Australia Ltd. and North Ltd., and data collected during the current study from mapping in the developing open pit. All the data will be presented as “strike/dip dip-direction” for planes and “trend-plunge” for lineations, using the North American right-hand rule. The rock exposed in the open pit during the current study was restricted to the Upper Volcaniclastic unit, with crosscutting Megacrystic, Feldspathic, Vesicular, and Mafic dykes (see Chapter 3). The upper extents of the pit are variably weathered, and primary rock was not encountered until the 1167RL pit floor along the northwest wall. As of May 2007, the pit

floor was at a depth of approximately 80 metres. The northeastern, eastern, and southern walls of the pit consist of transported lacustrine sediments and therefore provide no insights into the structural history of the deposit. In the upper, weathered horizon all original vein sulfides have been oxidized (mainly to goethite), original carbonates have been weathered out, and remnant quartz is commonly hard to find. A limited amount of the open pit was mappable over the course of the current study (Figure 4.2), and was mapped in detail at 1:100 and 1:200. As pit development progresses, mapping will continue into other lithological units, providing new structural relationships and interpretations.

The E42 deposit is made up of multiple different fault-bounded domains or blocks which are defined using 3D deposit models constructed from drillhole measurements (Figure 4.2, Table 4.1) (e.g. Smolonogov, 2003). In the data presented below, each fault block is described separately, or grouped with adjacent fault blocks displaying similar structure orientations. There has been significant deformation affecting the rock package after vein formation, which is at least partially responsible for the current orientations of fault blocks. For all of the principal stress directions proposed in this study, the interpreted axes are identified for the current orientations of structures in question, which may or may not be the orientations in which they were originally formed. All structural measurements are plotted on the lower hemisphere of an equal area (Schmidt) projection.

### **4.3 Review of Mineralizing Fluid Characteristics**

Bastrakov (2000) examined the geochemical fluid evolution, associated alteration, and thermodynamic properties of the mineralizing fluids at E42. Some vein sequences and interpretations from Bastrakov (2000) are not consistent with observations from the current study; however several important interpretations are made which are summarized here. Two stages of gold deposition are noted for the E42 deposit. One is refractory gold in pyrite, the associated fluid of which is interpreted as magmatic in origin. Derived fluid characteristics for hydrothermal infill, whether breccia cement or veins, are indistinguishable; gold was deposited at epithermal temperatures of 180-270°C. The second stage of gold is interpreted as remobilized from the first stage during the E42 epithermal system. Temperatures for remobilized gold are reported at 90-140°C, but no explanation is given regarding style of mineralization or related vein paragenesis. More work is required to link 3D structural

observations from the current study with the textural and fluid inclusion observations reported by Bastrakov (2000). Though the salinities of fluid inclusions from gold-bearing veins are higher than normal for epithermal deposits (~11 wt%), the homogenization temperatures indicate an epithermal environment of formation (Bastrakov, 2000). Gold-bearing veins have previously been interpreted as reopened by a later fluid which precipitated base metals and fractured early pyrite containing refractory gold, resulting in gold remobilization (Ashley, 2003a; McInnes, 2003; Borthwick, 2004). Further investigation into this proposed gold remobilization is required in light of the new structural observations described for the E42 epithermal system in this study. Late pyrite grains are described as smaller euhedral crystals commonly associated with sphalerite, and have slightly elevated Zn values compared to early pyrite (Borthwick, 2004). The Au:Ag ratios show a continuous range, independent of depth (average 1:1), rather than bimodal distribution, suggesting one gold depositional event at E42 (Bastrakov, 2000; Borthwick, 2004).

## **4.4 Radiometric Dating at E42 and Timing of Gold Mineralization**

### **4.4.1 Sericite Alteration Haloes**

While timing of gold mineralization initially appears well-constrained by the ages of pre- and post-mineral intrusive units (Section 3.3), large analytical errors and complexities in zircon zoning patterns preclude the definite age resolution of the gold-bearing epithermal system (Bastrakov, 2000; Tosdal pers. comm., 2007). Several attempts have been made to directly date gold mineralization at E42. One method attempted is the dating of sericite alteration associated with gold mineralization using  $^{40}\text{Ar}$ - $^{39}\text{Ar}$  methods. Perkins et al. (1995) reported  $^{40}\text{Ar}$ - $^{39}\text{Ar}$  ages of  $439\pm 4.5$  Ma and  $437.6\pm 4.5$  Ma for sericite associated with the main gold zone mineralization at E42. Carr et al. (1995) reported Pb isotopic data on galena and sphalerite, and suggested an age of  $>440$ Ma for mineralization. Based on these dates, gold mineralization at E42 is generally interpreted as occurring ca. 440 Ma. Several sericite samples have been submitted from the current study for dating, in an attempt to recreate the  $^{40}\text{Ar}$ - $^{39}\text{Ar}$  ages of Perkins et al. (1995). The submitted samples contain sericite which has been enclosed in late stage pyrite, as this inclusion minimizes the amount of Ar lost after sericite formation, thus resulting in a more accurate age. The results are not yet available.

Quartz-sericite alteration crosscutting the porphyry copper mineralization at E39 (Section 2.6.2) was dated by Perkins et al. (1995) at  $439.6 \pm 4.5$  Ma. Bastrakov (2000) suggests there was a regional tectonic event at  $\sim 440$  Ma which resulted in favourable conditions for gold mobilization in the E42 area and its subsequent deposition in related fault and fracture zones. The high Au:Ag ratios of the Cowal gold corridor prospects suggest a genetic link to local pre-existing porphyry copper mineralization that potentially enhanced the amount of gold available for later remobilization (Bastrakov, 2000). Two episodes of hydrothermal activity in the Cowal area are proposed: a magmatic-related episode at ca. 467-453 Ma and later hydrothermal remobilization at ca. 440 Ma during which the sericite alteration haloes were formed (Bastrakov, 2000). The 440 Ma sericite age may alternatively reflect partial Ar loss and/or resetting by a younger thermal event, similar to the results for the  $^{40}\text{Ar}$ - $^{39}\text{Ar}$  dating of vein adularia, see below (Section 4.4.2).

#### **4.4.2 Adularia in Gold-bearing Veins**

Four samples of adularia from four distinct inclined gold-bearing veins (three samples from the open pit, one from drillcore) were dated using  $^{40}\text{Ar}$ - $^{39}\text{Ar}$  methods to constrain the timing for gold deposition at E42. The results for these samples are plotted in Appendix A. Samples E42D1178-25770, E42RL1155-36, and E42RL1155-40 yielded plateau ages much younger than were expected:  $362.7 \pm 2.1$  Ma,  $344.5 \pm 2.1$  Ma, and  $356.3 \pm 1.8$  Ma, respectively. The fourth sample, E42RL1155-38, did not yield an interpretable plateau age. These are minimum ages and therefore do not reflect an accurate age of formation for the gold-bearing veins at Cowal; they rather reflect cooling and probable exhumation during a younger event. These ages fall within the youngest major orogenic cycle to affect the Lachlan Orogen, the Kanimblan Cycle ca. 380-320 Ma. In order to reset adularia, the E42 system needed to either be consistently at temperatures greater than  $\sim 150$ - $300^\circ\text{C}$  (McDougall and Harrison, 1999) spanning from vein formation until cooling, or the system had to reach temperatures over  $150$ - $300^\circ\text{C}$  after the gold-bearing veins had already cooled, and then cool a second time. Therefore, dates obtained from adularia place the cooling of the system to  $< 150$ - $300^\circ\text{C}$ , and thus the closure temperature of argon in adularia, some time during the Kanimblan Cycle.

## 4.5 Structure Fabrics

### 4.5.1 Bedding

Bedding measurements taken from the pit display an average orientation of 200/54 NW (Figure 4.3a). Normal grading within sandstone and mudstone, cross laminations in mudstone, basal scour marks, and load structures indicate bedding is upright. There is a clear clustering effect for the majority of bedding measurements taken from oriented drillcore at E42 and these correspond roughly with bedding measurements from the open pit. Average bedding measurements from drillhole data are slightly different on either side of the Cowal Fault (Figure 4.3b and c). West of the Cowal Fault the average bedding is 215/47 NW, which roughly corresponds to the average pit bedding measurement of 200/54 NW; the entire mapped pit area lies to the west of the Cowal Fault. Downhole bedding east of the Cowal Fault averages 228/33 NW, dipping more shallowly than bedding west of the fault.

### 4.5.2 Faults

Numerous faults are identifiable in the open pit either by offset bedding (Figure 4.4a), or by zones of intense brittle deformation and fracturing (Figure 4.4b). Faults range from <1m to >15m in thickness, with the Cowal Fault (previously the “Eastern Shear Zone” of Miles and Brooker, 1998) being the thickest fault cutting the deposit (Figure 4.1). There are two main fault populations mapped in the open pit, which both display normal-sense separation. The amount and sense of slip is unknown as no piercing points are traceable across the E42 deposit. The dominant population has an average orientation of 322/69 NE, with a second and less prominent cluster averaging 155/64 SW (Figure 4.3d), resulting in a dihedral angle of 50° (Figure 4.3e). These orientations suggest a possible conjugate relationship between the fault populations, although no unequivocal mutually crosscutting relationships are known. The intersection between the two major fault populations at E42 has a near horizontal plunge of 15° towards 328 (Figure 4.3e). This geometry is consistent with a normal-sense Andersonian stress field with a near horizontal intersection of conjugate faults (Anderson, 1951). Given the present fault geometry, bedding is inferred to have been tilted prior to the dominant faulting event at E42.

Two populations of late-stage (post-gold) brittle faults are present. Two southeast-dipping reverse-sense faults are identified in the open pit (Figure 4.3f) which crosscut gold-

bearing veins. These two faults are subparallel to the Nerang Thrust, a young deposit-scale fault which cuts most faults at E42 (Figure 4.1). A population of bedding parallel faults also postdates gold mineralization (Figure 4.3f and 4.4c). Northwest-trending faults locally display evidence of late-stage reactivation: disrupted vein fragments in the Cowal Fault indicate post-mineral reactivation (Figure 4.4b).

Faults identified from drillcore within each of the major E42 fault blocks have defined average orientations per block (Figure 4.5a). A northwest-trending pattern, similar to mapped pit faults, is observed, with the exception of block 19 (Figure 4.5a, Table 4.1). In fault block 19, faults strike predominantly southwest, perhaps due to a high proportion of bedding parallel faults in that block. Based on drillhole and pit mapping, the general orientation of faults is relatively consistent across the E42 deposit.

### **4.5.3 Dykes**

Four varieties of dykes are exposed in the open pit: Megacrystic, Feldspar-phyric, Mafic, and the Vesicular dyke. Dykes commonly intrude faults at E42. The Vesicular dyke is a late-stage dyke emplaced along the Central Fault (Figure 4.1), and visibly crosscuts gold-bearing veins. The Vesicular dyke also post-dates intense sericite-dominated alteration associated with the gold mineralization event. All other dyke varieties contain gold-bearing veins, commonly along dyke margins. Most dykes have variably experienced shearing post-emplacement, as the fault planes along which they propagated were reactivated. There are two dominant dyke orientations, averaging 331/79 NE and 168/76 SW, which parallel the main faults across the deposit (Figure 4.5b and c). A less common dyke population at 067/74 SE strikes perpendicular to the first two dyke sets (Figure 4.5b and c), and is defined by several Mafic dykes along the western pit wall (Figure 4.6). The intersection of the average dyke planes plunges 34° towards 338, slightly steeper than the intersection lineation of the fault planes, but in the same direction, and the resulting dihedral angle is 30° (Figure 4.5c).

From drillhole data, dykes to the west of the Cowal Fault are parallel to the dominant fault orientations found at E42, displaying north-northwest and south-southeast strikes (Figure 4.5d). Dykes in fault blocks to the east of the Cowal Fault, however, have slightly different orientations (Figure 4.5e) and display both steeply and moderately dipping dykes, with an average orientation of 191/75 W.

## 4.6 Vein Paragenesis

### 4.6.1 Previous Work

In the past, vein types at E42 have been described on the basis of vein wall geometry and mineralogy, with a minor emphasis on vein orientation (e.g. Bastrakov, 2000; Smolonogov, 2003). Borthwick (2004), for example, divided veins in drillcore into ten different types based primarily on macroscopic vein features and mineralogy without any reference to structural orientations. The current study would place these ten vein types into 4 or 5 different populations. Work based on exploration drilling has subdivided the veins at E42 into “dilatational” and “shear” vein categories (e.g. Simpson, 2003). “Dilatational” veins are described as parallel sided gold-bearing veins that dip moderately to the southwest. “Shear” veins occur as two types, gold-bearing (“mineralized shear”) and barren, and are characterized by irregular vein margins. The term “shear” is commonly used at the mine for veins that do not carry grade, and is not used to connote vein opening style (McInnes pers. comm., 2006). “Shear” veins are found in almost any orientation at E42 (Simpson, 2003), with some falling into the “dilatational” vein orientation (e.g. compare average orientations in Table 4.1). The current study recognizes more complex vein subdivisions than “dilatational” versus “shear”, and so this terminology will not be used.

“Stringer” veins are identified throughout the E42 drillcore and are characterized by widths  $\leq 1\text{mm}$ , irregular margins, subvertical orientations, and compositions dominated by pyrite. Late epidote stringer veins are identified at depth in the E42 breccia complex. Stringer veins across the deposit are paragenetically early (pre-gold event; Bastrakov, 2000), predominantly late and crosscutting late stage carbonate-chlorite veins (current study), or ubiquitous throughout the evolution of the Cowal rock package (Borthwick, 2004). These veins are not considered a key feature in the development of the E42 hydrothermal system, as they are present throughout the development of the system, both pre-, syn-, and post-gold.

### 4.6.2 Variations in Vein Composition along Length

Vein fill viewed on pit walls commonly varies in abundance and mineralogy along length. Consequently, the subdivision of vein types based strictly on mineralogy seen in drillcore may be misleading. In cases of noticeable vein variability along length, orientation is essential to correctly identify vein populations, especially where sheeted vein sets are

present. Thus, veins sharing similar, if not identical, mineralogy may be placed into the same population given that their orientations are comparable. This step decreases the amount of “noise” in a total vein data set resulting from the definition of unnecessary vein populations based on small differences in vein fill. Two examples from E42 are presented here. Figure 4.7a displays a fault parallel gold-bearing vein (295/74 NE). The vein is composed of barren, massive carbonate-chlorite at the bottom of the photo that transitions (over approximately 5cm) into an overlying calcite-pyrite-quartz-chlorite-sericite-galena-sphalerite-chalcopyrite-covellite-bearing section. This vein ranges from 1-8cm wide, and is traced ~8m up the pit wall. A drillhole cutting through the lower extent of the vein will reveal a barren carbonate vein, whereas a drillhole through the upper extent of the same vein will reveal a highly mineralized vein of the same orientation. Two additional examples of heterogeneous mineral distribution in veins appear in Figure 4.7b and c. In view of these examples, both vein mineralogy and orientation must be considered together when grouping veins into sets, as a neglect of either feature may complicate the vein paragenesis. Table 4.2 summarizes the characteristics of different vein populations defined by this study at E42.

### **4.6.3 Pre-gold Veins**

Multiple populations of barren carbonate-dominated veins span the evolution of the E42 deposit. Although they are temporally unconstrained with respect to each other, there are two calcite-dominated vein populations which formed prior to the gold-bearing veins at E42 (Figure 4.5f). The early carbonate vein sets cut all rock types, including the breccia complex (see Chapter 3), but cannot be assigned a relative age with respect to faulting and dyke emplacement. One population is roughly bedding parallel (209/43 NW) and the second is steeply dipping to the south-southwest (121/83 SW). Both vein sets are composed of calcite ± chlorite ± pyrite with variably chloritized margins. Vein widths range from 1mm up to 8mm (Figure 4.8a), averaging approximately 1mm, and vein margins are irregular. One vein of the steeply dipping population shows multiple openings, with the initial opening displaying both dextral and normal sense true dip-slip movement in the sheared vein calcite adjacent to wallrock (Figure 4.8b and c). The second stage calcite infill forms massive crystals in the centre of the vein; it is unclear at what stage in the structural history of the rock package this reopening occurred. Early bedding parallel calcite veins (209/43 NW) are typically thin ( $\leq 1$ mm), and direction of opening is indefinable from vein textures.

#### 4.6.4 Syn-gold Veins

Gold-bearing carbonate-base metal veins have four distinct orientations across the E42 deposit, and are found in nearly all rock units, including the E42 breccia complex (see Chapter 3). There are two steeply dipping populations of gold-bearing veins including steep fault-hosted hydrothermal breccia intervals, and two inclined populations of gold-bearing veins. Observations from the open pit suggest that high grade areas are more closely associated with the thickness of individual auriferous veins, regardless of their orientation, rather than their density. Thus, even though there may be a greater number of thin veins in a particular area, the grade will not necessarily be higher than an area containing a smaller number of thicker veins.

#### Steep Gold-bearing Carbonate-Base Metal Veins

The oldest carbonate-base metal veins form as two steeply dipping sets (Figure 4.9a) which parallel the dyke populations (Figure 4.5b). These two orientations are averaged at 331/73 NE and 069/76 SE (Figure 4.9b). Some veins are present within and along the margins of pre-mineral dykes. The latter population (069/76 SE) parallel an east-trending Mafic dyke exposed along the western pit wall (Figure 4.6). The abundance and frequency of gold-bearing veins in the open pit decreases as the distance from faults and dykes increases. Both vein sets have similar mineralogy consisting of calcite-quartz-pyrite  $\pm$  adularia  $\pm$  sphalerite  $\pm$  galena  $\pm$  chalcopyrite  $\pm$  covellite  $\pm$  visible gold  $\pm$  late stage ankerite infill of void space (Figure 4.8d and e). Detailed petrography by Bastrakov (2000) identified minor pyrrhotite within pyrite, as well as rare hessite ( $\text{Ag}_2\text{Te}$ ), altaite ( $\text{PbTe}$ ), and petzite ( $\text{Ag}_3\text{AuTe}_2$ ) associated with pyrite, galena, and gold. Gold is found as inclusions within pyrite, as well as between fractured pyrite grains (Figure 4.10a and b, respectively), and is commonly found associated with sphalerite. Pyrite grains are usually extensively fractured, with fractures variably filled by carbonate, sphalerite and galena, as well as gold (Figure 4.10b and c). Multiple generations of base metal vein fill are occasionally evidenced by crosscutting relationships in reactivated veins (Figure 4.10d). Late stage ankerite is the youngest vein component, commonly filling void space surrounding prismatic quartz (Figure 4.8e). Steep carbonate-base metal veins are traceable on metre-scales and locally up several bench heights in the open pit. Average vein thickness is 2-5mm, but reaches up to 10cm in

rare cases. Vein walls are variably planar to irregular, and opening directions are not evident. Vein textures at E42 are typical of epithermal systems (Dong et al., 1995) and include variably zoned crustiform quartz crystals (Figure 4.10e) and “feathery” quartz (Figure 4.10f).

No crosscutting relationships have been observed for the two steeply dipping gold-bearing vein populations; whether they formed coevally or at separate times is unknown. Both vein sets have similar mineralogy and steep orientations parallel to faults and dykes. The steep south-southeast-dipping vein population is less well developed than the dominant northwest-striking fault parallel population. It is unknown whether this lesser vein cluster is a deposit-wide feature, or merely locally associated with the Mafic dykes.

Orientations of steep gold-bearing veins from drillcore across E42 vary between fault blocks (Figure 4.9c and d, Table 4.1). The deposit-scale trend shows that there is no significant change in orientation of steep gold-bearing veins on either side of the Cowal Fault (Figure 4.9c and d), but data is sparse to the east of this fault.

### **Steep Fault-hosted Breccias**

The term “quartz-sulfide breccia” (QSB) has been used to describe steeply dipping high grade brecciated intervals (e.g. Smolonogov, 2003). Despite the name, the cement mineralogy of “QSB” intervals varies from barren quartz, quartz-sulfides, quartz-sulfides-ankerite, ankerite-sphalerite-pyrite, to barren ankerite. Three main stages of fault-hosted breccias have been identified and redefined based on the cement mineralogy (Table 4.3). Some of the breccia cement assemblages correspond to equivalent vein fill assemblages at E42, and it is inferred that stages of brecciation are likely linked to specific vein events. Breccia cement shows cockade and massive textures, although the latter predominates. Clasts display mainly clast-rotated organization and populations vary from monomictic to polymictic. Clast types include brecciated wallrock (predominantly volcanoclastic rocks) and older vein material (both barren and mineralized vein fragments). Clasts are generally angular to subangular, and the amount of matrix is negligible. Most brecciated intervals are spatially associated with major faults in the deposit and are discontinuous both laterally and vertically on decimetre to metre scales, making the prediction of high grade intervals difficult.

### Stage 1: Gold-bearing Breccias

Hydrothermal quartz  $\pm$  pyrite  $\pm$  sphalerite cement occurs in the oldest brecciated intervals (Figure 4.11a). Stage 1 breccias are commonly overprinted by stage 2 ankerite-sulfide-cemented breccias and/or stage 3 barren ankerite-cemented breccias (Figure 4.11b and c). Minor amounts of late barren ankerite fill is common (Figure 4.11a). The upper extent of a stage 1 breccia in the northwest corner of the pit (Figure 4.12) is found along a steep west-trending fault which extends 15m up the bench wall. The breccia is polymictic, auriferous (16ppm Au), and contains angular to subangular clasts of volcanic sandstone and mudstone enclosed within massive quartz-calcite-pyrite-sphalerite  $\pm$  chlorite cement. Also evident at the upper extent of this breccia interval are curved veins emanating from the breccia tip (Figure 4.12). These veins consist predominantly of calcite  $\pm$  pyrite and their orientations suggest formation related directly to brecciation. Stage 1 breccia intervals are steeply dipping, and trend generally to the north and west (Figure 4.13a). Some of these breccias also contain feldspar-phyric clasts, interpreted as dyke fragments, suggesting the breccias formed along pre-existing faults and dykes. Many gold-bearing breccia intervals are directly related to the Western and Corringale Faults, and also found directly above the Corringale Fault (Figure 4.1). No gold-bearing quartz-sulfide breccias are found west of the Western Fault. Hydrothermal breccias are not parallel to the inclined gold-bearing veins at E42; they all display steeply dipping, fault parallel orientations. There are no constraints on the lateral or vertical extents of these gold-bearing breccias, but they open the possibility for high grade, lateral “ore shoots” along faults in the E42 deposit.

### Stage 2: Ankerite-Pyrite-Sphalerite Breccias

Ankerite-pyrite-sphalerite  $\pm$  chalcopyrite  $\pm$  galena  $\pm$  quartz-cemented breccias characterize the second stage of fault-hosted breccias. This stage is found overprinting earlier stage 1 quartz-sulfide cemented breccias (Figure 4.11b). Stage 2 breccias are locally interpreted as reactivating faults used by stage 1 breccias. Stage 2 breccias are also found dipping moderately southeast (Figure 4.13a).

### Stage 3: Barren Ankerite Breccias

Stage 3 fault-hosted breccias are characterized by barren calcite-ankerite  $\pm$  chlorite infill. Clasts are dominated by wallrock volcanoclastic lithology, some containing veins (Figure 4.11d), and rare clasts of fragmented quartz-cemented breccia and dyke clasts. Stage 3 breccias locally overprint quartz-cemented breccias from stage 1 (Figure 4.11c) and commonly display euhedral ankerite crystal terminations in void spaces between clasts (Figure 4.11e). Late stage ankerite-cemented breccias are distributed along the northwest trend of deposit-scale faults, as well as dipping steeply to the east (Figure 4.13a). Ankerite feeder veins to some of these ankerite-cemented breccia intervals locally crosscut inclined gold-bearing veins (Figure 4.11f), indicating the ankerite brecciation event occurred after the gold mineralizing system at E42.

### **Inclined Gold-bearing Carbonate-Base Metal Veins**

The dominant gold-bearing veins at E42 are moderately southwest-dipping, with a smaller population developed parallel to bedding (Figure 4.9e). Average vein orientations are 101/42 SW and 185/39 W, respectively (Figure 4.9f). Inclined gold-bearing veins crosscut the older, steeply dipping auriferous vein populations. Apparent offsets of the steep gold-bearing veins are on mm-scale (Figure 4.14a and b). All documented crosscutting relationships exhibit this consistent temporal relationship (Figure 4.13b). The mineralogy of the inclined veins is identical to the older gold-bearing veins, consisting predominantly of quartz-calcite-pyrite  $\pm$  adularia  $\pm$  sphalerite  $\pm$  galena  $\pm$  chalcopyrite  $\pm$  visible gold  $\pm$  late stage ankerite. Pyrrhotite, hessite, petzite, and altaite have also been recorded (Miles and Brooker, 1998; Bastrakov, 2000). Fractures in pyrite are variably infilled by carbonate, sphalerite and galena, as well as gold (cf. Figure 4.10b and c). During the inclined carbonate-base metal veining event, bedding parallel planes of weakness were also reopened resulting in gold-bearing bedding-parallel veins (Figure 4.14c). As with the older steep gold-bearing veins, inclined vein textures include crustiform quartz crystals which occasionally show zonal textures (cf. Figure 4.10e) and “feathery” textures (cf. Figure 4.10f), characteristic of epithermal systems (Dong et al., 1995). Veins can be traced on metre-scales up several pit benches, with thicknesses varying from <1mm to 15cm and averaging 5-10mm (Figure 4.14d). Vein walls are variably planar to irregular.

Average inclined gold-bearing vein orientations within deposit-scale fault blocks are separated into distinct clusters on either side of the Cowal Fault (Figure 4.9c and d, Table 4.1). To the east of the Cowal Fault, inclined veins dip approximately southeast, as opposed to the predominant southwest-dipping orientation of inclined gold-bearing veins across E42.

### **Quartz-Pyrite ± Calcite Veins**

Quartz-pyrite ± calcite veins, characterized by irregular vein walls and widths of 1 to 10mm, are not common in the deposit (current study: 37 veins versus over 800 gold-bearing carbonate-base metal veins). Two distinct orientations are mapped; a steeply dipping, fault parallel population averaging 344/78 NE, and a moderately southwest dipping population at 144/52 SW (Figure 4.13c). Vein opening directions are not clear, as vein fill is massive or veins are too thin to distinguish any features. Some veins pinch and swell on half-metre to metre-scales. In at least one location, a steep 1-2mm wide quartz-pyrite vein is cut by an inclined, 4mm wide, quartz-pyrite vein (red poles, Figure 4.13c). The mapped quartz-pyrite ± calcite veins do not display crosscutting relationships with respect to gold-bearing vein sets at E42. In fact, their orientations correspond to the dominant steep and inclined gold-bearing vein sets (cf. Figure 4.9a and e). The variation in mineralogy along vein length occasionally seen at E42 (in this case, the absence of base metal sulfides), and the observed crosscutting relationship described above, both suggest that the quartz-pyrite ± calcite veins may actually correspond to the gold-bearing veins at E42.

### **4.6.5 Post-gold Veins**

Several generations of post-gold veins are dominated by carbonate-chlorite infill, and can be separated into three distinct vein stages. From oldest to youngest these are: carbonate reactivation of gold-bearing veins, steep north-striking carbonate veins, and three mutually crosscutting sets of late carbonate-chlorite ± hematite veins (Table 4.2).

### **Carbonate Reactivation of Gold-bearing Structures**

Hydrothermal activity following gold emplacement at E42 reactivated both steep and inclined gold-bearing vein populations, and barren calcite-ankerite ± chlorite was precipitated (Figure 4.15a). The average orientations of these veins, 141/42 SW and 320/77 NE (Figure 4.15b) are similar to the two dominant gold-bearing vein populations. Veins of this

population range from 1 to 5mm thick on average, with irregular margins, and can be followed for metres along strike. Some form along dyke margins, and crosscut subparallel gold-bearing veins (Figure 4.16a), whereas others form along the vein-wallrock interface of earlier veins (Figure 4.16b and c). No crosscutting relationships are observed between the two barren reactivated vein sets, however, based on relationships with other vein sets at E42, these two vein populations are placed within the same temporal interval of the paragenesis (Table 4.2). Therefore both sets of carbonate reactivated gold-bearing veins are assumed to have opened at around the same time.

### **Steep North-striking Carbonate Event**

The second post-gold carbonate-dominated veins trend north and are steeply dipping with an average orientation of 359/86 E (Figure 4.15c). Compositionally, these veins include calcite ± ankerite ± chlorite ± minor pyrite ± minor hematite. Vein widths range from 1mm to 1cm and margins are commonly irregular (Figure 4.17a and b). Veins locally exhibit multiple opening events (Figure 4.17c).

### **Youngest Carbonate-Chlorite-Hematite Veins and Faults**

Three distinct orientations define the youngest veins in the E42 sequence (Figure 4.15d). Two of the vein sets are mutually crosscutting (Figure 4.15e), and the third set has no definitive temporal relationship to date, but is assumed to be mutually crosscutting based on the other two vein sets. These populations average 358/36 E, 075/83 SE, and 201/43 NW, the latter being a bedding parallel vein set (Figure 4.15e and 4.18a). All three of these vein populations have calcite-ankerite-chlorite ± hematite ± pyrite fill. Late carbonate-dominated veins have irregular margins, vary in width from 1 to 8mm, and commonly display multiple opening events (Figure 4.17d and e). These veins cut all rock units at E42, including one of the late ankerite-cemented hydrothermal breccias. All three of these vein sets variably display carbonate-chlorite slickenfibres along vein walls (Figure 4.18b). Veins of the east-dipping population overwhelmingly display slickenfibres with reverse-sense, top-to-the-west displacement (Figure 4.15f). One of these fracture surfaces is the Nerang Thrust, a late stage reverse fault that extends across the E42 deposit. In contrast, many of the moderately west-dipping veins show reverse-sense, top-to-the-east displacement during vein formation (Figure 4.15f).

## 4.7 Geometry of Veins and Structures at E42

### 4.7.1 Fault and Dyke Development

To understand the structural history of the E42 deposit, it is helpful to return to the oldest structural fabric. As bedding is deposited sub-horizontally, bedding measurements in their current orientations can be rotated back to horizontal, and this same rotation applied to other structures to ascertain if the resulting orientations aid the interpretation of local structural evolution (e.g. Begbie et al., 2007). This method deals only with initial and final orientations; it offers no information regarding the deformation pathway taken. Rotating  $53^\circ$  about an axis oriented 020-00 reverts the average bedding orientation back to subhorizontal. Average fault and dyke orientations, when rotated the same amount, become variably southwest-dipping and shallower, losing the Andersonian conjugate geometry they exhibited while unrotated (Figure 4.19). Dykes (sills?) with shallow dips such as these might not seem unreasonable if they intruded along planes of weakness. Faults, however, if developed as true conjugate structures in an Andersonian regime, would display original geometries akin to their current unrotated orientations. Thus, rotation of the bedded volcanoclastic sequence likely took place prior to the main deposit-scale fault development. Based on current fault orientations and Andersonian kinematics, the main faulting at E42 is interpreted as occurring with  $\sigma_1$  subvertical,  $\sigma_3$  subhorizontal and northeast-directed, and  $\sigma_2$  subhorizontal and northwest-directed aligned with the intersection lineation of the two dominant fault populations (Figure 4.3e).

Deposit-scale faults are subparallel to fault splays in the Gilmore Fault Zone to the south (Figure 2.5) and potentially developed in direct association with it. Alternately, a shallowly northwest-plunging anticline-syncline pair is interpreted to the north of E42 (Figure 4.20), with local foliations subvertical to steeply dipping and trending approximately parallel to the interpreted axial trace (Ingpen, 1995). The northwest-trending faults throughout E42 may also be interpreted as tension fractures developed in the nose of a similar fold, accounting for their orientation parallel to axial cleavage in the north, and their normal-sense separation. The wavelength of such a fold would be larger than the E42 study area; there is no direct evidence for folding in either the open pit or drillcore.

## 4.7.2 Pre-gold Veins

Steep early carbonate veins are roughly fault and dyke parallel, suggesting that faults and dykes were already present when the carbonate-bearing fluids passed through the rock package, taking advantage of pre-existing structural heterogeneities. These veins possibly formed with north-directed subhorizontal minimum compressive stress ( $\sigma_3$ ), perpendicular to vein walls, but this is difficult to constrain given the exploitation of prior planes of weakness in the form of faults and dykes.

Early bedding parallel calcite veins have also reopened pre-existing heterogeneities, but in the form of bedding planes. It is difficult to constrain the stress axes at the time of vein formation, as above, however the tensional axis ( $\sigma_3$ ) was possibly oriented subvertical to steeply west-plunging, approximately perpendicular to vein walls.

## 4.7.3 Syn-gold Veins

### Steep Gold-bearing Carbonate-Base Metal Veins

Steep gold-bearing veins show no unequivocal internal direction of opening; mineral fill shows no growth fibres, and vein walls are generally sub-parallel. Steep auriferous veins sporadically exhibit stepped geometry (Figure 4.18c and 4.21), a feature commonly associated with fracture propagation through competent rocks as vein segments link to form through-going fluid pathways during the development of a hydrothermal system (Sibson, 2001). Fracture propagation will be dealt with in more detail below.

When a rock package contains fractures and anisotropies from previous deformational episodes, these planes may be preferentially reactivated during subsequent deformation depending on the orientation of the principal stress axes with respect to the fractures in question. Fracture reactivation can play a crucial role in the development of a hydrothermal system, as the ensuing deformation experienced by the rock package may be directly dependent on these pre-existing planes of weakness. Based on requirements of cohesionless reshear along a pre-existing fault (Figure 4.22a and b) (Sibson, 2000), the two average orientations for steep gold-bearing veins can be used to constrain stress at the time of vein formation. In 2D, for a rock with an average value of internal friction of 0.75,  $\theta_r = 0$  for pure extensional vein reactivation (Figure 4.22a and b) (Sibson, 2000). Extensional shear opening is possible along these planes for a  $\theta_r < \sim 4^\circ$  (Figure 4.23a). For  $\sim 4^\circ < \theta_r < \sim 27^\circ$ ,

cohesionless shear reactivation may occur along the pre-existing fracture planes, with  $\theta_r = \sim 27^\circ$  as the optimum angle for reactivation (Figure 4.23a) (Sibson, 2001). Once  $\theta_r = \sim 54^\circ$ , the field of severe misorientation is reached, and reactivation along the fracture plane will only occur when pore fluid pressure is greater than  $\sigma_3$ , or the rock may fail by the development of completely new fractures (Figure 4.23a). Given that the steep gold-bearing veins at E42 do not appear to have significant shear components, we can narrow the possibilities of the orientation of  $\sigma_1$  to within a few degrees ( $\sim 4^\circ$ ) of the pre-existing planes.

Two possible scenarios are presented here for the extensional refracture of faults and dykes (and parallel fractures) to form the steep gold-bearing vein populations. In constructing these two scenarios the stress axes are assumed to be fixed in the subvertical and subhorizontal planes due to the inability of the earth's surface to support a shear stress (Anderson, 1951). Scenario one assumes both vein sets opened at the same time. For coeval extensional refracture,  $\sigma_1$  must be oriented within a few degrees of both planes. This is only satisfied near their intersection lineation (Figure 4.23b). The overlap zone created by  $\sim 4^\circ$  envelopes (as defined by Sibson, 2001) defines a small domain of possible  $\sigma_1$  orientations for the synchronous extensional refracture of both steep vein sets (Figure 4.23b). With the maximum compressive stress thus defined as subvertical for the first scenario, both the intermediate and tensional stress axes ( $\sigma_2$  and  $\sigma_3$ ) must be contained within the subhorizontal plane.

The second scenario assumes the veins did not open simultaneously. While retaining Andersonian stress principles,  $\sigma_1$  is required to be either subvertical or subhorizontal. If  $\sigma_1$  is subhorizontal, then two distinct orientations of maximum compressive stress at  $90^\circ$  to each other are required in order to tensionally refracture the planes. One would be directed east-northeast and the other north-northwest. If  $\sigma_1$  is subvertical, then the intermediate and tensional stress axes ( $\sigma_2$  and  $\sigma_3$ ) must switch orientations in the horizontal plane, with  $\sigma_3$  oriented east-northeast and north-northwest at different times to open both vein sets. Scenario two requires a switch of the principal stress axes during formation of the steep veins. While this is a possible explanation and has been documented at other deposits (e.g. Tosdal et al., 1995), there is no crosscutting vein evidence to support such an event at E42. Hence, coeval vein opening, as described for scenario one, is adopted here as the simplest explanation of formation of two steeply dipping gold-bearing vein populations at E42.

## **Steep Fault-hosted Breccias**

Fault-hosted breccia intervals are laterally and vertically discontinuous across the E42 deposit, range from dm- to m-scale widths on average, and are consistently found associated with faults (e.g. Smolonogov, 2003). Matrix in these breccias is a minor component, suggesting that abrasion along fault planes was not the main cause of brecciation. Instead, these breccias are interpreted as forming due to decompression of hydrothermal fluids along fault planes with subsequent precipitation of hydrothermal cement as intraclast fill (see below). Timing of formation of quartz-sulfide breccias is linked to the development of early steep gold-bearing veins based on similar mineralogy and orientation. One of these veins extends upwards from a high grade, 15cm wide, quartz-calcite-pyrite-sphalerite-cemented breccia interval exposed in the pit (Figure 4.12) suggesting a close temporal relationship.

The simplest form of faults with multiple slip surfaces are those with “external paired slip surfaces”, two parallel slip planes between which all the varying degrees of ductile strain, cataclasis, and rotation are contained (Childs et al., 1996). At an offset along a fault trace there are three different structural possibilities: a fault bend, a transfer fault, or an overlap zone (Figure 4.24a). Overlap zones are known as “relay zones” once two subparallel faults have linked (Figure 4.24b) which is interpreted to be instantaneous (Childs et al., 1995). The upper extents of the quartz-sulfide breccia interval exposed in the pit shows a similar geometry to a stepover linkage between two subparallel veins (compare Figure 4.12, 4.18c, and 4.24b). Alternatively, this geometry is also consistent with tensional opening along a fault jog during fault movement (Figure 4.24c). There are two closely related scenarios proposed for the formation of quartz-sulfide cemented breccia intervals at E42.

### Quartz-Sulfide Breccia Formation – Scenario One

The first scenario for formation of these breccias is within a zone of weakness between two parallel planar faults (external paired slip surfaces) which is breached, resulting in brecciation. Two ways to breach a fault overlap zone include each of the external slip surfaces experiencing tip-line bifurcation in the overlap zone, or the overlap zone being breached by a secondary link fault (Figure 4.24b). A secondary link fault may form if the overlap zone accommodates shear by movement along small faults, resulting in breaching from the concentration of the strain onto a single linking fault which grows to intersect the

two overlapping segments (Figure 4.24b) (Childs et al., 1995). Tip-line bifurcation is scale independent (overlap and relay structures may have slip surface separations from mm to km-scale) and a single tip-line can be bifurcating on several different scales at the same time (Childs et al., 1996). In order to form quartz-sulfide breccia intervals, both fault traces might deflect towards one another by tip-line bifurcation resulting in an overlap zone breaching through two “hard-linkage” fractures (e.g. Gibbs, 1984), or the fault traces may be connected by a single hard-linkage fault (Figure 4.25a). With breaching of the overlap zone, a sudden decrease in pressure may be expected, as the resultant through-going structure enables fluid flow. Fluid flow potentially changes conditions immediately from lithostatic to hydrostatic pressure, if the external paired slip surfaces are connected to the surface. This sudden decrease in pressure may trigger instantaneous brecciation and massive fluid flow (e.g. Hedenquist and Henley, 1985) in the overlap zone (Figure 4.25a). The upper extent of the high grade breccia exposed in the open pit displays curved calcite ± pyrite veins emanating from the tip (Figure 4.12). The orientation of these veins suggest formation synchronous with brecciation, as the overlying rock fractured concentrically due to the impact of implosion fragmentation from overlap zone breach (Figure 4.25a).

#### Quartz-Sulfide Breccia Formation – Scenario Two

The second scenario describes breccia formation in fault bends, such as those formed by asperity bifurcation along a fault surface which removes an irregularity by generating a new slip surface (Figure 4.24c) (Childs et al., 1996). Fault bends may also form as two parallel faults are joined by a single hard-linkage fracture which does not trigger brecciation (Figure 4.24b). A fault bend is a region that experiences local contraction and extension depending on fault movement. Under contractional conditions, brecciation due to volatile exsolution in the hydrothermal fluid would not be expected as the pressure at the fault bend is too high. Once contractional pressure is relaxed due to a tensional inversion of the fault jog, the resultant decompression of the hydrothermal fluid triggers instantaneous brecciation (Figure 4.25b) (e.g. Hedenquist and Henley, 1985). In order to form the thin tensional vein extending off the top of the high grade breccia observed in the pit (Figure 4.12), there must be some component of tension perpendicular to the fault surface during fault movement. Breccia formation is commonly triggered by seismic rupturing, where fault movement causes

implosion and/or spalling of wallrock clasts into the dilational jog (e.g. Cox and Ruming, 2004). Brecciation may also be triggered by overpressuring from below, which can rupture the hydrothermal seal, in the form of vein fill or a fault sealed by impermeable gouge, and generate volatile exsolution (Sibson et al., 1988; Sibson, 2001; Cox et al., 2001).

#### Quartz-Sulfide Breccia Predictability

While quartz-sulfide fault-hosted breccia intervals consistently carry high gold grades, they cannot be predicted spatially. They are developed locally along deposit-scale faults, but due to the complex and unpredictable nature of fault development (e.g. Childs et al., 1995) there are no clear exploration vectors. Quartz-sulfide breccia zones are associated with vein-filled faults, and will potentially thin at upper and lower extents (based on field observations to date). All high grade breccia intervals at E42 are steeply dipping and fault parallel; no quartz-sulfide breccias are developed in the inclined gold-bearing vein orientation (Figure 4.13a). An absence of inclined hydrothermal breccias would be expected if the inclined gold-bearing veins failed to reach hydrostatic pressure conditions. Through-going inclined structures at E42 may have never reached the surface due to their shallow dip angles, and therefore the pressure drop needed for brecciation may have never been achieved. Figure 4.26 depicts the differential stress versus relative depth required to form veins in both extensional and compressional stress regimes. Rocks undergo tensional failure at greater depths and under lower fluid pressures within tensional regimes compared to compressional regimes (Figure 4.26). In other words, higher fluid pressure is needed to get extensional or extensional-shear veins formed in a compressional regime than in an extensional regime, at the same depth and differential stress conditions. In this same way, steep structures reopened under an extensional regime may have propagated and opened more effectively than those opened under a compressional regime (such as the inclined gold-bearing veins, see below), potentially attaining hydrostatic pressure conditions where the inclined veins did not, and accounting for the lack of inclined hydrothermal breccia intervals. Due to the association with steep fault parallel veins, these breccia intervals would be expected to develop laterally elongated in a west-northwest orientation. This lateral continuity allows for the potential creation of high grade ore shoots within the E42 deposit.

## Late Inclined Gold-bearing Veins

The majority of the late inclined auriferous vein population display planar, parallel sides and massive infill, providing no evidence for vein opening directions. A few veins of this population, however, display stepped geometry similar to the older steep gold-bearing veins (Figure 4.27a, b, and c). Stepped vein geometry is commonly associated with fracture and vein propagation as through-going fluid pathways form by vein linkage during the development of a hydrothermal system (Figure 4.21) (Sibson, 2001). Inclined gold-bearing veins are tensional in nature, but whether they opened as pure extensional or extensional shear veins is unknown. Some individual veins may be interpreted as opening as reverse-sense extensional shear veins based on wallrock geometry (Figure 4.27a), others display apparent normal-sense displacements (Figure 4.14a and b), but most are too thin to recognize opening styles. Nevertheless, based on known examples, we can infer that extensional shear was likely the dominant opening style for the inclined vein population.

Based on the evidence from vein wall geometry in Figure 4.27a, the tensional stress axis ( $\sigma_3$ ) is interpreted as subvertical, resulting in oblique dilation of inclined veins. The corresponding maximum and intermediate compressive stress axes ( $\sigma_1$  and  $\sigma_2$ , respectively) are contained within the plane perpendicular to  $\sigma_3$ , but cannot be given exact orientations. This defines a compressional stress regime for the formation of the inclined gold-bearing veins. Within a compressional regime, the formation of subhorizontal extensional veins requires the least amount of differential stress (Figure 4.26) (Sibson, 2001), which may explain why shallowly-dipping bedding planes were also preferentially reopened during this event. Some of the inclined veins potentially started as subhorizontal vein segments which progressively linked to form through-going structures in the style of fracture network geometry (Figure 4.21).

When considering the apparent normal-sense displacement across the inclined gold-bearing veins in Figure 4.14a and b, the triaxial stress ellipse would be interpreted with subvertical  $\sigma_1$  and subhorizontal  $\sigma_2$  and  $\sigma_3$ , defining an extensional regime for the formation of the inclined gold bearing veins. The structural evidence at this point remains ambiguous as to the exact directional opening of the inclined gold-bearing veins. Further work is required to determine consistent offsets across these veins, but for the current study the strongest structural evidence points toward subvertically directed tension.

During the inclined gold vein event there was likely reopening of earlier steeply dipping, fault parallel gold-bearing veins. Although there are several clear crosscutting relationships between these populations (Figure 4.13b and 4.14a, b), the close angular association of the east-striking steep veins and the inclined veins (cf. Figure 4.9a and e) suggest that either some of the steep gold-bearing veins may have been reactivated during the inclined gold event and/or that some steep veins opened for the first time during the inclined gold event.

#### **4.7.4 Post-gold Veins**

##### **Carbonate Reactivation of Gold-bearing Structures**

Two populations of barren carbonate veins reactivating gold-bearing veins are interpreted as opening approximately coevally. Some of these veins display evidence for extensional shear opening in the form of calcite growth fibres (Figure 4.27d). As with the formation of steep gold-bearing veins, the reshear criteria of Sibson (2001) can be applied to the barren reactivation of gold-bearing structures in order to attempt to constrain the stress ellipse during reopening. In 2D, an optimum angle  $\theta_r = \sim 27^\circ$  for reshear, and a maximum angle  $\theta_r = \sim 4^\circ$  for extensional reactivation exist for a given plane (Figure 4.23a). As these veins are interpreted as opening coevally,  $\sigma_1$  during pure extensional reopening would be oriented within a few degrees of both planes. This is only satisfied when  $\sigma_1$  is subhorizontal and directed northwest-southeast (Figure 4.28a). As some of these veins show extensional shear opening however (Figure 4.27d),  $\sigma_1$  may fall anywhere within the overlap zone of the  $\sim 27^\circ$  reactivation envelopes (Figure 4.28a). Therefore, it is likely that these two reactivated vein populations were reopened due to approximate northwest-directed, subhorizontal compression (Figure 4.28a) at some time after the main gold-bearing veining event at E42.

##### **Steep North-trending Carbonate Event**

No directional indications for vein opening are visible in examples from steeply dipping north-trending carbonate dominated veins, although there is evidence for at least two separate calcite infill stages, indicating multiple crack-seal events (Figure 4.17c). In the simplest scenario, veins likely formed in an Andersonian extensional stress regime, with  $\sigma_3$  oriented subhorizontally east-west, perpendicular to vein walls, and  $\sigma_1$  subvertical.

### **Late Carbonate Event, Carbonate-Chlorite-Hematite Veins and Faults**

As described above, three different vein sets are the youngest veins observed at E42. Two pairs are mutually crosscutting (Figure 4.15e), and the east-dipping population contains the Nerang Thrust, interpreted as cutting the majority of faults at E42, with the possible exception of the Cowal and related Burcher Faults (Smolonogov, 2003). Veins of the east-dipping population display slickenfibres with reverse-sense, top-to-the-west displacement whereas the moderately west-dipping veins show reverse-sense, top-to-the-east displacement (Figure 4.15f). The orientations of vein planes and their associated slickenfibres, accounting for the measured senses of displacement, suggest approximate east-northeast – west-southwest directed contraction for the youngest major structural event in the region (Figure 4.29a and b). Two of the vein sets define planar orientations that have been previously activated throughout the deformational history: 075/83 SE, parallel to the lesser dyke population, and 201/43 NW, parallel to bedding (Figure 4.15e). Slickenfibres were developed along these planes as reactivation structures. The third, moderately east-dipping orientation (358/36 E; Figure 4.15e) has not been recorded previously in the deformation history and therefore likely represents a newly formed fracture orientation.

Timing is unconstrained between the Nerang Thrust and the Cowal Fault, but interpretations suggest that the Cowal Fault may be the youngest active fault at E42 and accommodating the largest amount of displacement (Smolonogov, 2003). Structures within individual fault blocks are rotated across the Cowal Fault, including bedding, dykes, and gold-bearing veins (Figure 4.3b and c, 4.5d and e, and 4.9c and d). These changes in orientation are attributed to post-gold deformation which was partially accommodated along this major structure. There is scatter associated within each vein set across E42, resulting in less well-defined clusters of poles to veins. Deformation accommodated by the Cowal Fault and by the three sets of late carbonate-chlorite-hematite veins may be partially responsible for the scatter in vein orientations, by post-vein shuffling and displacement of the rock package.

## **4.8 Discussion**

### **4.8.1 Deposit-scale Structural Interpretations**

#### **Local Pre-gold Deformation**

Local bedding orientations at E42 do not suggest deposit-scale folding (cf. Simpson, 2003) as they fall within one fairly well-defined population, and there is no evidence of folding in the open pit (e.g. parasitic folds or axial planar cleavage). In addition, plan view reconstructions of the E42 host rocks (Figure 3.2) display linear contacts, which do not reflect a fold plunging moderately to the north-northwest as has been previously suggested (e.g. Simpson, 2003). A northwest-plunging syncline and anticline pair is interpreted to the north of E42 on a scale larger than the deposit (Figure 4.20), and so E42 may be situated on the southwestern limb of a similarly oriented anticline to the south of the mapped folds (Ingpen, 1995), or separated from this fold by an inferred fault (Figure 4.20). Folding such as this on a scale larger than the exposure at E42 may account for the current tilted bedding orientations at the deposit.

#### **Formation of Gold-bearing Vein System at E42**

One potential scenario for the development of both the early steep and late inclined gold-bearing veins at E42 involves a reversal of the local stress axes from subhorizontal tension to subhorizontal compression. Although there are no unequivocal opening directions for the inclined veins at this time, the scenario presented here is considered a viable structural model for the evolution of the E42 epithermal gold system. Further work is required, however, to determine the true directional nature of inclined gold-bearing vein opening. This will be possible as development of the E42 open pit progresses, exposing more primary rock with depth.

#### Steep Gold-bearing Vein Formation

Initial faulting in the E42 area likely developed under tensional stress directed approximately northeast and subvertical compression, assuming pure normal-sense displacement (Figure 4.30a). Ingpen (1995) suggests that northwest-trending deposit-scale faults may have developed as splays off of the regional Gilmore Fault to the south. Dykes

were emplaced along northwest-trending faults and along a less dominant east-striking orientation (Figure 4.30b). Two steep gold-bearing vein sets were subsequently opened within an extensional regime assuming veins are coeval (see Section 4.7.3). The maximum compressive stress was likely oriented subvertically (Figure 4.30c), and was equal to the vertical effective stress ( $\sigma_1 = \sigma_v = \rho gh$ , where  $\rho$  is rock density,  $g$  is acceleration due to gravity, and  $h$  is depth). In an idealized uniformly extensional stress regime,  $\sigma_2$  and  $\sigma_3$  in the subhorizontal plane are equivalent or very similar in value, reducing the resulting Mohr diagram from a 3D representation (Figure 4.31a) to an essentially 2D representation (where  $\sigma_2 = \sigma_3$  as in Figure 4.31b). To open both steep orientations as extensional veins the differential stress must be low, otherwise the fractures will be reactivated as extensional-shear or shear veins (e.g. Figure 4.22). A sufficiently low differential stress at deposit-scale, defining a near-isotropic stress state (Figure 4.31b), could have been attained following slip along a regional fault outside the E42 system. Movement along such a fault could result in the release of shear stress along the fault, followed by a decrease in the deposit-scale differential stress. Similar observations have been made for quartz vein systems hosted by strike-slip faults in the Mount Isa Inlier, Australia, where each slip episode along these faults was accompanied by the near-total relief of shear stress along these structures (Sibson et al., 2003a and b). In this near-isotropic stress state, the two steep planes of weakness will open with a slight increase of fluid pressure, or a reduction of confining pressure, causing tensile failure (Figure 4.31c). During formation of steep gold-bearing veins therefore, differential stress is likely low, with  $\sigma_1$  subvertical, and  $\sigma_2$  and  $\sigma_3$  near-equal and contained within the subhorizontal plane, oriented within the quadrants defined by the average vein orientations (Figure 4.23b). Permeability proximal to fault/fracture zones is at its highest immediately following rupture (e.g. Rowland and Sibson, 2004; Cox and Ruming, 2004), enabling hydrothermal ore-bearing fluids to precipitate vein fill.

#### Inclined Gold-bearing Vein Formation

Decreases in fluid pressure generally promote hydrothermal precipitation (Parry, 1998; Fournier, 1999). Steep extensional shear veins are sealed by hydrothermal precipitation, which results in a build up of fluid pressure as fluids rising from a magmatic source at depth come into contact with the ambient hydrothermal system (Bastrakov, 2000).

This process is known as fluid pressure cycling (Sibson, 2000 and 2001). As pyrite grains in both steep and inclined veins are extensively fractured and filled by carbonate, sulfides, and gold, there were likely multiple fluxes of fluid along these structures. Following a build-up of fluid pressure after steep gold-bearing vein infilling, there is a local stress switch which changes the tensional  $\sigma_3$  axis to subvertical (Figure 4.30d). The source of compression is unknown, but may have resulted from movement along a regional fault distal to the system (e.g. along the Gilmore Fault Zone) or local fault interactions. For example, a reverse-sense seismogenic event along the Gilmore Fault Zone may result in approximate east-west compression for the E42 fault block, in turn resulting in the exchange of stress axes from subhorizontal  $\sigma_3$  during steep vein formation to subvertical  $\sigma_3$  during inclined vein formation (Figure 4.30d).

Fluid overpressure, potentially due to rising magmatic volatile-rich fluids mixing with the existing background hydrothermal system at E42 (Bastrakov, 2000), reduces the effective vertical stress of a rock package. At a constant differential stress, a reduction in the effective vertical stress may result in a change of fracture opening style (Figure 4.26). Inclined veins at E42 are interpreted as opening after the compressional stress inversion, along with the reactivation of bed parallel planes due to high fluid pressures and their favorable orientation for reopening. Some inclined veins retain a stepped geometry (Figure 4.27a and b), and mm-scale stepovers (Figure 4.27c), although the majority display planar margins.

Local stress axes are interpreted to change from subvertical compression during the early steep vein fill (Figure 4.30c) to near vertical tension during late inclined vein fill (Figure 4.30d). This defines an almost instantaneous interchange of the maximum and minimum principal stress axes within the life of the hydrothermal system: a positive tectonic inversion (Sibson, 2001). Similar observations have been recorded for the vein-hosted precious metal McLaughlin hot spring deposit in northern California (Tosdal et al., 1995).

Two distinct gold-bearing vein sets exist at E42 displaying similar stepped geometry and mineralogy. Based on these observations, and the fact that most mineralizing hydrothermal systems are short-lived (ranging from a few thousand to a few hundred thousand years at most; Simmons et al., 2005), the auriferous vein sets are inferred to be closely associated temporally. Vein Au:Ag ratios show a continuous range of values rather than bimodal distribution, indicating that veins were likely not formed as two distinct

mineralization events (Borthwick, 2004). Changes in regional tectonic regimes are likely to be associated with major episodes of fluid redistribution within the crust (Sibson, 2001), and the favorable combination of changing strain states, high fluid flow, and gold-bearing fluids within the E42 area resulted in an economic concentration of gold.

## **4.8.2 Cowal Igneous Complex-scale Structural Interpretations**

### **Bounding Faults to the Cowal Igneous Complex**

The Cowal Igneous Complex (CIC) is bounded to the east by the Marsden Fault (Figure 4.32 and 4.33) which is a north-northeast trending, west-dipping thrust interpreted from seismic data (Glen et al., 2007a). To the west, the CIC is bounded by the Booberoi Fault, a structure that changes trend from north-south near the E42 deposit to northwest-southeast approaching Temora (Figure 4.20). See Chapter 2 for a detailed description of the Booberoi Fault. Interpretation of aeromagnetic data (Glen et al., 2007a) suggests that the southern parts of the CIC and the adjacent Fairholme Igneous Complex (Figure 2.8) to the west have been rotated into the Gilmore Fault Trend (see Chapter 2). Subsequently they became aligned along splay faults off the Gilmore Fault, and were activated as thrust sheets, which were later overthrust from the west by Ordovician turbidites along the steeply west-dipping Booberoi Fault (Glen et al., 2007a). The rotation observed between these igneous complexes is considered here as a parallel scenario for smaller-scale faults within the CIC.

### **Fault Blocks within the Cowal Igneous Complex**

Aeromagnetic geophysical surveys of the CIC provide useful clues about the local, largely unexposed, geology. Interpreted lineaments display similar orientations to both the north-trending Tullamore and northwest-trending Gilmore Trends (Chapter 2): the Booberoi Fault and parallel features, and the Marsden Lineament and parallel features, respectively (Figure 4.33). The E40 and E35 prospects, as well as the Marsden prospect, are found along the Marsden Lineament (Figure 4.33). The E41 and E42 deposits are closely spatially related, but are separated by a minor fault interpreted from the aeromagnetic data (Figure 4.33). There is a significant decrease in the number of gold-bearing veins in the area between these two deposits, but the exact geological constraints are not well known due to a lower frequency of exploration drillholes. Best-of-hole gold contours appear to isolate these

bodies by approximately 500m (Balind pers. comm., 2007). E41 has been described entirely on the basis of geophysical surveys and drill core logging as there is no outcrop (e.g. Zukowski et al., 2007).

At E41, a general trend defined between bedding and gold-bearing veins is comparable to that seen at E42 (Dykman, 2004). Gold-bearing veins measured at E41 display significantly more scatter compared to the E42 inclined gold-bearing vein population, but the angle between the average gold-bearing veins and bedding in both deposits is the same, approximately 52°-60° (Figure 4.28b). The similarity in bedding-vein orientations suggests that these two deposits might have been similarly oriented at one time, specifically during the auriferous hydrothermal event, and were subsequently deformed heterogeneously with respect to each other. Given the interpreted fault separating these deposits, one explanation is that E41 and E42 are situated in adjacent fault blocks which were heterogeneously deformed relative to each other. When envisioning this deformation, one might think of domino-style, parallel rotation of bordering fault blocks (e.g. Sibson, 2004). However, a simple domino-style rotation does not work in this case, as it would cause both blocks to exhibit the same post-rotation orientations. Instead, a heterogeneous rotation of one block with respect to the other is required, dependent on numerous factors including, but not constrained to, total fault displacements, fault orientations at surface and at depth, and relative lithological strengths. E41 veins display evidence for higher temperature conditions during formation (Chapter 2) suggesting that the E41 fault block may be upthrown relative to the E42 block, juxtaposing epithermal and epithermal/porphyry systems by post-mineral deformation.

#### **4.8.3 Macquarie Arc-scale Structural Interpretations**

The Lachlan Transverse Zone (LTZ) is a major basement structure represented in the Eastern Subprovince of the Lachlan Orogen by a corridor of west-northwest or west-trending faults and folds, and obliquely cuts the Macquarie Arc (Chapter 2) (Glen et al., 1998; Glen and Walshe, 1999). West-northwest trending structures are commonly found across the Macquarie Arc including: faults, dykes, and sheeted veins at Cadia Hill and Cadia Quarry (Holliday et al., 2002; Wilson et al., 2003), northwest-trending lineaments interpreted from aeromagnetic data spatially associated with porphyry deposits at Northparkes (Heithersay et

al., 1990; Hooper et al., 1996), and deposit-scale faults, dykes, and sheeted gold-bearing veins at E42.

Other analogies have been made between E42 and the alkalic deposits at Cadia and Northparkes regarding late stage phyllic faults containing anomalous sphalerite, galena, and chalcopyrite in the latter two districts. Late stage phyllic faults are interpreted as epithermal veins which have been telescoped on top of the porphyry environment. It is suggested that these faults are analogous to the gold-bearing veins at E42, and that the faults may be feeders to a similar style of carbonate-base metal epithermal vein system as E42 in the Cadia and Northparkes districts (Cooke et al., 2006).

### **Timing of Deformation**

The oldest recorded deformation in the Junee-Narromine Volcanic Belt is from Northparkes (Chapter 2, Figure 2.3), where tilted volcanoclastic sandstones and lavas of the Upper Ordovician Wombin Volcanics, dipping 35° to the east-southeast (Hooper et al., 1996), are intruded by subvertical monzonite dykes dated at ca. 440-439 Ma (U/Pb SHRIMP zircon dates: Perkins et al., 1990; Lickfold et al., 2007). The intrusions at Northparkes therefore indicate there was deformation in the Junee-Narromine Volcanic Belt prior to ~440 Ma. This may also apply for E42, based on the current geometry of faults and dykes with respect to bedding, which indicates that mineralization at E42 occurred post-tilting of the host rocks. See Chapter 2 for an overview of the major deformational episodes to affect the Lachlan Orogen, with specific reference to the Macquarie Arc (see also Table 4.4).

### **Benambran Cycle**

In this section, evidence for deformation at E42 is placed within the wider deformational framework provided by Ingpen (1995) and Glen (2005). The Benambran Cycle for the Lachlan Orogen is divided into two distinct short-lived orogenic episodes separated by a period of extension or relaxation (Glen, 2005). The two phases of Benambran orogeny reflect the accretion of the Macquarie Arc onto Gondwana, caused by the positioning of the allochthonous Bega Terrane outboard of the arc through northwards strike-slip transport along the eastern margin of Gondwana (Chapter 2, Figure 2.4b) (Glen et al., 2007c).

### Benambran Orogeny Phase 1 ca. 443 Ma

The first stage of deformation recorded by Ingpen (“D1” of Ingpen, 1995) evident in Late Ordovician rocks in the CIC region is interpreted here as equivalent to Phase 1 of the Benambran Orogeny of Glen (2005) (Table 4.4). This deformation is evidenced by foliation oriented 165/83 W in the oldest volcanic and sedimentary units proximal to and flanking the Booberoi and Gilmore Faults (Ingpen, 1995). Overprinting relationships of parallel foliations and cleavage development indicate multiple penetrative deformations along the Gilmore and associated faults, resulting from early northeast directed shortening (Ingpen, 1995) in response to northeast-southwest directed compression and dextral strike-slip displacement within the Gilmore Fault Zone. Regional northwest-trending folds developed at this time (Ingpen, 1995) could be the cause of tilted bedding at E42 prior to deposit-scale faulting and dyke emplacement (Figure 4.20).

Ingpen (1995) suggests that the faults at E42 possibly developed as conjugate faults in response to D1 deformation experienced by the region. Though he suggests that the deposit-scale faults may have developed as splays off of the Gilmore Fault, their current northwest trends would require their formation as reverse faults due to this northeast-southwest compression. Faults at E42 do not show reverse sense displacement and their development has been interpreted as normal sense with minor strike-slip components (Smolonogov, 2003). Current fault orientations at E42 require approximate northeast directed extension (Figure 4.30a), therefore they are likely not correlatable to Ingpen’s (1995) D1 episode.

### Extension after Phase 1 Deformation ca. 443-433 Ma

The first period of orogeny within the Benambran Cycle was followed by a ~10 Ma extensional phase (Glen, 2005) which coincides with the emplacement of shallow (1-3km) monzonitic intrusions in the Macquarie Arc (Glen et al., 2004; Crawford et al., 2007). The porphyries emplaced in the Macquarie Arc during this period (group 4 porphyries of Glen et al., 2007b) are syn-accretionary, variably mineralized, and locally intrude deformed and tilted volcanic and volcanoclastic sequences (Hooper et al., 1996). This period of crustal extension is when the E42 epithermal vein-hosted gold deposit potentially formed, supported by the  $^{40}\text{Ar}$ - $^{39}\text{Ar}$  ages of ca. 440 Ma obtained for hydrothermal sericite alteration associated with gold-bearing veins (Perkins et al., 1995). Attempts to recreate this sericite age are currently

in progress (Section 4.4.1), and once completed will hopefully resolve the mineralization age dispute for E42. A partial magmatic origin for the mineralizing fluids at E42 (Bastrakov, 2000), as well as the presence of nearby porphyry mineralization within the Cowal Igneous Complex (Section 2.6.2), raise the possibility of a temporal relationship of the epithermal system at E42 and the group 4 mineralizing porphyries of Glen et al. (2007b). Vein geometry and crosscutting relationships at E42 suggest that steep gold-bearing veins formed under uniform, subhorizontal tension with subvertical maximum compression (Figure 4.30c). Following a positive tectonic inversion, tension was directed subvertically, resulting in the opening of the inclined and bedding parallel gold-bearing vein populations (Figure 4.30d). Under local conditions of high pore fluid pressure, low vertical effective stress, and low differential stress, a relatively small change in the local stress regime, for instance due to local fault interactions, could result in a radical directional change in principal stress axes, even within an overall extensional orogenic stage.

#### Benambran Orogeny Phase 2 ca. 433-430 Ma

Although Ingpen (1995) attributes “D2” deformation potentially to the Siluro-Devonian Bowning Orogeny (a.k.a. Bindian Orogeny; Willman et al., 2002), Glen (2005) argues that no deformation occurred within the Macquarie Arc at this time. In order to reconcile these two models while remaining consistent with recorded overprinting deformational episodes, it is proposed here that Ingpen’s (1995) second period of compressional deformation, D2, be placed within Phase 2 of the Benambran Orogeny (Table 4.4). D2 is pervasively developed and is evident in the Gilmore and associated fault zones, as well as within the Cowal Igneous Complex, as steeply inclined north-trending, gently doubly plunging to subhorizontal folds at various scales (Ingpen, 1995). Folds display an average fold axis trending 347-04 NNW and are accompanied by a steeply east-northeast to east-southeast dipping axial planar cleavage (Ingpen, 1995).

#### **Tabberabberan Cycle**

##### Tabberabberan Orogeny ca. 411 Ma

The development of the strong foliation within the Booberoi Fault was included by Ingpen (1995) in D2. However, the Manna Conglomerate, which is deformed within this fault zone, is the basal unit to the Silurian-Devonian Ootha Group and therefore

depositionally postdates Phase 2 of the Benambran Orogeny. A minimum deformation age for the Booberoi Fault is reported as  $411 \pm 2$  Ma based on a  $^{40}\text{Ar}$ - $^{39}\text{Ar}$  sericite age (Lyons, 2000). Glen et al. (2007a) use this age to argue that deformation along the fault was Early Devonian in age. Both east-over-west and west-over-east subvertical reverse displacement is recorded along the Booberoi Fault, explained as deformation manifested on two different fault segment orientations (Ingpen, 1995). This is consistent with east-west shortening, and corresponds to orientations of temporally associated folds, cleavage, and conjugate dextral and sinistral faults observed within the Gilmore Fault Zone and adjacent regions (Ingpen, 1995).

The third deformational episode (“D3” of Ingpen, 1995) evident within the Gilmore Fault Zone and adjacent rocks is characterized by open to tight, steeply inclined to upright, moderately to steeply east and north-plunging folds, with rare associated cleavage. Small scale dextral displacements evident within the Booberoi Fault are attributed to D3 deformation, due to north-northeast trending compression (Ingpen, 1995). D3 is the last deformational episode recorded within the Gilmore Fault Zone and CIC (Ingpen, 1995). Therefore the latest deformation at E42, east-northeast directed compression evidenced by slickenfibres formation along late carbonate-chlorite-hematite veins at E42 (Figure 4.29), is placed within the Tabberabberan Orogeny (Table 4.4).

## **Kanimblan Cycle**

### Kanimblan Orogeny ca. 340 Ma

Regional mapping suggests that the CIC and adjacent Gilmore Fault Zone were not affected by either the “D4” or “D5” deformational episodes of Ingpen (1995). D4 is poorly constrained temporally, and D5 deformation is attributed to approximate east-west shortening during the Early Carboniferous Kanimblan Orogeny (Table 4.4) (Ingpen, 1995). Upper Devonian sedimentary units of the Junee-Narromine Volcanic Belt display evidence of Carboniferous thrusting and folding, with some strike-slip faults in accommodation zones along the Marsden Fault (Figure 4.32) (Glen et al., 2002).

Adularia from gold-bearing veins at E42 records the cooling and exhumation of the deposit, which is situated in the footwall to the Booberoi Fault. There are several potential mechanisms which may have resulted in this exhumation: erosion, deformation associated with rotation of the Cowal district as it rode up on a structurally lower fault, or normal-sense

reactivation of the Booberoi Fault to the west. There is evidence for multiple reactivations along the Booberoi Fault: the deposition of the basal Manna Conglomerate in a rift basin bounded to the east by the Booberoi Fault (Chapter 2), and the subsequent reverse-sense movement resulting in the stretching of this conglomerate within the fault zone. Given the range of dates obtained by  $^{40}\text{Ar}$ - $^{39}\text{Ar}$  dating of adularia (362.7 $\pm$ 2.1 Ma, 344.5 $\pm$ 2.1 Ma, and 356.3 $\pm$ 1.8 Ma), the E42 deposit was likely exhumed during the Kanimblan Cycle.

Fault Blocks		Bedding			Faults			Dykes			Mineralized Dilational			Mineralized Shear				
		strike	dip	n	strike	dip	n	strike	dip	n	strike	dip	n	strike	dip	strike	dip	n
1	W of Western & Wyrra	216	49	385	153	87	151	346	85	789	120	42	1192	116	48	336	87	379
2	Wyrra to Western	204	50	47	145	88	8	336	70	102	116	30	100	140	36	319	80	28
3	Western to Corringale/Central	218	52	166	159	89	63	2	87	127	123	39	169	93	50	303	83	46
4	Corringale to Central	218	40	205	347	86	81	166	89	170	116	32	329	120	34	360	71	135
5	W of Central above Nerang	n/a	n/a	2	169	80	4	136	60	7	127	29	6	n/a	n/a	n/a	n/a	4
6	Inside Nerang (W of Central)	n/a	n/a	0	n/a	n/a	0	n/a	n/a	3	n/a	n/a	5	n/a	n/a	n/a	n/a	0
7	Central to Clear Ridge	217	44	49	314	87	29	184	82	298	123	33	472	135	41	n/a	n/a	97
8	Clear Ridge to E contact, S	208	47	132	164	67	88	351	81	662	122	36	486	123	48	356	77	207
9	Wamboyne Splay to Wamboyne	n/a	n/a	1	337	77	6	343	82	34	n/a	n/a	2	n/a	n/a	n/a	n/a	0
10	E of Central above Nerang	199	64	13	347	74	9	360	89	135	139	34	79	101	35	n/a	n/a	40
11	Clear Ridge to Wamboyne, N	215	64	17	316	81	10	n/a	n/a	9	n/a	n/a	3	n/a	n/a	n/a	n/a	0
12	Wamboyne to Lonergans/Cowal	210	51	13	330	88	16	177	88	141	140	22	49	145	55	343	72	27
13	Lonergans to Cowal, N Bodels	n/a	n/a	0	n/a	n/a	0	n/a	n/a	4	n/a	n/a	1	n/a	n/a	n/a	n/a	0
14	Lonergans to Cowal, S Bodels	n/a	n/a	0	n/a	n/a	0	n/a	n/a	3	n/a	n/a	2	n/a	n/a	n/a	n/a	0
15	Inside Nerang (E of Central)	n/a	n/a	0	n/a	n/a	0	n/a	n/a	2	157	64	6	n/a	n/a	n/a	n/a	0
16	Cowal to Burcher	n/a	n/a	5	349	72	12	8	77	35	79	40	10	63	46	326	68	15
17	Burcher to Glenfidditch	200	27	50	334	85	5	207	87	27	84	36	57	44	55	n/a	n/a	17
18	Glenfidditch to G2	n/a	n/a	4	123	60	4	207	51	19	37	53	22	n/a	n/a	n/a	n/a	3
19	G2 to G3	245	40	39	214	77	10	188	52	31	n/a	n/a	2	n/a	n/a	n/a	n/a	9
20	East of G3	238	36	38	152	72	5	173	52	34	n/a	n/a	2	n/a	n/a	n/a	n/a	0

**Table 4.1** Summary of drillcore measurements within each deposit-scale fault block. For positions of fault blocks refer to Figure 4.2. n = number of structural measurements per block.

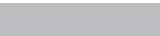
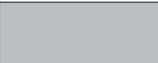
Feature	Relative Timing	Mineralogy	Average Orientation
Bedding			200/54 NW
Faults Dykes	tilting/folding		322/69 NE and 155/64 SW 331/79 NE, 168/76 W and 067/74 S
Early calcite veins Early calcite veins	? ?	calcite ± chlorite ± pyrite calcite ± chlorite ± pyrite	209/43 NW (bed parallel) 121/83 SW (fault parallel)
Early steep gold veins QSBs Late inclined gold veins Quartz-pyrite veins		calcite-quartz-pyrite-sphalerite-galena ± adularia ± chalcopyrite ± visible gold  various cement phases: qtz-sulfides, qtz-ank-sulfides, ank-sph, ank  calcite-quartz-pyrite-sphalerite-galena ± adularia ± chalcopyrite ± visible gold  quartz-pyrite ± sericite halo	331/73 NE and 069/76 S  ranges from steeply N to E-dipping  101/42 SW and 185/39 W (bed parallel)  144/52 SW and 344/78 NE
Carbonate reactivation Steep N-S carbonate veins Latest carb-chl-hem veins	3 ~coeval sets	calcite-ankerite ± chlorite  calcite-ankerite ± chlorite ± pyrite ± hematite calcite-ankerite-chlorite ± hematite ± pyrite	141/42 SW and 320/77 NE  359/86 E  358/36 E, 075/83 S, and 201/43 SW

**Table 4.2** Summary of average structures and vein orientations and compositions for E42.



Brecciation Stage	Cement composition	Average Orientation	Notes
1	quartz-pyrite-sphalerite (± calcite ± chlorite ± late ankerite)	Steeply dipping, E-W and N-S trending	Red, purple and yellow poles on Figure 4.13a
Post-1 Pre-2?	barren quartz or quartz-ankerite	Steeply dipping, E-W trending	Black poles on Figure 4.13a, can crosscut Stage 1, but no relative timing with other stages
2	ankerite-sphalerite-pyrite (± chalcopyrite ± galena ± quartz)	Steep to moderately dipping to the E-SE	Green poles on Figure 4.13a
3	barren ankerite ± calcite ± chlorite	Steeply dipping to the NE-ESE	Yellow and blue poles on Figure 4.13a

**Table 4.3** Summary of fault-hosted breccia stages: relative timing, mineralogy, and average orientations.

<b>Carboniferous</b>	Late	305Ma				
		327Ma				
	Early	340Ma	 Kanimblan	D5 	 D5	
		362Ma				
<b>Devonian</b>	Late			D4? 		
		381Ma	 main stage Tabberabberan		 D4?	
	Middle	396Ma	 early stage Tabberabberan		D3 	 D3
	Early	418Ma				
<b>Silurian</b>	Late			D2 		
		426Ma				
	Early	433Ma	 Phase 2 Benambran		D1 	 D2
443Ma		 Phase 1 Benambran	 D1			
<b>Ordovician</b>	Late				<i>reinterpreted Ingpen (1995)</i>	
			<i>Glen (2005)</i>	<i>Ingpen (1995)</i>		

**Table 4.4** Schematic time-space plot of deformational events in the Macquarie Arc.

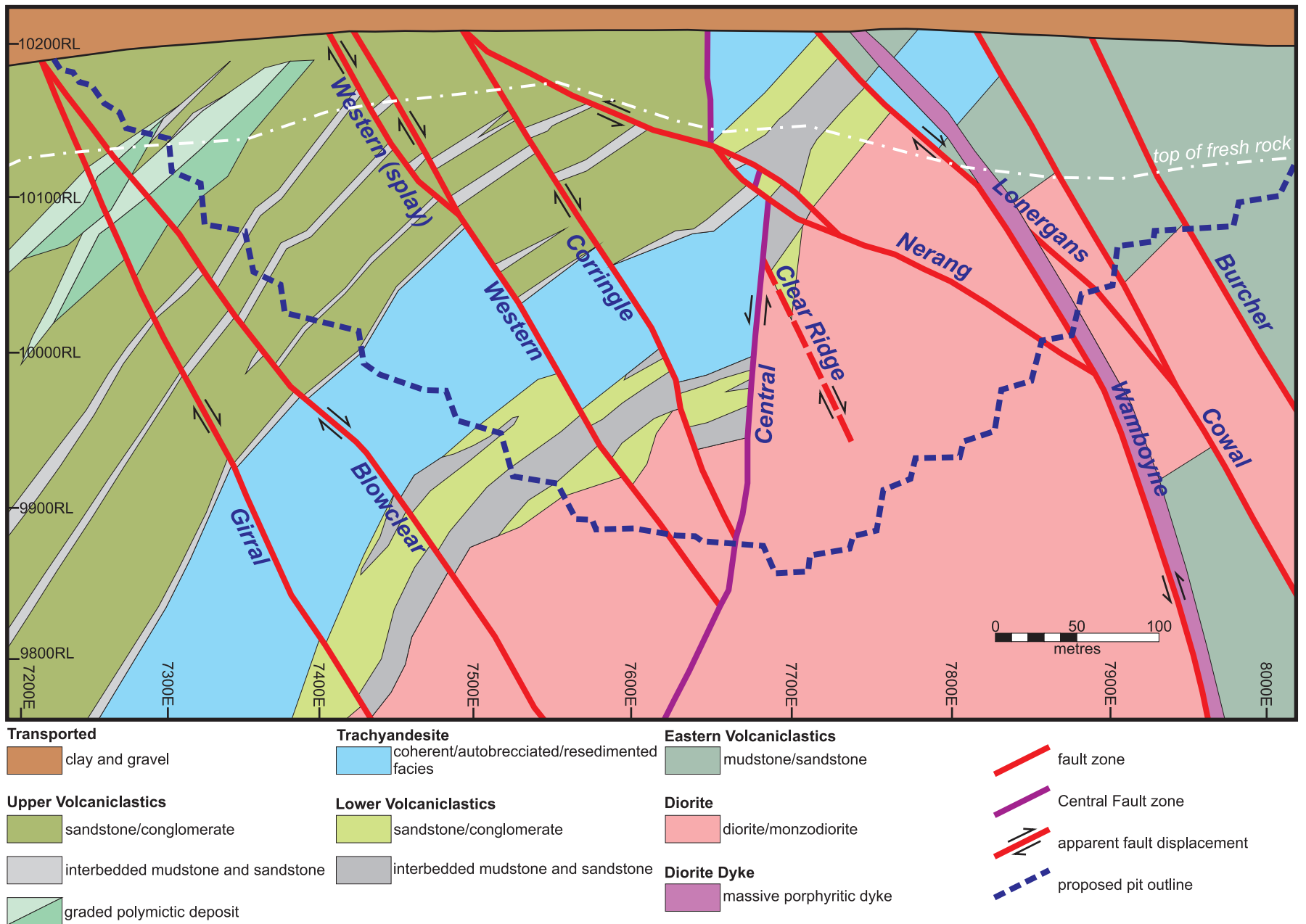
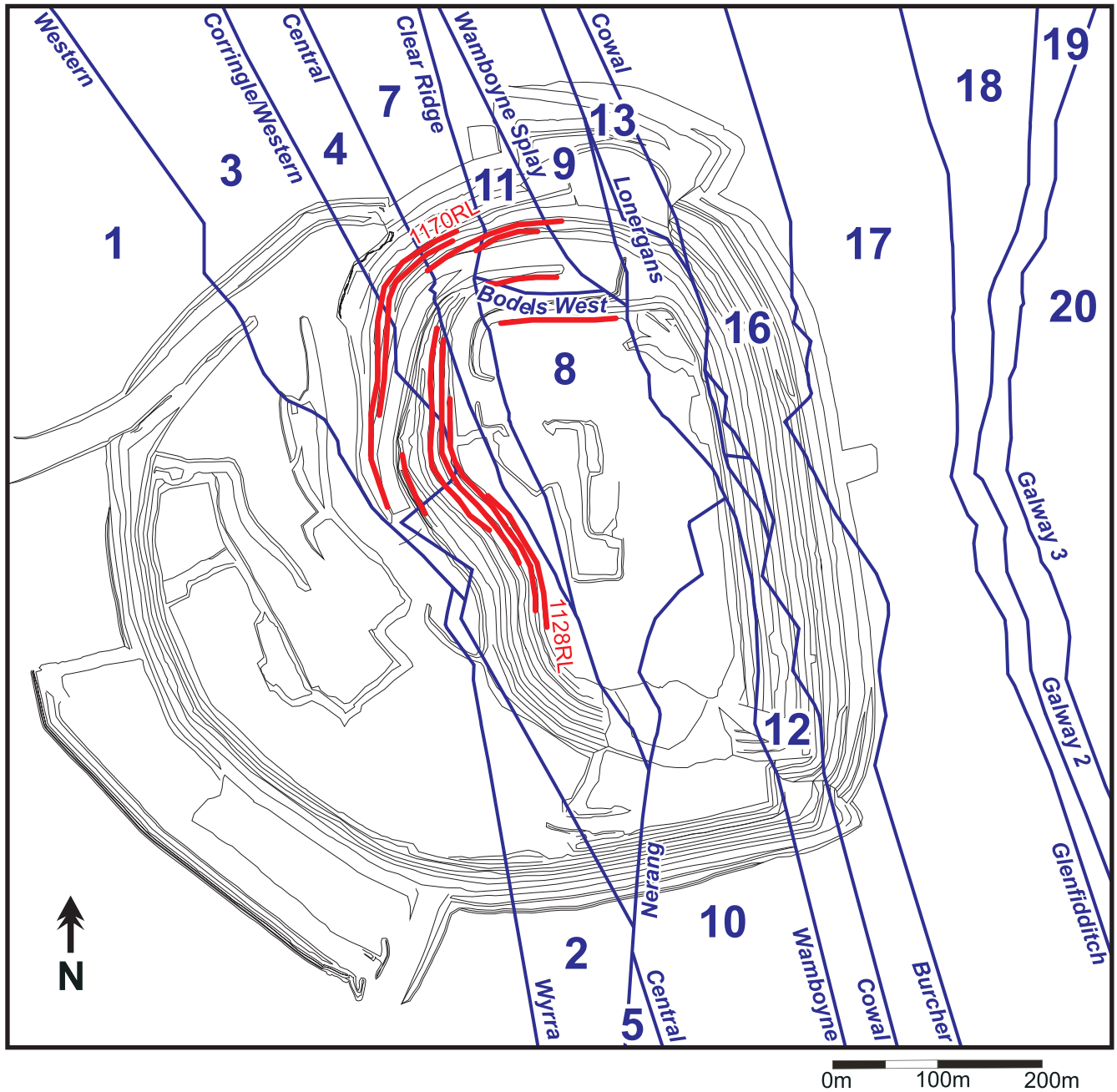


**Figure 4.1** Schematic east-west cross section through E42 along 7800N. Modified from Dijkmans (2003).



- extent of open pit
- bench faces mapped in this study
- deposit-scale faults bounding structural domains or “fault blocks”
- 3** numbered fault blocks, refer to Table 4.1

**Figure 4.2** Endeavour 42 open pit plan as of May 2007 and numbered fault blocks. Ground level is at 1200RL, and pit floor is at 1128RL. Bench heights are 3 metres.

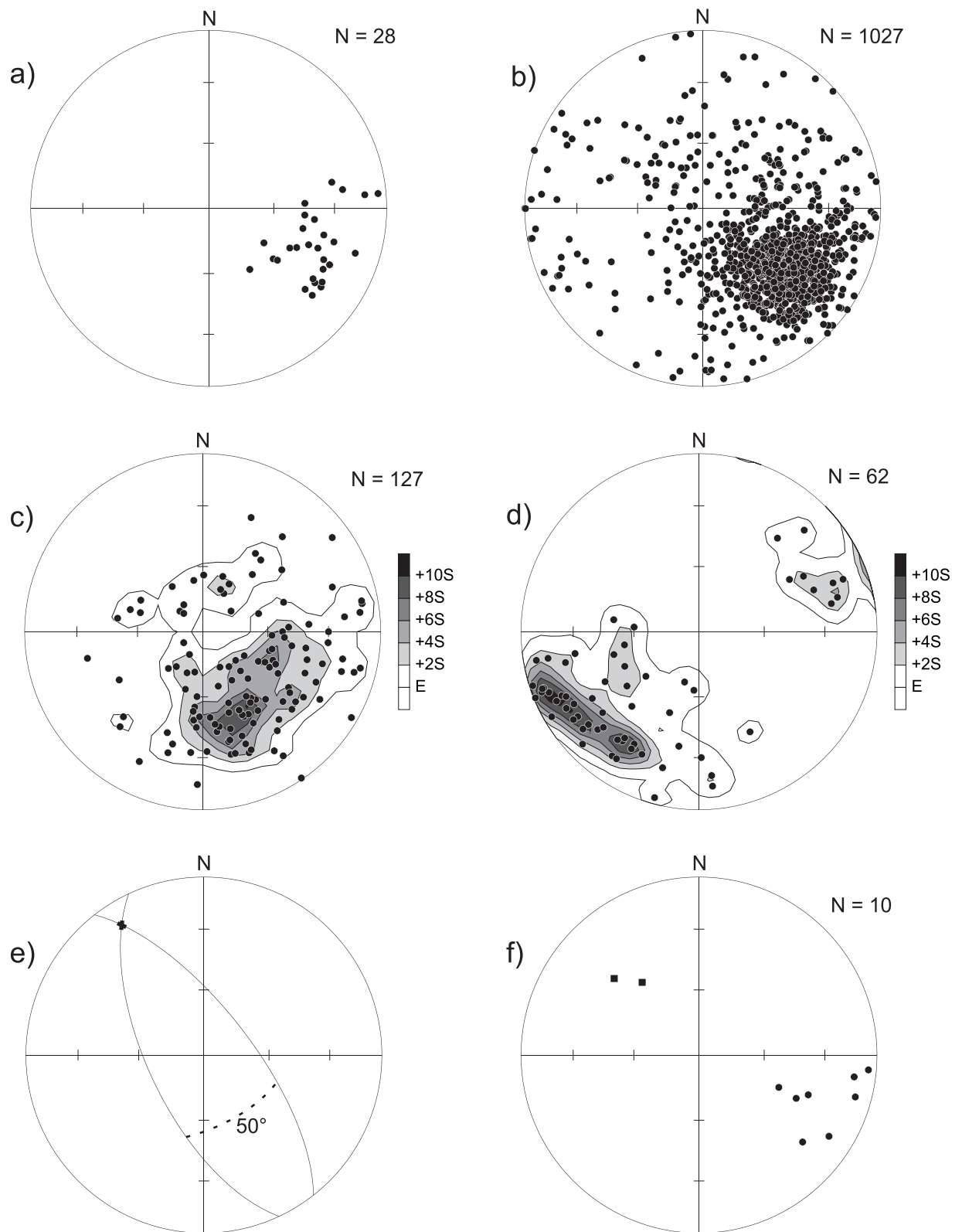


**Figure 4.3** a) Bedding in open pit. b) Bedding from drillholes west of the Cowal Fault. c) Bedding from drillholes east of the Cowal Fault. d) Dominant NW-trending deposit-scale faults. e) Average dominant fault planes and intersection lineation at 328-15. f) Late faults subparallel to Nerang Thrust (squares) and late bed parallel faults (circles).

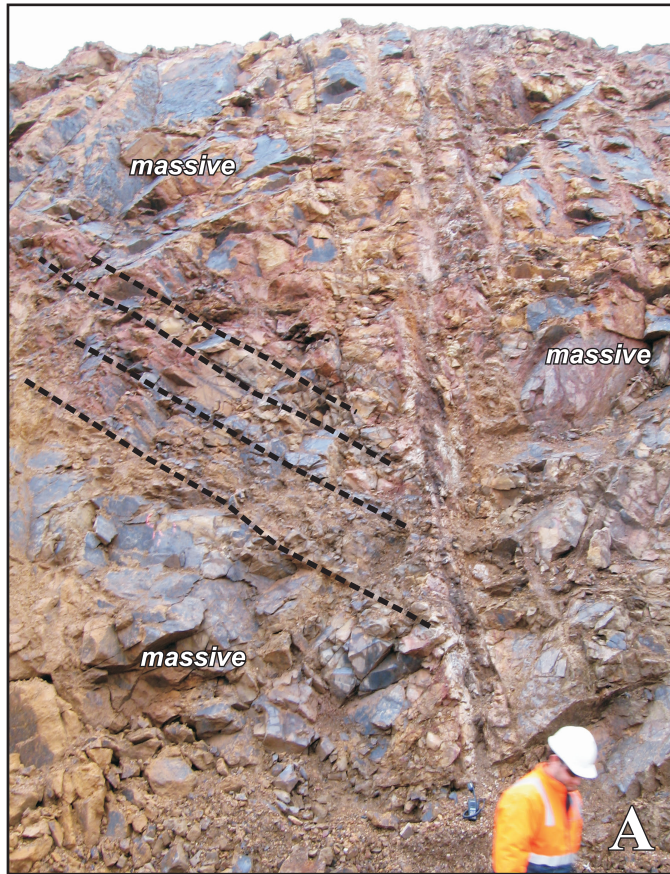


**Figure 4.4** a) Bedding (marked by dashed lines) offset by a steeply dipping vein-filled fault approx. 20cm wide, located to the right of centre. Photo is west facing. b) Deformation visible within the Cowal Fault. Light coloured clast in centre is an isolated quartz vein fragment surrounded by sheared fine-grained fault gouge. Hammer for scale, photo is north facing. c) Quartz-calcite-pyrite-adularia-sphalerite-galena-gold vein offset by late slip along bedding planes. Notebook for scale, photo is west facing.



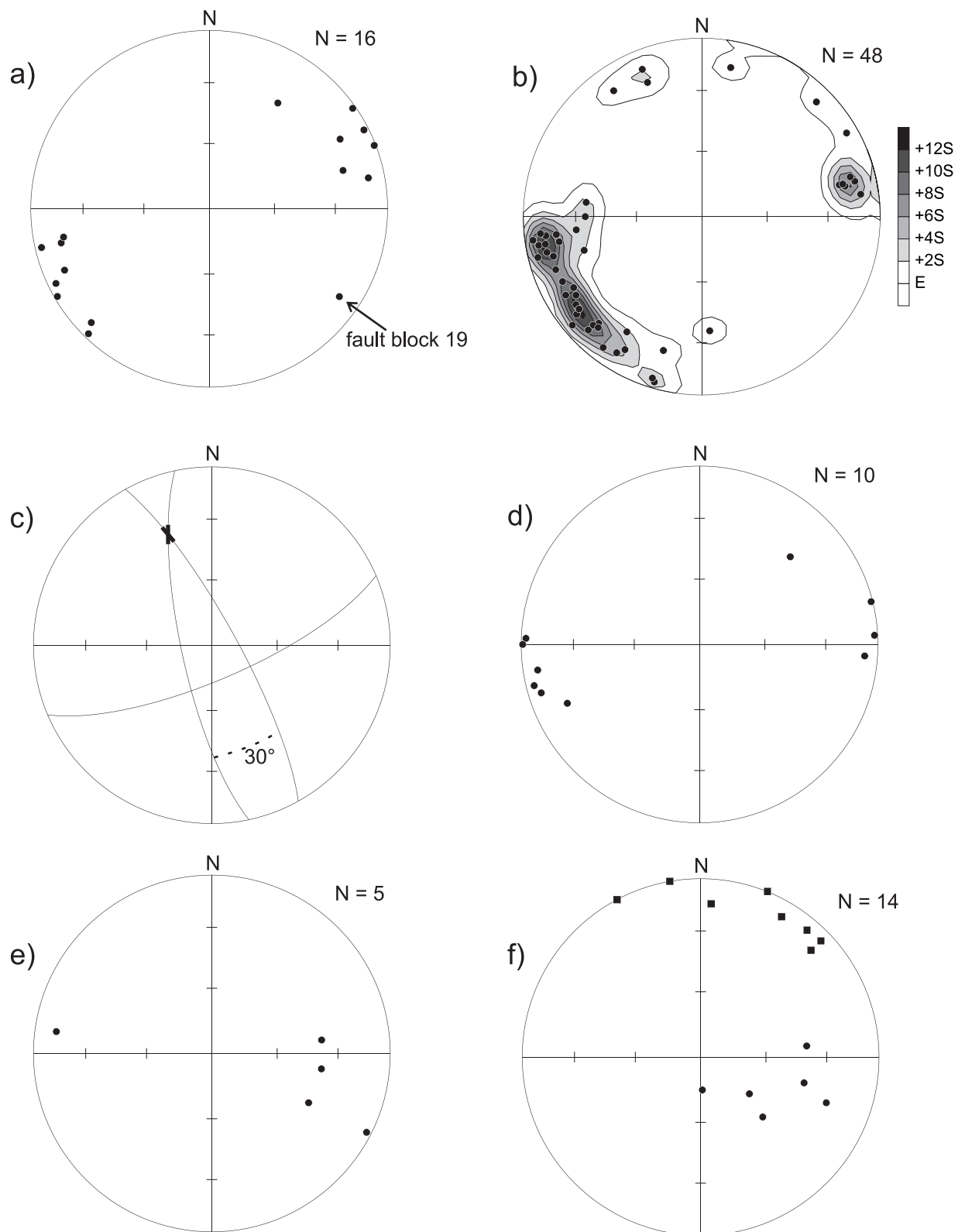


**Figure 4.5** a) Average fault orientations within each E42 fault block, drillhole data. b) Dyke contacts, three main populations. c) Three average dyke orientations, with shallow intersection lineation at 338-34. d) Average dyke orientations for each E42 fault block west of the Cowal Fault, drillhole data. e) Average dyke orientations for each E42 fault block east of the Cowal Fault, drillhole data. f) Early carbonate veins crosscut by later gold-bearing veins. Squares represent steep, east-striking population; circles represent bedding parallel population.

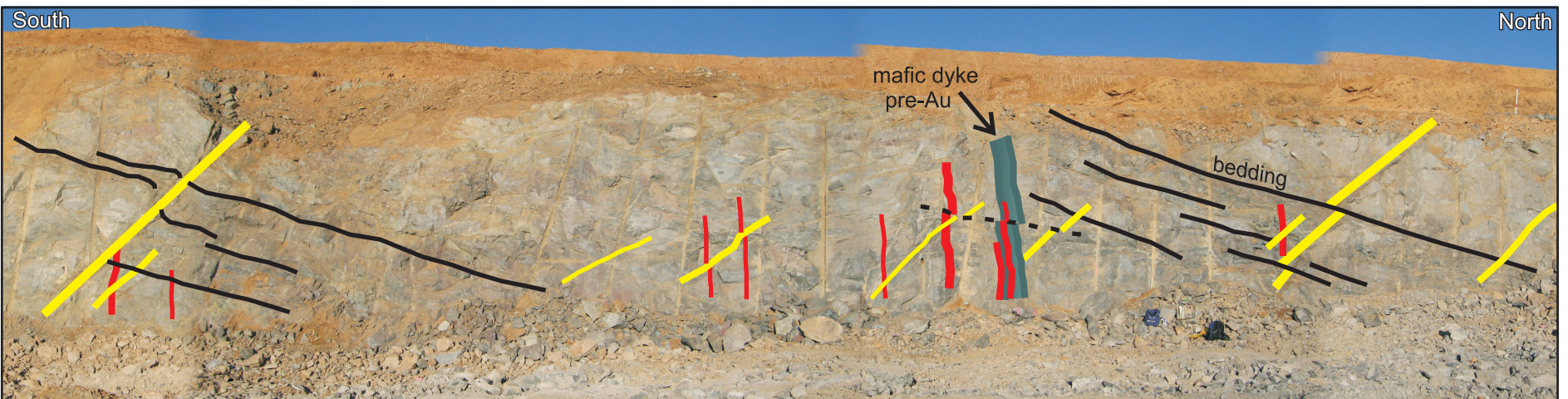


**Figure 4.6** Panoramic photo of the western wall of the 1155RL bench in the E42 open pit. Yellow lines are the inclined gold-bearing vein population; red lines indicate one of the steeply dipping gold-bearing vein sets (the steep, fault parallel gold-bearing vein set is not well-represented in this exposure). East-striking pre-mineral mafic dyke is marked in grey, and bedding is marked by black lines. Note yellow inclined veins crosscutting red steep veins, as well as late stage bed-parallel offset of several gold-bearing veins. Backpacks for scale.

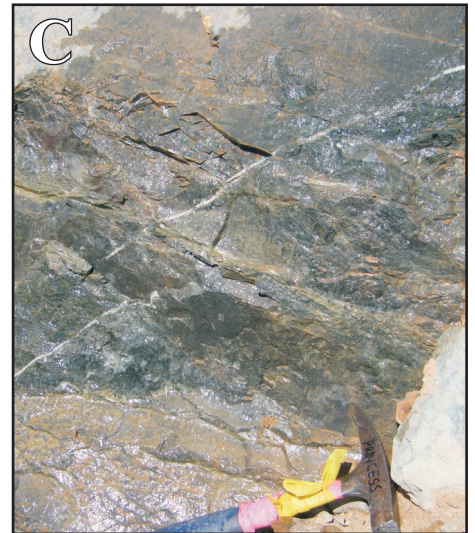
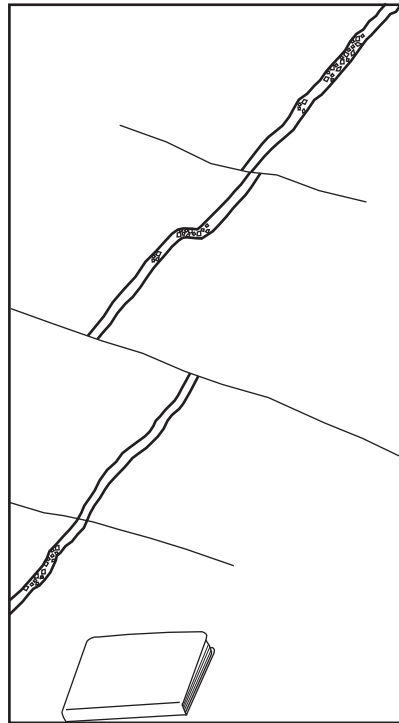


upper section of vein:  
calcite-pyrite-quartz-chlorite-  
sericite-galena-sphalerite-  
chalcopryite-covellite

lower section of vein:  
barren calcite-chlorite



B



C

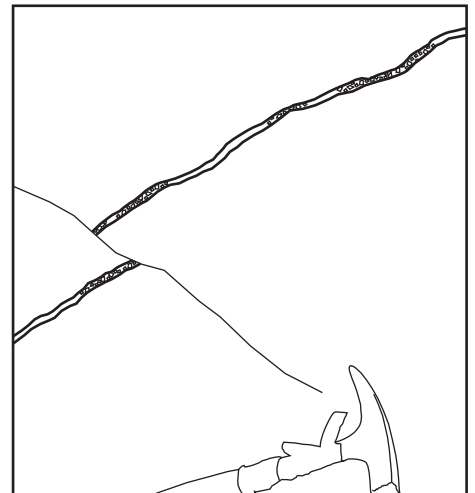


**Figure 4.7** a) Subvertical, fault-parallel gold-bearing vein in open pit displaying sharp variation in vein composition along length. b) and c) Inclined gold-bearing veins in open pit displaying changing vein composition along length. Sulfides noted by small squares in vein, barren vein fill is white. All photos are west facing.

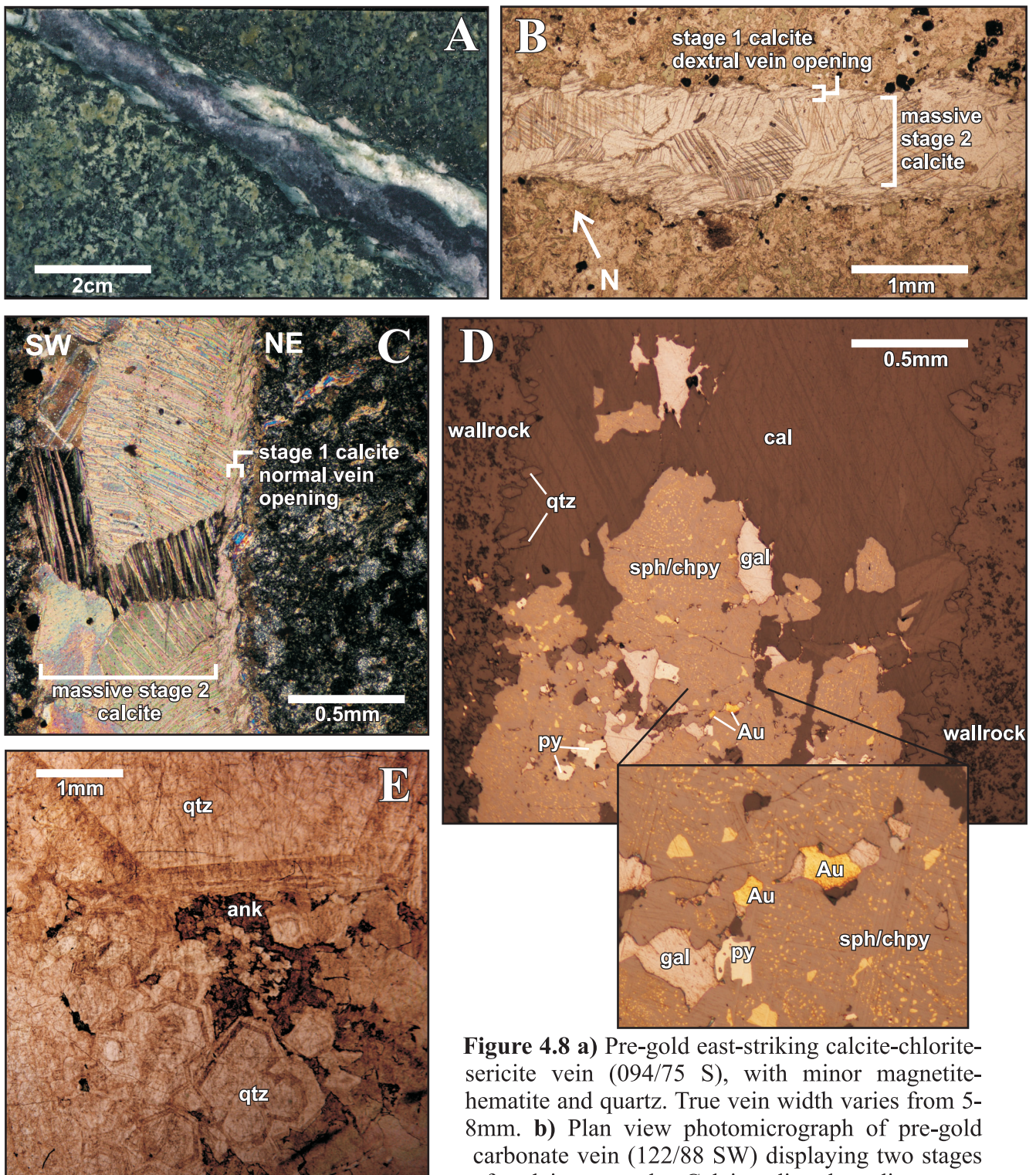


**Figure 4.8** a) Pre-gold east-striking calcite-chlorite-sericite vein (094/75 S), with minor magnetite-hematite and quartz. True vein width varies from 5-8mm. b) Plan view photomicrograph of pre-gold carbonate vein (122/88 SW) displaying two stages of calcite growth. Calcite directly adjacent to

wallrock displays a component of dextral sense opening and second stage calcite is massive and found along centre of vein. Plane polarized light. c) Cross sectional view photomicrograph of same vein as in b), displaying two stages of calcite growth, stage 1 shows a component of normal sense vein opening. Cross polarized light. d) Fault parallel, steeply dipping gold-bearing vein under both cross polarized and reflected light. Quartz (qtz), calcite (cal), sphalerite with chalcopyrite disease (sph/chpy), galena (gal), pyrite (py) and gold (Au). e) Photomicrograph of barren section of inclined gold-bearing vein under plane polarized light. Late ankerite (ank) growing into void space between prismatic, zoned quartz crystals.

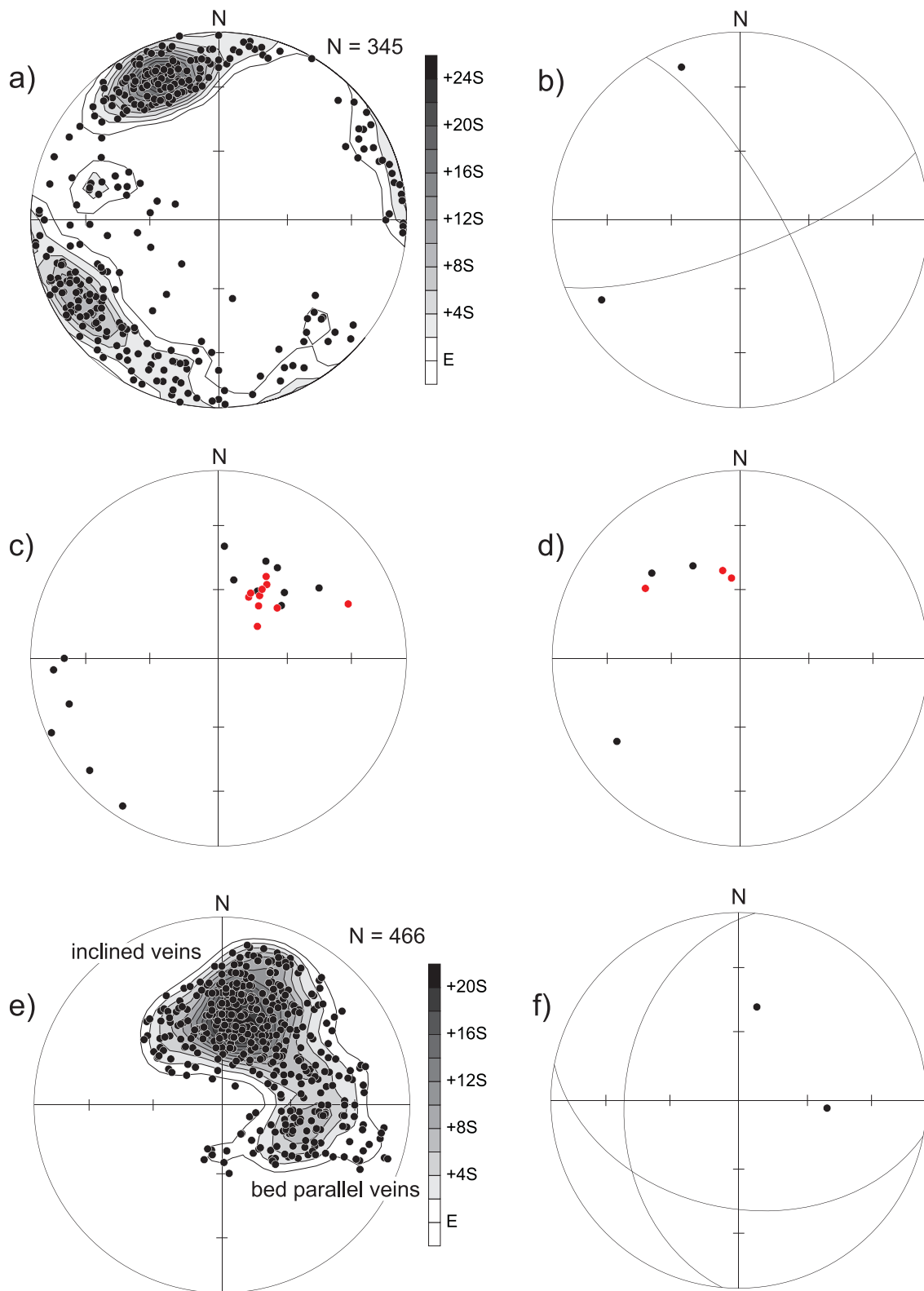


**Figure 4.9** a) Steep, dyke parallel gold-bearing veins b) Average planes for early, steep gold-bearing vein populations. c) and d) Average steep gold-bearing veins (“mineralized shear” from Barrick drillcore logging, black circles) and average inclined gold-bearing veins (“mineralized dilational” from Barrick drillcore logging, red circles) for fault blocks c) west of the Cowal Fault and d) east of the Cowal Fault. e) Inclined and bed parallel gold-bearing veins. f) Average orientation of inclined and bed parallel gold-bearing vein sets.

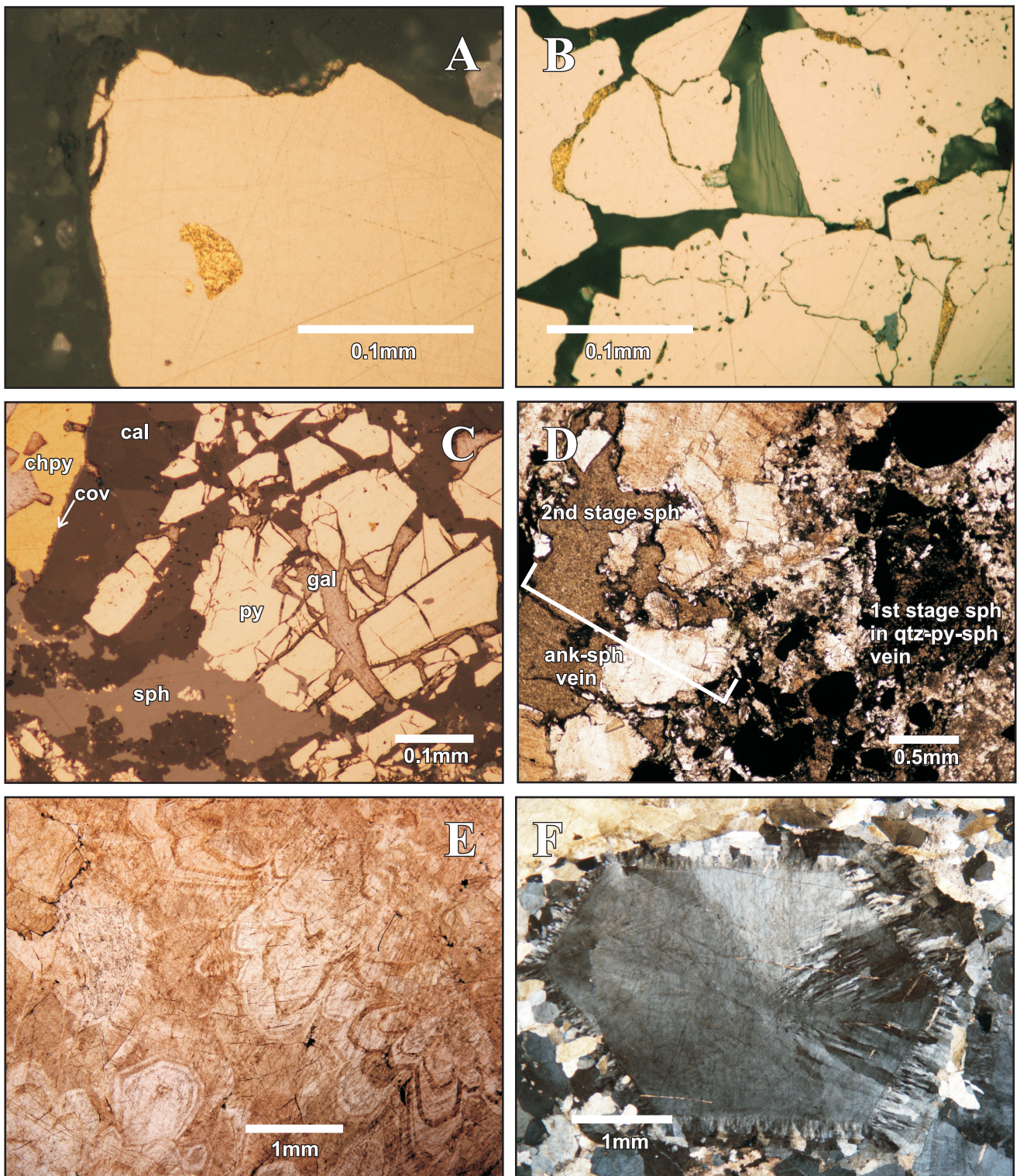


**Figure 4.10** a) Gold inclusion in unfractured pyrite grain. b) Gold along fractures between pyrite grains. c) Fractured pyrite (py) grains infilled by sphalerite (sph), galena (gal), chalcopyrite (chpy), and calcite (cal). Rare covellite found rimming chalcopyrite grains. d) Ankerite-sphalerite vein reactivating a quartz-pyrite-sphalerite vein, evidence for at least two stages of base metal deposition along a fault parallel gold-bearing vein (292/74 NE), plane polarized light. e) Crustiform vein quartz displaying internal zonation, plane polarized light. f) Prismatic vein quartz showing feathery recrystallization textures, cross polarized light.

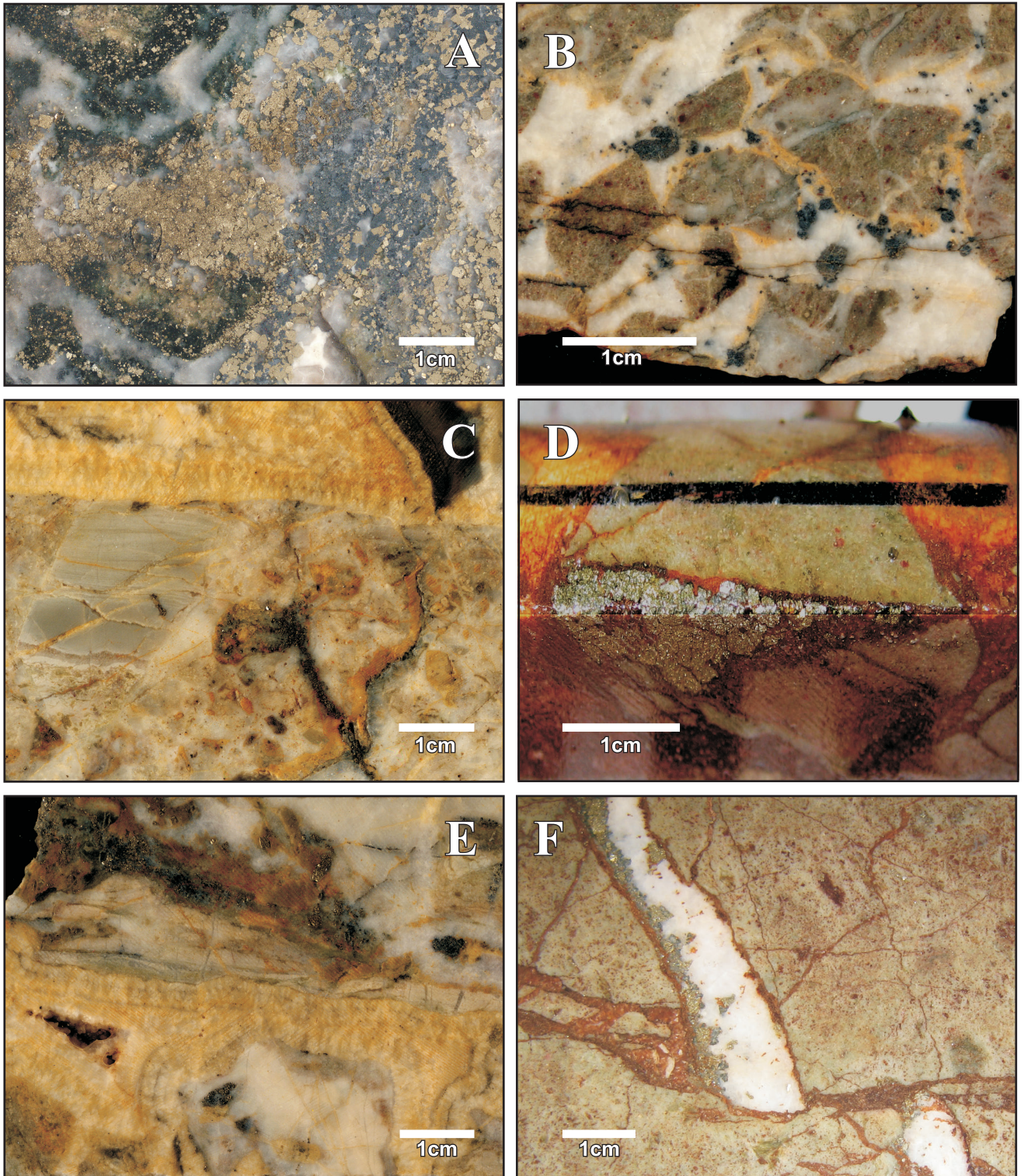


**Figure 4.11** a) Stage 1 fault-hosted breccia: quartz-pyrite-sphalerite cement. Note late, white ankerite infill between prismatic quartz crystals at bottom of photo. b) Stage 2 breccia (ankerite-sphalerite cement) with entrained stage 1 breccia clasts (stage 1 quartz cement truncated at clast margins). c) Stage 3 barren ankerite-cemented breccia crosscutting stage 1 quartz-pyrite-cemented breccia. d) A clast of volcanoclastic sandstone with a pyrite-calcite vein truncated at the clast margin, found within stage 3 barren ankerite-cemented breccia. Ankerite weathers to deep orange/rust color. e) Stage 3 barren ankerite-cement brecciating stage 1 quartz-pyrite-sphalerite breccia. Note crustiform ankerite textures and triangular void space. f) Rust-colored ankerite feeder vein crosscutting inclined quartz-pyrite-sphalerite-gold vein.

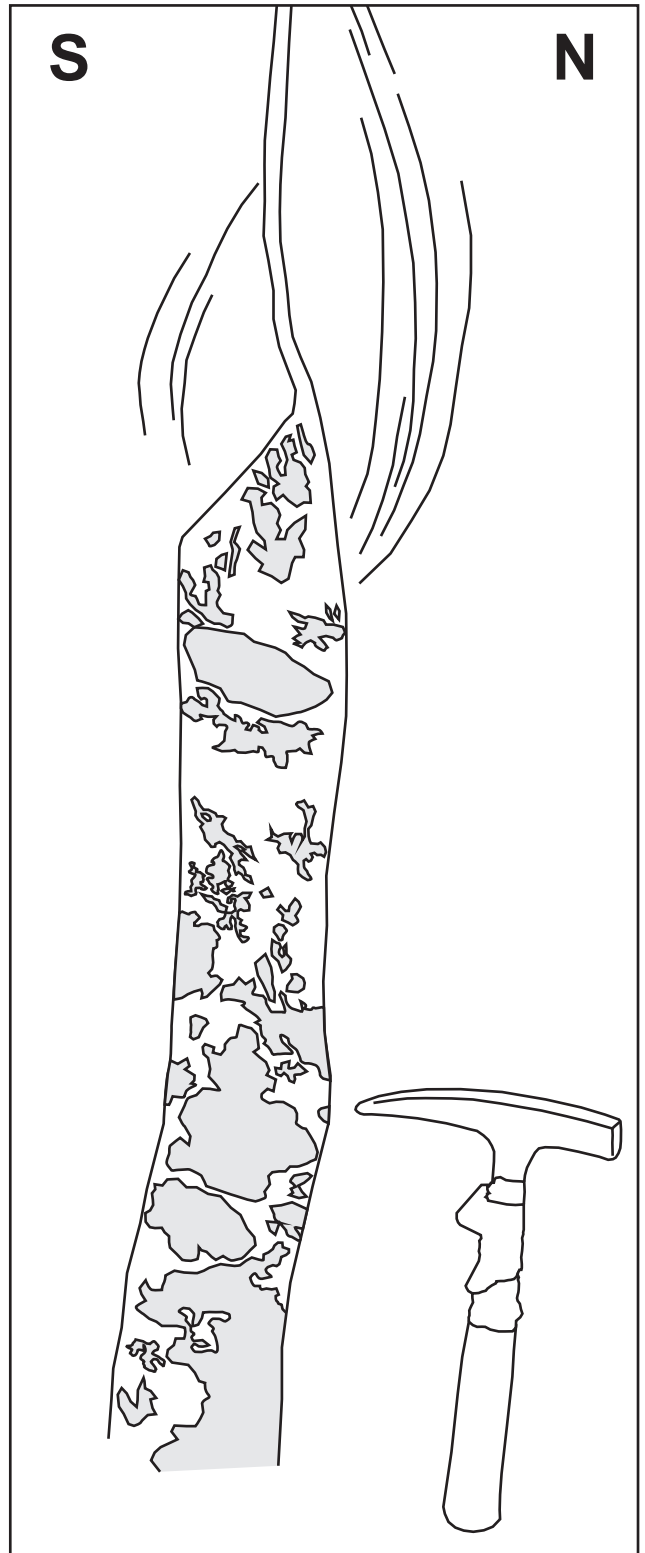


**Figure 4.12** A fault-hosted breccia along west wall of the open pit, 1155RL. It is a polymictic, gold-bearing (16ppm Au), quartz-calcite-pyrite-sphalerite  $\pm$  chlorite cemented breccia, containing angular to subangular clasts of volcanic sandstone and mudstone enclosed within massive cement. The breccia body is subvertical and west-striking, see Figure 4.13a. Note the curved calcite-pyrite veins emanating from breccia tip.

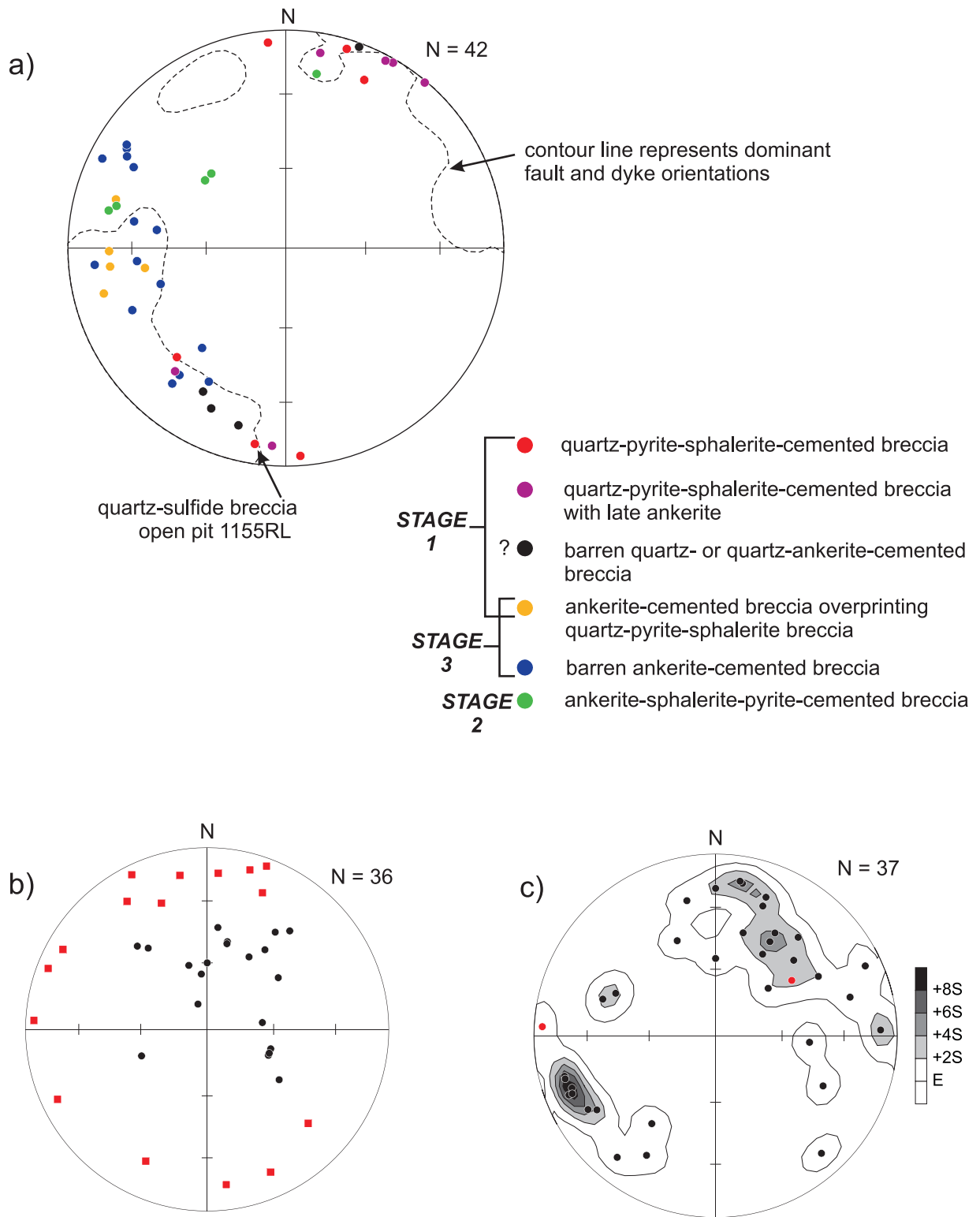


**Figure 4.13** a) Measured margins of hydrothermal brecciated intervals from drillcore and open pit. Mineralogy and stages indicated by colored circles. Average deposit-scale fault and dyke orientations marked by dotted contour lines. b) All crosscutting gold-bearing vein pairs observed at E42. Steep fault parallel veins (red squares) consistently crosscut by inclined and bed parallel veins (black circles). c) Two populations of quartz-pyrite veins. Red poles indicate steep vein crosscut by inclined vein.

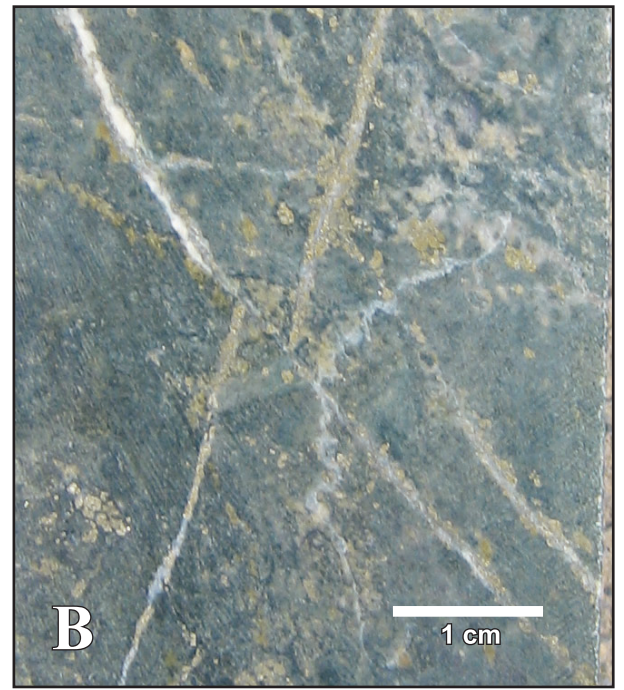
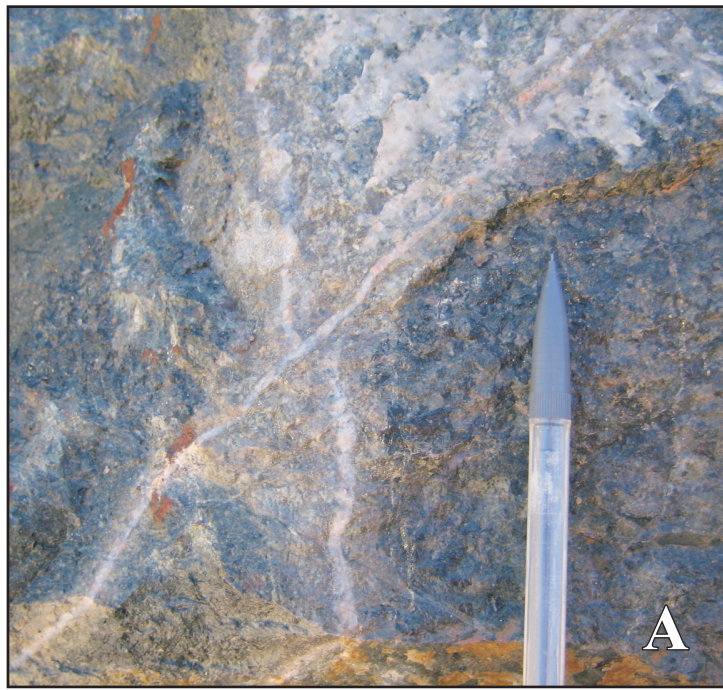


**Figure 4.14** a) Inclined gold-bearing vein crosscutting steep, fault parallel gold-bearing vein, open pit. b) Inclined gold-bearing vein crosscutting steep, fault parallel gold-bearing vein, core sample E42D1112 409.2m. c) Inclined gold-bearing vein at low angles to bedding defined by interlayered volcanoclastic mudstones and fine to medium grained sandstones. This vein is included in the bed parallel gold vein population, see Figure 4.9e. d) Inclined gold-bearing vein in open pit showing planar walls and thin, subparallel veins of similar mineralogy on either side. Pit photos are all west facing.

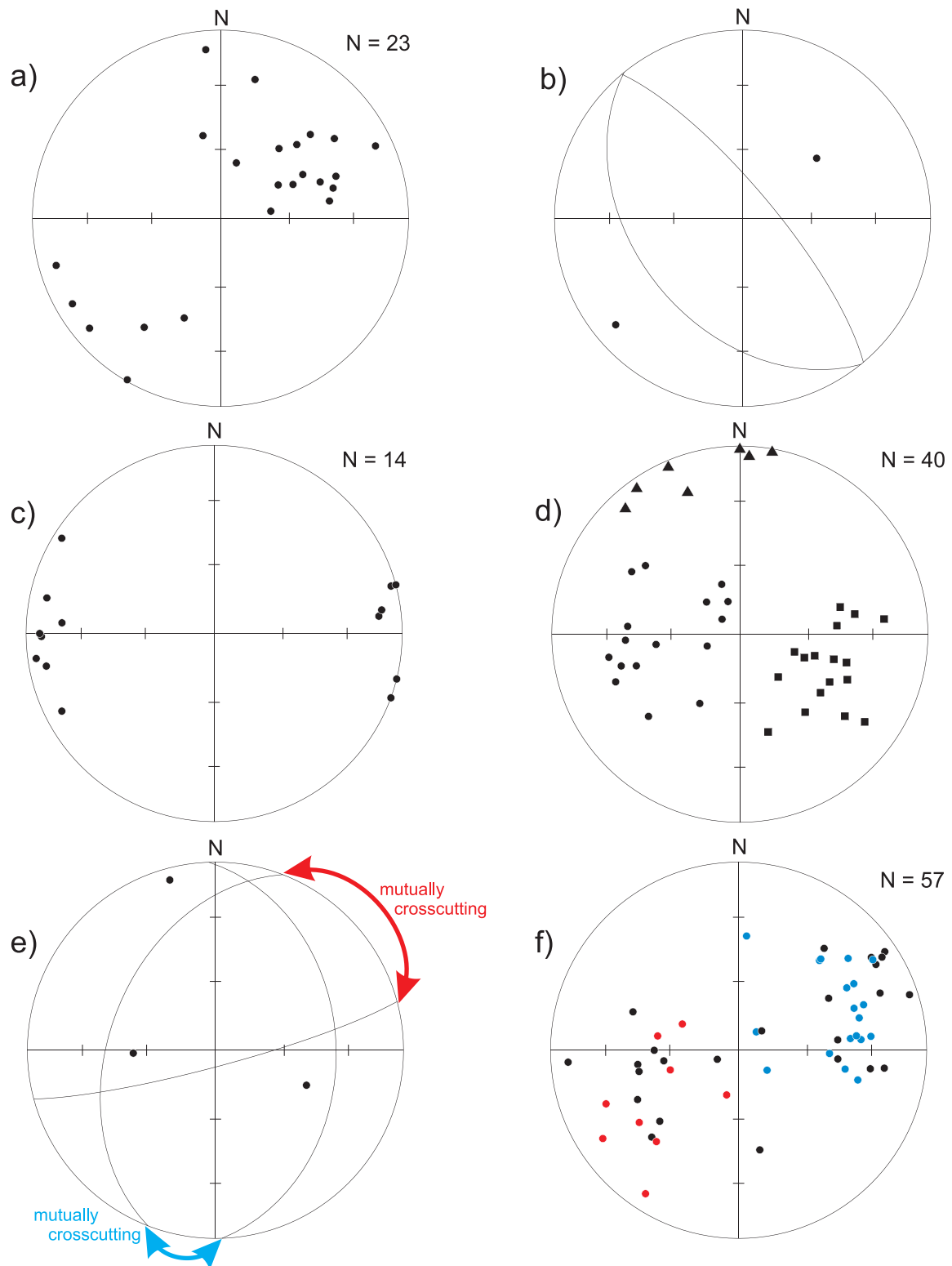


**Figure 4.15** a) Carbonate veins reactivating gold-bearing veins. b) Average measurements for carbonate veins reactivating gold-bearing veins. c) Steep north-trending carbonate veining event. Veins crosscut the carbonate veins from a) and b) and are crosscut by late veining from d). d) Three main populations of late carbonate-chlorite-hematite veins. In combination, these veins visibly crosscut all other vein types at E42. Triangles - steep fault parallel; circles - moderately east dipping; squares - bedding parallel. e) Average poles and planes for three late vein sets from d). Two pairs are mutually crosscutting. f) Lineations defined by slickenfibres developed on late carbonate veins. Blue circles - reverse sense movement, top-to-the-west; red circles - reverse sense movement, top-to-the-east; black circles - direction of movement unclear.

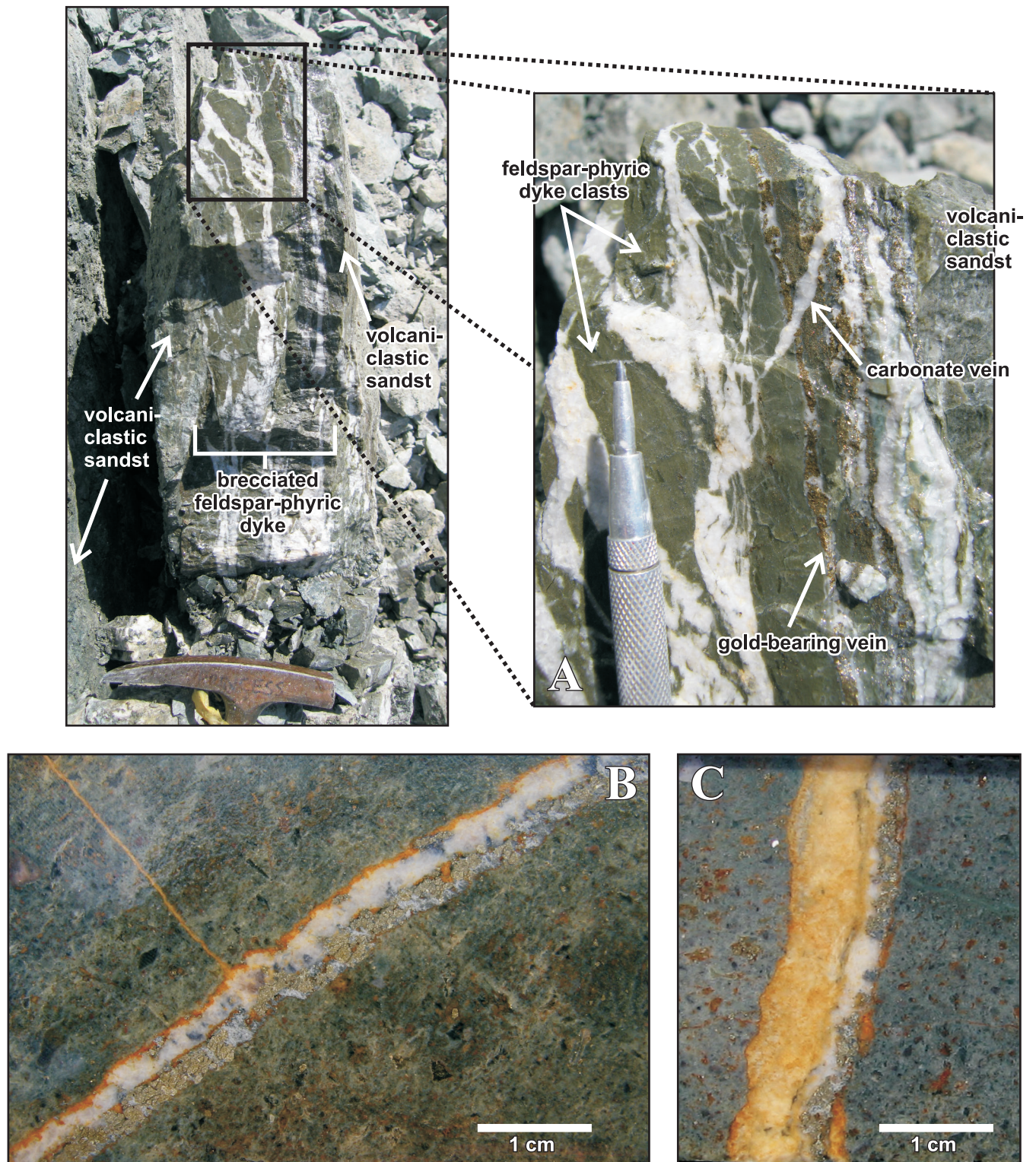


**Figure 4.16 a)** Subvertical north-striking feldspar-phyric dyke emplaced in fine to medium-grained volcaniclastic sandstone, open pit 1128RL. Steep gold-bearing veins form along dyke margin, are included in fault/dyke parallel vein population, see Figure 4.9a. Later carbonate veins reactivate dyke margin, crosscut the gold-bearing veins and locally brecciate the dyke. **b)** and **c)** Gold-bearing veins (dominantly calcite-pyrite-quartz-sphalerite) reopened along weakness at vein margin. Barren ankerite vein fill weathers to orange/red color in core.

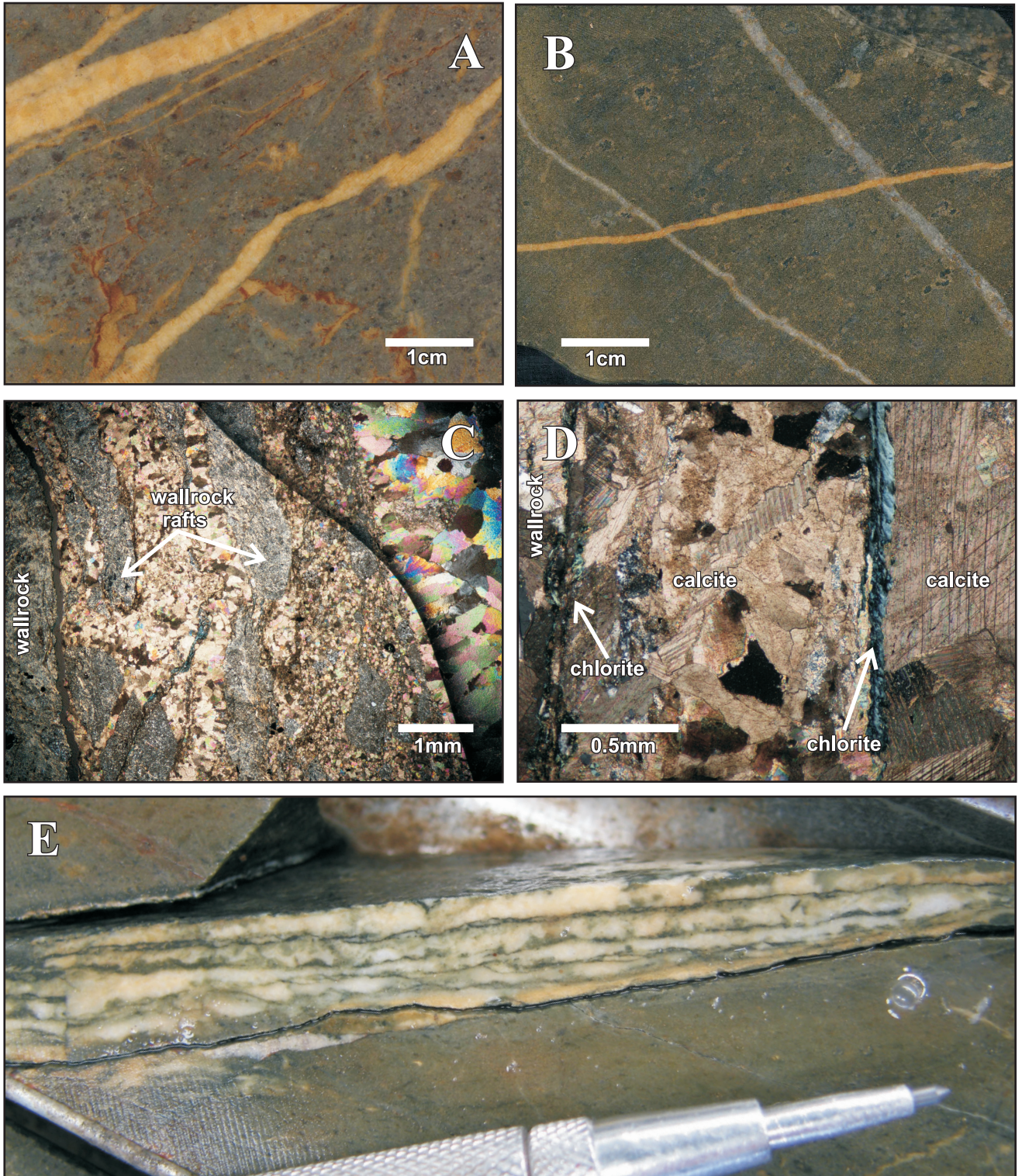


**Figure 4.17** a) and b) steep north-striking carbonate veins, dominantly ankerite, displaying irregular margins. Note vein in b) is crosscutting two calcite-pyrite veins associated with gold-bearing veins. c) Steep north-striking carbonate vein displaying at least two opening events. Fine-grained calcite with wallrock rafts represents first opening, with coarser-grained calcite to the right of the photomicrograph representing second opening, cross polarized light. Black line through photo is due to an uneven thin section. d) Late carbonate-chlorite vein displaying multiple openings, shown by layered chlorite and carbonate away from vein wall (on the left), cross polarized light. e) Late carbonate-chlorite vein displaying multiple opening episodes.

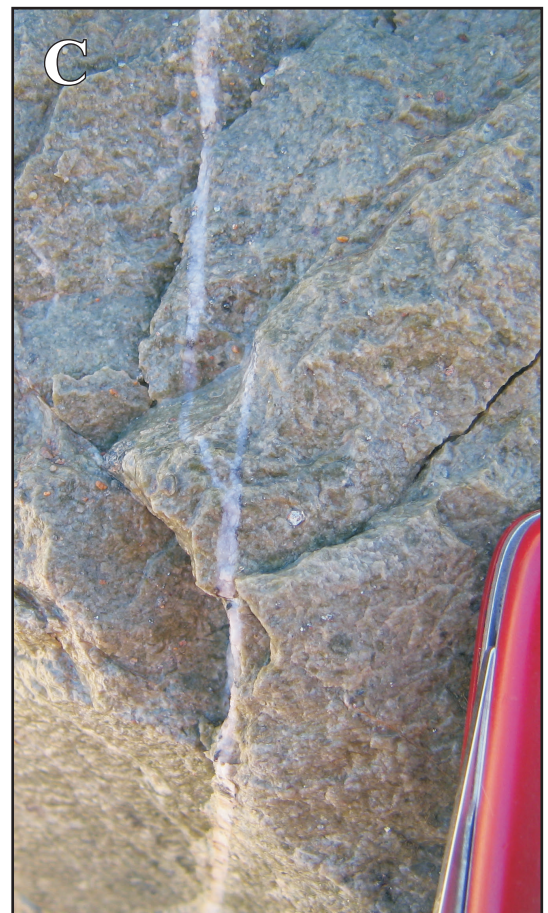


**Figure 4.18** a) Bedding parallel vein from one of the youngest carbonate-chlorite-hematite vein populations. Host rock is fine-grained volcanoclastic sandstone and mudstone. b) Example of reverse-sense carbonate-chlorite slickenfibres commonly exhibited by youngest carbonate-chlorite-hematite vein populations. c) Stepped geometry displayed by steep fault parallel quartz-carbonate-pyrite vein, similar to stepped geometry shown by several inclined gold-bearing veins. Pocketknife for scale, photo is west facing.

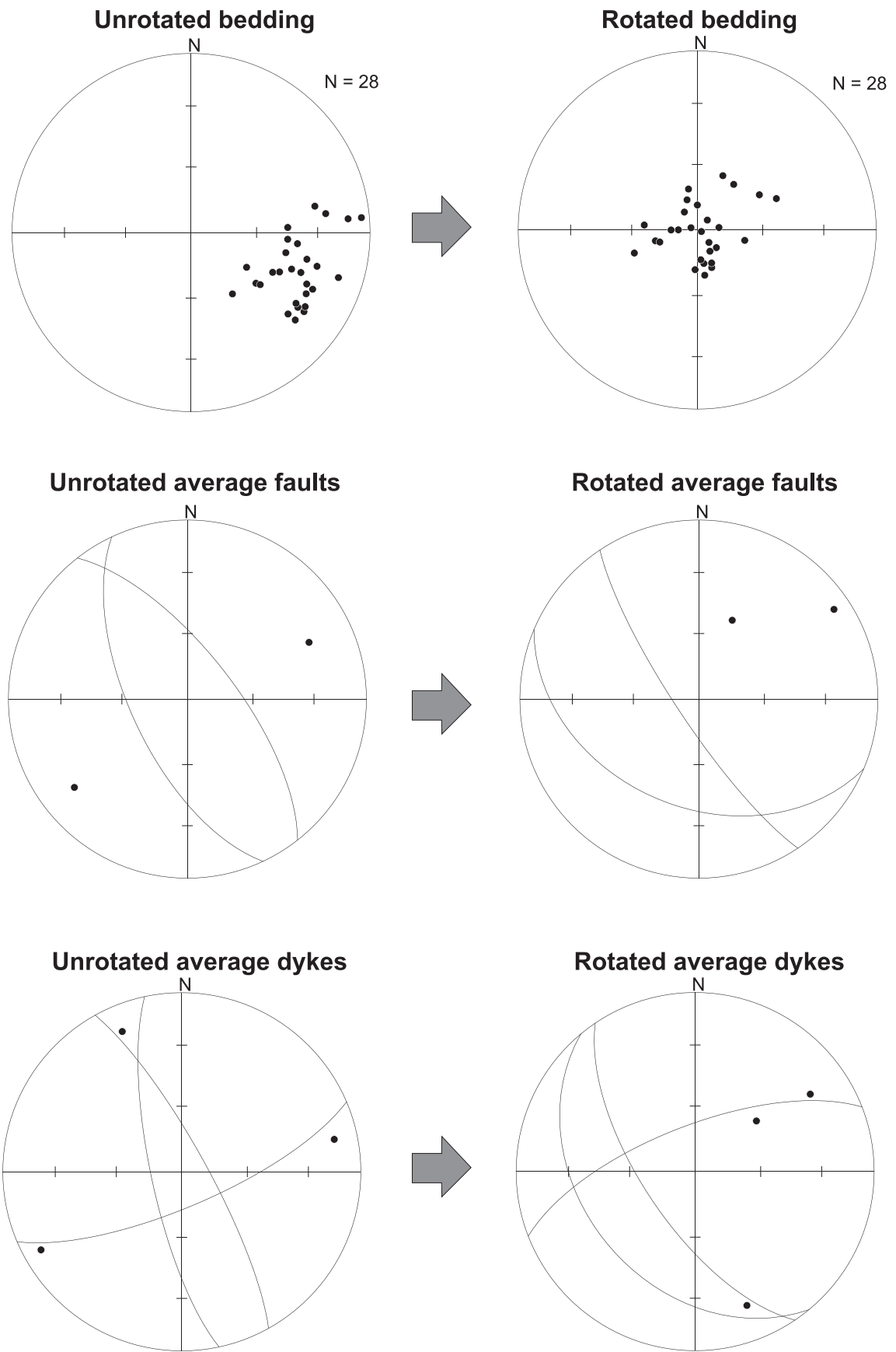


**Figure 4.19** Rotation of bedding, faults, and dykes by  $53^\circ$  about axis oriented 020-00.

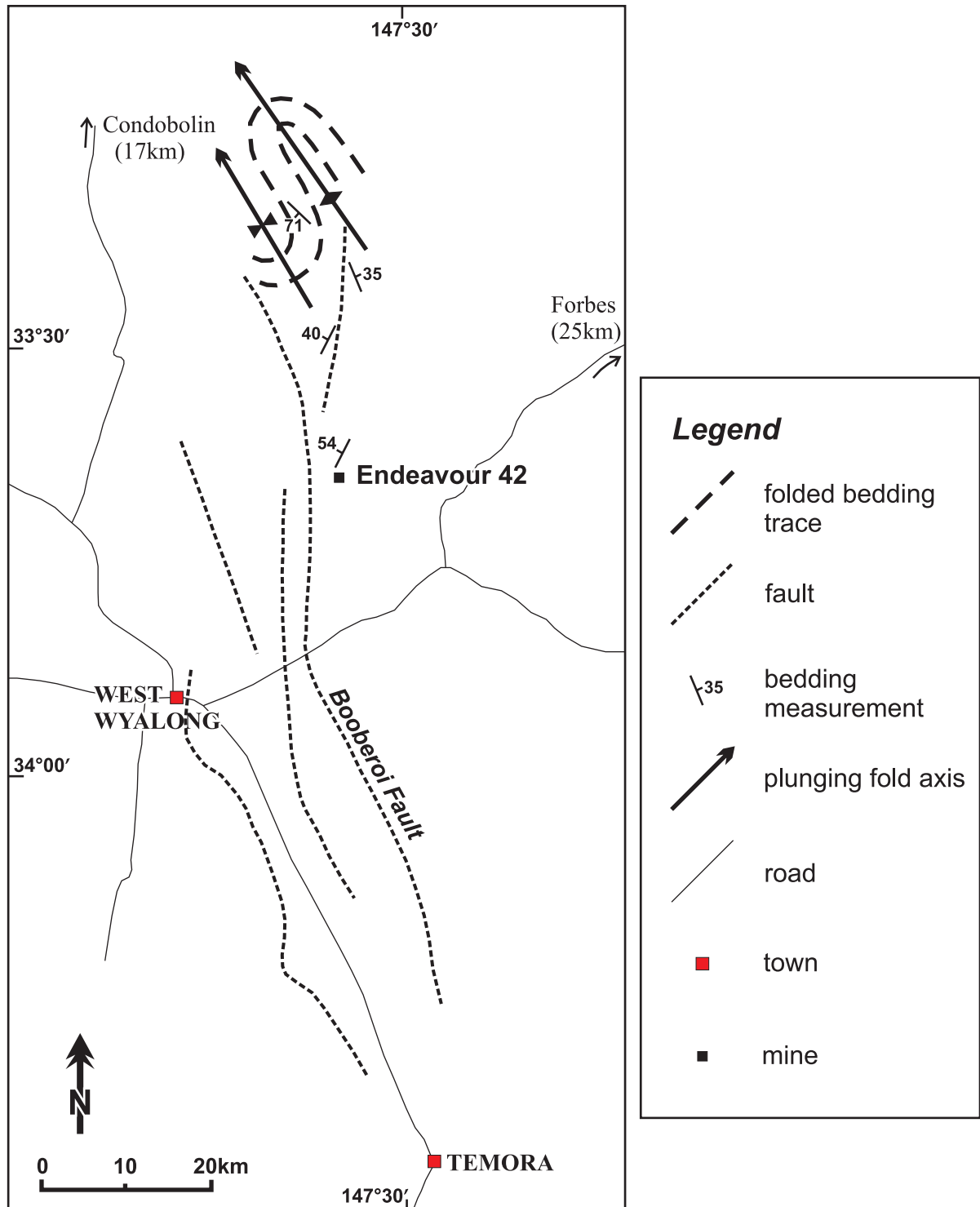


**Figure 4.20** Map of West Wyalong and surrounding area with selected structural interpretations and measurements taken from Ingpen (1995). Note the shallowly northwest-plunging anticline-syncline pair to the north of the E42 deposit.

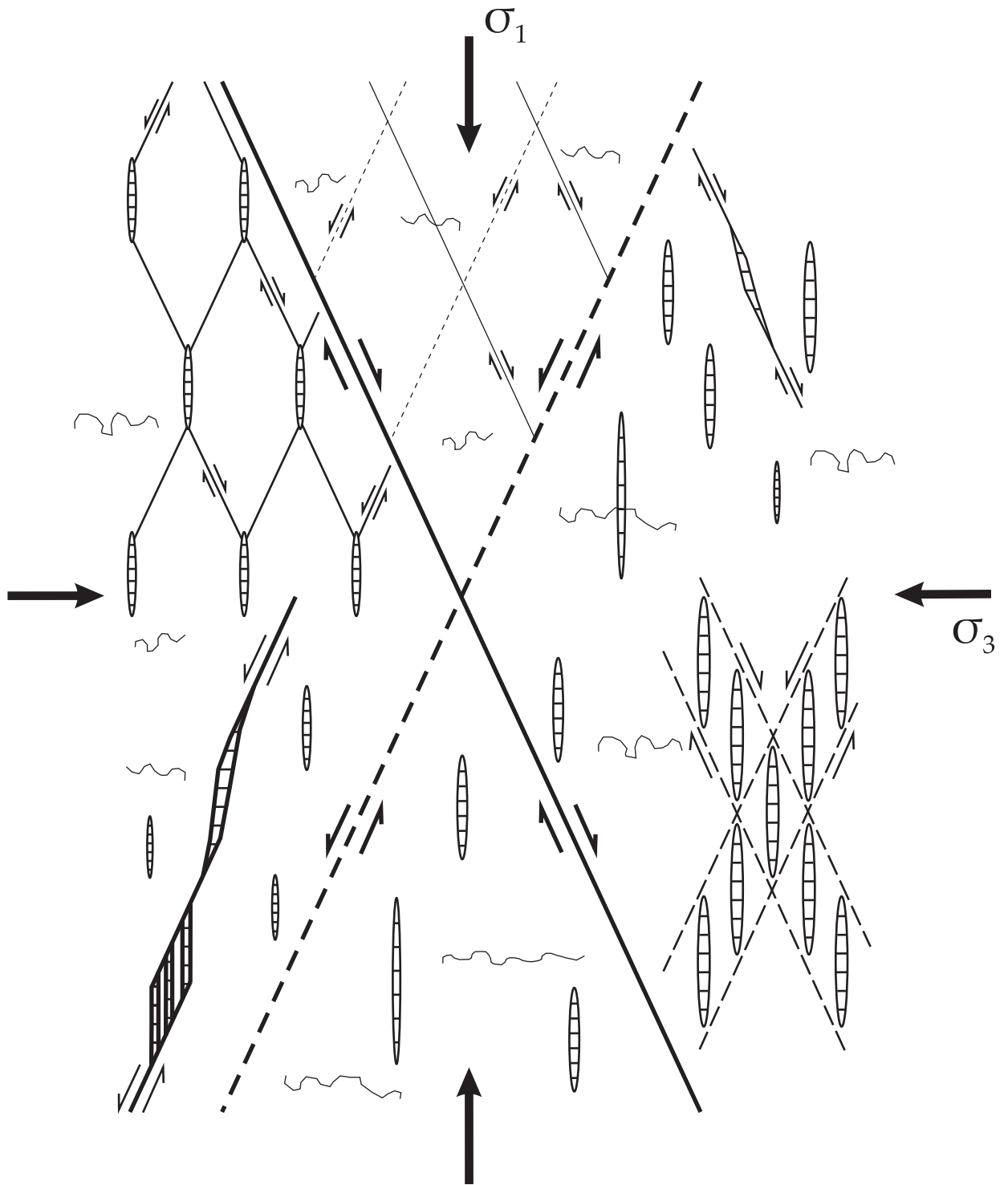


**Figure 4.21** Structural permeability in a triaxial stress regime. Faults are defined by shear sense indicators, extensional and extensional shear fractures are defined by cross-hatched patterns, and stylolites are defined by squiggly lines. The intermediate stress axis is oriented perpendicular to the page. After Sibson, 2001.

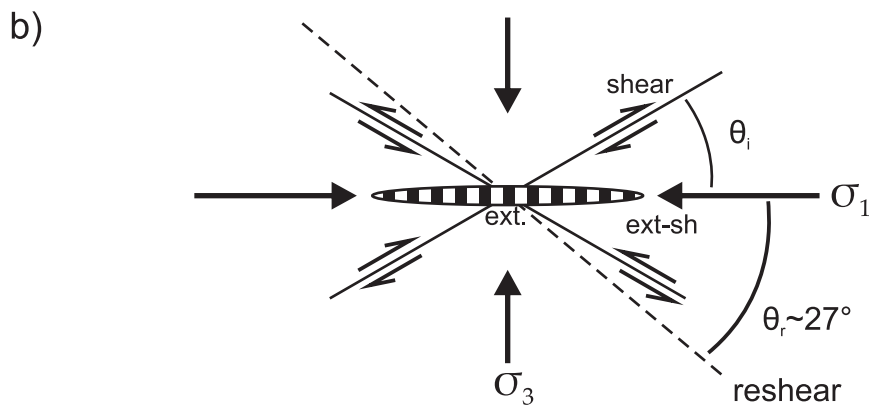
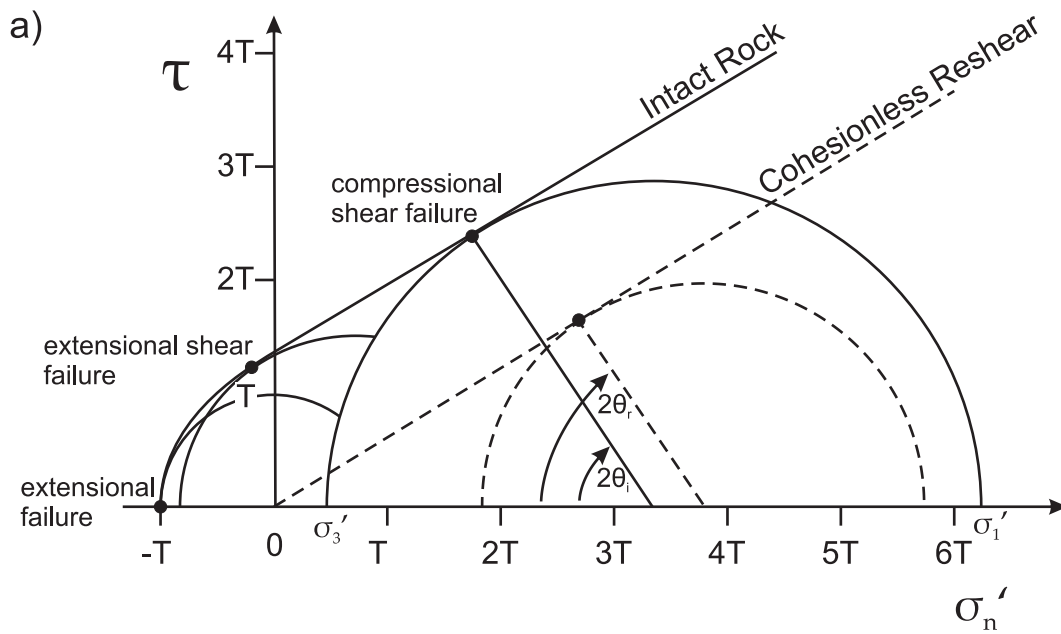


**Figure 4.22 a)** Composite 2D failure envelope for intact rock (bold line) and the reshear condition for a cohesionless fault (dashed line) plotted on a Mohr diagram (shear stress,  $\tau$ , vs. effective normal stress,  $\sigma'_n$ , normalized to rock tensile strength,  $T$ ). A representative average value for the coefficient of internal friction of 0.75 is used. After Sibson, 2001. **b)** Expected orientations of newly formed shear, extensional shear (ext-sh), and extensional (ext.) fractures relative to principal stress axes, in 2D. Optimal angle of reshear  $\theta_r \sim 27^\circ$  shown. After Sibson, 2001.

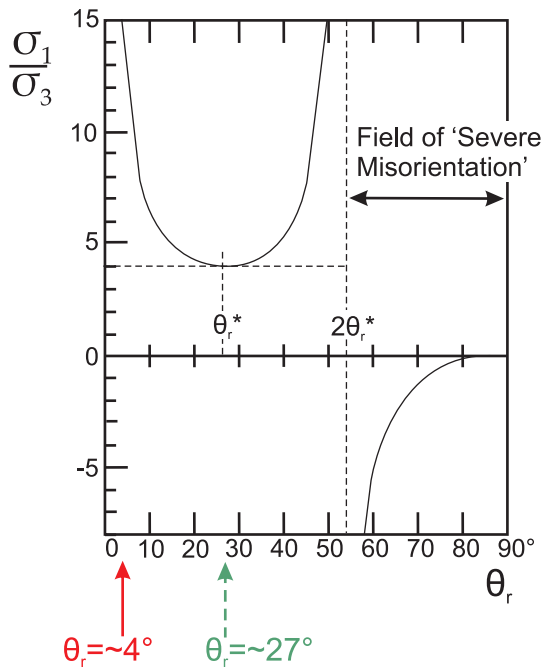
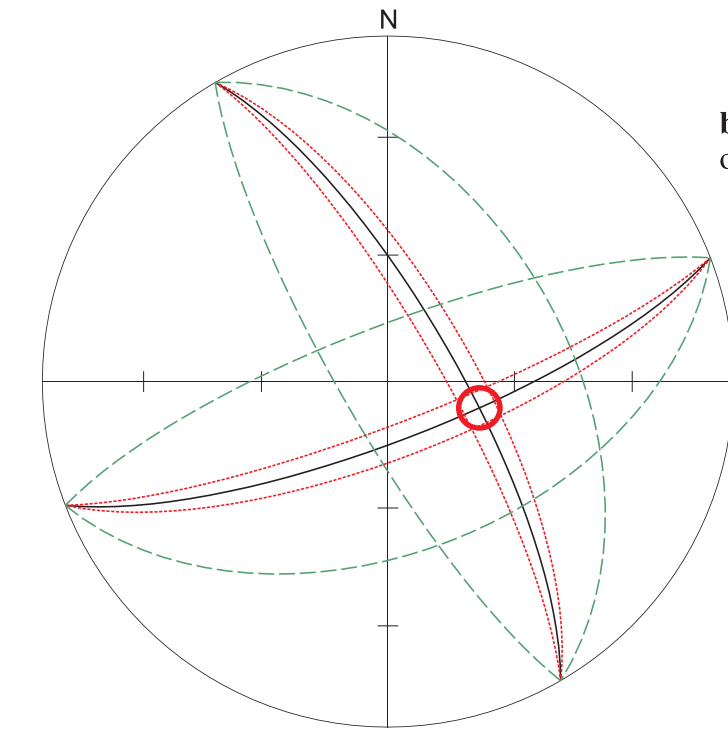
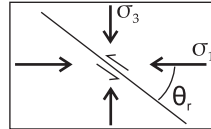


**Figure 4.23 a)** Ratio of greatest to least effective principal stresses ( $\sigma_1'/\sigma_3'$ ) required for reshear of a cohesionless fault in 2D plotted against the reactivation angle  $\theta_r$ .  $\theta_r^*$  is the optimum angle for reactivation, where the stress ratio reaches a positive minimum. Frictional lock up occurs at  $2\theta_r^*$ , above which reactivation will only occur when pore fluid pressure is greater than the minimum compressive stress ( $P_f > \sigma_3$ ). An average representative value of 0.75 is used for the coefficient of internal friction; after Sibson, 2001.



**b)** Principal compressive stress axis orientation for the coeval tensional opening of both steep gold-bearing vein populations.

- Average planes for early, steep gold-bearing vein populations
- - - Reactivation envelope of  $\theta_r \approx 4^\circ$  around average vein planes indicating area where  $\sigma_1$  must be located for tensional vein formation
- - - Reactivation envelope of the optimum angle of reshear  $\theta_r \approx 27^\circ$
- Area defining the orientation of  $\sigma_1$  for the coeval tensional opening of both steep gold-bearing vein populations

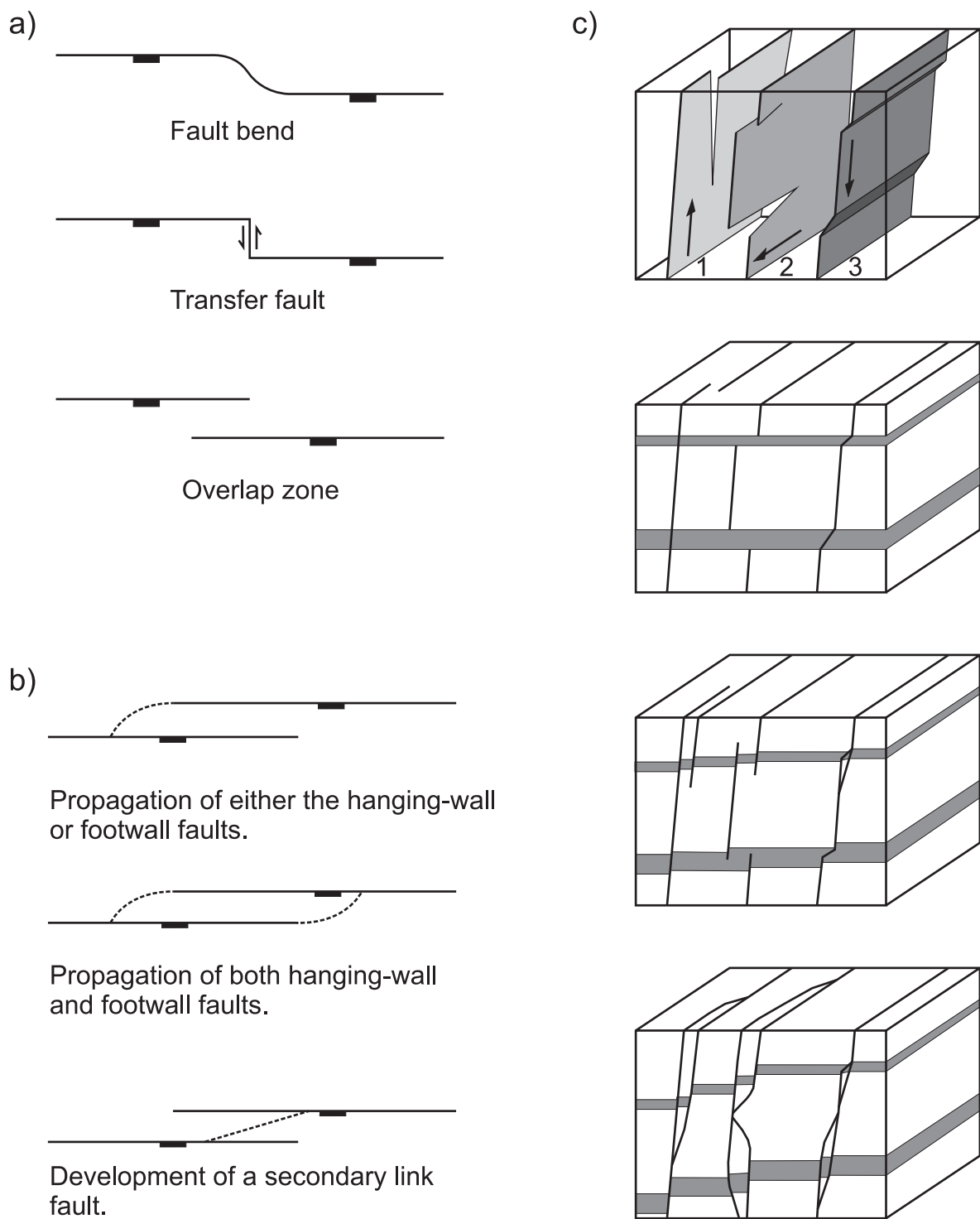
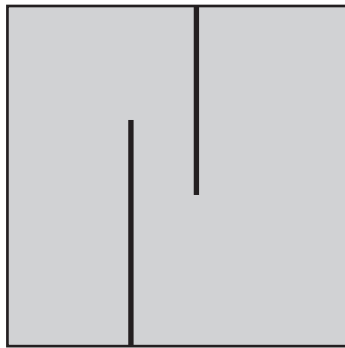
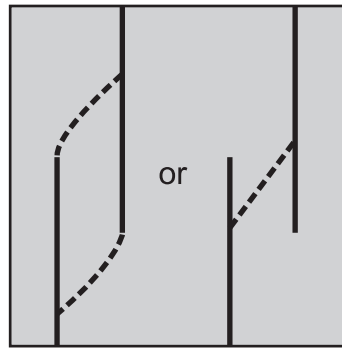


**Figure 4.24** a) Schematics of possible structures at an offset in a fault trace; after Childs et al., 1995. b) Possible linkages for a breached relay zone; after Childs et al., 1995. c) Simple models of tip line and asperity bifurcations for three normal fault geometries. Arrows indicate propagation directions which could cause these geometries. Faults 1 and 2 display tip line bifurcation and fault 3 displays asperity bifurcation. Less competent layers (e.g. shale) are shaded; after Childs et al., 1996.

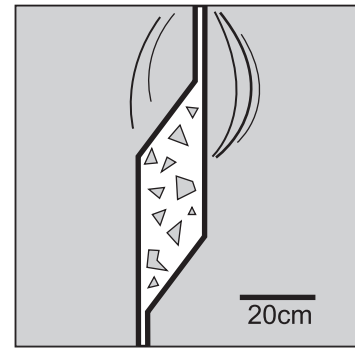
a) Scenario One - breaching of fault overlap zone



Two distinct, subparallel fault planes

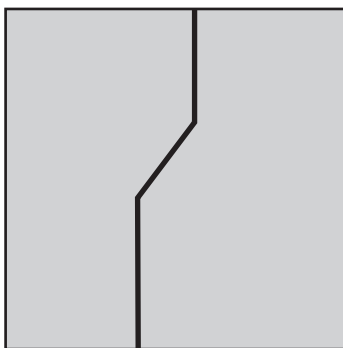


Tip-line bifurcation or the development of a secondary link fault results in breaching of overlap zone. Creates through-going pathway for fluid and a decrease in pressure

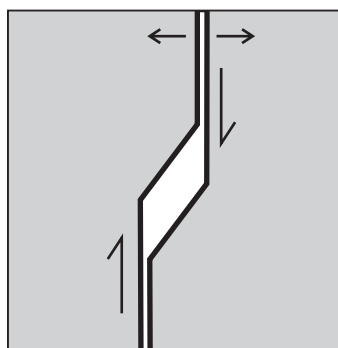


Brecciation within low pressure region; formation of curved "impact" veins

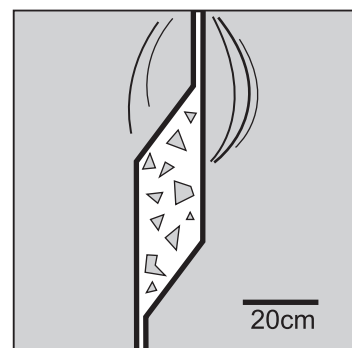
b) Scenario Two - asperity bifurcation along fault surface



Fault bend; result of asperity bifurcation during displacement



Fault movement and creation of low pressure region in fault bend



Brecciation within low pressure region; formation of curved "impact" veins

**Figure 4.25** Quartz-sulfide breccia formation. **a)** Scenario one is a breaching of the fault overlap zone either by tip-line bifurcation of the two subparallel planar faults, or by the development of a single hard-linkage fault. **b)** Scenario two is an asperity bifurcation along a fault surface.

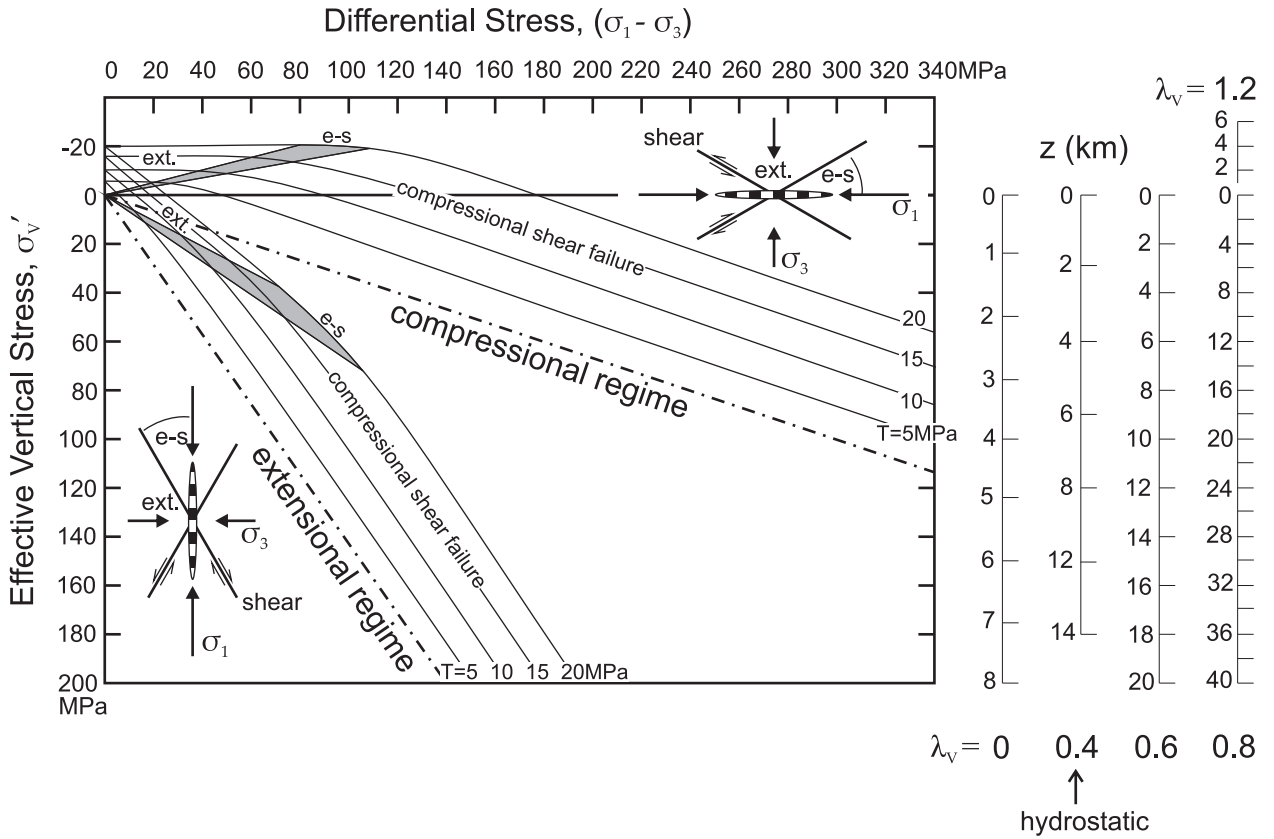


**Figure 4.26** Brittle failure modes with effective vertical stress ( $\sigma_v'$ ) versus differential stress ( $\sigma_1 - \sigma_3$ ) for extensional ( $\sigma_v = \sigma_1$ ) and compressional ( $\sigma_v = \sigma_3$ ) regimes. Effective vertical stress can be related to depths ( $z$ ) for different pore fluid factors ( $\lambda_v$ ). Dashed lines indicate the optimal cohesionless reshear for pre-existing faults. Extensional (ext.), extensional-shear (e-s), and compressional shear failure zones are indicated for both regimes. Schematic vein insets describe the expected orientations of brittle structures with respect to principal stress directions. After Sibson, 2001.

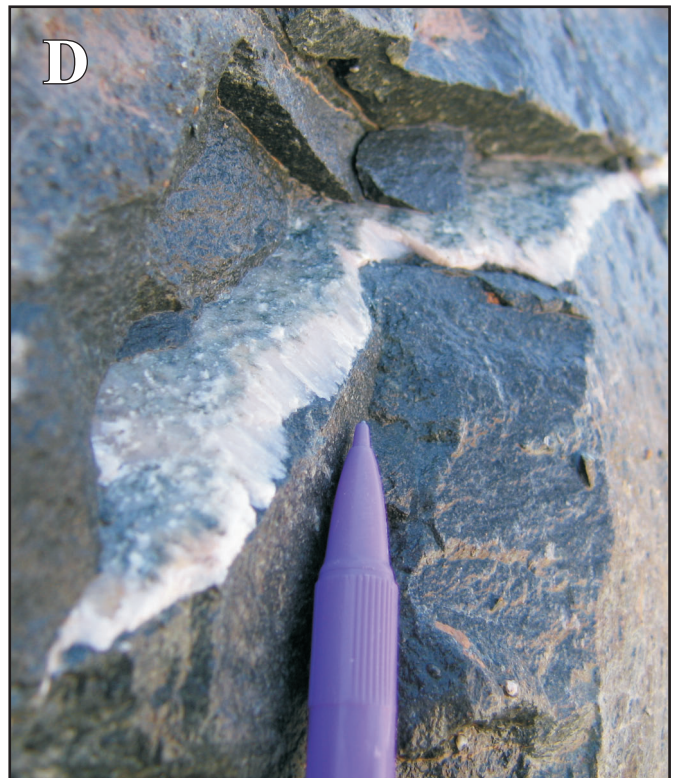
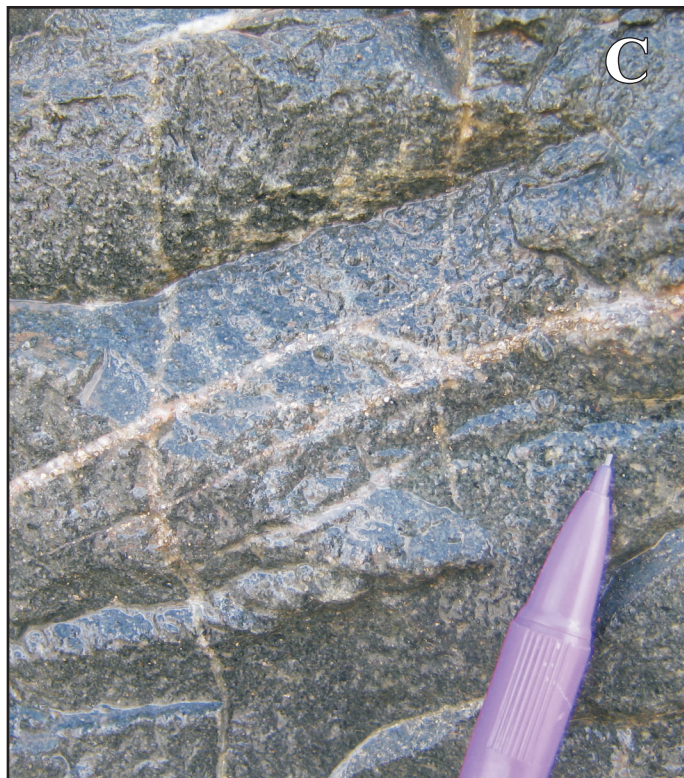
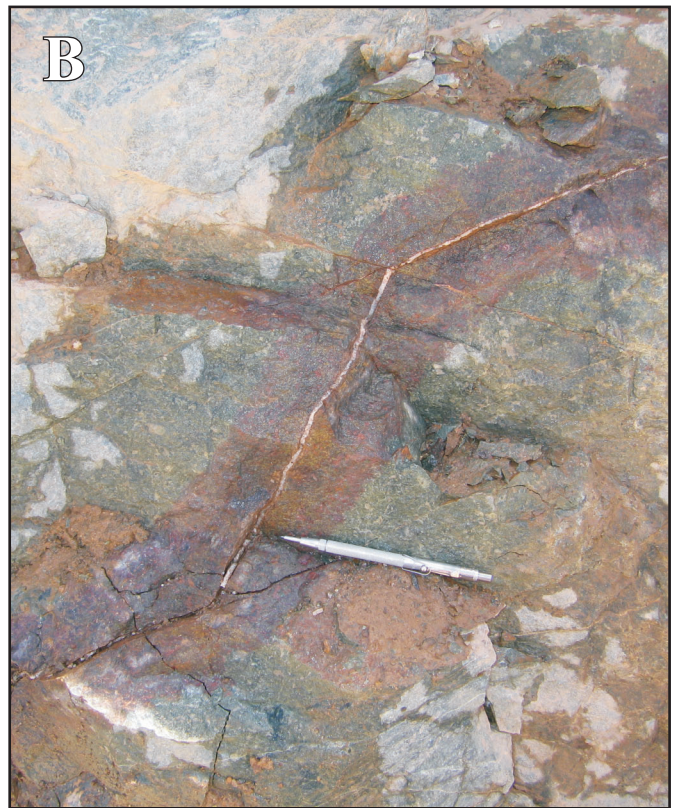


**Figure 4.27** a) Stepped geometry in inclined gold-bearing vein. Vein outlined, with subvertical extensional shear opening direction marked by white arrows, inferred from vein wall geometry. Photo is west facing. b) and c) Stepped geometry in inclined gold-bearing veins, note small linkage veins showing mirrored geometry between b) and c). Photos are west-facing. d) Vein growth fibres showing extensional shear opening. This vein belongs to the population of reactivated gold-bearing veins. Photo is north-facing.

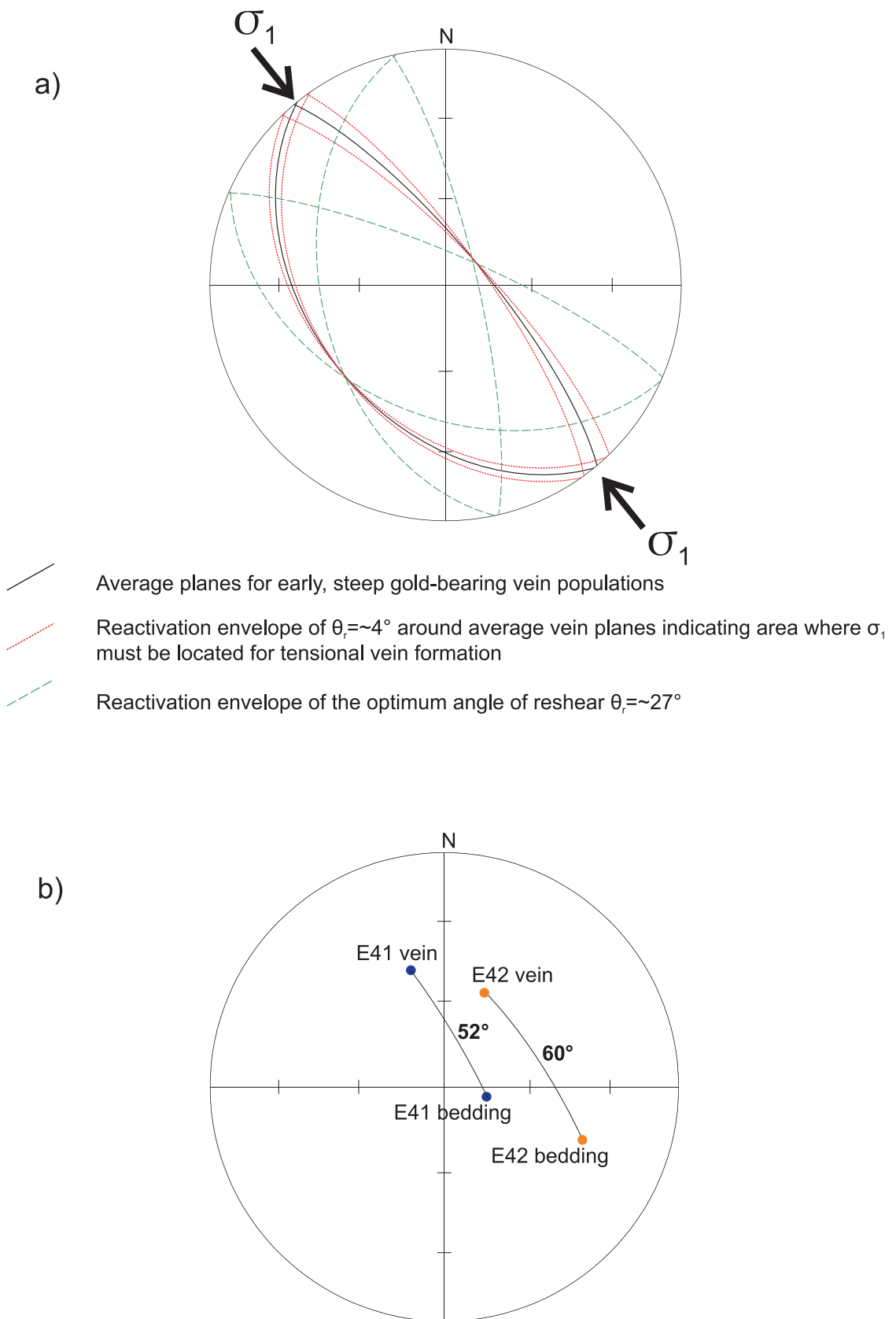


**Figure 4.28** a) Principal compressive stress axis orientation for carbonate reactivation of gold-bearing structures. b) Angle between poles to bedding and poles to main gold-bearing vein populations for E41 and E42.

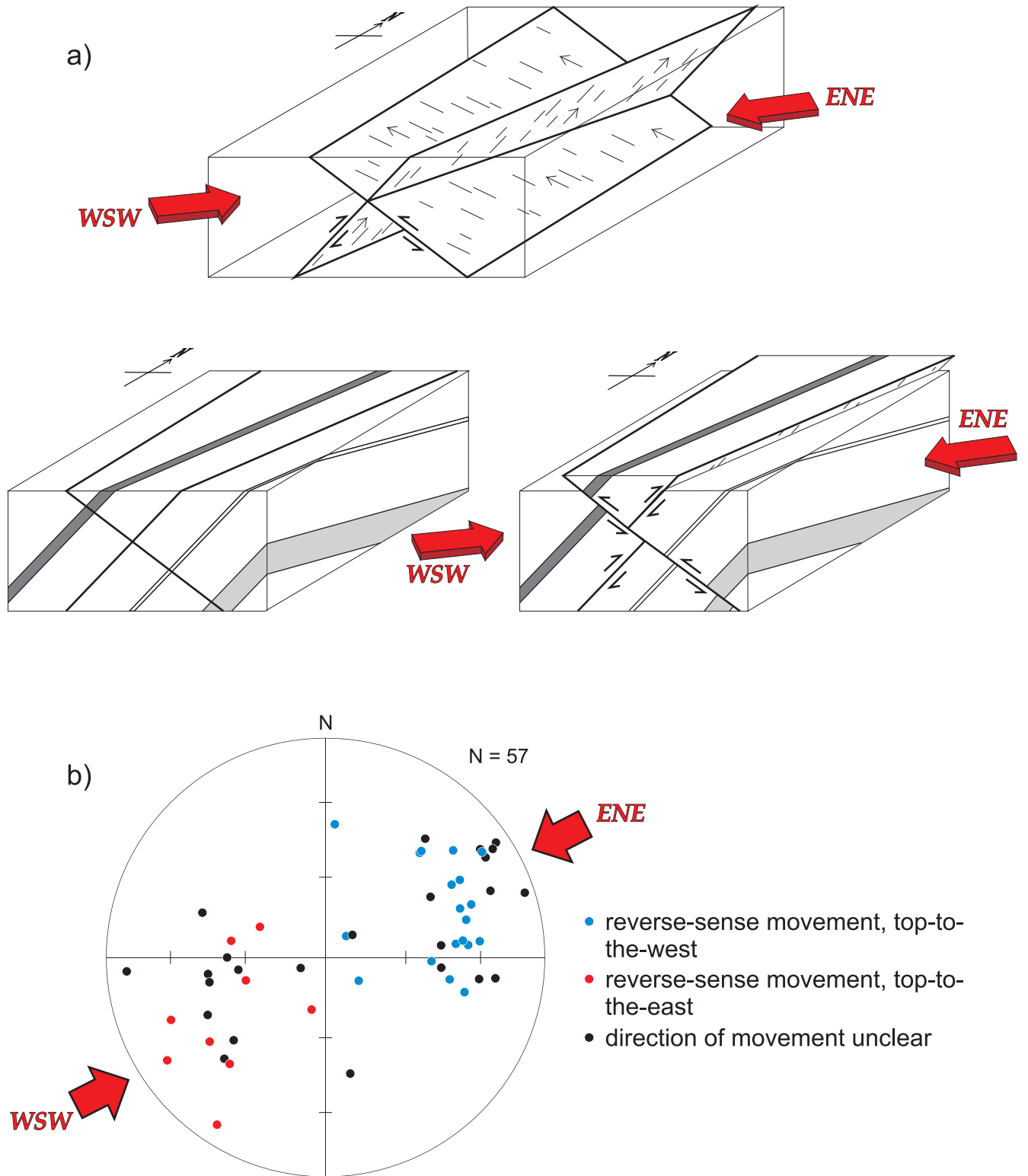


**Figure 4.29** a) Schematic block diagrams for late stage slickenfibres formation during ENE-WSW directed contraction. b) Lineations defined by slickenfibres developed on late carbonate veins.

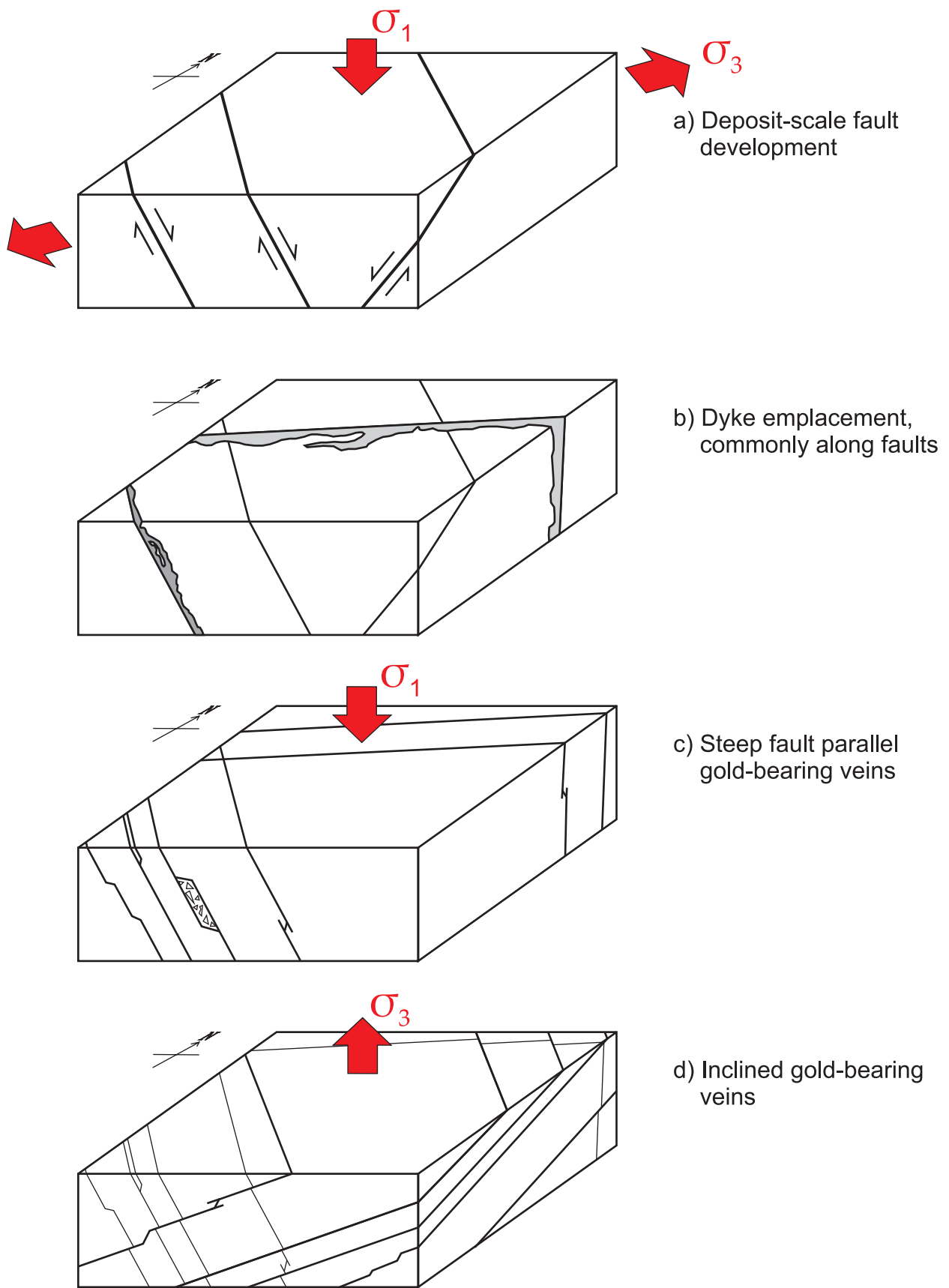
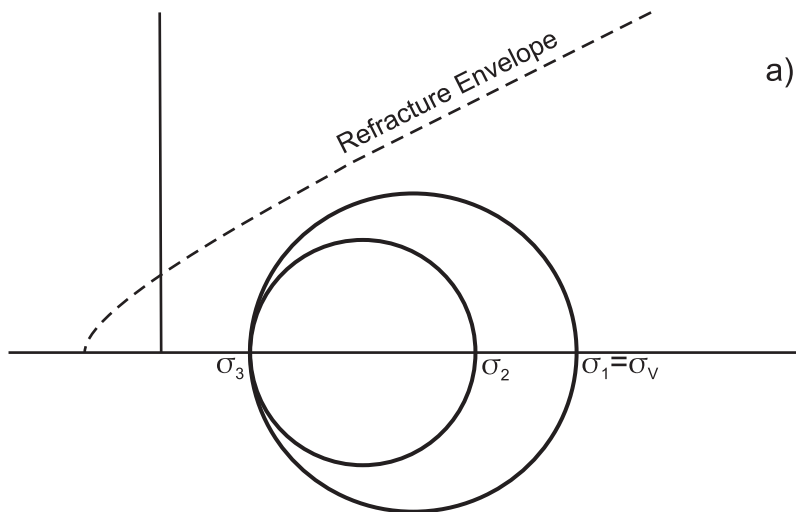
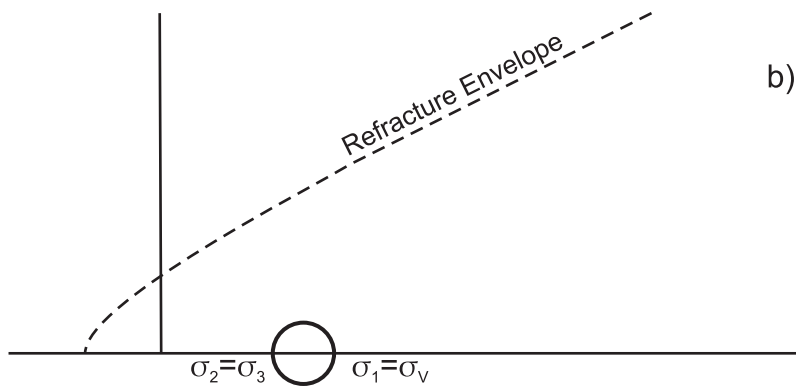


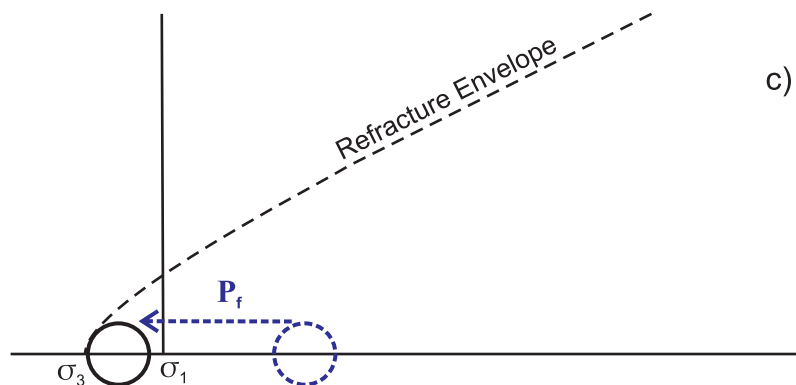
**Figure 4.30** Schematic block diagrams for the distribution of gold-bearing veins at E42.



a) Triaxial stress state prior to release of shear stress along regional fault.  $\sigma_1 = \sigma_v = \rho gh$ , where  $\rho$  is rock density,  $g$  is acceleration due to gravity, and  $h$  is depth



b) Near isotropic stress state at E42 following movement along regional fault from a). Uniform extension where  $\sigma_2$  and  $\sigma_3$  are subequal and differential stress is low



c) Vein formation when rocks under low differential stress experience an increase in fluid pressure  $P_f$ , causing tensile failure

**Figure 4.31** Mohr diagrams for the extensional refracture of steep faults and dykes.

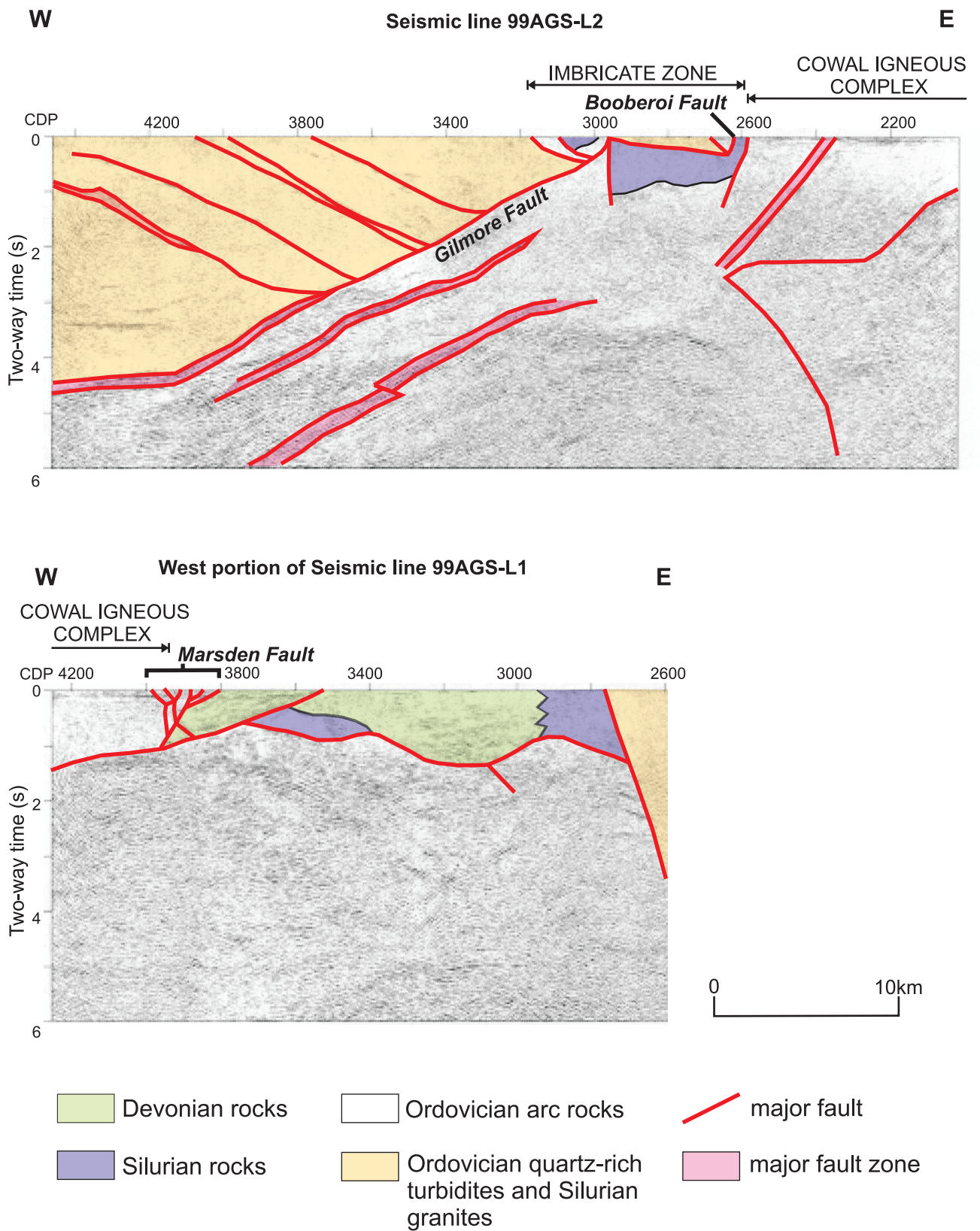


**Figure 4.32** Interpreted migrated shallow (6s TWT) seismic profiles across the western (99AGS-L2) and eastern (99AGS-L1) parts of the Junee-Narromine Volcanic Belt. Vertical scale equal to horizontal scale, assuming average crustal velocity of 6000 m/s. Simplified from Glen et al., 2002.

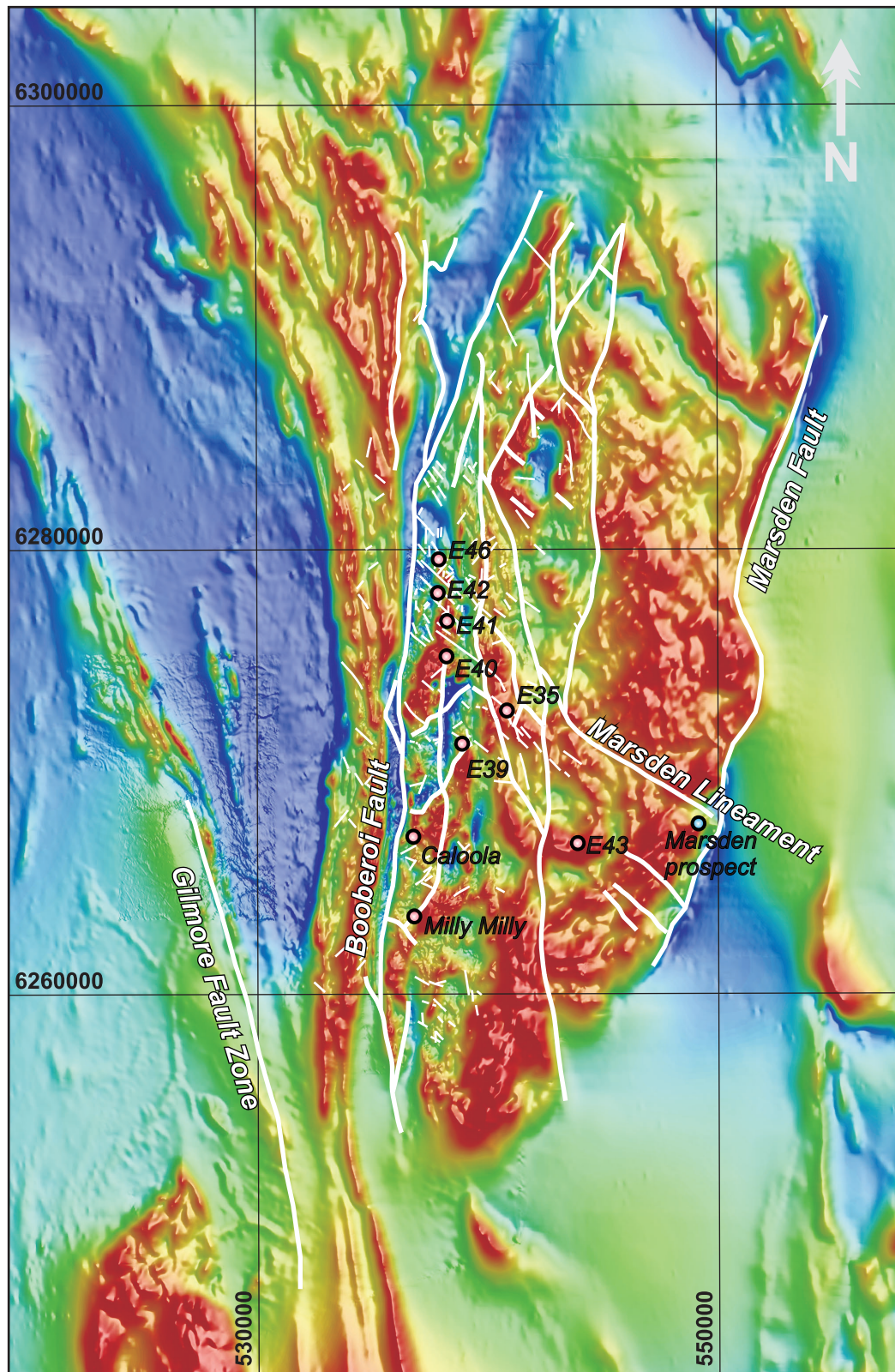


**Figure 4.33** Aeromagnetic survey over the Cowal Igneous Complex. Selected lineaments marked from Pittard (2006): “major” interpreted faults and lineaments marked by thick white lines, “minor” interpreted faults and lineaments marked by thin white lines. Prospects owned by Barrick Gold of Australia Ltd. marked by pink circles, the Marsden prospect (blue circle) owned by Newcrest Mining Ltd. Compare to Cowal Igneous Complex geology map, Figure 2.8. Geophysical image courtesy of Barrick Gold of Australia Ltd.

## **CHAPTER 5: GEOCHEMICAL ZONATION AT E42**

### **5.1 Introduction**

Several alteration styles exist at E42, differing in mineral assemblages and spatial distribution. The alteration zonation is well documented in several papers, reports, and theses, including Miles and Brooker (1998), McInnes (2003), and Strickland (2005). The principal characteristics of the alteration assemblages defined in these studies are summarized below, and in Table 5.1. At E42 there are four distinct alteration assemblages, which are, in interpreted order of formation: chlorite-carbonate-hematite  $\pm$  epidote, chlorite-carbonate-pyrite, K-feldspar-quartz, and lastly sericite-quartz  $\pm$  carbonate. The latter is structurally controlled and most intensely developed adjacent to high fluid flow faults and veins. Alteration assemblage mineralogy is a function of element mobility, which is reflected in the variations in K-, Ca-, and Na-metasomatism. Chemical alteration indices, such as the alteration box plot of Large et al. (2001), can be used to define alteration trends in hydrothermal systems. Horizontal and vertical zonation of precious metals, base metals, and potential pathfinder elements within wallrock adjacent to high-grade veins at E42 are also defined, and may be used as deposit-scale vectors to ore.

### **5.2 E42 Deposit-scale Alteration**

#### **5.2.1 Chlorite-Carbonate-Hematite $\pm$ Epidote**

A weak to moderately pervasive alteration assemblage (“background propylitic” alteration of McInnes, 2003) is developed in all lithological units at E42 except post-mineral dykes, and comprises predominantly chlorite-carbonate(calcite)  $\pm$  hematite/magnetite  $\pm$  epidote  $\pm$  albite  $\pm$  actinolite  $\pm$  prehnite  $\pm$  K-feldspar (Miles and Brooker, 1998; McInnes, 2003). Alteration is characterized by selective pervasive replacement of plagioclase and mafic minerals by albite and chlorite, respectively (McInnes, 2003). Within the Upper Volcaniclastic unit, this alteration stage is characterized by selective pervasive chlorite-calcite (McInnes, 2003)  $\pm$  sericite (Bastrakov, 2000; this study). The diorite sill contains well developed epidote as part of this alteration assemblage (Miles and Brooker, 1998), and is characterized by chlorite-epidote-carbonate-albite  $\pm$  magnetite alteration (Ashley, 2003b).

Chlorite-carbonate-hematite  $\pm$  epidote alteration is interpreted as representing the earliest and most regionally extensive alteration phase at E42, either related to the emplacement of diorite/granodiorite intrusions in the Cowal Igneous Complex, or to low grade regional metamorphism (Miles and Brooker, 1998). It is overprinted by all other alteration assemblages as well as gold mineralization.

### **5.2.2 Chlorite-Carbonate-Pyrite**

The chlorite-carbonate-pyrite (“advanced propylitic” alteration of McInnes, 2003) overprints the chlorite-carbonate(calcite)-hematite  $\pm$  epidote phase, and is characterized by black chlorite and pyrite. This alteration assemblage consists of chlorite-carbonate(calcite)-pyrite  $\pm$  hematite  $\pm$  leucoxene  $\pm$  K-feldspar  $\pm$  sericite (McInnes, 2003). It affects all rock units at E42 except in post-mineral dykes, and is predominantly found as selective pervasive alteration, irregular veinlets, and clotty disseminations (Miles and Brooker, 1998) proximal to structural fluid conduits which are commonly gold-bearing (McInnes, 2003).

Timing relationships relative to other alteration phases at E42 are difficult to resolve due to a paucity of spatial associations, but observations from the current study suggest sericite-quartz  $\pm$  carbonate alteration (see below) overprints black chlorite-carbonate-pyrite alteration in the Upper Volcaniclastic unit. An association with earliest fault development as well as gold mineralization has been suggested for the advanced propylitic alteration phase by McInnes (2003). In the current study, this alteration is defined as pre-sericite-quartz  $\pm$  carbonate alteration due to spatial relationships mapped in the open pit. This is in contrast to Miles and Brooker (1998), who describe the black chlorite-carbonate-pyrite alteration assemblage as overprinting the sericite-dominated alteration phase.

### **5.2.3 K-feldspar-Quartz**

The K-feldspar-quartz alteration phase is weakly developed and is restricted almost exclusively to the trachyandesite lava unit (Miles and Brooker, 1998). It is characterized by irregular patches of pink-red K-feldspar and grey quartz which are sporadically associated with epidote alteration, and rare mm-scale haloes developed along gold-bearing vein walls (McInnes, 2003). This alteration assemblage overprints background propylitic alteration, but the timing of development remains unconstrained with respect to black chlorite-carbonate-pyrite and sericite-dominated alteration.

The almost exclusive spatial restriction of this alteration assemblage to the trachyandesite lava suggests that host rock composition is a determining factor in the development of K-feldspar-quartz haloes and irregular patches.

#### **5.2.4 Sericite-Quartz $\pm$ Carbonate**

Sericite-quartz  $\pm$  carbonate alteration (“phyllitic” alteration of McInnes, 2003) commonly overprints other alteration assemblages at E42, and is characterized by extensive sericitization and destruction of original rock textures and older magnetic susceptibility (McInnes, 2003). The alteration assemblage consists of sericite-quartz  $\pm$  carbonate(ankerite)  $\pm$  pyrite  $\pm$  leucoxene  $\pm$  albite  $\pm$  chlorite  $\pm$  illite, and is found in all rocks at E42 except post-mineral dykes, but is most extensively developed in the Upper Volcaniclastic unit (McInnes, 2003). Sericite-dominated alteration is most commonly formed as fine-grained haloes to subvertical fault zones (Figure 5.1a), quartz-sulfide-bearing veins, fault-hosted hydrothermal breccias, and intervals of abundant ankerite veins that have reopened subvertical faults and veins (McInnes, 2003; this study). Haloes typically grade into background propylitic assemblages over cm to m-scales. Subvertical sericite-dominated alteration haloes are associated with gold-bearing and barren faults and veins; the post-gold diorite dyke, for example, displays late barren ankerite veins with sericite haloes (McInnes, 2003). Sericite-dominated alteration haloes are thinner (mm-scale) and less well developed along inclined gold-bearing veins as compared to subvertical veins and faults (Figure 5.1b). In general, sericite-quartz  $\pm$  carbonate alteration tends to be more poorly developed with depth at E42 (Miles and Brooker, 1998; McInnes, 2003). Relative timing of this alteration assemblage and the K-feldspar-quartz assemblage is difficult to constrain as they are generally spatially distinct.

Sericite-quartz  $\pm$  carbonate alteration haloes are better developed in the Upper Volcaniclastic unit than other rock types, probably due to its clastic, more permeable nature compared to the coherent trachyandesite and diorite units where fluid flow is restricted along fractures. Inclined veins do not show the same intense, texturally destructive sericite development as seen along steeply dipping fault parallel veins. Sericite-quartz  $\pm$  carbonate alteration is interpreted as the youngest alteration to affect the E42 deposit (McInnes, 2003; current study).

## **5.3 Geochemical Zonation of Sericite Alteration Haloes**

A characteristic feature of many hydrothermal ore deposits is the predictable lateral and vertical distribution of minerals and metals (e.g. Buchanan, 1981; Silberman and Berger, 1985; Guilbert and Park, 1986; Hedenquist et al., 2000; Albinson et al., 2001). Zonation may be recognized both on district and outcrop scale, and provides clues about the geochemical and spatial evolution of a hydrothermal system. Geochemical zonation may be defined both within vein mineral assemblages and wallrock alteration assemblages, although patterns in the latter can be highly irregular and more difficult to characterize (Silberman and Berger, 1985). The current study identifies variations in elemental compositions both laterally and vertically along sericite-dominated alteration haloes associated with gold mineralized structures at E42. The characterization of deposit-scale geochemical zonation patterns will aid in defining vectors to ore, and may be applicable to larger-scale, regional mineral exploration.

### **5.3.1 Sampling and Analytical Methods**

Wallrock surrounding subvertical faults and fault parallel gold-bearing veins was sampled at regular lateral intervals, from the most intensely sericitized out to background propylitic alteration. This provides a lateral sample distribution for sericite-quartz  $\pm$  carbonate alteration haloes at E42. Comparing samples from benches of different elevations in the open pit and samples from different depths in drillcore provides a vertical distribution for sericite-dominated alteration haloes. Intervals vary between sample locations and were chosen depending on the width of the alteration halo and available exposure. Figure 5.1a, for example, shows the location of one group of samples from RL1167 in the open pit. Vein material in the wallrock was avoided during sampling. Sericite alteration haloes associated with inclined gold-bearing veins were consistently too thin to sample (e.g. Figure 5.1b) therefore all samples presented here are from haloes to subvertical fault parallel structures.

Rock samples were initially shipped to SGS Laboratories in West Wyalong, where they were crushed using a low chrome steel mill and analyzed for Au using fire assay fusion with atomic absorption spectroscopy (AAS). Samples crushed by chrome steel mills likely have excess Cr values, but Cr was not used in the geochemical discussion below. Further details on the methodology used by SGS Laboratories are available at

<<http://www.geochem.sgs.com/geochem>>. Pulps returned from the SGS Laboratories were then shipped to ALS Chemex in Orange and analyzed by 4 acid “near total” digestion for 48 elements (ALS Chemex code ME-MS61). This method uses both inductively coupled plasma emission spectroscopy (ICP-AES) and inductively coupled plasma mass spectroscopy (ICP-MS). Hg was added to the multielement package by a separate digestion method (ALS Chemex code Hg-MS42). Further details on the methodology used by ALS Chemex are available at <<http://www.alsglobal.com/Mineral/DivisionProfile.aspx>>. Appendix B contains the multielement data from samples taken over the course of this study, and Table 5.2 shows the elemental detection limits.

### **5.3.2 Compositional Variations**

Initially, sericite alteration haloes were sampled in the Upper and Lower Volcaniclastic units, the trachyandesite lava, and the diorite, with the majority of samples taken from the Upper Volcaniclastic unit. To accurately delineate and compare geochemical variations within the alteration assemblages of the volcaniclastic rocks, this unit must be compositionally homogeneous. Immobile trace elements are used to distinguish compositional variations in volcanic rocks (e.g. Winchester and Floyd, 1977; Pearce, 1996). Plotting Zr/TiO<sub>2</sub> versus Nb/Y classifies the volcaniclastic units at E42 as basalt to andesite in composition (Figure 5.2). The volcaniclastic rocks display juvenile volcanic clasts mixed with other volcanic and minor non-volcanic clasts (see Chapter 3) and are interpreted as medial to distal from a volcanic centre (cf. Simpson and Cooke, 2006), but are included here in the immobile trace element plot for coherent volcanic rocks for ease of comparison. This plot shows that the volcaniclastic rocks are, in general, compositionally homogeneous and thus geochemical variations within different alteration haloes are largely unaffected by protolith compositions. Samples from the lava and diorite are not included in the data presentation and discussion below, as there are too few samples from each of these units to properly define geochemical variations.

### **5.3.3 Alteration Indices**

Different alteration indices are used to measure the intensity of diagenetic and hydrothermal alteration associated with ore deposits. Two of these, the Ishikawa alteration index (AI; Ishikawa et al., 1976) and the chlorite-carbonate-pyrite index (CCPI), measure the

intensity of chlorite, carbonate, sericite, and pyrite alteration, and are plotted against each other as the “alteration box plot” of Large et al. (2001). The upper right half of the alteration box plot is a graphical representation of hydrothermal alteration associated with ore deposits (Figure 5.3a), whereas the lower left half represents diagenetic alteration (Large et al., 2001). Although Large et al. (2001) used the alteration box plot to characterize different alteration trends within volcanic rocks associated with sea-floor massive sulfide deposits, the same methodology has been applied to epithermal ore deposits to understand the relationship between mineralogy and intensity of alteration (Gemmell, 2007).

In this study, samples from the E42 deposit are distinguished based on distance from gold-bearing structures and the relative width of the accompanying sericite-dominated alteration halo. These samples are referred to as distance-normalized (DN) and are assigned a numerical value by dividing the distance of the sample from gold-bearing structures by the width of the alteration halo. Normalization allows the comparison of all samples across the deposit, regardless of individual halo widths. DN values distinguish proximal-to-vein samples (<1.0), medial samples (1.0-5.0), and distal or “background altered” samples (>5.0, Figure 5.3b).

Samples most distal to veins (filled diamond symbols) represent the least altered rock compositions at E42, and plot almost exclusively in the “least altered” box of the alteration box plot (Figure 5.3b). Although there is some scatter, distal-to-vein samples display a linear trend from the “least altered” box to the top right “chlorite-pyrite” corner of the plot (Figure 5.3b). This is consistent with early alteration found at E42 characterised by background propylitic and patchy black chlorite-carbonate-pyrite alteration assemblages. Two major components of these alteration assemblages in the volcanoclastic units are chlorite and pyrite, which explain the observed trend.

Proximal- and medial-to-vein samples are represented by empty and filled triangular symbols, respectively. Proximal samples exhibit a negative trend line approaching the “sericite” point along the left side of the alteration box plot (Figure 5.3b). This is consistent with the sericite-quartz ± carbonate alteration assemblage associated with fluid flow structures throughout the deposit, characterized predominantly by sericite in the Upper Volcanoclastic unit. Therefore, there are two distinct hydrothermal alteration trends visible in

rocks from E42, one from background alteration and the other from alteration associated with structures that experienced high fluid flow.

#### 5.3.4 Horizontal Zonation

When hydrothermal alteration is accompanied by notable volume or mass changes in the country rock, direct comparisons between altered and unaltered rock types are not possible (e.g. Gresens, 1967; Warren et al., 2007). As calculating the exact mass changes for each element is beyond the scope of this study, the effects of mass transfer will be examined qualitatively. Using graphical methods proposed by Warren et al. (2007), mass transfer can be related to the associated hydrothermal mineral assemblages using molar element ratios calculated from whole-rock geochemical data. This approach is similar to the Pearce element ratio technique (Stanley and Madiesky, 1994) where effects of volume changes are eliminated by comparing molar ratios with the same denominator, allowing for the delineation of mineral zonation. For the purposes of these calculations, aluminum is assumed to be immobile during hydrothermal alteration (Stanley and Madiesky, 1994; Warren et al., 2007).

Geochemical and mineralogical gradients due to hydrothermal alteration can be identified by plotting  $K/Al$  (molar) versus  $(2Ca+Na+K)/Al$  (molar) (Figure 5.4). Samples are plotted as distance-normalized groups to delineate the patterns of K-, Ca-, and Na-metasomatism with respect to distance from veins. In general, the distal-to-vein samples ( $DN > 5.0$ ) show a tendency for lower K values than the proximal- and medial-to-vein samples, although there is some scatter as well as overlap in the dataset (Figure 5.4). This is equivalent to the sericite-dominated alteration assemblage immediately adjacent to veins having slightly higher K concentrations than the background alteration assemblage. Addition of K may be due to fluid flow along these structures forming K-feldspar (adularia in veins), K-mica (sericite in alteration halo), and K-rich clays (possible illite in alteration halo). Proximal-to-vein samples ( $DN < 1.0$ ) plot along a horizontal trend (Figure 5.4). The horizontal trend indicates there is no K loss or gain within the sericite-dominated alteration halo and the lateral spread of the trend indicates there is variable intensity of Ca- and Na-metasomatism affecting the proximal-to-vein samples (Figure 5.4). Some of these samples plot along the line of slope 1, indicating nearly complete removal of Ca and Na. A few samples plot to the right of the plagioclase-albite-K-feldspar line (Figure 5.4), potentially due

to the presence of Ca in calcite and mafic minerals in the background altered host rocks and/or carbonate veinlets. Plotting the effects of K-, Ca-, and Na-metasomatism (molar  $K/(2Ca+Na+K)$ , after Warren et al., 2007) against the true horizontal distance from veins (Figure 5.5a) displays an overall decrease in metasomatism away from veins, although there is significant scatter. This scatter would likely be less pronounced in a larger scale geochemical sample set, which was not attainable during the current study. The negatively sloped trend line in Figure 5.5a may be attributed to decreasing K concentrations and/or increasing Ca and Na concentrations with distance from the vein, the specific geochemical details of which are beyond the scope of this study, which is consistent with observations from Figure 5.4.

Given this tendency for K-gain and/or Ca- and Na-loss closer to gold-bearing structures, subsequent examination of metals and potential pathfinder element concentrations versus molar  $K/(2Ca+Na+K)$  values broadly defines elemental zonation at E42. In general, concentrations of Au, Ag, As, Hg, Sb, Tl, Cu, Pb, and Zn all increase with K-gain and/or Ca- and Na-loss, i.e. closer to high fluid flow structures (Figure 5.6). A small number of samples plot as outliers from the general trend, at much higher concentrations than the surrounding sample population (e.g. As, Pb, and Zn plots, Figure 5.6). Some elemental concentrations display significant scatter in their plots, for example Ag and Cu (Figure 5.6), although even when considering outlier samples general trends can be defined. Au, As, Sb, Pb, Zn, and possibly Ag and Cu, display a jump in elemental concentrations at a  $K/(2Ca+Na+K)$  molar value of approximately 0.8-0.9, which are values proximal-to-vein (Figure 5.6). In addition to the proximal-to-vein peak, there is a smaller peak exhibited by Ag, As, Hg, Sb, Pb, Zn, and possibly Cu, at a value of approximately 0.4-0.5 for  $K/(2Ca+Na+K)$  molar. Tl and Sb show an overall positive trend with increasing values of  $K/(2Ca+Na+K)$ , although there is significant scatter in the datasets (Figure 5.6).

High elemental concentrations proximal to veins (values of 0.8-0.9 for  $K/(2Ca+Na+K)$  molar) are likely due to the direct influence of fluid compositions, and subsequent vein fill, on the adjacent wallrock. Pb and Zn are present in gold-bearing veins at E42 as galena and sphalerite, with scarce lead telluride (altaite; Bastrakov, 2000). Cu may be present in the wallrock as fine disseminated chalcopyrite associated with pyrite from black chlorite-carbonate-pyrite and sericite-dominated alteration assemblages. Au and Ag are

present in veins as free gold, refractory gold in pyrite, and as the silver and gold-silver tellurides hessite and petzite, respectively (Bastrakov, 2000). Sb and As are common substitutes for sulfur in sulfides, and Hg is a pathfinder element that is commonly closely associated with gold and silver. In tellurides, Sb and Hg are known to substitute for the differentiating components (e.g. As or Au), and Sb is known to substitute for Te in rare cases (e.g. in montbrayite). Tl has been recognized as an element commonly concentrated in altered host rocks of various ore deposits, including epithermal vein systems, and shows a distinctive positive correlation to K in silicate minerals (Gemmell et al., 2006). The small peak in elemental concentrations for Ag, As, Hg, Sb, Pb, Zn, and possibly Cu, at a value of approximately 0.4-0.5 molar for  $K/(2Ca+Na+K)$  may be due to the presence of microveinlets in the wallrock. Two lithological planes of weakness are generally associated with vein formation and hydrothermal alteration. A change in rock strength occurs at the vein-wallrock interface and at the interface between the vein alteration halo and the background altered host rock. Microveinlets subparallel to the main vein may form along the sericite-dominated alteration halo interface, potentially accounting for the smaller peak observed at values of 0.4-0.5  $K/(2Ca+Na+K)$  molar. Background altered samples (filled diamond symbols) are not found with  $K/(2Ca+Na+K)$  molar values  $>0.53$  (Figure 5.5a), suggesting that an alteration boundary likely exists between 0.4 and 0.6, which supports the microveinlet theory presented here. Individual anomalous elemental concentrations, such as those shown by As, Pb, Zn, could be due to nugget effects in the sample, possibly due to a thin vein or disseminated mineralization in the wallrock.

Metals and potential pathfinder elements plotted relative to horizontal distance from gold-bearing veins display correlation trends with negative slopes, and with no obvious or consistent peaks (Figure 5.7). Au, Cu, and Pb concentrations drop off significantly after distances greater than one metre laterally from high-grade veins. Ag, As, Hg, Sb, Tl, and Zn tend to decrease in concentration more gradually over 5-7 metres, and therefore define slightly larger haloes to gold-bearing veins (Figure 5.7). These negatively sloping trends are similar to those seen over greater horizontal distances (100s of metres) at other low-sulfidation epithermal Au-Ag deposits such as El Peñón (Chile), Mt. Muro (Indonesia), and Sleeper (Nevada) (Warren et al., 2007). Two notable differences to the patterns observed at E42 are slightly positive slopes for Sb and Zn with increasing distance from the vein ore

bodies at El Peñón. This is attributed in part to hypogene and supergene vertical zonation of these elements, respectively (Robbins, 2000; Warren et al., 2004). In summary, the highest concentrations of precious metals, base metals, and pathfinder elements are observed in rocks that show the greatest levels of K-gain and/or Ca- and Na-loss, which are rocks commonly proximal to ore bodies.

### **5.3.5 Vertical Zonation**

Vertical elemental zonation in hydrothermal vein systems is a widespread and well-documented feature (e.g. Buchanan, 1981; Guilbert and Park, 1986; Albinson et al., 2001). One generalized model for this zoning is the “Emmons reconstructed vein” (Guilbert and Park, 1986) which suggests that metals such as Mo, W, and Sn will precipitate at deep levels, early in the development of the system, from high temperature fluids (hypothermal). These are followed by Cu, and then Pb, Zn, Mn, and Ag as the fluids rise and cool (mesothermal). With continued rising and cooling (epithermal), fluids typically precipitate precious and volatile metals such as Au, Sb, and Hg. This idealised model is generally accurate in typifying the vertical metal zonation of hydrothermal systems, but there are many exceptions (e.g. Silberman and Berger, 1985).

At E42, the available geochemical sampling extends to just over 400m depth due to the limits of drilling at the deposit. Documented vertical metal zonation patterns for three end members of low sulfidation precious metal and base metal-rich epithermal deposits in Mexico are known to extend to depths approaching 2km (Albinson et al., 2001). Although there is a much shallower range of geochemical samples available at E42, some precious metal, base metal, and potential pathfinder elemental zoning patterns are observed (Figure 5.8). Similar nugget effects to those seen with samples compared horizontally are seen in the vertical zonation sample sets, see the As, Pb, and Zn plots (Figure 5.8). In general, concentrations of Au, Ag, As, Hg, Sb, Tl, Cu, Pb, and Zn all exhibit decreasing values with depth (Figure 5.8). This is consistent with an overall K-loss and/or Ca- and Na-gain with depth (Figure 5.5b) and with the association of lower precious metal, base metal, and pathfinder elemental concentrations with these K-, Ca-, and Na-metasomatic trends (Figure 5.6). In the case of Au, Cu, Pb, and Zn, there is a distinct drop in elemental concentrations at depths of approximately 50-100m (Figure 5.8). In contrast, Ag, As, Hg, Sb, and Tl exhibit a more gradual decrease in concentration with depth. At a depth of approximately 400m, there

appears to be a slight increase in the concentrations of Ag, As, Sb, Tl, and possibly Au, but this may be an artefact of a larger sample set at this depth relative to the paucity of samples taken in the interval from 200-400m (Figure 5.8). All of the whole rock samples in this study were taken from below the base of weathering, and therefore below the extents of economic supergene gold mineralization (Bywater pers. comm., 2006). The direct correlation of depth with decreasing elemental concentrations may be indicative of a root zone to the mineralized supergene blanket within the primary rock, which decreases with depth as the effects of weathering and oxidization also decrease. Alternatively, this upward increase in precious metal, base metal, and pathfinder element concentrations may represent the base of a classic primary fluid alteration plume, the top of which was removed by erosion, and the remainder of which was subsequently oxidized.

### **5.3.6 Interpretation**

At E42 several geochemical and mineralogical patterns in the host rocks provide vectors toward economic veins. The development of sericite-quartz  $\pm$  carbonate alteration haloes, though not exclusively associated with ore bodies, provide evidence for faults and veins which experienced high fluid flow. Sericite-dominated alteration haloes associated with high grade veins tend to show slightly elevated concentrations of K which is accompanied by variable Ca- and Na-loss. This metasomatic pattern is observed in many other low sulfidation epithermal Au-Ag deposits (e.g. Warren et al., 2007). K-gain and/or Ca- and Na-loss in alteration haloes is best developed proximal to high grade structures, as well as high up in the E42 hydrothermal system. This trend in K-, Ca-, and Na-metasomatism is also associated with higher concentrations of precious metals, base metals, and potential pathfinder elements, indicating that concentrations decrease with horizontal distance from high grade veins, and with increased depth within the E42 system. The positive correlation observed between Tl and K enrichment suggests that Tl may substitute for K in the K-rich minerals (adularia, sericite, and possible illite) due to similar ionic charges and radii (Gemmell, 2007). Similar elemental zonation patterns are seen at larger scales (10s to 100s of metres) at El Peñón, Mt. Muro, and the Sleeper deposit; all well documented low sulfidation epithermal Au-Ag deposits (Warren et al., 2007). A direct relationship between epithermal mineralization and K-gain has been observed and defined in many epithermal deposits and models of Au deposition (e.g. Reed and Spycher, 1985;

Warren et al., 2007). There is a tendency in the alteration haloes at E42 to display these same patterns, with K-gain and/or Ca- and Na-loss as gold-bearing veins are approached, although the geochemical trends are not unequivocal. In general, however, varying degrees of K-, Ca- and Na-metasomatism can be graphically represented using the molar element ratio diagram of K/Al versus  $(2Ca+Na+K)/Al$  after Warren et al. (2007), which can provide vectors toward zones more likely to exhibit epithermal Au mineralization.

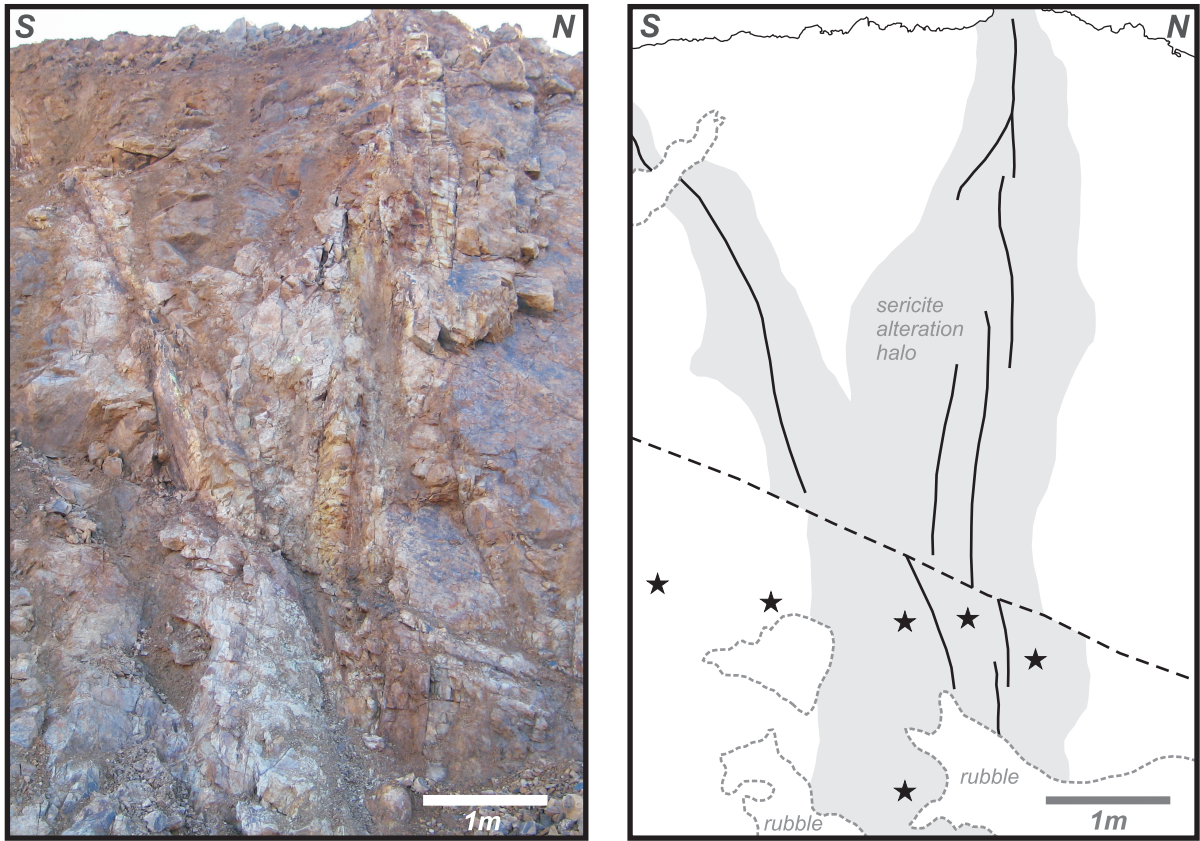
<b>Alteration Assemblage</b>	<b>Mineralogy</b>	<b>Predominant Rock Type</b>	<b>Distinguishing Characteristics</b>
chlorite-carbonate-hematite ± epidote  “background propylitic” <i>McInnes, 2003</i>	chlorite-carbonate(calcite) ± hematite/magnetite ± epidote ± albite ± actinolite ± prehnite ± K-feldspar	all rock types except post-mineral dykes	- selective pervasive replacement of plagioclase and mafic minerals by albite and chlorite, respectively  - selective pervasive chlorite-calcite± sericite in Upper Volcaniclastic unit  - well developed epidote in diorite
chlorite-carbonate-pyrite  “advanced propylitic” <i>McInnes, 2003</i>	chlorite-carbonate(calcite)-pyrite ± hematite ± leucoxene ± K-feldspar ± sericite	all rock types except post-mineral dykes	- characterized by black chlorite and pyrite  - found in irregular veinlets and clotty disseminations
K-feldspar-quartz	K-feldspar-quartz ± epidote	trachyandesite lava	- found as irregular patches of pink-red K-feldspar and grey quartz, sporadically associated with epidote  - rare mm-scale haloes to gold bearing veins
sericite-quartz ± carbonate  “phyllic alteration” <i>McInnes, 2003</i>	sericite-quartz ± carbonate (ankerite) ± pyrite ± leucoxene ± albite ± chlorite ± illite	all rock types except post-mineral dykes  most extensively developed in Upper Volcaniclastic unit	- fine grained haloes to subvertical faults, gold-bearing veins, fault-hosted hydrothermal breccias, and ankerite veins which reopened subvertical faults and veins

**Table 5.1** Summary of alteration assemblages, their predominant rock types, and distinguishing characteristics.

Element	Detection limit	Element	Detection limit
Ag	0.01 ppm	Nb	0.1 ppm
Al	0.01 %	Ni	0.2 ppm
As	0.2 ppm	P	10 ppm
Ba	10 ppm	Pb	0.5 ppm
Be	0.05 ppm	Rb	0.1 ppm
Bi	0.01 ppm	Re	0.002 ppm
Ca	0.01 %	S	0.01 %
Cd	0.02 ppm	Sb	0.05 ppm
Ce	0.01 ppm	Sc	0.1 ppm
Co	0.1 ppm	Se	1.0 ppm
Cr	1.0 ppm	Sn	0.2 ppm
Cs	0.05 ppm	Sr	0.2 ppm
Cu	0.2 ppm	Ta	0.05 ppm
Fe	0.01 %	Te	0.05 ppm
Ga	0.05 ppm	Th	0.2 ppm
Ge	0.05 ppm	Ti	0.005 %
Hf	0.1 ppm	Tl	0.02 ppm
In	0.005 ppm	U	0.1 ppm
K	0.01 %	V	1.0 ppm
La	0.5 ppm	W	0.1 ppm
Li	0.2 ppm	Y	0.1 ppm
Mg	0.01 %	Zn	2.0 ppm
Mn	5.0 ppm	Zr	0.5 ppm
Mo	0.05 ppm	Hg	0.005 ppm
Na	0.01 %	Au	0.01 ppm

**Table 5.2** Detection limits for multielement geochemical data, from ALS Chemex. Further details available at <<http://www.alsglobal.com/Mineral/DivisionProfile.aspx>>

a)



b)

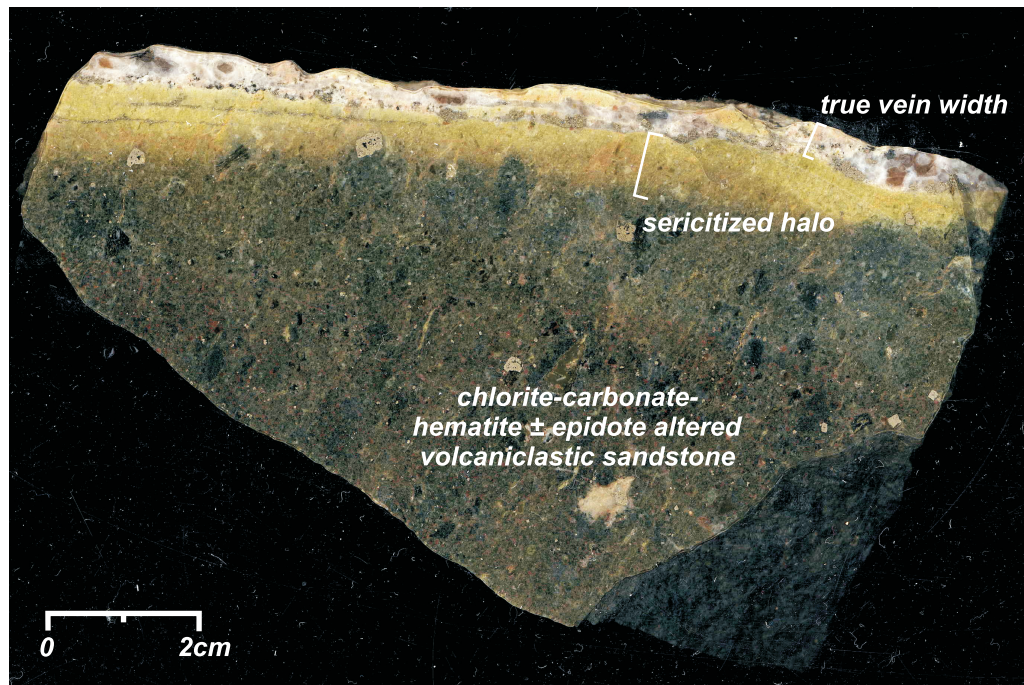


**Figure 5.1** a) Fault zone from RL1167 showing intense sericitization. Geochemical sample locations marked by stars. b) Gold-bearing vein of the inclined population, displaying a mm-scale sericite-dominated alteration halo.

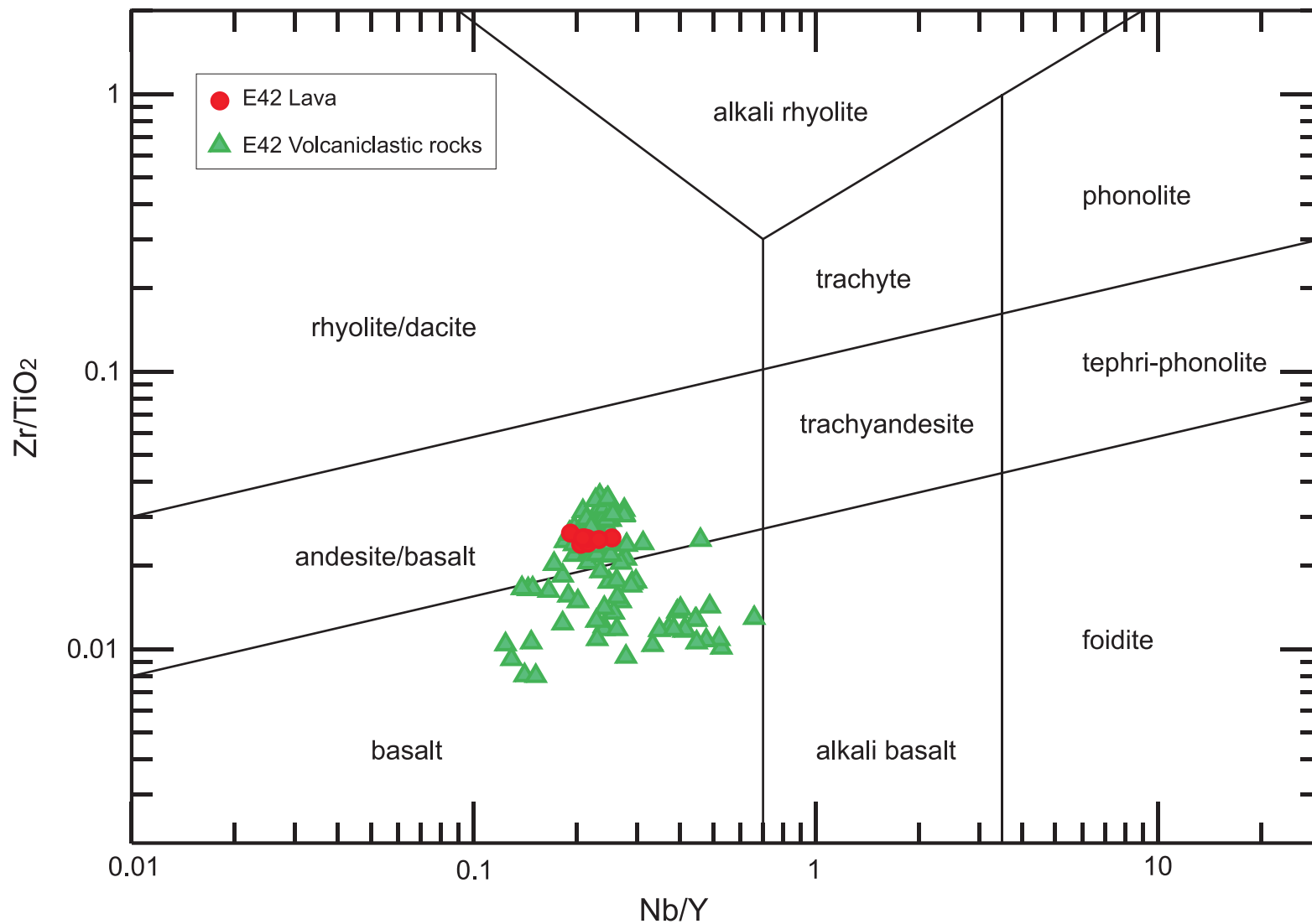


**Figure 5.2** Modified Winchester and Floyd (1977)  $Zr/TiO_2$  versus  $Nb/Y$  diagram (Pearce, 1996) for the trachyandesite lava and the Upper and Lower volcaniclastic rocks at E42.

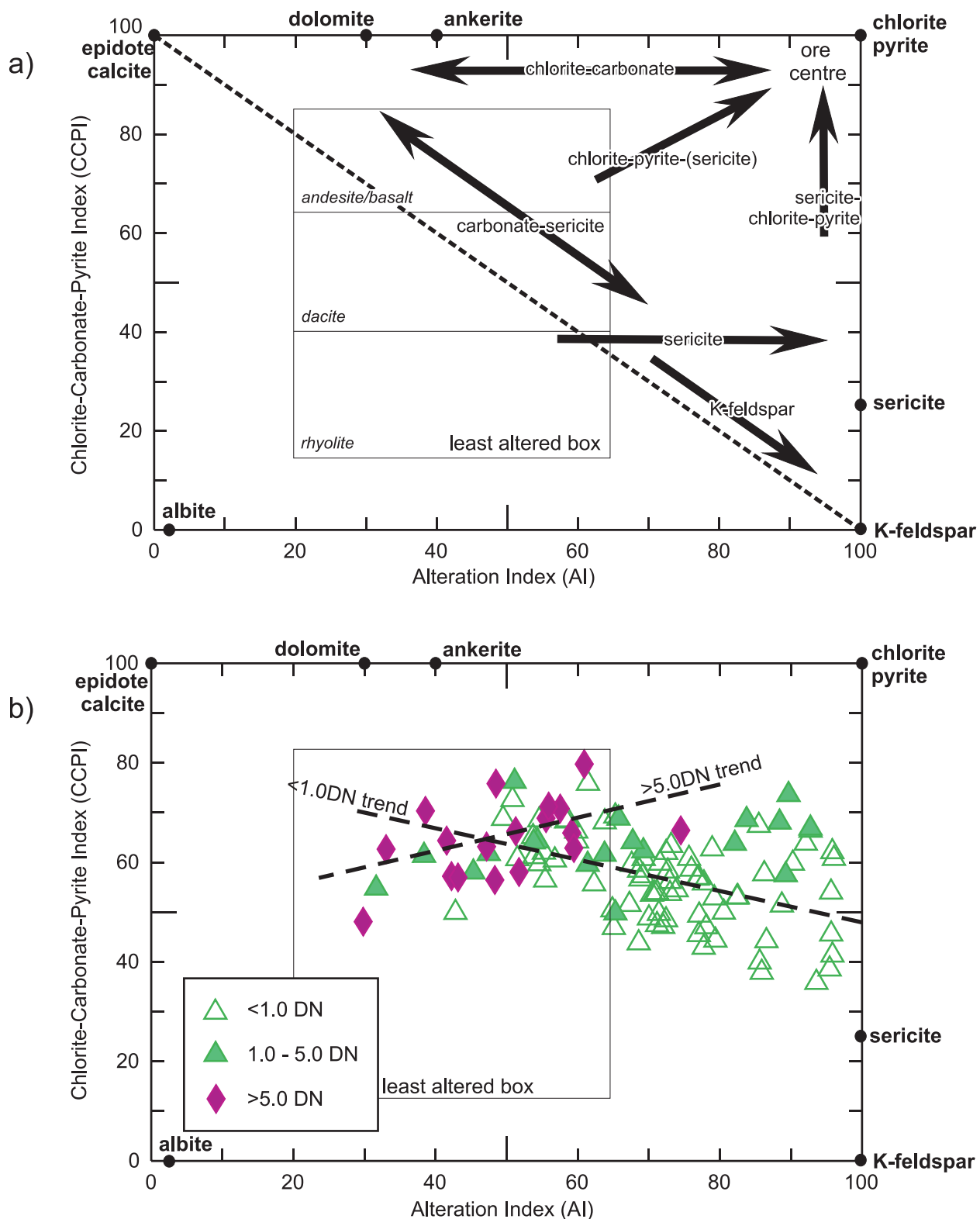


**Figure 5.3** a) Alteration index (AI)-chlorite-carbonate-pyrite index (CCPI) box plot showing principal hydrothermal alteration trends in rocks associated with ore deposits, after Large et al. (2001).  $AI = 100(MgO+K_2O)/(MgO+K_2O+Na_2O+CaO)$ ,  $CCPI = 100(FeO+MgO)/(FeO+MgO+Na_2O+K_2O)$ . b) Alteration box plot (CCPI vs. AI) for distance-normalized geochemical samples from E42 (distance normalization, DN = distance from vein/width of alteration halo). Trendlines calculated by linear regression using Microsoft Excel software.

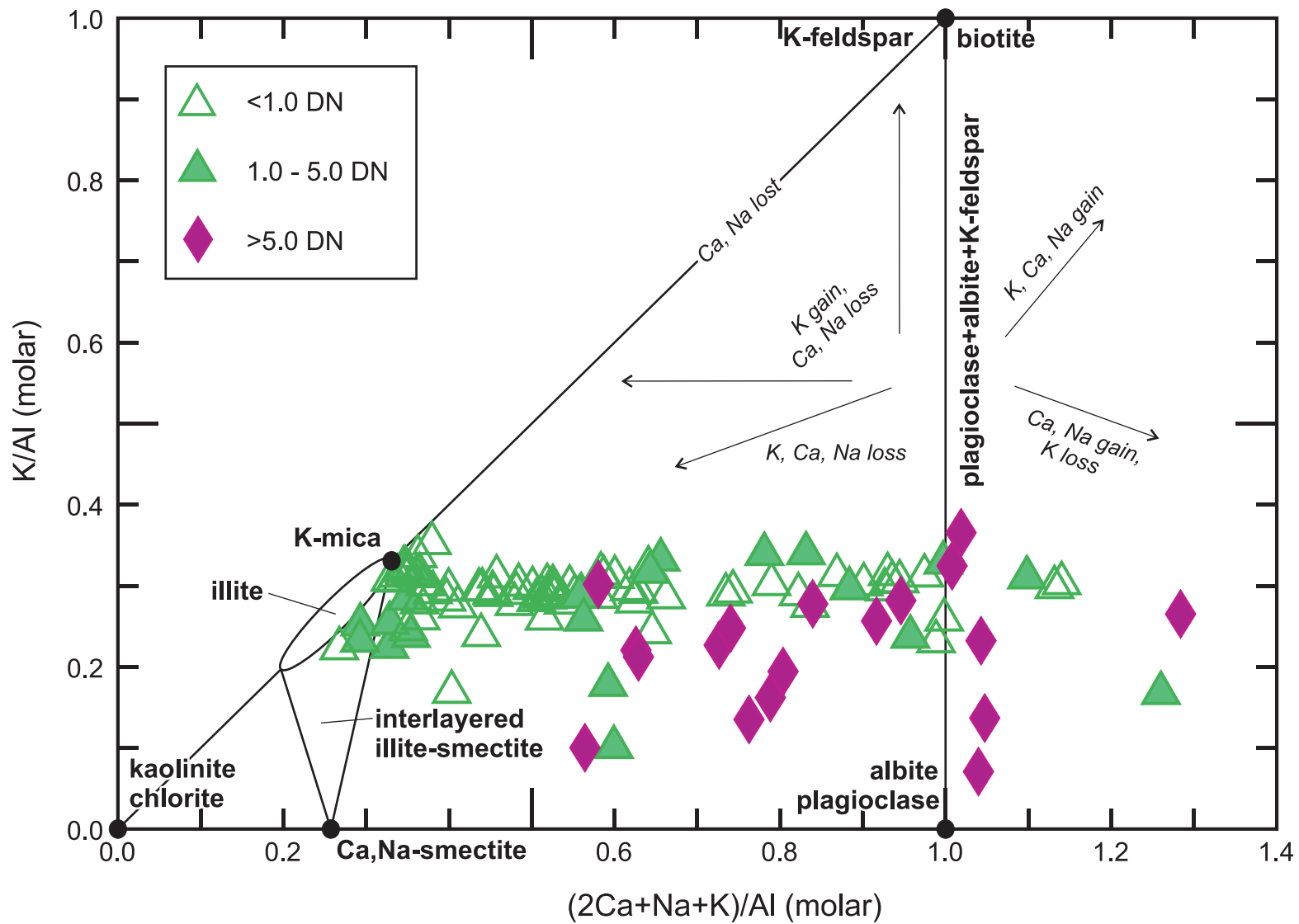


**Figure 5.4** Molar element ratio plot of K/Al versus (2Ca+Na+K)/Al for distance-normalized geochemical samples from E42 (distance normalization, DN = distance from vein/width of alteration halo). Plot after Warren et al. (2007). Mass transfer processes shown with arrows.

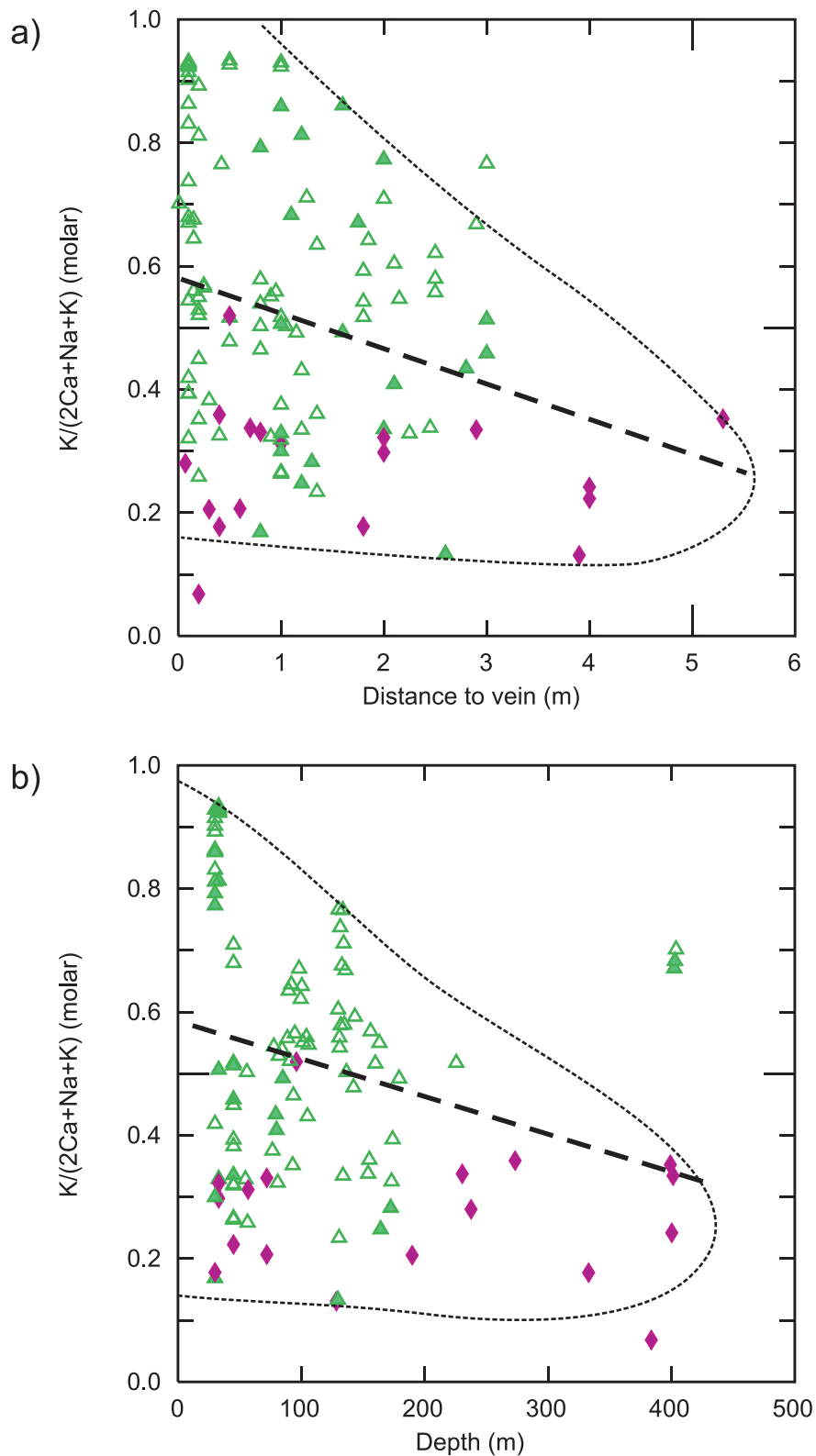


**Figure 5.5** Molar  $K/(2Ca + Na + K)$  values versus **a)** distance from gold bearing veins and **b)** depth. All samples are volcanoclastic rocks, with filled diamond symbols representing “background altered” samples, open triangle symbols representing “sericite altered” samples, and filled triangle symbols representing the transition zone between alteration assemblages. Trendlines calculated by linear regression using Microsoft Excel software. Best-fit envelopes interpreted by hand.

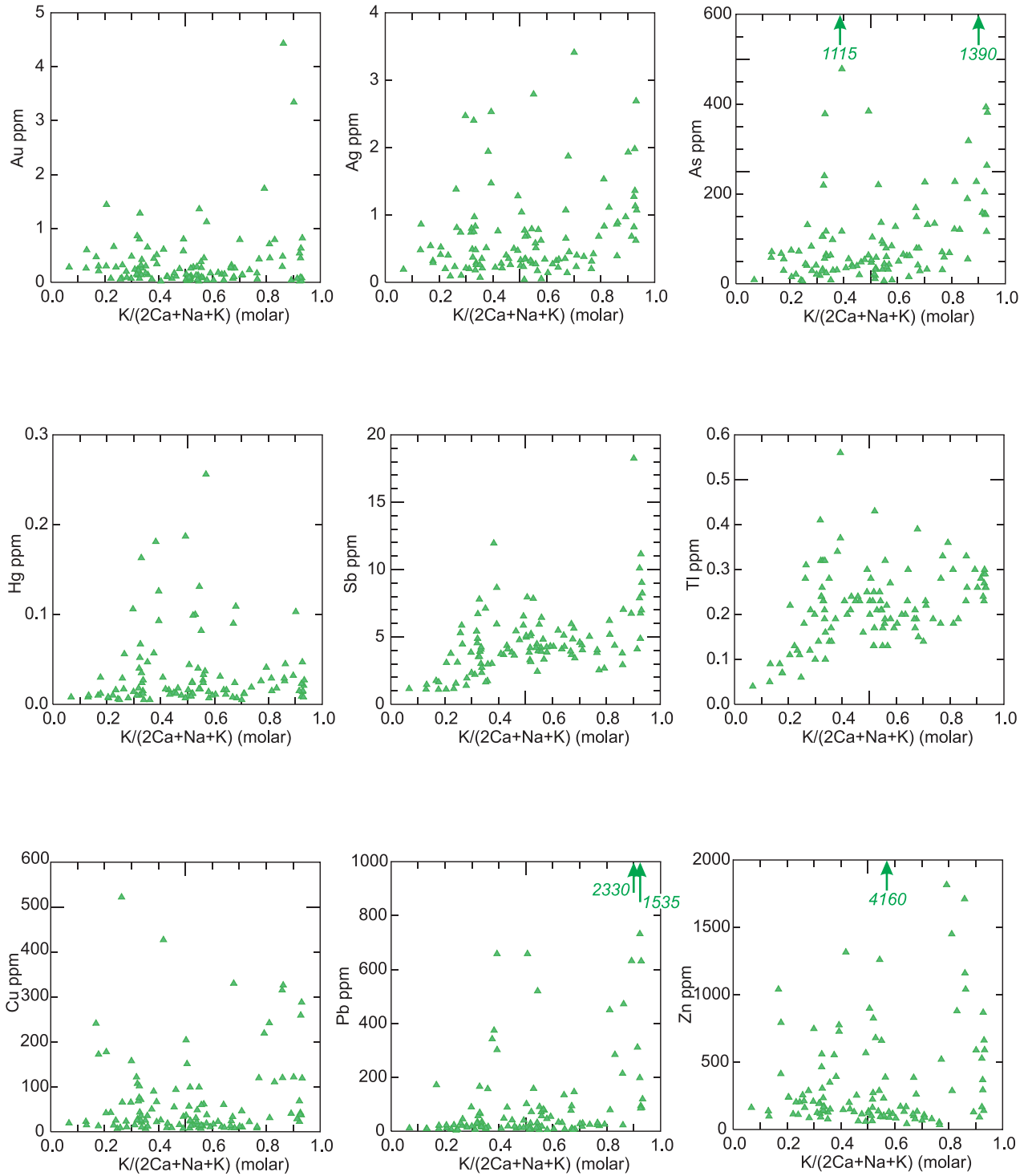


**Figure 5.6** Concentrations of metals and potential pathfinder elements versus molar  $K/(2Ca + Na + K)$  values for samples surrounding gold bearing veins at E42. Lateral distance to vein decreases as  $K/(2Ca + Na + K)$  increases, as per Figure 5.5. Positions of outlier samples with elemental concentrations greater than vertical scale are noted by arrows.

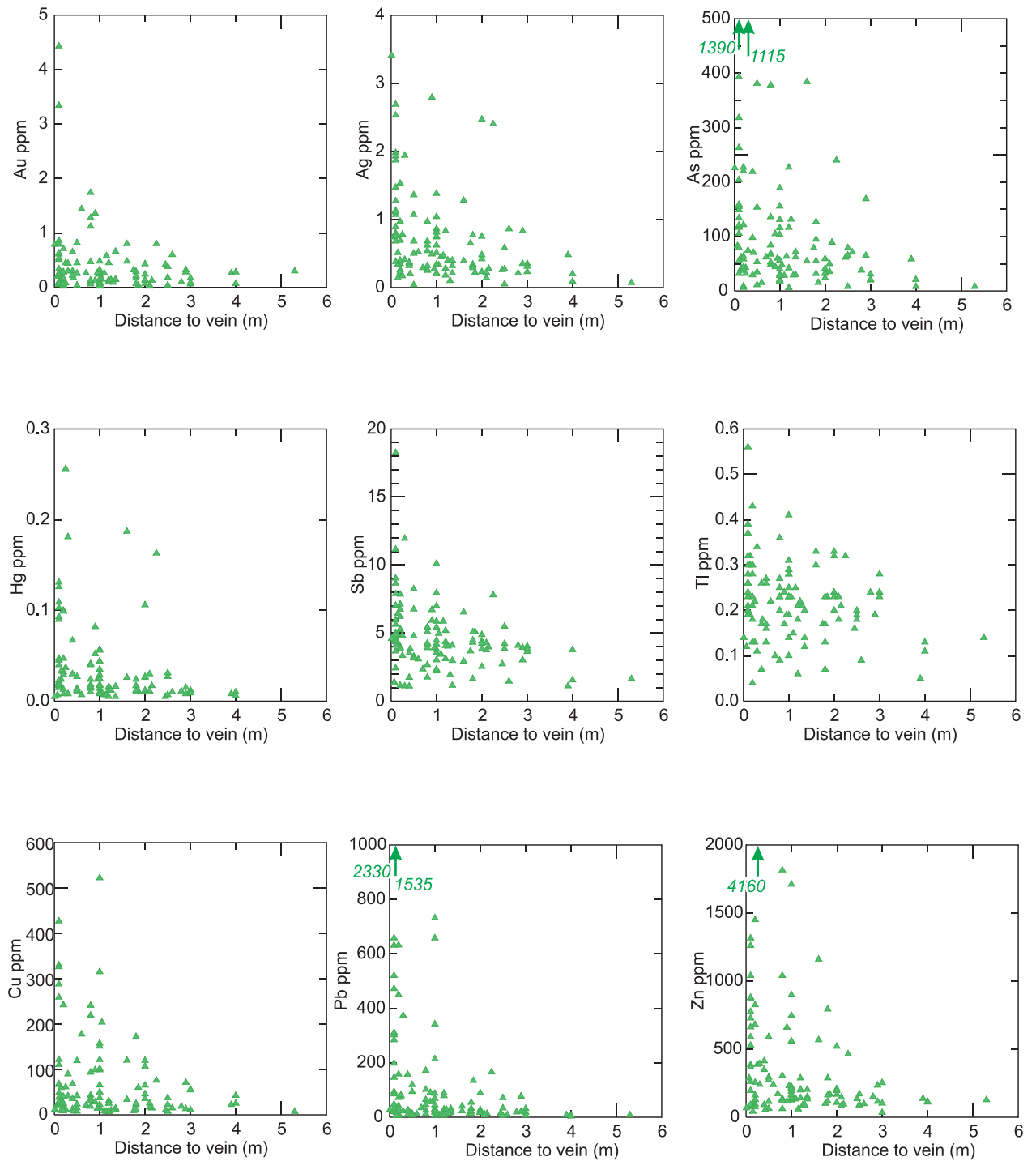


**Figure 5.7** Concentrations of metals and potential pathfinder elements versus distance from gold bearing veins at E42. All plots display a decrease in elemental concentrations with increasing distances from veins. Positions of outlier samples with elemental concentrations greater than vertical scale are noted by arrows.

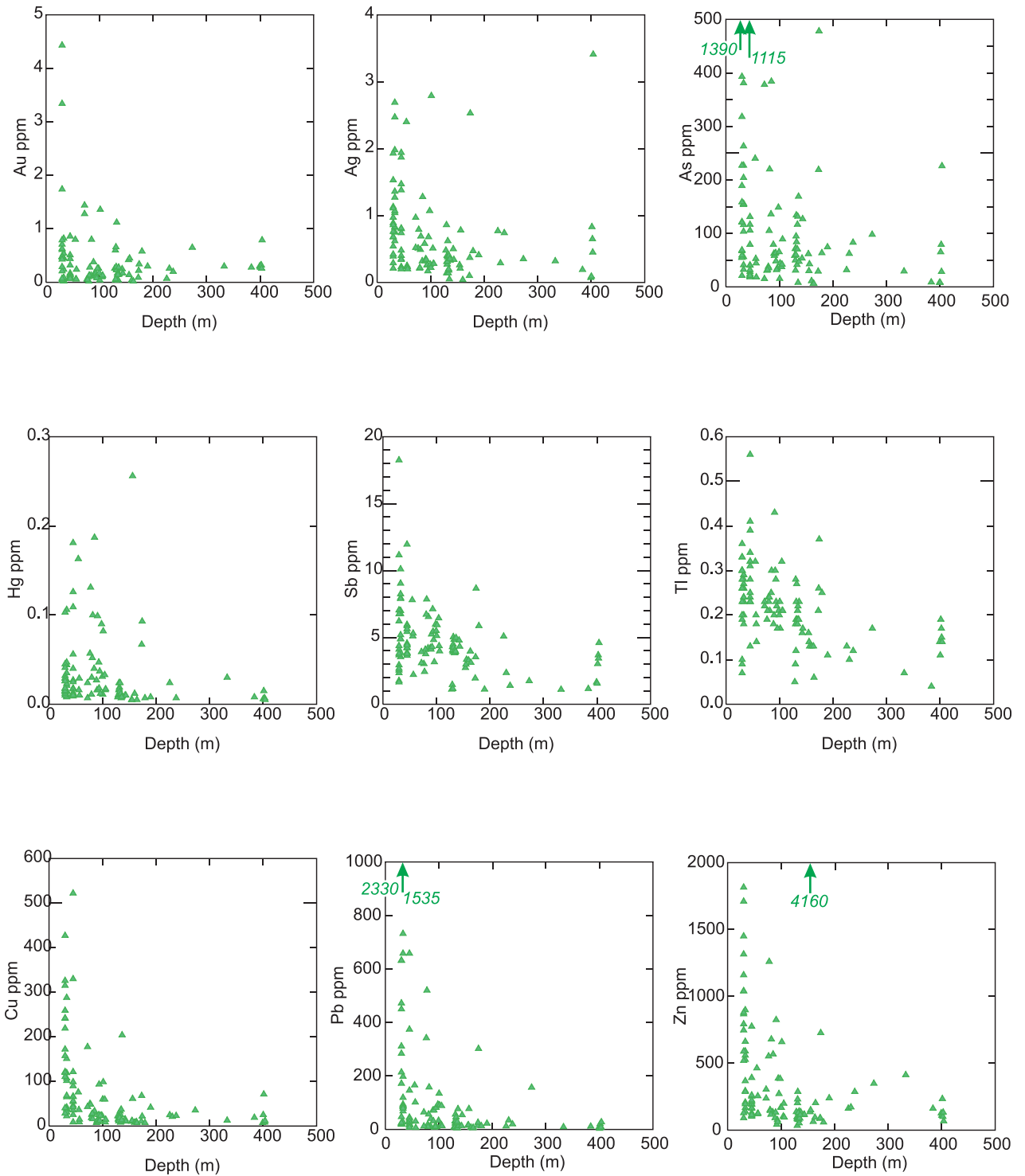


**Figure 5.8** Concentrations of metals and potential pathfinder elements versus depth at E42. All plots display a decrease in elemental concentrations with increasing depth. Positions of outlier samples with elemental concentrations greater than vertical scale are noted by arrows.

## CHAPTER 6: SUMMARY

### 6.1 Conclusions

Endeavour 42 is a structurally controlled, vein- and fault-hosted epithermal gold deposit which developed independent of host lithology. The rock package was tilted early in the structural history, and subsequently faulted under northeast directed tension, forming a set of possibly conjugate normal faults. Following dyke emplacement along several deposit-scale faults, two sets of early, barren carbonate-dominated veins formed, one along bedding planes and the other developing parallel to deposit-scale faults.

The formation of the gold-bearing epithermal system at E42 spanned at least two different structural regimes, with early auriferous vein sets crosscut and offset by later ones. Early, steeply dipping fault parallel gold-bearing veins formed along two different planes of weakness in the host rocks: the dominant northwest-trending fault population, and an east-striking dyke population. Both steep gold-bearing vein sets are interpreted as opening coevally under subhorizontally distributed tension with a subvertical maximum compressive stress ( $\sigma_1$ ). High grade fault-hosted breccia intervals are found intermittently across E42 and are interpreted as hydrothermally cemented breccia bodies formed by fluid decompression along faults, triggering volatile exsolution and brecciation. Fault-hosted breccias are grouped temporally with early steep gold-bearing veins due to similar mineralogy and orientations. Steep gold-bearing veins are crosscut by two sets of inclined gold-bearing veins: one developed along bedding planes (dipping moderately to the northwest), and the other dipping moderately to the southwest. Inclined veins are interpreted as opening coevally in a compressional stress regime, with the maximum and intermediate compressive stress axes ( $\sigma_1$  and  $\sigma_2$ , respectively) unconstrained within the horizontal plane, and subvertically directed tension ( $\sigma_3$ ).

Five separate generations of post-gold carbonate-dominated barren veins are identified for E42, each clearly defined temporally by crosscutting vein relationships. These include a reactivation of gold-bearing veins, reactivation of north-trending faults, and three approximately coeval sets of carbonate-chlorite veins. Two of the latter three vein sets exploit pre-existing anisotropies in the rock package, whereas the third appears to be a newly generated fracture orientation. In general, the evolution of the E42 deposit involves a series

of structural reactivation events, with multiple stages of fluid flow along pre-existing planes of weakness in the rock package such as bedding planes, faults, dykes, and veins.

By looking at relative timing relationships of faults, dykes, and veins, and comparing them with regional studies in the area, the E42 epithermal deposit and host rocks can be placed in a larger tectonic context. The vein-hosted gold system at E42 likely developed in the period of overall crustal extension, ca. 443-433 Ma, following the northeast-southwest directed compression of Phase 1 of the Benambran Orogeny (Glen, 2005).

As a structurally controlled deposit, the generation of permeability and through-going structures in the rock package at E42 plays a key role in the development of the epithermal system. Subparallel fractures are commonly joined via secondary hard linkages in their overlap zones, creating through-going fluid pathways and eventually fracture networks. This mode of fracture propagation is observed in steeply dipping and inclined gold-bearing veins at E42, as well as within fault-hosted high grade breccia intervals. When fluid pathways become sealed, due to mineral precipitation for example, the permeability along the pathway is greatly diminished. This increases the possibility of overpressuring from rising fluid, which may eventually cause brittle failure followed by the exsolution of volatiles along the structure. This decompression may result in brecciation, followed by precipitation of hydrothermal cement, which is variably gold-bearing at E42. The variation in permeability along structures greatly influences ore grade and distribution, as evidenced by veins and high grade fault-hosted breccia intervals at E42. As is also clearly observed at the E42 deposit, the presence of pre-existing weaknesses and anisotropies in a rock package are critical to its subsequent structural and hydrothermal evolution.

High grade faults and veins across the E42 deposit exhibit sericite-quartz  $\pm$  carbonate alteration haloes ranging from cm to m-scale thickness. Multielement analyses of these haloes indicate both lateral zonation patterns away from gold-bearing structures, and vertical zonation patterns within the E42 system. Compared to pervasive background chlorite-carbonate-hematite  $\pm$  epidote alteration, these sericite-dominated alteration haloes exhibit overall K-gain, and varying degrees of Ca- and Na-loss, a trend also observed high in the E42 hydrothermal system and becoming less pronounced with depth. Metals and potential pathfinder elements, including Au, Ag, As, Hg, Sb, Tl, Cu, Pb, and Zn, all display increasing concentrations towards high-grade structures, with a positive peak in Ag, As, Hg, Sb, Pb, and

Zn concentrations found consistently at values of 0.4-0.5 for  $K/(2Ca+Na+K)$  molar, likely due to the presence of microveinlets in the wallrock at the interface between background propylitic and sericite-dominated alteration. Au, Cu, and Pb display a sharp decrease in concentration at approximately one metre laterally from high grade faults and veins, whereas Ag, As, Hg, Sb, Tl, and Zn display larger dispersion haloes, decreasing in concentration more gradually over 5-7 metres. Vertical zonation within E42 shows a distinct drop in Au, Cu, Pb, and Zn at depths of 50-100 metres, and a more gradual decrease in Ag, As, Hg, Sb, and Tl over approximately 400 metres. Decreasing elemental concentrations with depth may indicate a root zone to the overlying supergene mineralization blanket, or the base of a classic alteration plume.

## 6.2 Exploration Implications

Mineralization at E42 is independent of lithology, with gold-bearing veins cutting all rock types with the exception of the vesicular and diorite dykes. Density of steeply dipping gold-bearing veins increases as faults and dykes are approached. High grade areas in the open pit tend to be more closely associated with the thickness of individual veins rather than their total number, regardless of whether the gold-bearing veins are steep or inclined. Targeting faults, dykes and through-going structures for exploration also increases the chance of discovery of additional high grade fault-hosted breccia intervals, although the latter are spatially unpredictable, forming discontinuously both laterally and vertically along faults.

Metal and pathfinder elements display specific patterns within sericite-alteration haloes proximal to high grade faults and veins at E42. These patterns are defined both laterally and vertically, and similar trends have been found at other low-sulfidation epithermal Au-Ag deposits worldwide, such as El Peñón (Chile), Mt. Muro (Indonesia), and Sleeper (Nevada) (Warren et al., 2007). Whole rock geochemistry, therefore, is a viable exploration tool for these types of ore deposits.

The Cowal Igneous Complex, host to multiple gold and copper prospects, is found at the intersection between two major Macquarie Arc-scale structural trends: the Gilmore and the Tullamore Trends. Major fault systems such as these commonly provide crustal-scale pathways for mineralizing fluids, and the intersection point between two major trends provides an ideal environment for structurally controlled ore deposition. Areas exhibiting

high fault density potentially have increased rock permeability, which in turn increases the chances for ore deposit formation, as is seen in the Cowal Igneous Complex and the Cowal “gold corridor”.

### **6.3 Future Work**

Due to the fact that primary rock exposures in the pit at the time of this study were limited to the Upper Volcaniclastic unit, a detailed comparative vein study between major E42 rock types was not undertaken. Distinguishing variations in vein thickness, density, length, and even mineralogy between different host rocks at E42 may provide useful information for future work in the area. Factors such as competency and wallrock composition may have significant effects on vein development. Minor comparative work has been previously attempted from drillcore observations, but viewing the vein distribution with respect to host rock lithology in 3D will undoubtedly provide many new insights, as it has for the Upper Volcaniclastic unit and structural paragenesis defined in this study.

Similarly, the examination of sericite-dominated alteration haloes to high grade structures may be useful in host rocks other than the Upper Volcaniclastic unit, to see if the geochemical signatures are different. Examining why sericite-dominated haloes are not as well developed in other rock types may provide a better understanding and definition of the overall distribution and characteristics of alteration phases at E42.

While there are multiple stages of fluid flow described along specific vein populations and fault-hosted hydrothermally cemented breccia intervals, the detailed chemical evolution of fluids at E42 remains undefined. A comprehensive textural and chemical study of vein mineralogy would ideally link structural observations with the geochemical evolution of the epithermal system.

The extent of the E42 deposit to depth is still unknown. With deeper drilling, the true size of the epithermal system may be determined, as well as potential sources for the mineralizing fluids.

## REFERENCES

- Albinson, T., Norman, D.I., Cole, D. and Chomiak, B. (2001)** Controls on formation of low-sulfidation epithermal deposits in Mexico: constraints from fluid inclusion and stable isotope data, SEG Special Publication 8, p. 1-32.
- Anderson, E.M. (1951)** The dynamics of faulting and dyke formation, with applications to Britain, Edinburgh, Oliver and Boyd, 191 p.
- Anderson, H. (2003)** The geology of the dykes associated with the E42 deposit, unpublished internal report, Barrick Gold of Australia Ltd.
- Ashley, P.M. (2003a)** Petrographic report on twenty-six samples of drill core from the Cowal Gold Project, Central Western, New South Wales, unpublished Barrick internal report, May, 105 p.
- Ashley, P.M. (2003b)** Petrographic report on thirty-two samples of drill core from the Cowal Gold Project, Central Western, New South Wales, unpublished Barrick internal report, October, 122 p.
- Barrick (2007)** Fourth quarter and year-end report 2007, Barrick Gold Corporation Press Release February 21, 2008, 106 p.
- Barron, L.M. (1999)** Metamorphism, Dubbo 1:250 000 Geological Sheet SI/55-4, 2<sup>nd</sup> edition, Explanatory notes, Geological Survey of New South Wales, Sydney.
- Barron, L.M. and Barron, B.J. (1996)** The limburgite suite in the Bathurst-Dubbo area, Geological Survey of New South Wales Quarterly Notes, v. 99, p. 1-24.
- Bastrakov, E.N. (2000)** Gold metallogenesis at the Lake Cowal prospect, NSW, unpublished PhD. thesis, Australian National University, 114 p.
- Begbie, M.J., Spörli, K.B. and Mauk, J.L. (2007)** Structural evolution of the Golden Cross epithermal Au-Ag deposit, New Zealand, Economic Geology, v. 102, p. 873-892.
- Borthwick, V.E.A. (2004)** Characterisation of veining at the E42 gold deposit, Lake Cowal, NSW, unpublished BSc. thesis, University of Sydney, 122 p.
- Buchanan, L.J. (1981)** Precious metal deposits associated with volcanic environment in the southwest, in Relations of Tectonics to Ore Deposits in the Southern Cordillera, Dickinson, W.R. and Payne, W.D., eds, Arizona Geological Society Digest, v. 14, p. 247-284.
- Cannell, J. (2003)** Lithological units of the E42 deposit, description, classification and depositional setting, unpublished internal report, Barrick Gold of Australia Ltd., 36 p.

**Carr, G., Dean, J.A., Suppel, D.W. and Heithersay, P.S. (1995)** Precise lead isotope fingerprinting of hydrothermal activity associated with Ordovician to Carboniferous metallogenic events in the Lachlan Fold Belt of New South Wales, *Economic Geology*, v. 90, p. 1467-1505.

**Childs, C., Watterson, J. and Walsh, J.J. (1995)** Fault overlap zones within developing normal fault systems, *Journal of the Geological Society, London*, v. 152, p. 535-549.

**Childs, C., Watterson, J. and Walsh, J.J. (1996)** A model for the structure and development of fault zones, *Journal of the Geological Society, London*, v. 153, p. 337-340.

**Collins, W.J. (1998)** Evaluation of petrogenetic models for Lachlan Fold Belt granitoids: implications for crustal architecture and tectonic models, *Australian Journal of Earth Sciences*, v. 45, p. 483-500.

**Collins, W.J. and Hobbs, B.E. (2001)** What caused the Early Silurian change from mafic to silicic (S-type) magmatism in the eastern Lachlan Fold Belt? *Australian Journal of Earth Sciences*, v. 48, p. 25-41.

**Collins, W.J. and Vernon, R.H. (1992)** Palaeozoic arc growth, deformation and migration across the Lachlan Fold Belt, southeastern Australia, *Tectonophysics*, v. 214, p. 381-400.

**Cooke, D.R., Wilson, A.J., House, M.J., Wolfe, R.C., Walshe, J.L., Lickfold, V. and Crawford, A.J. (2006)** Alkalic porphyry Au-Cu and associated mineral deposits of the Ordovician to Early Silurian Macquarie Arc, NSW: Alkalic project annual report, Year 1 - Epithermal Module - Update to Project Supporters, West Wyalong NSW, November 2006, p. 5.1-5.20.

**Cox, S.F., Knackstedt, M.A. and Braun, J. (2001)** Principles of structural control on permeability and fluid flow in hydrothermal systems, *Reviews in Economic Geology*, v. 14, p. 1-24.

**Cox, S.F. and Ruming, K. (2004)** The St. Ives mesothermal gold system, Western Australia – a case of golden aftershocks? *Journal of Structural Geology*, v. 26, p. 1109-1125.

**Crawford, A.J., Cooke, D.R. and Fanning, C.M. (2007a)** Geochemistry and age of magmatic rocks in the unexposed Narromine, Cowal and Fairholme Igneous Complexes in the Ordovician Macquarie Arc, central western New South Wales, *Australian Journal of Earth Sciences*, v. 54, p. 243-271.

**Crawford, A.J., Meffre, S., Squire, R.J., Barron, L.M. and Falloon, T.J. (2007b)** Middle and Late Ordovician magmatic evolution of the Macquarie Arc, Lachlan Orogen, New South Wales, *Australian Journal of Earth Sciences*, v. 54, p. 181-214.

**David, V., Glen, R. and Spencer, R. (2004)** Geophysical and geological interpretation of the Junee-Narromine Volcanic Belt, Extended Abstract, ASEG 17<sup>th</sup> Geophysical Conference and Exhibition, Sydney, 2004.

**Dong, G., Morrison, G. and Jaireth, S. (1995)** Quartz textures in epithermal veins, Queensland – classification, origin, and implication, *Economic Geology*, v. 90, p. 1841-1856.

**Dykman, V.J. (2004)** Comparison of structures between E41 and E42, unpublished internal report, Barrick Gold of Australia Ltd., 21 p.

**Fergusson, C.L. (2003)** Ordovician-Silurian accretion tectonics of the Lachlan Fold Belt, southeastern Australia, *Australian Journal of Earth Sciences*, v. 50, p. 475-490.

**Fergusson, C.L. and Coney, P.J. (1992)** Convergence and intraplate deformation in the Lachlan Foldbelt of southeastern Australia, *Tectonophysics*, v. 214, p. 417-439.

**Finlayson, D.M., Korsch, R.J., Glen, R.A., Leven, J.H. and Johnstone, D.W. (2002)** Seismic imaging and crustal architecture across the Lachlan transverse zone, a possible early cross-cutting feature of eastern Australia, *Australian Journal of Earth Sciences*, v. 49, p. 311-321.

**Foster, D.A., Gray, D.R. and Burcher, M. (1999)** Chronology of deformation within the turbidite-dominated Lachlan Orogen: implications for the tectonic evolution of eastern Australia and Gondwana, *Tectonics*, v. 18, p. 452-485.

**Fournier, R.O. (1999)** Hydrothermal processes related to movement of fluid from plastic into brittle rock in the magmatic-epithermal environment, *Economic Geology*, v. 94, p. 1193-1211.

**Gemmell, J.B. (2007)** Hydrothermal alteration associated with the Gosowong epithermal Au-Ag deposit, Halmahera, Indonesia: mineralogy, geochemistry and exploration implications, *Economic Geology*, v. 102, p. 893-922.

**Gemmell, J.B. and the AMIRA P588 Team (2006)** Exploration implications of hydrothermal alteration associated with epithermal Au-Ag deposits, AESC2006, Melbourne, Australia, p. 1-4.

**Gibbs, A.D. (1984)** Structural evolution of extensional basin margins, *Journal of the Geological Society, London*, v. 141, p. 609-620.

**Glen, R.A. (1991)** Inverted transtensional basin setting for gold and copper and base metal deposits at Cobar, New South Wales, *BMR Journal of Geology and Geophysics*, v. 12, p. 13-24.

**Glen, R.A. (1992)** Thrust, extensional and strike-slip tectonics in an evolving Palaeozoic orogen – a structural synthesis of the Lachlan Orogen of southeastern Australia, *Tectonophysics*, v. 214, p. 341-380.

**Glen, R.A. (1995)** Thrust and thrust-associated mineralization in the Lachlan Orogen, *Economic Geology*, v. 90, p. 1402-1429.

**Glen, R.A. (2004)** Plate tectonics of the Lachlan Orogen: a framework for understanding its metallogensis, Abstracts of the Geological Society of Australia, v. 74, p. 33-36.

**Glen, R.A. (2005)** The Tasmanides of eastern Australia, in Vaughan, A.P.M., Leat, P.T. and Pankhurst, R.J. (eds.) Terrane Processes at the Margins of Gondwana, Geological Society of London, Special Publications, v. 246, p. 23-96.

**Glen, R.A., Clare, A. and Spencer, R. (1996)** Extrapolating the Cobar Basin model to the regional scale: Devonian basin-formation and inversion in western New South Wales, in Cook, W.G., Ford, A.J.H., McDermott, J.J., Standish, P.N., Stegman, C.L. and Stegman, T.M. (eds.) The Cobar Mineral Field – 1996, Australasian Institute of Mining and Metallurgy, Melbourne, Spectrum Series 3/96, p. 43-83.

**Glen, R.A., Crawford, A.J. and Cooke, D.R. (2003)** Tectonic setting of porphyry copper-gold mineralization in the Macquarie Arc, in Blevin, P.L., Jones, M. and Chappell, B.W. (eds.) Magmas to Mineralisation: the Ishihara Symposium, Geoscience Australia Record, v. 2003/14, p. 65-68.

**Glen, R.A., Crawford, A.J. and Cooke, D.R. (2007b)** Tectonic setting of porphyry Cu-Au mineralisation in the Ordovician – Early Silurian Macquarie Arc, eastern Lachlan Orogen, New South Wales, Australian Journal of Earth Sciences, v. 54, p. 465-479.

**Glen, R.A., Dawson, M.W. and Colquhoun, G.P. (2006)** Eastern Lachlan Orogen Geoscience Database (on DVD-ROM) Version 2, NSW Department of Primary Industries – Minerals, Geological Survey of New South Wales, Maitland, NSW, Australia.

**Glen, R.A. and Fleming, G.D. (2000)** Interpreted basement geology, central part of the Junee-Narromine Volcanic Belt, NSW (S/I, 55-3, 55-7, 55-11) 1:500 000 scale, Geological Survey of New South Wales, Sydney.

**Glen, R.A., Korsch, R.J., Direen, N.G., Jones, L.E.A., Johnstone, D.W., Lawrie, K.C., Finlayson, D.M. and Shaw, R.D. (2002)** Crustal structure of the Ordovician Macquarie Arc, eastern Lachlan Orogen, based on seismic-reflection profiling, Australian Journal of Earth Sciences, v. 49, p. 323-348.

**Glen, R.A., Meffre, S. and Scott, R.J. (2007c)** Benambran orogeny in the eastern Lachlan Orogen, Australia, Australian Journal of Earth Sciences, v. 54, p. 385-415.

**Glen, R.A. and Percival, I.G. (2003)** Convergent and transform boundaries along the SE Australian sector of the proto-Pacific Gondwana margin in the Ordovician, in Fuetterer, D.K. (ed.) 9<sup>th</sup> International Symposium on Antarctic Earth Sciences, Potsdam, p. 120-121.

**Glen, R.A., Scheibner, E. and VandenBerg, A.H.M. (1992)** Paleozoic intraplate escape tectonics in Gondwanaland and major strike-slip duplication in the Lachlan Orogen of southeastern Australia, Geology, v. 20, p. 795-798.

**Glen, R.A., Spencer, R., Willmore, A., David, V. and Scott, R.J. (2007a)** June-Narromine Volcanic Belt, Macquarie Arc, Lachlan Orogen, New South Wales: components and structure, *Australian Journal of Earth Sciences*, v. 54, p. 215-241.

**Glen, R.A., Stewart, I.R. and Percival, I.G. (2004)** Narooma Terrane: implications for the construction of the outboard part of the Lachlan Orogen, *Australian Journal of Earth Sciences*, v. 51, p. 859-884.

**Glen, R.A. and Walshe, J.L. (1999)** Cross-structures in the Lachlan Orogen: the Lachlan Transverse Zone example, *Australian Journal of Earth Sciences*, v. 46, p. 641-658.

**Glen, R.A., Walshe, J.L., Barron, L.M. and Watkins, J.J. (1998)** Ordovician convergent-margin volcanism and tectonism in the Lachlan sector of east Gondwana, *Geology*, v. 26, p. 751-754.

**Gray, D.R. and Foster, D.A. (1997)** Orogenic concepts – application and definition: Lachlan Fold Belt, eastern Australia, *American Journal of Science*, v. 297, p. 859-891.

**Gray, D.R. and Foster, D.A. (1998)** Character and kinematics of faults within the turbidite-dominated Lachlan Orogen: implications for tectonic evolution of eastern Australia, *Journal of Structural Geology*, v. 20, p. 1691-1720.

**Gray, D.R. and Foster, D.A. (2004)** Tectonic evolution of the Lachlan Orogen, southeastern Australia: historical review, data synthesis and modern perspectives, *Australian Journal of Earth Sciences*, v. 51, p. 773-817.

**Gray, D.R., Foster, D.A. and Bierlein, F.P. (2002)** Geodynamics and metallogeny of the Lachlan Orogen, *Australian Journal of Earth Sciences*, v. 49, p. 1041-1056.

**Gresens, R.L. (1967)** Composition-volume relationships of metasomatism, *Chemical Geology*, v. 2, p. 47-65.

**Guilbert, J.M. and Park, C.F. (1986)** *The Geology of Ore Deposits*, W.H. Freeman and Co., 985 p.

**Hedenquist, J.W., Arribas, A. and Gonzalez-Urien, E. (2000)** Exploration for epithermal gold deposits, *Reviews in Economic Geology*, v. 13, p. 221-244.

**Hedenquist, J.W. and Henley, R.W. (1985)** Hydrothermal eruptions in the Waiotapu geothermal system, New Zealand: their origin, associated breccias, and relation to precious metal mineralization, *Economic Geology*, v. 80, p. 1640-1668.

**Heithersay, P.S., O'Neill, W.J., Van der Helder, P., Moore, C.R. and Harbon, P.G. (1990)** Goonumbla porphyry copper district – Endeavour 26 North, Endeavour 22 and Endeavour 27 copper-gold deposits, in *Geology of the Mineral Deposits of Australia and Papua New Guinea*, ed. F.E. Hughes, p. 1385-1398 (The Australian Institute of Mining and Metallurgy: Melbourne)

**Holliday, J.R., Wilson, A.J., Blevin, P.L., Tedder, I.J., Dunham, P.D. and Pfitzner, M. (2002)** Porphyry gold-copper mineralization in the Cadia district, eastern Lachlan Fold Belt, New South Wales, and its relationship to shoshonitic magmatism, *Mineralium Deposita*, v. 37, p. 100-116.

**Hooper, B., Heithersay, P.S., Mills, M.B., Lindhorst, J.W. and Freyberg, J. (1996)** Shoshonite-hosted Endeavour 48 porphyry copper-gold deposit, Northparkes, central New South Wales, *Australian Journal of Earth Sciences*, v. 43, p. 279-288.

**Ingpen, I.A. (1995)** Geological, structural and tectonic history of the Temora, West Wyalong, Grenfell and Forbes area, New South Wales: implications for the structural controls on gold and copper mineralization, unpublished MSc. thesis, Monash University, 197 p.

**Ishikawa, Y., Sawaguchi, T., Iwaya, S. and Horiuchi, M. (1976)** Delineation of prospecting targets for Kuroko deposits based on modes of volcanism of underlying dacite and alteration haloes, *Mining Geology*, v. 26, p. 105-117 (in Japanese with English abs.)

**Keay, S., Collins, W.J. and McCullough, M.T. (1997)** A three-component Sr-Nd isotopic mixing model for granitoid genesis, Lachlan fold belt, eastern Australia, *Geology*, v. 25, p. 307-310.

**Large, R.R., Gemmill, J.B., Paulick, H. and Huston, D.L. (2001)** The alteration box plot: a simple approach to understanding the relationship between alteration mineralogy and litho geochemistry associated with volcanic-hosted massive sulfide deposits, *Economic Geology*, v. 96, p. 957-971.

**Lickfold, V., Cooke, D.R., Crawford, A.J. and Fanning, C.M. (2007)** Shoshonitic magmatism and formation of the Northparkes porphyry Cu-Au deposits, New South Wales, *Australian Journal of Earth Sciences*, v. 54, p. 417-444.

**Lyons, P. (2000)** Structural geology, in Lyons, P., Raymond, O.L. and Duggan, M.D. (eds.) *Forbes 1:250 000 Geological Sheet SI 55-7 (2<sup>nd</sup> edition) Explanatory notes*, Australian Geological Survey Organisation Record 2000/20, p. 156-158.

**McDougall, I. and Harrison, T.M. (1999)** *Geochronology and thermochronology by the <sup>40</sup>Ar/<sup>39</sup>Ar method – second edition*, Oxford, U.K., Oxford Monographs on Geology and Geophysics 9, 269 p.

**McInnes, P. (2003)** Hydrothermal alteration and associated gold mineralization at the E42 gold deposit, Barrick Gold of Australia Ltd., unpublished internal report, 23 p.

**McInnes, P., Miles, I.N., Radclyffe, D. and Brooker, M. (1998)** Endeavour 42 (E42) gold deposit, Lake Cowal, *Geology of Australian and Papua New Guinean Mineral Deposits*, Monograph series – Australian Institute of Mining and Metallurgy, v. 22, p. 581-585.

**McPhie, J., Doyle, M. and Allen, R. (1993)** Volcanic textures: a guide to the interpretation of textures in volcanic rocks, University of Tasmania, Centre for Ore Deposit and Exploration Studies (publisher), Australia, 196 p.

**Meffre, S., Scott, R.J., Glen, R.A. and Squire, R. (2007)** Re-evaluation of contact relationships between Ordovician volcanic belts and the quartz-rich turbidites of the Lachlan Orogen, Australian Journal of Earth Sciences, v. 54, p. 363-383.

**Miles, I.N. and Brooker, M.R. (1998)** Endeavour 42 deposit, Lake Cowal, New South Wales: a structurally controlled gold deposit, Australian Journal of Earth Sciences, v. 45, p. 837-847.

**Miller, J.M., Dugdale, L.J. and Wilson, C.J.L. (2001)** Variable hangingwall palaeotransport during Silurian and Devonian thrusting in the western Lachlan Fold Belt: missing gold lodes, synchronous Melbourne Trough sedimentation and Grampians Group fold interference, Australian Journal of Earth Sciences, v. 48, p. 901-909.

**Morand, V.J. and Gray, D.R. (1991)** Major fault zones related to the Omeo Metamorphic Complex northeastern Victoria, Australian Journal of Earth Sciences, v. 38, p. 203-221.

**Munroe, S., Johnston, A., Simpson, R. and Hillsdon, P. (2005)** Cowal Gold Project: Structural controls on mineralization and target identification, internal report for Barrick Australia Ltd., SRK Consulting Engineers and Scientists, SRK Project Number BKG003, 61 p.

**Parry, W.T. (1998)** Fault-fluid compositions from fluid inclusion observations and solubilities of fracture-sealing minerals, Tectonophysics, v. 290, p. 1-26.

**Pearce, J.A. (1996)** A user's guide to basalt discrimination diagrams in Trace element geochemistry of volcanic rocks: applications for massive sulphide exploration, edited by D.A. Wyman, Geological Association of Canada, short course notes, v. 12, p. 79-113.

**Perkins, C., McDougall, I. and Walshe, J.L. (1990)**  $^{40}\text{Ar}/^{39}\text{Ar}$  and U-Pb geochronology of the Goonumbla porphyry Cu-Au deposits, New South Wales, Australia, Economic Geology, v. 85, p.1808-1824.

**Perkins, C., Walshe, J.L. and Morrison, G. (1995)** Metallogenic episodes of the Tasman Fold Belt system, eastern Australia, Economic Geology, v. 90, p. 1443-1466.

**Pittard, K. (2006)** Cowal Aeromagnetic and Gravity Interpretation - 2006, Barrick Gold of Australia Ltd., unpublished internal report.

**Purvis, A. C. (2002)** Mineralogical report No. 8209, Pontifex and Associates, unpublished petrological report, 32 p.

**Raymond, O.L., Duggan, M.B., Lyons, P., Scott, M.M., Sherwin, L., Wallace, D.A., Krynen, J.P., Young, G.C., Wyborn, D., Glen, R.A., Percival, I.G. and Leys, M. (2000b)** Forbes Second Edition (1:250 000 geological map SI55-7), Australian Geological Survey Organisation, Canberra and the Geological Survey of New South Wales, Orange.

**Raymond, O.L., Pogson, D.J., Wyborn, D., Henderson, G.A.M., Krynen, J., Meakin, S., Morgan, E.J., Scott, M.M., Stuart-Smith, P., Wallace, D.A., Warren, A.Y.E. and Watkins, J.J. (1998)** Bathurst 1:250 000 Geological Sheet SI/55-8. Geological Survey of New South Wales, Sydney and Australian Geological Survey Organisation, Canberra.

**Raymond, O., Sherwin, L., Lyons, P. and Scott, M. (2000a)** The Jemalong Trough: an extension of Silurian-Devonian rifting in the eastern Lachlan fold belt, Geological Society of Australia Abstracts Series, no. 59, p. 409.

**Reed, M.H. and Spycher, N.F. (1985)** Boiling, cooling, and oxidation in epithermal systems: a numerical modeling approach, Reviews in Economic Geology, v. 2, p. 249-272.

**Robbins, C.H. (2000)** Geology of the El Peñón gold-silver deposit, northern Chile, Geology and Ore Deposits 2000: The Great Basin and Beyond, Geological Society of Nevada Symposium, Reno, 2000, Proceedings, p. 249-264.

**Rowland, J.V. and Sibson, R.H. (2004)** Structural controls on hydrothermal flow in a segmented rift system, Taupo Volcanic Zone, New Zealand, Geofluids, v. 4, p. 259-283.

**Sibson, R.H. (2000)** A brittle failure mode plot defining conditions for high-flux flow, Economic Geology, v. 95, p. 41-48.

**Sibson, R.H. (2001)** Seismogenic framework for hydrothermal transport and ore deposition, Reviews in Economic Geology, v. 14, p. 25-50.

**Sibson, R.H. (2004)** Controls on maximum fluid overpressure defining conditions for mesozonal mineralization, Journal of Structural Geology, v. 26, p. 1127-1136.

**Sibson, R.H., Begbie, M.J. and Ghisetti, F.C. (2003a)** Stress field cycling coupled to fluid flow recorded in quartz vein systems hosted by strike-slip faults, Proterozoic Mt. Isa Inlier, Australia, Geological Society of New Zealand, Annual Conference abstract, Dunedin.

**Sibson, R.H., Begbie, M.J., Ghisetti, F.C. and Blenkinsop, T.G. (2003b)** Cyclical stress field switching and (total?) relief of fault shear stress recorded in quartz vein systems hosted by Proterozoic strike-slip faults, Mt. Isa, Australia, Eos Transactions, American Geophysical Union 2003 fall meeting, San Francisco, v.84, no.46, p.1075.

**Sibson, R.H., Robert, F. and Poulsen, K.H. (1988)** High-angle reverse faults, fluid-pressure cycling, and mesothermal gold-quartz deposits, Geology, v. 16, p. 551-555.

- Silberman, M.L. and Berger, B.R. (1985)** Relationship of trace-element patterns to alteration and morphology in epithermal precious-metal deposits, *Reviews in Economic Geology*, v. 2, p. 203-232.
- Sillitoe, R.H. (2000)** Gold-rich porphyry deposits: descriptive and genetic models and their role in exploration and discovery, *Reviews in Economic Geology*, v. 13, p. 315-345.
- Simmons, S.F., White, N.C., and John, D.A. (2005)** Geological characteristics of epithermal precious and base metal deposits, *Economic Geology 100<sup>th</sup> Anniversary Volume*, p. 485-522.
- Simpson, R. (2003)** Cowal gold project E42 deposit: structural geology report, unpublished internal report, Barrick Gold of Australia Ltd., 17 p.
- Simpson, K., and Cooke, D. (2006)** Volcanic Facies Architecture of the E46 Prospect, Lake Cowal, NSW: Alkalic project annual report, Year 1 - Epithermal Module - Update to Project Supporters, West Wyalong NSW, November 2006, p. 6.1-6.7.
- Smolonogov, S. (2003)** Cowal gold project E42 deposit geology report, unpublished internal report, Barrick Gold of Australia Ltd., 162 p.
- Soesoo, A., Bons, P.D., Gray, D.A. and Foster, D.A. (1997)** Divergent double subduction: tectonic and petrologic consequences, *Geology*, v. 25, p. 755-758.
- Spencer, R. (2004)** Gravity map of New South Wales, scale 1:2 500 000, Geological Survey of New South Wales, Sydney.
- Stanley, C.R. and Madeisky, H.E. (1994)** Lithogeochemical exploration for hydrothermal ore deposits using Pearce element ratio analysis, *Geological Association of Canada Short Course Notes 11*, p. 193-212.
- Stern, R.J., Bloomer, S.H., Lin, P., Ito, E. and Morris, J. (1988)** Shoshonitic magmas in nascent arcs: new evidence from submarine volcanoes in the Northern Marianas, *Geology*, v. 16, p. 426-430.
- Strickland, T.J. (2005)** Geology of the E42 breccia complex at the Cowal Au deposit, NSW, Australia, unpublished BSc. thesis, University of Tasmania, 133 p.
- Stuart-Smith, P.G. (1991)** The Gilmore Fault Zone – the deformational history of a possible terrane boundary within the Lachlan Fold Belt, New South Wales, *BMR Journal of Australian Geology and Geophysics*, v. 12, p. 35-49.
- Teysier, C. and Tikoff, B. (1995)** Oblique plate motion and continental tectonics, *Geology*, v. 23, p. 447-450.

**Tosdal, R.M., Sherlock, R.L., Nelson, G.C., Enderlin, D.A. and Lehrman, N.J. (1995)** Precious metal mineralization in a fold and thrust belt: the McLaughlin hot spring deposit, northern California, *Geology and Ore Deposits of the American Cordillera*, symposium proceedings, Geological Society of Nevada, v. 2, p. 839-854.

**VandenBerg, A.H.M. and Stewart, I.R. (1992)** Ordovician terranes of southeastern Lachlan Fold Belt: stratigraphy, structure and palaeogeographic reconstruction, *Tectonophysics*, v. 214, p. 177-192.

**VandenBerg, A.H.M., Willman, C.E. and Maher, S.E.A. (2000)** The Tasman Fold Belt system in Victoria: geology and mineralization of Proterozoic to Carboniferous rocks, Geological Survey of Victoria, Melbourne, Special Publication, 463 p.

**Vassallo, J., Glen, R.A. and David, D. (2003)** Structural re-evaluation of the Hill End Trough, eastern Lachlan Orogen, NSW, *Abstracts of the Geological Society of Australia*, v. 72, p. 74.

**Walshe, J.L., Heithersay, P.S. and Morrison, G.W. (1995)** Toward an understanding of the metallogeny of the Tasman Fold Belt system, *Economic Geology*, v. 90, p. 1382-1401.

**Warren, I., Simmons, S.F. and Mauk, J.L. (2007)** Whole-rock geochemical techniques for evaluating hydrothermal alteration, mass changes, and compositional gradients associated with epithermal Au-Ag mineralization, *Economic Geology*, v. 102, p. 923-948.

**Warren, I., Zuluaga, J.I., Robbins, C.H., Wulftange, W.H. and Simmons, S.F. (2004)** Geology and geochemistry of epithermal Au-Ag mineralization in the El Peñón district, northern Chile, *Society of Economic Geologists Special Publication 11*, p. 113-139.

**Williams, I.S. and Chappell, B.W. (1998)** Crustal evolution in southeastern Australia: a zircon viewpoint, *The Bruce Chappell Symposium: granites, island arcs, the Mantle and ore deposits*, Record of the Australian Geological Survey Organization, 1998/33, 44 p.

**Willman, C.E., VandenBerg, A.H.M. and Morand, V.J. (2002)** Evolution of the southeastern Lachlan Fold Belt in Victoria, *Australian Journal of Earth Sciences*, v. 49, p. 271-289.

**Wilson, A.J., Cooke, D.R. and Harper, B.L. (2003)** The Ridgeway gold-copper deposit: a high-grade alkalic porphyry deposit in the Lachlan Fold Belt, NSW, Australia, *Economic Geology*, v. 98, p. 1637-1656.

**Winchester, J.A. and Floyd, P.A. (1977)** Geochemical discrimination of different magma series and their differentiation products using immobile elements, *Chemical Geology*, v. 20, p. 325-343.

**Wyborn, D. (1992)** The tectonic significance of Ordovician magmatism in the eastern Lachlan fold belt, *Tectonophysics*, v. 214, p. 177-192.

**Zukowski, W., Cooke, D.R., Deyell, C.L. and McInnes, P. (2007)** Alkalic epithermal or porphyry? Hydrothermal alteration and vein paragenesis at the E41 gold prospect, Cowal district, New South Wales, Australia. 9th Biennial SGA meeting, Dublin, p. 403-406.

## **APPENDIX A:**

### **Vein Adularia $^{40}\text{Ar}$ - $^{39}\text{Ar}$ : Detailed Dating Methodology, Data Tables, and Summary Plots**

## METHODOLOGY

The samples were crushed, washed in deionized water, dried at room temperature and sieved to obtain the size fraction between 0.25 mm and 0.15 mm. Mineral separates were hand-picked, washed in acetone, dried, wrapped in aluminum foil and stacked in an irradiation capsule with similar-aged samples and neutron flux monitors (Fish Canyon Tuff sanidine (FCs), 28.02 Ma (Renne et al., 1998)).

The samples were irradiated on January 4 through January 6, 2007 at the McMaster Nuclear Reactor in Hamilton, Ontario, for 90 MWH, with a neutron flux of approximately  $6 \times 10^{13}$  neutrons/cm<sup>2</sup>/s. Analyses (n=48) of 16 neutron flux monitor positions produced errors of <0.5% in the J value.

The samples were analyzed on February 27, 2007, at the Noble Gas Laboratory, Pacific Centre for Isotopic and Geochemical Research, University of British Columbia, Vancouver, BC, Canada. The mineral separates were step-heated at incrementally higher powers in the defocused beam of a 10W CO<sub>2</sub> laser (New Wave Research MIR10) until fused. The gas evolved from each step was analyzed by a VG5400 mass spectrometer equipped with an ion-counting electron multiplier. All measurements were corrected for total system blank, mass spectrometer sensitivity, mass discrimination, radioactive decay during and subsequent to irradiation, as well as interfering Ar from atmospheric contamination and the irradiation of Ca, Cl and K (Isotope production ratios:  $(^{40}\text{Ar}/^{39}\text{Ar})_{\text{K}}=0.0302 \pm 0.00006$ ,  $(^{37}\text{Ar}/^{39}\text{Ar})_{\text{Ca}}=1416.4 \pm 0.5$ ,  $(^{36}\text{Ar}/^{39}\text{Ar})_{\text{Ca}}=0.3952 \pm 0.0004$ ,  $\text{Ca}/\text{K}=1.83 \pm 0.01(^{37}\text{Ar}_{\text{Ca}}/^{39}\text{Ar}_{\text{K}})$ ).

## RESULTS

Details of the analyses, including plateau (spectrum) and inverse correlation plots, are presented in Excel spreadsheets. The plateau and correlation ages were calculated using Isoplot ver.3.09 (Ludwig, 2003). Errors are quoted at the 2-sigma (95% confidence) level and are propagated from all sources except mass spectrometer sensitivity and age of the flux monitor. The best statistically-justified plateau and plateau age were picked based on the following criteria:

1. Three or more contiguous steps comprising more than 50% of the  $^{39}\text{Ar}$ ;
2. Probability of fit of the weighted mean age greater than 5%;
3. Slope of the error-weighted line through the plateau ages equals zero at 5% confidence;
4. Ages of the two outermost steps on a plateau are not significantly different from the weighted-mean plateau age (at  $1.8\sigma$ , six or more steps only);
5. Outermost two steps on either side of a plateau must not have nonzero slopes with the same sign (at  $1.8\sigma$ , nine or more steps only)

## REFERENCES

Ludwig, K.R. 2003. Isoplot 3.09 A Geochronological Toolkit for Microsoft Excel. Berkeley Geochronology Center, Special Publication No. 4

Nomade, S., Renne, P.R., Vogel, N., Deino, A.L., Sharp, W.D., Becker, T.A., Jaouni, A.R., Mundil R. 2005. Alder Creek sanidine (ACs-2): A Quaternary Ar/ Ar dating standard tied to the Cobb Mountain geomagnetic event. *Chemical Geology* 218 (2005) 315– 338.

Renne, P.R., C.Swisher, C.C., III, Deino, A.L., Karner, D.B., Owens, T. and DePaolo, D.J., 1998. Intercalibration of standards, absolute ages and uncertainties in  $^{40}\text{Ar}/^{39}\text{Ar}$  dating. *Chemical Geology*, 145(1-2): 117-152.

E42D1178-25770 Adularia

Laser Power(%)	Isotope Ratios 40Ar/39Ar	38Ar/39Ar	37Ar/39Ar	36Ar/39Ar	Ca/K	Cl/K	%40Ar atm	f 39Ar	40Ar*/39ArK	Age
2	125.025±0.019	0.261±0.031	0.073±0.057	0.232±0.038	0.453	0.048	53.38	0.13	57.001±3.114	833.27±36.46
2.2	47.920 0.005	0.119 0.026	0.092 0.040	0.028 0.062	0.584	0.023	15.53	0.47	39.778 0.560	619.45 7.38
2.4	21.953 0.005	0.019 0.025	0.283 0.015	0.004 0.058	1.808	0.001	3.67	1.61	20.897 0.124	351.66 1.90
2.6	21.592 0.005	0.016 0.022	0.641 0.013	0.002 0.074	4.095	0	1.77	3.92	21.100 0.115	354.76 1.75
2.7	21.549 0.007	0.014 0.029	0.617 0.016	0.002 0.141	3.941	0	0.67	3.28	21.276 0.167	357.45 2.54
2.8	21.849 0.004	0.013 0.040	0.121 0.019	0.001 0.127	0.78	0	0.33	3.11	21.615 0.097	362.60 1.48
2.9	22.014 0.004	0.013 0.054	0.021 0.036	0.001 0.310	0.136	0	0.2	2.95	21.795 0.116	365.35 1.75
3	22.012 0.005	0.013 0.035	0.014 0.042	0.000 0.361	0.088	0	0.12	4.07	21.845 0.116	366.09 1.76
3.1	22.378 0.004	0.012 0.084	0.009 0.042	0.001 0.448	0.058	0	0.04	1.94	22.133 0.146	370.45 2.21
3.2	22.140 0.004	0.013 0.048	0.009 0.060	0.000 0.600	0.059	0	0.26	10.04	21.992 0.115	368.32 1.74
3.3	22.307 0.004	0.013 0.055	0.006 0.161	0.000 1.208	0.039	0	0.12	5.6	22.163 0.163	370.92 2.47
3.5	21.796 0.004	0.014 0.043	0.008 0.068	0.000 0.324	0.049	0	0.3	17.2	21.657 0.096	363.24 1.47
3.7	21.958 0.005	0.016 0.059	0.005 0.139	0.000 1.947	0.034	0	0.13	6.24	21.817 0.228	365.68 3.45
3.8	21.876 0.005	0.016 0.056	0.003 0.187	0.001 0.357	0.018	0	0.99	16.58	21.585 0.146	362.14 2.22
3.9	21.835 0.005	0.017 0.043	0.002 0.242	0.001 0.271	0.011	0.001	1.08	17.97	21.525 0.129	361.24 1.96
4	22.199 0.005	0.018 0.112	0.001 0.797	0.000 1.015	0.009	0.001	0.12	4.89	22.045 0.165	369.12 2.50
Total/Average	22.098±0.001	0.016±0.008	0.207±0.001	0.001±0.049	0.379	0.005		100	21.613±0.024	

J =0.010299±0.000010

Volume 39ArK =2062.07

Integrated Date = 365.65±0.80

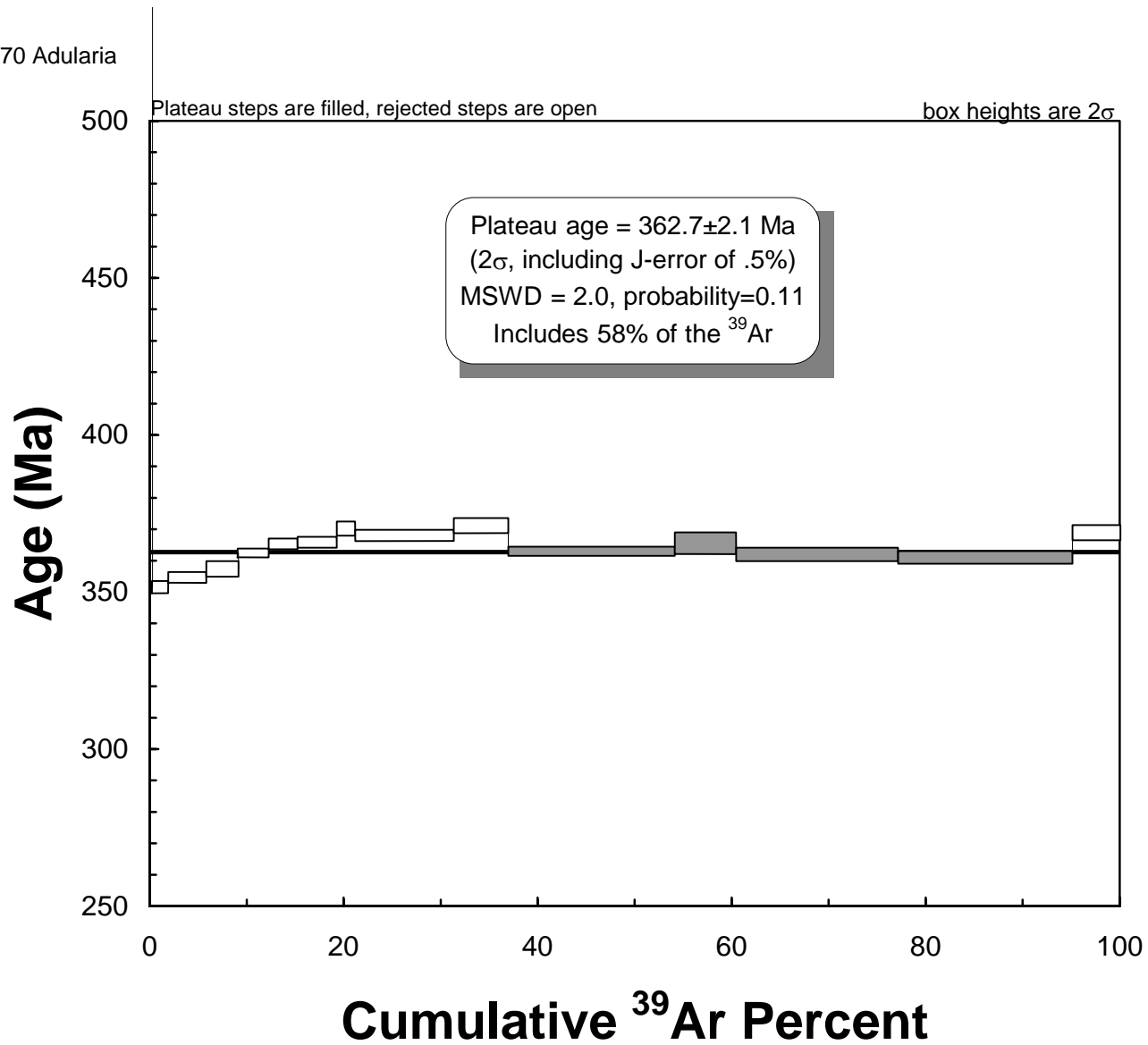
Volumes are 1E-13 cm3 NPT

Neutron flux monitors: 28.02 Ma FCs (Renne et al., 1998)

Isotope production ratios: (40Ar/39Ar)K=0.0302±0.00006, (37Ar/39Ar)Ca=1416.4±0.5, (36Ar/39Ar)Ca=0.3952±0.0004,

Ca/K=1.83±0.01(37ArCa/39ArK).

E42D1178-25770 Adularia



E42RL1155-36 Adularia

Laser Power(%)	Isotope Ratios 40Ar/39Ar	38Ar/39Ar	37Ar/39Ar	36Ar/39Ar	Ca/K	Cl/K	%40Ar atm	f 39Ar	40Ar*/39ArK	Age
2	121.409±0.008	0.709±0.032	0.054±0.197	0.120±0.046	0.368	0.155	28.77	1.28	85.346±1.770	1137.64±17.50
2.2	26.526 0.007	0.062 0.032	0.120 0.034	0.009 0.158	0.794	0.011	8.58	4.32	23.806 0.446	395.49 6.66
2.4	21.291 0.005	0.020 0.063	0.393 0.018	0.004 0.102	2.59	0.001	4.14	8.74	20.171 0.151	340.43 2.32
2.6	21.712 0.006	0.016 0.129	0.154 0.024	0.004 0.199	1.007	0	4.31	5.61	20.412 0.273	344.14 4.18
2.8	21.420 0.006	0.016 0.084	0.017 0.065	0.003 0.234	0.113	0	2.94	7.59	20.499 0.231	345.48 3.54
3	21.606 0.005	0.018 0.048	0.014 0.066	0.003 0.102	0.091	0.001	3.87	10.58	20.547 0.147	346.22 2.26
3.2	21.350 0.004	0.020 0.043	0.005 0.080	0.003 0.065	0.035	0.001	3.79	14.33	20.362 0.108	343.37 1.65
3.4	21.886 0.005	0.025 0.030	0.001 0.441	0.003 0.095	0.007	0.002	2.98	14.63	21.055 0.120	353.99 1.84
3.5	22.535 0.004	0.027 0.027	0.000 2.415	0.002 0.110	0.001	0.003	1.92	18.22	21.947 0.113	367.54 1.71
3.6	24.625 0.005	0.037 0.032	0.000 2.394	0.003 0.127	0.004	0.005	3.13	9.05	23.598 0.167	392.38 2.49
3.7	27.488 0.007	0.052 0.047	ERR	0.005 0.109	0.004	0.009	4.62	4.25	25.739 0.249	424.11 3.66
5	39.349 0.006	0.121 0.039	ERR	0.009 0.285	0.012	0.024	4.05	1.39	36.392 0.762	574.11 10.30
Total/Average	23.754±0.001	0.036±0.006	0.190±0.002	0.004±0.017	0.347	0.018		100	20.397±0.031	

J =0.010296±0.000010

Volume 39ArK =330.41

Integrated Date =375.82±0.98

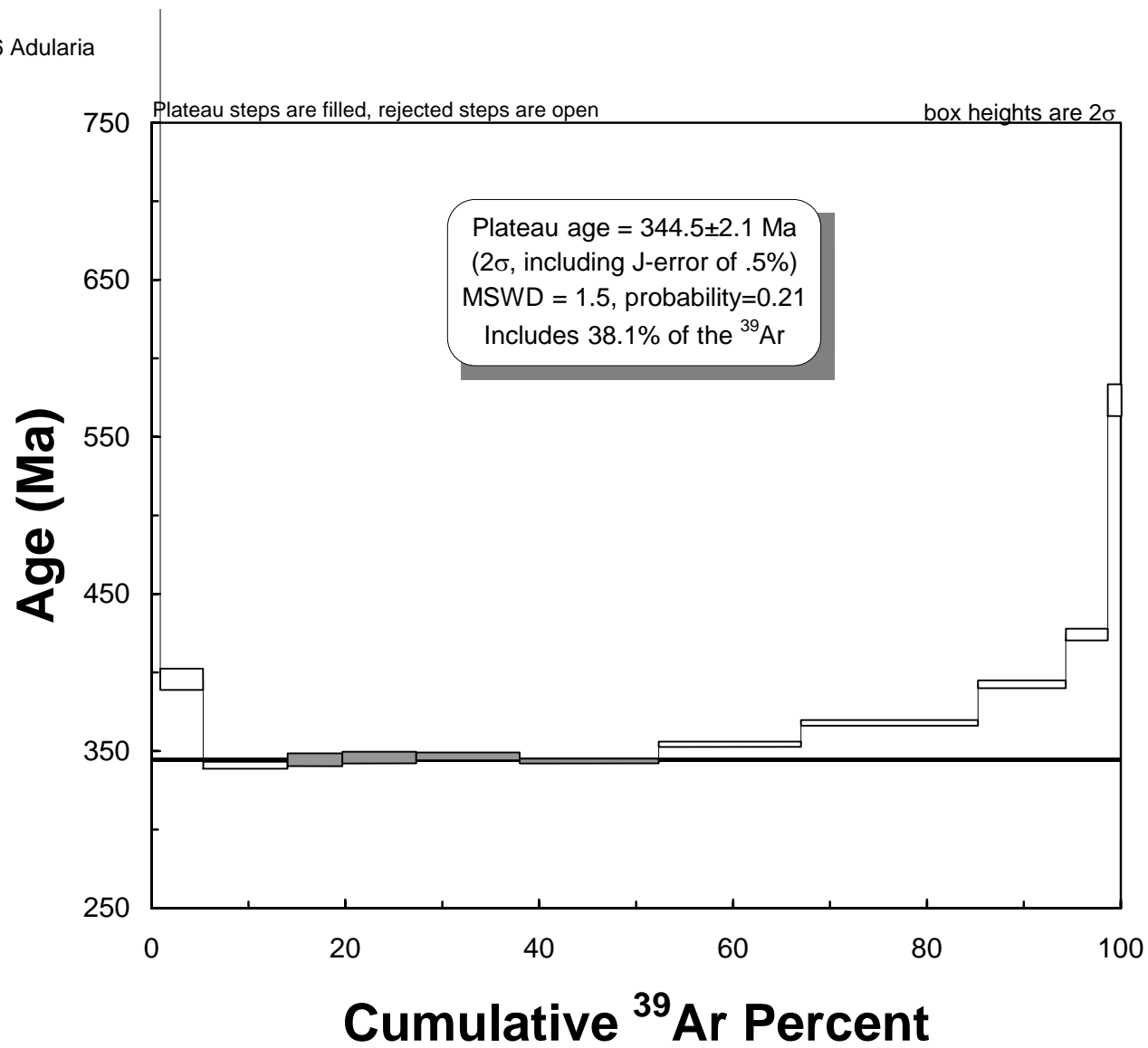
Volumes are 1E-13 cm3 NPT

Neutron flux monitors: 28.02 Ma FCs (Renne et al., 1998)

Isotope production ratios: (40Ar/39Ar)K=0.0302±0.00006, (37Ar/39Ar)Ca=1416.4±0.5, (36Ar/39Ar)Ca=0.3952±0.0004,

Ca/K=1.83±0.01(37ArCa/39ArK).

E42RL1155-36 Adularia



E42RL1155-38 Adularia

Laser Power(%)	Isotope Ratios 40Ar/39Ar	38Ar/39Ar	37Ar/39Ar	36Ar/39Ar	Ca/K	Cl/K	%40Ar atm	f 39Ar	40Ar*/39ArK	Age
2	35.668±0.007	0.065±0.090	0.037±0.088	0.054±0.036	0.258	0.009	44.02	0.85	19.325±0.583	327.26±9.03
2.2	19.316 0.005	0.015 0.085	0.115 0.027	0.003 0.164	0.771	0	4.09	3.83	18.255 0.191	310.62 2.98
2.4	21.192 0.019	0.014 0.063	0.440 0.023	0.002 0.155	2.952	0	2	5.84	20.588 0.418	346.72 6.41
2.6	20.775 0.004	0.014 0.027	0.504 0.014	0.002 0.106	3.381	0	1.11	9.21	20.421 0.102	344.16 1.56
2.7	21.528 0.005	0.013 0.064	0.025 0.047	0.001 0.134	0.166	0	0.91	5.42	21.115 0.112	354.78 1.71
2.8	21.874 0.005	0.013 0.081	0.015 0.107	0.001 0.382	0.104	0	0.75	3.5	21.403 0.174	359.16 2.65
2.9	22.402 0.005	0.014 0.034	0.017 0.044	0.003 0.089	0.117	0	4.07	5.43	21.279 0.138	357.26 2.11
3	21.349 0.004	0.013 0.046	0.012 0.050	0.001 0.266	0.083	0	0.83	8.58	21.015 0.114	353.24 1.74
3.1	21.247 0.004	0.014 0.039	0.007 0.058	0.001 0.168	0.045	0	0.91	10.09	20.912 0.101	351.68 1.54
3.3	21.617 0.004	0.015 0.062	0.003 0.230	0.001 0.234	0.019	0	1.18	4.32	21.103 0.131	354.59 2.01
3.5	21.607 0.004	0.017 0.028	0.000 0.907	0.001 0.107	0.002	0.001	0.97	14.65	21.282 0.097	357.31 1.48
3.6	22.167 0.004	0.016 0.030	0.000 1.137	0.001 0.195	0.002	0	0.55	8	21.879 0.107	366.39 1.62
3.7	22.477 0.004	0.017 0.020	0.000 5.085	0.001 0.319	0.001	0.001	0.63	10.61	22.197 0.116	371.20 1.76
3.8	22.654 0.005	0.017 0.029	0.000 6.027	0.001 0.115	0.002	0.001	0.91	6.64	22.260 0.112	372.15 1.70
3.9	23.153 0.005	0.016 0.064	0.000 7.093	0.002 0.412	0.003	0	1.26	3.04	22.514 0.238	375.98 3.59
Total/Average	21.623±0.001	0.016±0.006	0.299±0.001	0.001±0.023	0.547	0.001		100	21.204±0.022	

J =0.010292±0.000010

Volume 39ArK =690.45

Integrated Date =356.13±0.75

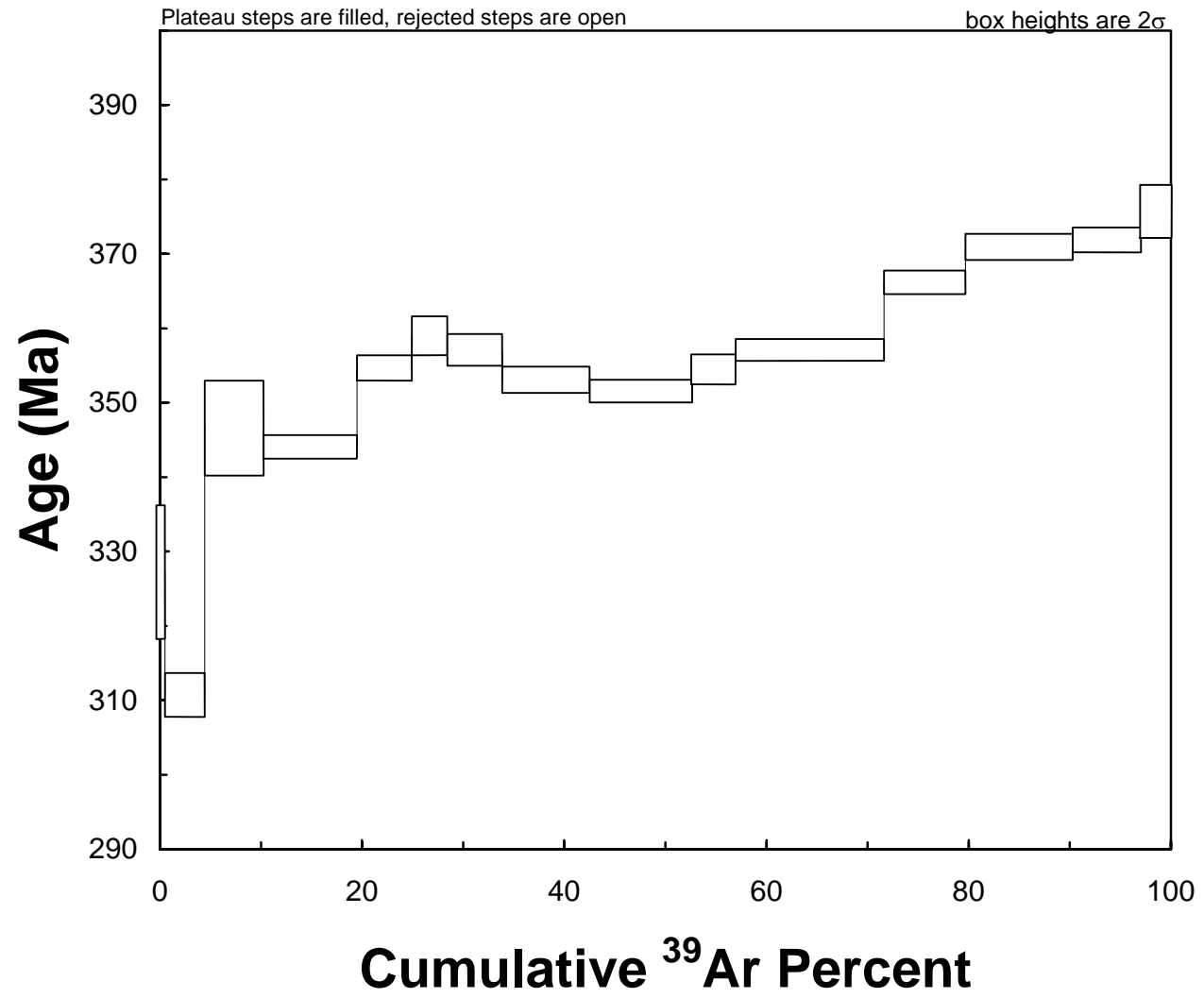
Volumes are 1E-13 cm3 NPT

Neutron flux monitors: 28.02 Ma FCs (Renne et al., 1998)

Isotope production ratios: (40Ar/39Ar)K=0.0302±0.00006, (37Ar/39Ar)Ca=1416.4±0.5, (36Ar/39Ar)Ca=0.3952±0.0004,

Ca/K=1.83±0.01(37ArCa/39ArK).

E42RL1155-38 Adularia



E42RL1155-40 Adularia

Laser Power(%)	Isotope Ratios 40Ar/39Ar	38Ar/39Ar	37Ar/39Ar	36Ar/39Ar	Ca/K	Cl/K	%40Ar atm	f 39Ar	40Ar*/39ArK	Age
2	88.993±0.010	0.223±0.038	0.072±0.068	0.108±0.026	0.488	0.043	35.42	0.58	56.687±0.975	829.27±11.43
2.2	28.070 0.004	0.050 0.021	0.130 0.025	0.009 0.061	0.867	0.008	8.41	3.52	25.493 0.191	420.41 2.81
2.4	19.703 0.005	0.016 0.027	0.391 0.013	0.002 0.123	2.597	0	2.77	6.21	19.025 0.128	322.66 1.99
2.6	20.298 0.004	0.016 0.048	0.805 0.013	0.003 0.085	5.356	0	2.6	9.22	19.692 0.110	332.99 1.69
2.7	21.349 0.004	0.016 0.029	0.900 0.013	0.005 0.040	5.984	0	5.15	10.89	20.187 0.108	340.62 1.66
2.8	21.281 0.005	0.014 0.056	0.572 0.014	0.002 0.217	3.801	0	0.63	2.77	20.896 0.150	351.49 2.29
2.9	21.570 0.005	0.014 0.052	0.176 0.022	0.001 0.338	1.171	0	0.49	2.82	21.194 0.151	356.04 2.30
3	21.476 0.004	0.013 0.038	0.018 0.033	0.001 0.227	0.119	0	0.41	6.76	21.240 0.096	356.74 1.47
3.1	21.512 0.004	0.013 0.030	0.015 0.048	0.001 0.216	0.102	0	0.42	6.41	21.269 0.102	357.19 1.56
3.2	21.436 0.004	0.013 0.046	0.016 0.035	0.001 0.224	0.105	0	0.46	7.45	21.200 0.103	356.12 1.57
3.3	21.419 0.004	0.013 0.043	0.013 0.036	0.000 0.420	0.085	0	0.29	6.36	21.204 0.106	356.19 1.62
3.4	21.517 0.004	0.013 0.029	0.010 0.062	0.001 0.332	0.07	0	0.52	5.05	21.226 0.114	356.53 1.74
3.5	21.420 0.005	0.013 0.058	0.010 0.052	0.001 0.201	0.065	0	0.6	5.89	21.130 0.110	355.06 1.68
3.6	21.640 0.005	0.014 0.041	0.006 0.044	0.001 0.243	0.043	0	0.97	6.84	21.284 0.119	357.41 1.82
3.7	21.541 0.004	0.014 0.027	0.005 0.097	0.001 0.155	0.033	0	0.94	6.05	21.181 0.100	355.84 1.53
3.8	21.415 0.004	0.014 0.024	0.004 0.079	0.001 0.233	0.027	0	0.53	5.57	21.133 0.108	355.10 1.64
4.1	21.596 0.004	0.015 0.039	0.004 0.038	0.001 0.131	0.027	0	1.04	7.62	21.236 0.098	356.67 1.50
Total/Average	21.744±0.001	0.017±0.005	0.830±0.001	0.002±0.013	1.52	0.003		100	21.171±0.018	

J =0.010294±0.000010

Volume 39ArK =972.08

Integrated Date =355.69±0.62

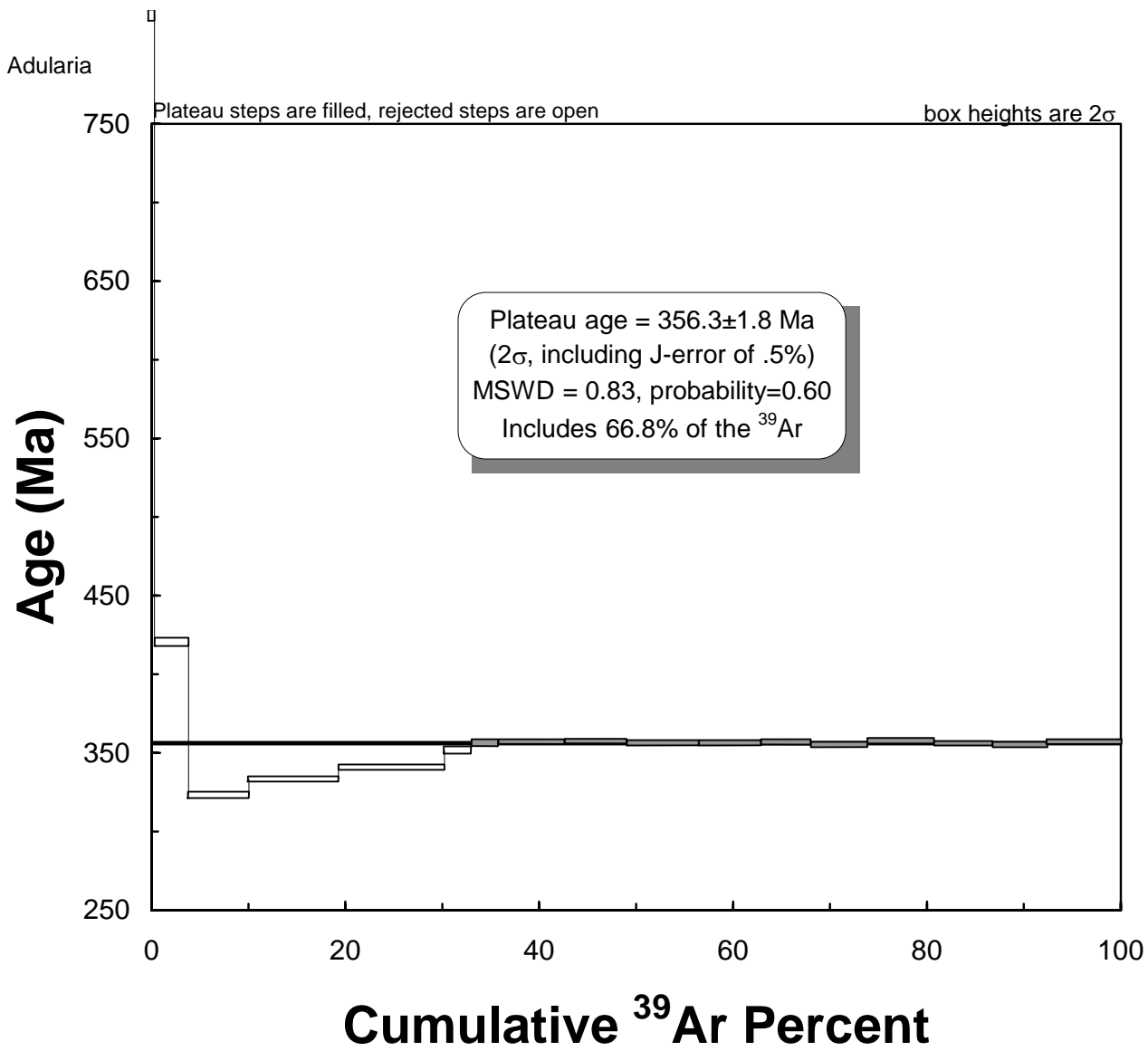
Volumes are 1E-13 cm3 NPT

Neutron flux monitors: 28.02 Ma FCs (Renne et al., 1998)

Isotope production ratios: (40Ar/39Ar)K=0.0302±0.00006, (37Ar/39Ar)Ca=1416.4±0.5, (36Ar/39Ar)Ca=0.3952±0.0004,

Ca/K=1.83±0.01(37ArCa/39ArK).

E42RL1155-40 Adularia



## **APPENDIX B:**

### **48 Multielement + Hg + Au Geochemistry Data Tables**

Sample ID		E42D1000- 16755	E42D1000- 16865	E42D1000- 16975	E42D1000- 17390	E42D1000- 17750	E42D1000- 17850	E42D1009- 12550	
True Depth (m)		154.23	155.24	156.26	160.08	163.39	164.31	96.14	
	Units	Detect. limit							
Ti	%	0.005	0.327	0.322	0.298	0.259	0.297	0.198	0.348
Al	%	0.01	7.96	7.59	6.95	6.71	7.19	5.57	7.6
Fe	%	0.01	4.12	3.73	2.17	1.52	2	4.32	4.44
Mg	%	0.01	1.17	0.98	0.42	0.46	0.46	1.25	1.5
Ca	%	0.01	3.59	3.09	1.11	1.28	1.17	2.93	1.48
Na	%	0.01	0.06	0.05	0.07	0.08	0.09	0.06	0.11
K	%	0.01	3.62	3.44	3.01	2.81	2.97	1.91	3.32
S	%	0.01	1.05	0.37	0.59	0.03	0.04	0.58	0.24
Ag	ppm	0.01	0.26	0.21	0.78	0.04	0	0	0.68
As	ppm	0.2	61.5	29.8	42.7	11.1	6.2	6	34.7
Au	ppm	0.01	0.42	0.14	0.45	0.04	0.02	0	0.26
Ba	ppm	10	610	500	500	210	150	90	220
Be	ppm	0.05	1.21	1.14	1.88	1.92	2.21	0.7	1.41
Bi	ppm	0.01	0.08	0.02	0.04	0.02	0.02	0.03	0.01
Cd	ppm	0.02	0.5	0.67	39.4	0.21	0.13	0.15	0.45
Ce	ppm	0.01	56.6	62.6	41	58.6	50.1	48.1	41
Co	ppm	0.1	7.4	6.3	4.1	2.2	2.4	8.6	11.9
Cr	ppm	1	0	0	1	3	4	4	12
Cs	ppm	0.05	2.76	2.7	3.21	2.65	4.66	1.65	1.69
Cu	ppm	0.2	10.1	11.9	61.3	7.8	9.3	6.9	23.4
Ga	ppm	0.05	19.4	18.2	15.85	15.45	17.65	14.75	18.8
Ge	ppm	0.05	0.15	0.15	0.12	0.13	0.1	0.15	0.17
Hf	ppm	0.1	4.4	4.1	4	4.1	4.3	3.3	3.5
Hg	ppm	0.005	0.005	0.005	0.256	0.012	0	0.005	0.012
In	ppm	0.005	0.067	0.051	0.044	0.033	0.056	0.07	0.046
La	ppm	0.5	26.6	26	16.9	23.7	20	19.6	18.7
Li	ppm	0.2	3.9	4.8	4.5	4	5.4	12.1	17.8
Mn	ppm	5	2010	2340	981	811	720	1510	940
Mo	ppm	0.05	0.39	0.48	2.28	1.24	1.85	0.51	0.61
Nb	ppm	0.1	4.6	4.4	4.4	4.5	4.8	3.9	3.4
Ni	ppm	0.2	1	1.6	1.7	2.4	2	3.1	3.2
P	ppm	10	1030	940	900	830	880	550	1500
Pb	ppm	0.5	14.7	16.5	77.4	7.6	5.3	6.7	9.4
Rb	ppm	0.1	58.9	53.6	47.3	53.6	49.1	30.5	56.4
Re	ppm	0.002	0	0	0.006	0	0	0	0.002
Sb	ppm	0.05	2.73	2.98	3.34	3.29	3.96	3.11	3.16
Sc	ppm	0.1	10	9.8	8.6	8.3	11.3	8.3	15.6
Se	ppm	1	1	0	1	1	0	0	1
Sn	ppm	0.2	1.4	1.2	1.1	1.2	1.3	1.4	0.8
Sr	ppm	0.2	203	218	221	240	215	180.5	101.5
Ta	ppm	0.05	0.23	0.21	0.22	0.23	0.24	0.19	0.23
Te	ppm	0.05	0.18	0.18	0.53	0	0	0	0.5
Th	ppm	0.2	3.5	3.3	3.3	3.4	3.5	2.8	2.6
Tl	ppm	0.02	0.16	0.14	0.13	0.13	0.13	0.06	0.17
U	ppm	0.1	1.9	1.3	1.7	2.1	1.9	1.5	1.5
V	ppm	1	38	40	31	24	51	39	94
W	ppm	0.1	2.5	2.3	2	1.4	1.5	0.9	1.8
Y	ppm	0.1	24.9	22.4	17.2	17.9	20.3	17.2	14.5
Zn	ppm	2	136	150	4160	63	95	204	272
Zr	ppm	0.5	133.5	128	121.5	126	132.5	113.5	110.5
<b>Alteration Index</b>			55.2	56.8	72.4	68.6	71.2	51.1	74.5
<b>CCP Index</b>			62.0	60.4	48.4	43.8	47.4	76.2	66.4

Sample ID	E42D1019- 25320	E42D1060- 10060	E42D1060- 10140	E42D1060- 15330	E42D1060- 15460	E42D1060- 15585	E42D1060- 9460	E42D1060- 9530
True Depth (m)	225.60	84.37	85.04	128.57	129.66	130.71	79.34	79.93
Ti	0.281	0.327	0.354	0.269	0.237	0.294	0.336	0.329
Al	5.69	8.51	8.91	7.67	7.38	8.01	8.29	7.97
Fe	3.15	4.46	5.84	3.54	4.12	4.52	4.77	4.11
Mg	0.48	0.81	0.87	0.87	1.14	1.09	1.1	1.07
Ca	1.19	1.64	2.1	2.18	3.54	1.64	2.68	2.86
Na	0.04	0.07	0.07	3.45	2.81	3.29	0.05	0.06
K	2.56	3.88	4.09	1.52	1.79	2.68	4.07	3.92
S	0.38	0.75	3.5	0.8	1.37	1.4	0.61	0.53
Ag	0.77	0.32	1.28	0.48	0.86	0.4	0.21	0.22
As	31.6	136	384	58.3	71.1	72	37.8	35.2
Au	0.07	0.13	0.8	0.26	0.6	0.66	0.1	0.02
Ba	170	700	290	140	80	400	610	1270
Be	0.88	1.37	1.48	1	1.07	0.99	1.23	1.46
Bi	0.07	0.4	0.09	0.04	0.05	0.04	0.05	0.03
Cd	0.88	0.38	4.34	0.18	0.37	0.14	0.53	0.48
Ce	50.3	47.3	54.7	58.8	59.1	60.5	46.1	52.5
Co	8.9	10.4	17.4	5	7.2	7.8	10.6	9.4
Cr	12	16	18	2	2	2	11	10
Cs	2.55	2.74	3.14	0.74	1.02	0.76	2.93	3.11
Cu	24.8	30.4	33.7	22.3	14.9	14.3	18.5	25.7
Ga	14.5	18.4	21.6	16.25	15.85	19.4	19.5	19.9
Ge	0.13	0.15	0.15	0.13	0.16	0.17	0.15	0.15
Hf	3.2	4	3.9	4.7	4.4	4.9	4.2	4.1
Hg	0.024	0.04	0.187	0.008	0.01	0.016	0.011	0.03
In	0.054	0.053	0.041	0.043	0.031	0.032	0.066	0.071
La	21.5	19.2	22.1	24	24.6	29.2	17.9	21.4
Li	5.2	4.1	4	5.7	4.4	10.3	3.2	3
Mn	1075	1495	1620	1790	1935	1565	1845	1985
Mo	0.69	0.6	1.07	0.71	0.82	0.71	0.4	0.37
Nb	4	4.3	4.2	5.1	4.7	5.2	4.4	4.6
Ni	3.5	7.7	10	3	3.2	4	6.6	5.4
P	1090	890	970	670	750	900	950	980
Pb	12.2	13	40.1	8.5	9.4	23.1	18.8	10.2
Rb	45.5	71.5	74.6	20	27.3	29.1	76	73.8
Re	0	0	0	0.002	0	0	0.002	0
Sb	5.08	4.2	6.54	1.11	1.46	1.16	4.09	3.76
Sc	15	20.1	23.5	9.9	10	12.4	18.4	18.1
Se	1	1	0	0	0	0	0	0
Sn	1.3	1.3	1.6	1.3	1.3	1.4	1.2	1.3
Sr	99.3	60.7	65	405	432	446	62.4	61.4
Ta	0.19	0.21	0.21	0.23	0.22	0.24	0.23	0.23
Te	0.56	0.22	1.05	0.32	0.59	0.13	0	0
Th	2.6	3.2	3.1	3.9	3.6	4.1	3.5	3.6
Tl	0.13	0.25	0.3	0.05	0.09	0.12	0.24	0.23
U	1.5	1.5	1.7	2	1.8	2	1.7	1.6
V	84	126	150	28	36	50	113	103
W	2.6	3.1	4.8	2	2.9	3.6	2.5	2.3
Y	14.3	18.7	19	20.6	19.1	20.4	19.2	20.4
Zn	162	136	568	137	98	203	151	146
Zr	111	130.5	130.5	145.5	138	149.5	123	129
<b>Alteration Index</b>	69.3	71.6	67.7	29.8	31.6	42.8	63.8	61.4
<b>CCP Index</b>	60.7	59.8	64.1	48.1	54.7	49.9	61.6	59.5

Sample ID	E42D1060- 9650	E42D1060- 9760	E42D1061- 10590	E42D1061- 10705	E42D1061- 10820	E42D1061- 10955	E42D1061- 11100	E42D1061- 11160
True Depth (m)	80.93	81.85	88.82	89.78	90.74	91.88	93.09	93.60
Ti	0.316	0.293	0.233	0.302	0.285	0.227	0.255	0.223
Al	8.44	7.45	6.81	8.12	7.47	6.29	7.19	6.33
Fe	4	3	2.14	3.44	2.78	1.53	2.72	1.92
Mg	1.25	0.56	0.38	0.51	0.53	0.3	0.81	0.53
Ca	3.94	1.47	1.08	0.94	1.39	0.7	2.77	1.54
Na	0.08	0.07	0.06	0.07	0.09	0.06	0.09	0.05
K	3.73	3.35	2.78	3.39	3.11	2.66	3.01	2.68
S	1.35	1.63	0.91	0.61	0.55	0.48	0.42	0.36
Ag	0.49	0.69	0.58	0.32	0.35	0.34	0.26	0.26
As	105	220	79.1	62.2	58.4	62.1	63.4	48.1
Au	0.13	0.28	0.38	0.15	0.12	0.15	0.17	0.11
Ba	1200	820	600	1090	1110	620	2460	850
Be	1.24	1.22	1.76	2.23	1.47	2.16	1.46	2.02
Bi	0.31	0.03	0.08	0.14	0.04	0.04	0.05	0.02
Cd	0.38	4.08	0.53	0.51	6.41	0.09	0.25	0.21
Ce	47.5	31.6	54.1	64.6	68.3	55.6	59.5	57.4
Co	9.7	9	3.5	6.1	5.7	3.8	7.8	4.8
Cr	10	10	0	0	1	0	0	1
Cs	2.54	2.46	1.35	1.51	2.04	1.35	2.5	1.3
Cu	27.8	15.8	7.3	11.2	13.7	9.1	24.9	93.6
Ga	18.4	16.95	15.35	20.3	19.3	15.7	16.35	15.35
Ge	0.15	0.1	0.11	0.15	0.14	0.1	0.12	0.1
Hf	3.7	3.5	4.1	5.1	4.6	4.3	4.6	4
Hg	0.052	0.1	0.027	0.016	0.099	0.016	0.047	0.018
In	0.038	0.04	0.039	0.059	0.053	0.046	0.057	0.053
La	19.6	13	22.6	30.6	32.4	23.2	26.3	24.7
Li	3.7	5	1.8	2.6	3.4	2.8	3.9	3
Mn	1975	679	742	1465	1325	418	1750	1045
Mo	5.92	4.05	1.48	2.54	2.99	1.8	2.19	3.29
Nb	4.2	4	4.9	5.6	5.5	4.6	4.9	4.5
Ni	7.1	8.1	1.9	3.1	2.4	1.8	2.8	1.8
P	940	830	760	1140	1100	840	940	870
Pb	56.8	158	71.3	31.7	71.9	7.5	11.2	10.5
Rb	68.5	59.8	59.1	66.5	59	54.9	53.2	55.6
Re	0.004	0.003	0	0.002	0.003	0.002	0.004	0.003
Sb	6.71	7.85	4.22	4.1	5.23	4.29	7.12	5.44
Sc	16.7	14.8	6.6	10.9	10.2	8	9.2	8
Se	0	0	0	1	0	0	0	1
Sn	1.2	1.4	1.5	1.7	1.6	1.5	1.3	1.4
Sr	97.2	56.7	172	200	203	158	210	168
Ta	0.2	0.19	0.25	0.27	0.3	0.25	0.26	0.23
Te	0.11	0.25	0.26	0.19	0.22	0.24	0.11	0.07
Th	3	2.7	3.9	4.3	4.3	3.7	3.7	3.4
Tl	0.24	0.21	0.18	0.2	0.43	0.3	0.28	0.23
U	1.5	2	1	1.1	1.6	2.4	2.1	2.2
V	99	91	12	28	27	20	27	18
W	2.3	3.1	1.9	2.5	4.1	2.5	3.1	2.1
Y	18.2	12.8	17.8	20.3	20	19.7	19.7	18.3
Zn	117	680	92	133	825	42	77	62
Zr	125.5	117.5	123	153.5	144	135	144.5	125
<b>Alteration Index</b>	53.9	69.8	71.4	77.8	69.1	77.7	55.4	64.9
<b>CCP Index</b>	61.1	53.7	49.7	55.8	53.5	42.9	56.4	50.4

Sample ID	E42D1061- 11305	E42D1061- 11715	E42D1061- 11870	E42D1061- 11985	E42D1061- 12080	E42D1061- 12425	E42D1061- 12530	E42D1061- 12625
True Depth (m)	94.81	98.25	99.55	100.51	101.31	104.20	105.09	105.88
Ti	0.256	0.293	0.261	0.356	0.278	0.292	0.281	0.331
Al	6.76	7.51	6.68	9.03	6.89	7.31	7.33	7.68
Fe	2.84	3.51	3.08	2.55	3.78	2.09	2.85	3.02
Mg	0.55	0.44	0.46	0.54	0.6	0.45	0.68	0.54
Ca	1.08	0.74	0.85	1	1.13	1.19	1.94	1.35
Na	0.07	0.08	0.07	0.1	0.09	0.08	0.13	0.07
K	2.89	3.21	2.91	3.8	2.89	3.12	3.03	3.32
S	0.14	1.6	0.84	0.08	0.8	0.22	0.19	0.47
Ag	0.17	1.07	0.27	0.22	2.79	0.51	0.28	0.28
As	31.8	148.5	65.2	15.4	44.2	37.3	42	89.1
Au	0.08	0.26	0.18	0.04	1.36	0.1	0.11	0.13
Ba	550	620	300	1400	310	540	590	1030
Be	1.56	1.22	1.05	2.39	1.3	1.73	1.47	1.78
Bi	0.02	0.17	0.05	0.06	0.12	0.22	0.03	0.03
Cd	2.6	2.78	0.95	0.9	4.82	0.35	1.18	0.36
Ce	60	58.8	62.9	63.1	59.1	60.2	60.4	63.3
Co	4.5	10.1	8.1	3.2	9	8.6	3.3	4.8
Cr	0	0	0	1	2	1	1	2
Cs	1.79	2.31	2.2	2.75	2.56	1.82	2.28	1.32
Cu	12.2	23.8	22.3	60.1	98.8	59.7	8.7	14.6
Ga	16.55	19.25	17	22.7	17	19	18.05	19
Ge	0.13	0.13	0.14	0.14	0.14	0.13	0.14	0.17
Hf	4.2	4.9	4.5	5.7	4.3	4.1	4.8	4.9
Hg	0.037	0.09	0.031	0.011	0.082	0.033	0.016	0.017
In	0.065	0.064	0.055	0.059	0.051	0.053	0.045	0.063
La	25.3	24	26.5	26.2	24.6	28.7	25.2	29.6
Li	3.6	4.6	3.8	4.5	3.9	4	4	3.5
Mn	1745	738	1470	1250	1370	884	1950	1660
Mo	1.44	1.71	1.06	1.15	1.45	1.1	0.84	1.15
Nb	4.7	5.3	4.8	6.3	5	5.4	5.4	5.2
Ni	1.7	3.1	2.9	1.4	3.6	3.5	2.1	1.5
P	880	960	960	1120	940	940	950	1080
Pb	81.2	93.5	33.2	134.5	90.7	18	88.5	12.9
Rb	58.9	58.9	54.3	73.3	52.7	64.6	55.5	66
Re	0	0.002	0	0.002	0.002	0.002	0	0.002
Sb	4.82	5.97	5.49	5.12	5.93	6.44	4.36	3.97
Sc	9.8	11.5	10.5	12.9	10.9	11.7	10.7	11.3
Se	1	1	1	0	1	0	0	0
Sn	1.5	1.8	1.5	1.7	1.4	1.5	1.4	1.6
Sr	143.5	132	155	267	186	176	178.5	150
Ta	0.24	0.27	0.24	0.33	0.24	0.27	0.27	0.26
Te	0.06	0.73	0.19	0.13	1.54	0.13	0.09	0.13
Th	3.6	4	3.6	4.8	3.5	4.1	4.2	4
Tl	0.22	0.21	0.2	0.23	0.17	0.32	0.21	0.21
U	1.9	2.1	2	2	1.8	1.8	2.1	2.4
V	25	32	30	37	34	34	30	35
W	2.3	3.9	3.6	3.3	2.7	2.4	2.9	3.3
Y	19.7	22.7	20.8	24.9	21.5	21.7	25.9	23.3
Zn	387	385	170	168	660	104	199	96
Zr	132	152.5	137.5	182.5	130.5	130	147	153
<b>Alteration Index</b>	73.2	80.1	76.9	78.1	72.4	71.8	62.3	71.2
<b>CCP Index</b>	56.1	56.9	56.8	47.0	61.9	47.0	55.6	53.9

Sample ID	E42D1061- 15490	E42D1061- 15605	E42D1061- 15690	E42D1061- 15855	E42D1061- 15960	E42D1061- 16090	E42D1061- 16295	E42D1061- 16980
True Depth (m)	129.91	130.87	131.59	132.97	133.85	134.94	136.66	142.41
Ti	0.299	0.318	0.342	0.31	0.34	0.329	0.268	0.284
Al	7.17	7.72	7.66	7.87	8.75	8.18	8.7	7.34
Fe	3.45	3.53	2.12	2.18	3.89	3.33	4.31	3.07
Mg	0.55	0.61	0.31	0.4	1.19	0.61	0.87	0.75
Ca	0.92	1.21	0.51	0.75	3.82	1.23	2	1.7
Na	0.11	0.1	0.1	0.09	0.09	0.11	0.07	0.07
K	3.02	3.2	3.27	3.36	3.82	3.56	4.06	3.14
S	0.29	0.31	0.66	0.3	1.02	0.11	0.69	0.37
Ag	0.14	0.27	0.38	0.14	0.18	0.05	0.33	0.5
As	49.8	60	134	41.3	116.5	8	47.2	53.4
Au	0.04	0.27	0.23	0.07	0.14	0.04	0.15	0.25
Ba	180	270	540	420	230	780	160	200
Be	1.08	1.23	2.04	1.24	0.87	1.86	1.29	1.63
Bi	0.02	0.03	0.02	0.03	0.05	0.02	0.05	0.07
Cd	0.18	1.19	0.23	0.08	0.74	0.19	0.42	0.39
Ce	61.8	54.6	65.3	65.8	63.4	62.7	20	57.8
Co	7	6.2	6.4	8.3	4.7	5.4	11.8	8.3
Cr	1	0	0	0	0	0	17	0
Cs	3.3	2.79	2.29	2.79	3.71	3.68	4.49	2.92
Cu	16.5	14.4	21.9	33.2	25	37.3	204	15.3
Ga	18.55	17.85	20.3	19.4	20.2	19.5	19.2	17.5
Ge	0.14	0.15	0.12	0.12	0.16	0.15	0.11	0.14
Hf	4.3	4.4	4.6	4.9	4.7	4.7	2.9	4.2
Hg	0.011	0.024	0.019	0.024	0.012	0.007	0.009	0.01
In	0.039	0.037	0.033	0.037	0.087	0.037	0.067	0.075
La	25.9	25.7	27.7	27.8	30.7	25.4	8.8	24.1
Li	4.2	3.9	3.7	3.8	4.1	4.6	5.9	3.8
Mn	1290	1515	522	517	2080	1260	1740	1310
Mo	1.58	0.75	2	1.55	0.5	0.93	1.23	0.99
Nb	4.7	4.6	4.8	5	4.8	4.9	6.9	4.5
Ni	2.5	1.7	1.9	1.9	1.7	1	5.8	2.8
P	930	1030	1060	990	1050	950	880	800
Pb	8.4	56.3	24.7	5.5	28.9	5.5	13.7	13.5
Rb	54.8	58.4	67.3	64.5	63.4	71.2	72.9	55.2
Re	0	0	0.003	0.002	0	0.002	0	0
Sb	4.29	3.92	5.03	4.84	4.08	3.86	4.97	4.78
Sc	9.9	9.9	10.5	9.5	9.4	9.9	11.8	8.4
Se	0	0	1	0	0	0	0	0
Sn	1.2	1.2	1.7	1.4	1.5	1.2	1.2	1.4
Sr	221	242	270	210	193.5	278	138.5	172.5
Ta	0.23	0.23	0.24	0.25	0.25	0.25	0.45	0.22
Te	0.09	0.16	0.26	0.11	0.12	0.06	0.27	0.55
Th	3.6	3.7	3.8	4	4	4.1	2.6	3.6
Tl	0.18	0.19	0.19	0.19	0.21	0.19	0.23	0.16
U	2	1.9	2.5	2.3	2	2.1	1.5	1.7
V	43	40	48	32	35	33	111	35
W	2.1	2.2	2.4	2.3	5.4	3	3.3	3.2
Y	21.4	21.5	21.9	21.1	24.7	22.5	15	20.3
Zn	84	231	78	78	141	89	136	114
Zr	135.5	135	143	149.5	147.5	147.5	110.5	135
<b>Alteration Index</b>	76.0	72.7	84.0	80.1	54.6	73.9	68.6	67.0
<b>CCP Index</b>	58.6	58.2	44.3	45.4	59.6	54.4	58.4	57.3

Sample ID	E42D1063- 15530	E42D1063- 15650	E42D1063- 15750	E42D1063- 15942	E42D1063- 16025	E42D1063- 16190	E42D1063- 20570	E42D1063- 20660
True Depth (m)	130.25	131.25	132.09	133.70	134.40	135.78	172.51	173.27
Ti	0.351	0.353	0.358	0.3	0.324	0.356	0.307	0.312
Al	8.45	8.18	8.12	7.67	7.97	8.08	7.86	7.83
Fe	1.96	2.53	3.08	2.59	3.06	3.03	3.8	4.06
Mg	0.25	0.45	0.43	0.31	0.37	0.33	0.66	0.79
Ca	0.48	1.39	1.15	0.41	0.61	0.75	4.55	3.62
Na	0.09	0.09	0.08	0.09	0.08	0.08	0.06	0.06
K	3.57	3.39	3.26	3.1	3.26	3.21	3.53	3.45
S	0.19	0.67	0.56	0.34	0.62	1.05	1.09	1.59
Ag	0.31	0.31	0.62	0.2	0.4	0.35	0.1	0.37
As	30.8	94.7	84	70.4	131.5	169	28.9	219
Au	0.06	0.29	1.12	0.17	0.14	0.28	0.09	0.22
Ba	400	470	380	390	500	1030	490	460
Be	2.15	2.38	2.91	2.38	2.35	2.63	1.48	1.47
Bi	0.03	0.03	0.05	0.01	0.03	0.06	0.05	0.13
Cd	0.06	1.58	0.64	0.13	0.32	0.31	0.16	0.2
Ce	47.5	59.3	48	55.2	55	55.1	59.5	64.3
Co	5.3	10.3	7.6	4.4	7.2	6.4	6	7.7
Cr	11	9	13	6	5	8	0	1
Cs	2.8	2.33	1.9	1.57	1.91	2.24	2.56	3.75
Cu	11.1	21.8	18.5	7.9	9.9	13.3	10.4	68
Ga	19.7	19.1	19.15	18.65	20.4	20.7	18.2	19.4
Ge	0.11	0.15	0.13	0.12	0.13	0.13	0.16	0.17
Hf	4.1	4.6	3.8	5.2	5.2	4.7	4.9	4.7
Hg	0	0.017	0.014	0	0.012	0.008	0	0.067
In	0.059	0.076	0.052	0.046	0.059	0.066	0.065	0.065
La	19.5	23.9	19.3	21.8	21.9	22	28	27
Li	4.3	3.7	3.5	2.7	2.9	3.1	3.6	4.9
Mn	514	584	1090	709	872	799	1780	1520
Mo	1.56	2.65	1.24	1.14	1.29	1.14	0.71	1.05
Nb	4.7	5.3	4.4	5.8	5.6	5.2	5.2	5
Ni	3.5	6.1	4.3	3.8	4.9	3.4	2.1	2.7
P	1030	1100	1090	840	1020	1070	950	970
Pb	31.4	32	46.2	23.8	29.2	76.7	14.1	25.8
Rb	78.1	66	61.5	53.1	60.7	62.6	70.5	68.4
Re	0	0.003	0	0	0	0	0	0
Sb	4.03	4.48	4.25	3.83	4.03	3.94	1.94	3.53
Sc	15.8	17.6	18.2	12.5	15.1	15.5	11.4	12.1
Se	0	0	0	0	1	1	0	0
Sn	1.4	1.4	1.4	1.6	1.6	1.6	1.5	1.5
Sr	62.9	64.4	71.7	60.2	67.7	72.2	183.5	139
Ta	0.24	0.26	0.22	0.29	0.28	0.26	0.26	0.25
Te	0.12	0	0.1	0	0.11	0.06	0	0.08
Th	3.2	3.6	2.9	4.3	4.2	3.8	4.1	4
Tl	0.28	0.23	0.27	0.18	0.22	0.19	0.21	0.26
U	1.6	1.8	1.4	2.5	2.3	2.1	2.1	2
V	118	104	111	62	83	87	35	42
W	3.1	3	2.8	2.6	3.5	3.4	2.1	2.2
Y	18.7	22.1	18.5	24.1	22.9	21	24.4	22.7
Zn	34	288	130	53	89	115	86	91
Zr	128	143.5	129.5	162	157.5	142.5	150.5	143
<b>Alteration Index</b>	85.6	70.0	73.0	85.9	82.5	79.2	45.3	51.5
<b>CCP Index</b>	39.9	48.8	53.7	49.9	53.0	52.8	58.0	60.7

Sample ID	E42D1063- 20750	E42D1063- 6525	E42D1063- 6670	E42D1063- 6730	E42D1080- 18575	E42D1111- 6340	E42D1111- 30960	E42D1111- 38440
True Depth (m)	174.02	54.72	55.94	56.44	179.42	56.98	273.36	332.9
Ti	0.345	0.289	0.277	0.229	0.477	0.404	0.328	0.365
Al	7.91	8.92	8.34	7.23	8.57	8.01	6.82	7.57
Fe	5.15	5.1	2.63	4.02	2.5	5.34	4.33	4.41
Mg	0.9	1.08	0.51	1.27	0.39	1.29	1.51	1.37
Ca	2.58	3.59	1.45	3.89	1.81	2.39	3.04	0.8
Na	0.08	0.15	0.16	0.1	0.08	0.67	0.31	3.13
K	3.35	3.55	3.13	2.7	3.55	2.63	3.61	1.48
S	2.55	2.13	0.45	1.13	0.38	0.43	0.43	0.32
Ag	2.53	2.4	0.25	0.23	0.47	0.2	0.35	0.32
As	478	240	52.7	44.2	63.3	18.1	97.8	29.2
Au	0.34	0.8	0.06	0.06	0.58	0.24	0.65	0.3
Ba	370	620	2020	730	270	560	690	400
Be	1.1	0.68	1.83	1.57	3.26	1.07	1.3	0.81
Bi	0.26	0.03	0.06	0.03	0.04	0.02	0.02	0.06
Cd	4.18	2.74	0.35	0.85	0.13	0.09	1.25	2.02
Ce	45.4	16.05	20.4	24.8	39	57.4	48.3	58.1
Co	16.8	42.8	7.7	14.8	7.5	9.4	9.6	8.5
Cr	22	2	7	13	6	24	55	58
Cs	2.25	3.58	3.35	2.59	3.5	1.13	1.18	0.35
Cu	21.8	75.9	36.2	8.9	7.3	14.9	35.4	12.6
Ga	19.15	16.15	15.3	12.9	20	19.35	16.5	20.1
Ge	0.16	0.13	0.09	0.11	0.1	0.21	0.18	0.21
Hf	3.5	1.7	1.5	1.2	3	4.9	4.1	4.8
Hg	0.093	0.163	0.016	0.029	0.007	0.01	<0.005	0.03
In	0.044	0.053	0.034	0.029	0.05	0.048	0.054	0.055
La	19.1	6.6	8.7	11	15.9	27.1	23.5	27.4
Li	4.6	6.1	7.2	5.1	5	18.4	17.7	15.7
Mn	2070	2220	784	2520	929	1860	2020	1385
Mo	1.57	2.5	1.3	1.48	0.58	1.4	0.59	1.36
Nb	4.2	2.7	2.5	2.2	4	4.6	3.9	4.6
Ni	9.6	9	3.8	5.4	2.5	1.9	5.5	4.5
P	900	720	740	570	1890	1270	1000	1020
Pb	302	165.5	101.5	30.1	13.2	6.4	157	9.2
Rb	65.3	63.8	53.2	45.5	53.9	45.2	60	21.6
Re	0	0	0	0	0	0.002	0.002	<0.002
Sb	8.66	7.8	5.09	5.3	5.86	2.21	1.74	1.1
Sc	25.5	28.1	20.9	18.7	18.7	13.8	13.5	14
Se	0	0	0	0	0	2	1	2
Sn	1.4	0.7	0.6	0.6	1.1	1.2	1	1.5
Sr	111	76	77.2	96.1	164	144	223	239
Ta	0.2	0.15	0.13	0.11	0.21	0.28	0.25	0.28
Te	0.12	0.14	0	0	0.16	0.09	0.09	0.16
Th	2.6	0.9	0.8	0.7	2.1	3.5	2.9	3.5
Tl	0.37	0.32	0.2	0.18	0.25	0.14	0.17	0.07
U	1.6	0.5	0.5	0.4	1.3	2.4	1.8	2.1
V	156	198	164	140	162	66	76	70
W	3.5	2.9	2.6	2.4	3	1.8	1.9	3.4
Y	15.6	10.3	7.5	7.9	15.6	21.2	19.1	20.1
Zn	727	464	121	255	59	125	349	413
Zr	117.5	56.8	47.7	35.8	107.5	150.5	128	148
<b>Alteration Index</b>	59.8	53.7	67.3	49.0	65.1	55.5	59.5	43.2
<b>CCP Index</b>	66.2	65.1	51.5	68.2	46.8	68.9	62.9	57.0

Sample ID	E42D1111- 46100	E42D1111- 46230	E42D1111- 46340	E42D1111- 46455	E42D1111- 46520	E42D1111- 46630	E42D1170- 21930	E42D1170- 26620
True Depth (m)	399.24	400.36	401.32	402.31	402.88	403.83	189.92	230.54
Ti	0.387	0.35	0.328	0.43	0.422	0.411	0.317	0.318
Al	8.11	7	8.03	8.75	9.33	8.11	7.29	5.17
Fe	4.82	4.2	5.11	4.23	5.21	4.03	4.75	5.22
Mg	1.2	1.05	1.28	0.81	1	0.6	1.01	0.97
Ca	1.72	2.01	2.86	0.61	0.6	0.5	0.96	1.47
Na	0.83	1.33	0.09	0.17	0.14	0.15	2.79	0.15
K	2.59	1.97	2.88	3.01	3.03	2.89	1.71	1.59
S	0.18	0.19	0.48	0.41	0.18	1.56	0.48	0.53
Ag	0.07	0.09	0.83	0.65	0.45	3.41	0.41	0.29
As	7.9	8	65.1	79	28.4	226	74.3	62.1
Au	0.3	0.28	0.32	0.32	0.26	0.79	0.3	0.26
Ba	580	420	820	830	760	720	270	170
Be	1.37	1.14	1.24	2.4	2.21	2.41	0.86	0.84
Bi	<0.01	0.01	0.03	0.02	0.18	0.11	0.05	0.07
Cd	0.07	0.12	0.1	0.03	0.17	0.06	0.64	0.2
Ce	58.5	55.3	39.5	82.9	80.7	70.9	58.4	69.1
Co	9.3	8.1	21	9.8	10.5	14.9	7.4	12.2
Cr	34	36	27	35	33	43	42	61
Cs	1.2	1.1	2.22	2.12	1.86	1.79	0.59	0.9
Cu	7.2	25.2	71.3	8.7	8.3	11.7	41.6	21
Ga	20.4	18.75	17.65	25.2	26.3	23.9	16.95	16
Ge	0.22	0.18	0.18	0.24	0.27	0.22	0.2	0.2
Hf	4.7	4.4	3	5.4	6	5.6	4.7	4.4
Hg	<0.005	0.006	0.015	<0.005	0.007	0.005	0.008	<0.005
In	0.097	0.114	0.05	0.04	0.038	0.024	0.048	0.085
La	28.4	26.6	18.9	39.9	38.8	34.9	26.9	34.8
Li	19.2	16.3	17.7	24.4	32.4	19.1	17.4	21.1
Mn	1295	1450	1710	759	895	549	1265	2310
Mo	1.25	1.11	1.05	0.89	0.61	1.26	1.19	1.53
Nb	4.3	4.2	3	5.3	5.6	5.2	4.3	4
Ni	1.8	2	7.2	3.1	3.6	3.3	2.5	3.6
P	1050	920	900	1540	1540	1310	1000	910
Pb	8.3	3.3	20.8	10.4	7.6	27.6	22.4	34.5
Rb	47	36.4	71.1	52.5	49.9	44.1	24.8	25.8
Re	0.004	<0.002	<0.002	0.002	0.002	<0.002	<0.002	0.002
Sb	1.65	1.55	3.02	3.68	3.43	4.59	1.11	2.35
Sc	12.7	11.7	23.6	16.2	17.4	13.1	9.7	10.2
Se	1	2	1	2	2	2	1	1
Sn	1.7	1.7	0.9	1.7	1.7	1.8	1.2	1.1
Sr	130.5	145.5	131	193	195.5	193	410	125
Ta	0.27	0.26	0.2	0.31	0.34	0.3	0.28	0.22
Te	<0.05	<0.05	0.81	0.27	0.16	1.85	0.21	0.07
Th	3.4	3.2	2	4	4.4	4	3.5	3.1
Tl	0.14	0.11	0.19	0.17	0.15	0.14	0.11	0.1
U	2.3	2.2	1.4	2.7	3.1	2.6	2.5	1.6
V	61	59	162	73	72	53	35	45
W	1.2	1.9	3.6	3.4	2.2	2.9	3.5	3.2
Y	18	17.3	16.5	25.7	27.1	24	20.1	21
Zn	127	110	234	101	133	68	240	172
Zr	148	139	100.5	167.5	185	173	148	139
<b>Alteration Index</b>	59.2	47.2	57.6	82.1	83.8	83.2	42.3	60.9
<b>CCP Index</b>	65.9	63.2	70.8	63.8	68.5	62.7	57.2	79.7

Sample ID	E42D1170- 27440	E42D1170- 44320	E42D1321- 8455	E42D1321- 8580	E42RL1128- 13	E42RL1128- 15	E42RL1155- 8	E42RL1155- 9
True Depth (m)	237.64	383.82	76.63	77.76	72	72	45.00	45.00
Ti	0.277	0.378	0.249	0.241	0.309	0.347	0.379	0.305
Al	6.03	7.53	7.13	7.17	6.96	8.15	10.35	9.24
Fe	3.41	5.8	3.38	3.27	5.19	5.88	7.84	6.34
Mg	0.8	1.85	0.9	0.73	1.08	1	1.31	1.54
Ca	1.85	1.96	1.98	0.97	2.87	6.09	3.28	4.22
Na	1.27	3.97	0.18	0.11	0.04	0.09	0.17	0.13
K	2.24	0.77	2.5	2.48	2.8	3.13	4.33	3.95
S	0.66	0.03	0.38	0.38	1.64	0.34	1.99	0.73
Ag	0.74	0.19	0.51	0.79	0.97	0.52	1.47	0.74
As	83	8.7	30.5	31.8	378	15.1	116.5	28.1
Au	0.2	0.28	0.06	0.05	1.28	1.44	0.51	0.15
Ba	340	250	270	410	390	180	580	610
Be	0.91	0.9	1.78	1.43	1.15	0.96	0.83	0.99
Bi	0.04	0.01	0.03	0.03	0.06	0.04	0.18	0.11
Cd	1.44	0.08	3.43	8.45	1.16	0.31	6.07	0.39
Ce	50.8	45.1	60.3	59.3	45.8	33.1	24.8	26.7
Co	5.3	16.6	5.6	5.3	12.2	20.3	29.4	21.7
Cr	72	32	0	1	64	46	45	41
Cs	0.86	0.26	2.48	1.85	2.24	3.06	3.51	2.98
Cu	23.1	18.9	49.9	48.3	43.1	177.5	66.5	121.5
Ga	16.05	16.95	17.4	16.8	15.5	16.55	21.7	17.75
Ge	0.16	0.19	0.17	0.15	0.16	0.16	0.28	0.16
Hf	4	3.2	4.7	4.6	3.6	2.3	3.2	3.3
Hg	0.007	0.008	0.057	0.131	0.024	0.007	0.126	0.018
In	0.035	0.057	0.065	0.03	0.055	0.066	0.051	0.044
La	23.8	21.5	25.3	25.1	21.6	15.2	9.4	10.3
Li	10.4	9.7	10	17.6	12.4	14.9	4.8	4.6
Mn	1310	1460	1360	1095	1355	1935	2720	2450
Mo	0.66	1.1	0.4	1.43	0.91	0.74	2.83	0.67
Nb	3.5	3.1	4.9	4.9	3.4	2.4	3.6	2.9
Ni	1.9	3.6	2.4	3.1	5.7	12.3	12.5	9.6
P	860	1720	590	550	880	850	1520	930
Pb	19.8	11.3	342	520	64.4	12	658	30.2
Rb	35.5	11	46.6	56.6	56.2	56.2	71.3	75.1
Re	0.002	0.002	0	0.002	<0.002	<0.002	0.003	0
Sb	1.39	1.16	3.02	2.43	3.92	3.09	5.95	5.42
Sc	8.9	18.3	8.8	8	16.6	27.8	0	0
Se	2	1	0	0	1	1	1	0
Sn	1	0.8	1.6	1.2	1	0.7	1	0.6
Sr	179.5	439	109.5	63.2	106	145	69.5	88.3
Ta	0.22	0.21	0.25	0.23	0.26	0.21	0.29	0.19
Te	0.39	<0.05	0.25	0.47	0.27	0.17	0.6	0.21
Th	2.9	2.3	4.1	4.1	2.5	1.5	2.9	2.3
Tl	0.12	0.04	0.19	0.21	0.23	0.22	0.56	0.41
U	1.7	1.6	2.4	2	1.8	1.1	2.5	1.5
V	40	165	25	23	106	220	251	200
W	2.2	1.3	2.3	2	3.1	1.6	2.7	1.6
Y	17.1	16.4	20.2	19.8	17.3	13.2	13.7	16.9
Zn	287	162	553	1260	305	238	775	191
Zr	120	98.2	142	139.5	112.5	71.5	97.2	103
<b>Alteration Index</b>	48.3	33.0	59.9	73.6	55.9	38.6	60.5	54.6
<b>CCP Index</b>	56.4	62.6	64.2	63.3	71.2	70.3	69.2	68.5

Sample ID	E42RL1155- 10	E42RL1155- 11	E42RL1155- 12	E42RL1155- 13	E42RL1155- 14	E42RL1155- 15	E42RL1155- 16
True Depth (m)	45.00	45.00	45.00	45.00	45.00	45.00	45.00
Ti	0.276	0.345	0.326	0.299	0.273	0.693	0.578
Al	9.06	8.89	9.13	9.28	8.16	10.7	8.9
Fe	5.29	6.04	6.33	6.33	6.65	3.88	6.82
Mg	1.16	0.87	1.48	1.83	1.86	0.54	1.04
Ca	3.84	1.9	4.37	5.66	4.95	1.01	3.13
Na	0.13	0.13	0.14	0.13	0.12	0.18	0.11
K	3.89	3.32	4.13	4.07	3.52	4.82	3.89
S	0.49	0.18	1.74	1.5	0.89	1.05	5.16
Ag	0.48	0.35	0.8	0.81	1.38	1.87	1.94
As	23.8	19.6	105.5	131	40.4	79	1115
Au	0.14	0.17	0.86	0.32	0.08	0.1	0.44
Ba	560	430	680	360	280	550	230
Be	0.97	1.13	0.84	0.83	0.72	0.75	0.67
Bi	0.04	0.02	0.08	0.06	0.07	0.02	0.09
Cd	0.6	0.24	0.87	0.62	0.5	17.65	8.56
Ce	28	39.2	21.7	33.5	36.3	37.5	43.4
Co	16.9	13.1	23.1	22.4	18.8	17.3	17.5
Cr	42	30	47	48	34	9	4
Cs	3.09	2.09	2.93	3.36	4.4	4.57	2.91
Cu	35.5	54.6	25.3	65.4	522	330	89.8
Ga	16.6	15.8	18.95	17.25	15.65	22.8	17.9
Ge	0.12	0.18	0.15	0.16	0.18	0.13	0.18
Hf	2.3	2.3	2.8	2.7	2.5	5	4.3
Hg	0.027	0.012	0.04	0.056	0.017	0.109	0.181
In	0.043	0.037	0.041	0.048	0.048	0.064	0.032
La	10.9	16.2	7.7	13.2	14.1	17.2	18.8
Li	3.7	17.3	4.2	2.6	3	4.4	3.6
Mn	2360	1820	2540	2930	2810	530	1540
Mo	0.9	1.72	1.82	0.72	0.77	1.99	2.06
Nb	2.5	4.3	2.4	2.2	2.2	9.8	8.1
Ni	16.5	10.9	11.2	10.8	13.2	8.6	10.3
P	1120	1110	1110	1040	1170	1900	1660
Pb	16.3	17.5	34.1	44.9	20.9	146	374
Rb	73.7	66.6	61.6	74.3	63.1	88.4	60.5
Re	0	0.002	0.002	0	0.002	0	0.003
Sb	4.24	3.64	4.55	4.46	5.86	5.63	11.95
Sc	0	0	0	0	0	0	0
Se	0	0	0	0	1	2	1
Sn	0.6	0.5	0.7	0.6	0.6	1.4	1
Sr	90.7	65.2	99.2	84	73.3	36.8	45.3
Ta	0.15	0.23	0.13	0.12	0.12	0.6	0.51
Te	0.09	0.06	0.28	0.43	0.44	0	0.28
Th	1.5	2.1	1.7	1.8	1.7	3.6	3.2
Tl	0.32	0.24	0.32	0.31	0.28	0.39	0.34
U	1.1	1.4	1.4	1.1	1.5	1.9	2.3
V	172	192	253	232	208	264	224
W	1.2	2	1.8	1.9	1.7	3.3	4.9
Y	12.4	11.2	14.5	14.8	15.9	21.9	20.6
Zn	167	253	196	162	212	261	392
Zr	68.3	67.8	88.1	82.3	75.3	147	131.5
<b>Alteration Index</b>	54.4	65.8	54.1	49.5	50.8	80.2	58.6
<b>CCP Index</b>	64.2	68.8	67.2	68.8	72.6	49.3	68.5

Sample ID	E42RL1155- 17	E42RL1155- 18	E42RL1155- 19	E42RL1155- 20	E42RL1155- 21	E42RL1167- 10	E42RL1167- 11
True Depth (m)	45.00	45.00	45.00	45.00	45.00	33.00	33.00
Ti	0.245	0.253	0.281	0.252	0.239	0.712	0.628
Al	8.72	8.99	9.34	8.8	6.51	10.6	9.68
Fe	4.04	3.88	3.34	4.89	4.72	2.45	4.86
Mg	0.85	0.63	0.43	0.74	1.53	0.41	0.38
Ca	2.08	1.57	0.59	1.67	3.85	0.06	0.06
Na	0.17	0.19	0.17	0.12	0.08	0.17	0.15
K	3.54	3.63	3.51	3.65	2.19	4.89	4.71
S	0.18	0.14	0.35	0.29	0.68	0.18	0.64
Ag	0.4	0.34	0.23	0.23	0.2	0.82	1.36
As	39.9	18.2	31.9	21.2	20.9	155.5	153.5
Au	0.07	0.1	0.13	0.09	0.07	0.02	0.45
Ba	940	790	830	750	1720	420	540
Be	1.37	1.57	1.96	0.93	0.97	0.86	0.96
Bi	0.02	0.19	0.02	0.02	0.05	0.71	0.08
Cd	0.64	1.07	0.06	0.12	0.15	0.47	0.95
Ce	24.8	29.6	35	26.1	36.5	46.5	42.6
Co	9.9	9.7	11.8	13.1	15.6	2.3	2.1
Cr	5	18	20	30	41	74	107
Cs	3.17	2.68	2.86	2.09	1.97	1.96	2.81
Cu	8.7	98.9	46.1	56.1	42.5	22.4	42
Ga	13.85	14.95	16.55	15.5	13.7	20.7	21
Ge	0.12	0.11	0.11	0.16	0.11	0.11	0.12
Hf	2.4	2.5	2.7	2.4	2.9	4.3	3.7
Hg	0.013	0.025	0.012	0.009	0.01	0.009	0.014
In	0.032	0.036	0.023	0.02	0.039	0.039	0.06
La	10.2	12.4	15	10.6	15	19.1	18.2
Li	2.7	2.7	11	7.4	17.5	5.4	6.3
Mn	1545	1295	371	1515	1470	102	62
Mo	0.56	0.99	1.17	0.93	0.63	1.15	0.97
Nb	3.2	3.4	3.8	3.2	3.2	7.2	6
Ni	4.2	10.5	10.1	16.1	15.8	12.9	13.3
P	870	920	970	900	850	820	1080
Pb	41.1	29.2	17.2	7.3	7.5	732	94
Rb	66.9	73.3	75	72.1	43.3	68.5	61
Re	0	0.002	0.002	0	0	0	0
Sb	3.86	4.2	4.41	3.85	3.77	10.1	6.76
Sc	0	0	0	0	0	43.7	39
Se	0	0	1	0	0	0	0
Sn	0.5	0.5	0.7	0.6	0.7	1.2	1.1
Sr	84.5	75.7	69.8	56.9	112	250	256
Ta	0.19	0.2	0.21	0.19	0.18	0.52	0.44
Te	0	0	0	0.08	0.16	1.07	1.04
Th	1	1.1	1.4	1.1	2	3.8	3.3
Tl	0.23	0.25	0.23	0.23	0.13	0.29	0.27
U	0.9	0.7	1.1	0.6	1.1	2.2	1.9
V	103	110	116	117	123	337	338
W	1.9	1.5	1	1	0.6	10	9.2
Y	12.9	13	13.1	11.1	11.5	13.6	11.5
Zn	130	223	108	102	114	167	293
Zr	71.3	74.4	80.9	71	84.3	120	113.5
<b>Alteration Index</b>	64.4	68.8	82.4	69.2	48.5	95.5	95.7
<b>CCP Index</b>	59.5	56.6	52.9	62.3	75.8	38.5	53.9

Sample ID	E42RL1167- 12	E42RL1167- 16	E42RL1167- 18	E42RL1167- 19	E42RL1167- 20	E42RL1167- 21	E42RL1167- 6
True Depth (m)	33.00	33.00	33.00	33.00	33.00	33.00	33.00
Ti	0.695	0.467	0.366	0.378	0.448	0.417	0.442
Al	10.6	10.75	8.81	9.44	9.4	9.51	8.25
Fe	2.85	3.14	6.21	5.52	3.91	4.48	2.7
Mg	0.4	0.41	0.31	1.35	0.33	1.13	0.31
Ca	0.05	0.05	4.23	4.58	2.14	4.74	0.07
Na	0.16	0.15	0.17	0.09	0.14	0.1	0.1
K	4.93	4.78	4.19	3.85	4.52	4.47	3.85
S	0.18	0.11	0.02	0.33	0.01	0.48	0.06
Ag	0.62	2.69	0.75	2.47	1.04	0.75	1.98
As	116	263	56.1	40.9	103.5	32.4	155
Au	0.03	0.08	0.07	0.07	0.03	0.24	0.09
Ba	380	290	520	320	390	310	720
Be	0.71	1.01	1.11	0.8	1.46	1.04	1.59
Bi	0.13	0.11	0.25	0.08	0.25	0.05	0.62
Cd	0.59	1.22	5.15	8.51	22.2	8.52	1.22
Ce	44.5	21	21.2	23	31.5	22.3	37.3
Co	5.9	13.4	30.8	19.4	15.7	17.1	2.2
Cr	114	1	0	1	14	1	8
Cs	1.83	2.66	2.49	2.1	3.55	3.34	1.51
Cu	37.2	288	101.5	65.1	151	107	38.2
Ga	21.6	22.8	18.95	19.3	22.6	19.95	21.6
Ge	0.09	0.11	0.14	0.14	0.12	0.12	0.1
Hf	4.4	2.8	2.3	2.2	3.2	2.4	3.6
Hg	0.008	0.021	0.035	0.106	0.044	0.01	0.047
In	0.037	0.062	0.064	0.07	0.082	0.062	0.048
La	18.1	9.9	8.5	9.6	12.9	9.2	15.8
Li	7.2	3.7	5.6	10.1	3.6	3.9	3.3
Mn	400	1335	3710	1425	1510	1635	319
Mo	1.03	1.14	1.15	0.92	1.16	0.78	2.7
Nb	7.4	4.9	4.2	4.1	5	4.4	4.5
Ni	12.7	1.7	4.5	3.9	5.6	4.7	1.1
P	610	350	690	690	1110	720	520
Pb	87.2	1535	68.5	89.2	658	27.2	85.1
Rb	66.6	75.9	65.2	62.4	79.6	77.7	87.3
Re	0	0	0	0	0	0	0
Sb	6.99	9.03	3.54	3.85	7.95	4.88	4.88
Sc	37.2	24.9	19.6	21.7	27.3	25.7	22.2
Se	0	1	0	0	1	1	0
Sn	1.2	0.8	0.7	0.7	1	0.7	1.1
Sr	183.5	216	107.5	155.5	72	98.9	320
Ta	0.56	0.33	0.29	0.28	0.31	0.29	0.23
Te	0.79	0.6	0.33	0.14	0.66	0.23	0.8
Th	3.8	1.4	1.1	1.1	2.1	1.2	3
Tl	0.29	0.26	0.23	0.2	0.28	0.24	0.23
U	2.3	1.1	0.9	0.7	1.5	0.8	1.8
V	314	182	141	146	185	164	152
W	9.4	4.2	1.8	1.3	4.3	3.9	3.3
Y	15.5	13.2	18.4	17.1	18.6	18.3	15.1
Zn	140	662	559	208	898	196	368
Zr	124.5	92.4	77.1	76	111	81.9	129
<b>Alteration Index</b>	95.9	95.9	47.5	51.3	65.3	51.8	95.7
<b>CCP Index</b>	41.3	44.2	61.7	66.2	49.7	58.0	45.5

Sample ID	E42RL1167- 7	E42RL1167- 8	E42RL1167- 9	E42RL1170- 10	E42RL1170- 11	E42RL1170- 12	E42RL1170- 13
True Depth (m)	33.00	33.00	33.00	30.00	30.00	30.00	30.00
Ti	0.396	0.564	0.614	0.362	0.631	0.378	0.39
Al	8.55	8.96	10.1	8.38	10.1	9.24	9.51
Fe	4.04	4.92	6.57	6.56	7.55	6.66	7.48
Mg	0.44	0.33	0.37	0.91	1.07	0.99	1.16
Ca	0.31	0.06	0.06	0.09	0.2	0.31	0.22
Na	0.12	0.13	0.13	0.26	1.79	3.57	3.51
K	3.51	4.05	4.72	3.81	2.47	1.35	1.38
S	0.01	0.09	0.23	0.01	0.02	0.02	0.03
Ag	0.83	1.27	1.07	0.39	0.76	0.54	0.29
As	227	204	381	54.7	55.2	67.1	54.9
Au	0.45	0.54	0.82	0.48	0.61	0.47	0.21
Ba	520	860	490	760	730	770	770
Be	1.81	1.2	1.48	1.74	1.6	0.89	0.83
Bi	0.08	0.47	0.28	0.11	0.05	0.06	0.04
Cd	1.1	1.68	2.18	3.38	5.05	1.96	1.61
Ce	52.6	35.9	35.6	49.2	47.1	31.4	38.5
Co	10.7	6	2.6	24.2	45.5	24	29.8
Cr	7	133	127	10	5	35	37
Cs	1.41	4.58	5.32	2.62	3.12	0.96	1.32
Cu	30.7	68.2	119	120	427	241	172
Ga	20.5	20.6	19.65	16.6	20.8	17.4	18.6
Ge	0.12	0.13	0.17	0.14	0.15	0.11	0.15
Hf	3.8	3.4	3.7	3.4	4.4	2	2.5
Hg	0.015	0.023	0.027	0.026	0.017	0.01	0.012
In	0.073	0.149	0.155	0.059	0.06	0.055	0.058
La	22.7	15.5	15.4	20.8	17.3	12.4	15.5
Li	12.3	8	6.3	17.8	12.2	11.1	14.8
Mn	718	440	81	3050	4250	3020	2810
Mo	2.16	1.48	1.62	0.77	1.08	1.24	1.17
Nb	4.3	6	5.7	3.2	8.4	2.1	2.4
Ni	3.6	15.9	14.8	19.9	17.9	18.5	21.1
P	1350	980	1340	680	850	1070	570
Pb	78.6	198	119	22.7	47.2	171.5	21.4
Rb	60.6	63.6	59.7	82.4	65.2	20.3	19.5
Re	0	0	0	0	0.002	0	0
Sb	5.18	7.89	8.24	2.93	3.68	1.76	1.65
Sc	20.9	46.5	42.8	20.7	24.7	31.3	31.8
Se	0	0	0	0	0	0	0
Sn	1.2	1.1	0.9	0.9	1.2	0.6	0.7
Sr	168	172	171	50.1	157.5	194	171.5
Ta	0.24	0.39	0.44	0.23	0.64	0.16	0.16
Te	0.19	4.18	2.93	0.32	0.05	0.21	0.19
Th	3.1	3	3.5	2.7	3.8	1.2	1.7
Tl	0.18	0.24	0.26	0.33	0.2	0.09	0.07
U	1.8	2	2.5	1.8	2.7	2.6	2.9
V	134	307	332	164	248	266	276
W	3.1	12.9	12.7	2.5	1.6	2.4	2.2
Y	19.9	13.5	13.9	22.2	24.1	16.3	16.3
Zn	287	527	590	1160	1315	1040	793
Zr	135.5	120	119	99.2	123	57.9	68.6
<b>Alteration Index</b>	89.3	95.4	96.0	92.8	63.8	38.4	41.6
<b>CCP Index</b>	57.4	57.6	60.7	66.8	68.1	61.3	64.4

Sample ID	E42RL1170- 14	E42RL1170- 15	E42RL1170- 16	E42RL1170- 2	E42RL1170- 3	E42RL1170- 4	E42RL1170- 5
True Depth (m)	30.00	30.00	30.00	30.00	30.00	30.00	30.00
Ti	0.639	0.403	0.361	0.622	0.71	0.376	0.521
Al	10.7	9.82	8.87	9.83	10.55	10.2	9.52
Fe	7.94	7.11	7.34	3.92	2.14	2.24	8.21
Mg	0.57	0.6	1.28	0.37	0.37	0.35	0.34
Ca	0.06	0.09	0.31	0.39	0.14	0.06	0.11
Na	0.18	0.31	2.78	0.14	0.18	0.18	0.15
K	5.46	4.43	2.28	4.29	4.81	4.52	4.31
S	0.2	0.06	0.04	0.01	0.06	0.09	0.44
Ag	1.13	0.89	0.21	1.53	0.97	0.68	1.93
As	393	318	21	121.5	227	158.5	1390
Au	0.63	4.43	0.48	0.71	0.04	0.07	3.34
Ba	790	330	430	430	500	560	540
Be	1.56	1.41	0.8	1.24	0.73	0.74	0.96
Bi	0.02	0.04	0.03	0.22	0.04	0.03	0.04
Cd	5.06	3.67	1.73	3.01	0.92	0.53	4.73
Ce	40.4	24.8	25.5	41.5	50.3	21.9	48.6
Co	46.5	12.8	26.3	26	1.7	1.1	2.5
Cr	6	34	43	5	5	11	5
Cs	0.99	2.51	1.65	3.46	1.71	1.46	1.43
Cu	259	326	157.5	242	40.4	28.4	121.5
Ga	23.3	19.7	16.6	23.2	25.1	18.6	19.6
Ge	0.22	0.16	0.14	0.13	0.12	0.07	0.18
Hf	4.4	1.9	1.8	4.3	5.1	2.2	4.1
Hg	0.015	0.045	0.014	0.029	0.032	0.015	0.103
In	0.053	0.054	0.047	0.042	0.038	0.04	0.095
La	19.3	11.1	10.3	15.4	21.9	9.4	20.2
Li	6.8	8.1	15.6	8.5	3.7	3.1	3.7
Mn	5530	975	1895	2210	176	105	248
Mo	2.43	1.2	0.81	2.53	1.44	0.39	2.26
Nb	8.3	2.2	1.9	9.6	10.3	3	7
Ni	10	14.2	27.3	21.9	1.6	0.9	1.9
P	1080	850	1090	1670	1910	610	2150
Pb	631	472	18.4	450	632	311	2330
Rb	73.2	67	29.3	83.9	79.7	72.7	61.3
Re	0	0	0	0	0	0	0
Sb	11.15	7.03	2.34	6.21	6.74	4.1	18.25
Sc	25	35	31.4	29	25.1	25	25.5
Se	0	0	0	0	0	0	1
Sn	1.3	0.7	0.6	1.3	1.3	0.7	1.1
Sr	306	96.6	168.5	54.1	870	347	1370
Ta	0.6	0.15	0.13	0.6	0.74	0.21	0.51
Te	0.37	0.56	0.15	0.06	0.21	0.06	1.11
Th	3.7	1.1	1.1	3.9	4.7	1.4	3.8
Tl	0.3	0.26	0.1	0.3	0.3	0.28	0.26
U	2.4	1.6	3.6	2.6	2.7	1	2.3
V	298	342	296	246	273	251	254
W	6.4	3.8	1.1	5.1	7.7	3.3	5.6
Y	20	14.5	13.5	23.9	15.6	6.7	14.3
Zn	868	1040	747	1450	129	91	589
Zr	125	53.7	48.4	144.5	153	66.1	123.5
<b>Alteration Index</b>	95.8	92.1	53.8	88.7	93.6	94.9	94.2
<b>CCP Index</b>	62.1	63.8	64.0	51.4	35.8	37.8	67.3

Sample ID	E42RL1170- 6	E42RL1170- 7	E42RL1170- 8	E42RL1170- 9
True Depth (m)	30.00	30.00	30.00	30.00
Ti	0.339	0.352	0.387	0.393
Al	9.13	9.87	9.22	9.2
Fe	5.54	6.57	3.92	7.74
Mg	0.85	1.08	0.44	1.03
Ca	0.08	0.26	0.11	0.11
Na	0.23	0.33	0.23	0.35
K	3.33	3.63	2.97	3.09
S	0.03	0.01	0.08	0.01
Ag	0.86	0.42	1.11	0.68
As	189	58.9	120.5	68.6
Au	0.29	0.43	0.79	1.74
Ba	550	400	470	730
Be	1.16	1.12	1.33	2.62
Bi	0.12	0.03	0.06	0.06
Cd	3.82	1.64	2.02	3.13
Ce	58.7	25.9	46.8	30.9
Co	24.4	19.9	16	28.6
Cr	23	12	11	21
Cs	4.38	5.23	1.9	3.97
Cu	315	119.5	110.5	219
Ga	17.95	18.15	18.1	18.15
Ge	0.16	0.14	0.11	0.2
Hf	5.6	2.1	3	2.4
Hg	0.029	0.026	0.018	0.041
In	0.047	0.051	0.067	0.067
La	23.5	11.2	22.6	11.9
Li	12.9	25.1	7.7	30.3
Mn	1435	1695	1310	3290
Mo	0.75	0.58	1.3	0.77
Nb	5.2	2.8	3.3	2.6
Ni	15.3	10.5	3.6	32.4
P	670	1060	850	1070
Pb	214	19.8	284	25.3
Rb	57.6	61.8	45	75.2
Re	0	0	0	0.002
Sb	3.79	2.54	4.37	2.67
Sc	18.4	27.4	21.4	27
Se	0	0	0	0
Sn	1	0.5	0.9	0.8
Sr	100	65.4	439	87.9
Ta	0.34	0.2	0.2	0.21
Te	0.19	0.07	0.53	0.11
Th	5.2	1.5	2.6	2.1
Tl	0.23	0.33	0.19	0.36
U	3.7	1.4	1.9	1.5
V	140	227	157	242
W	2.7	1.8	3.1	2
Y	21.7	12.2	13.7	21
Zn	1710	520	879	1815
Zr	173	63.7	90.7	68
<b>Alteration Index</b>	92.8	88.4	90.3	89.7
<b>CCP Index</b>	66.4	68.0	59.8	73.6